AD-754 249

INTERFACE AND MECHANICS RESEARCH IN FIBER REINFORCED COMPOSITES

Harry R. Nara

Case Western Reserve University

Prepared for:

Air Force Materials Laboratory

March 1972

DISTRIBUTED BY:

NTIS

National Technical Information Service
U. S. DEPARTMENT OF COMMERCE
5285 Port Royal Road, Springfield Va. 22151

AD754249

AFML-TR-71-260

INTERFACE AND MECHANICS RESEARCH IN FIBER REINFORCED COMPOSITES

H.R. Nara

Case Western Reserve University

TECHNICAL REPORT AFML-TR-71-260

March 1972

D D C
RECEIVED
JAN 17 1973
B

Reproduced by
NATIONAL TECHNICAL
INFORMATION SERVICE
U S Department of Commerce
Springfield VA 22151

Approved for public release; distribution unlimited.

AIR FORCE MATERIALS LABORATORY

AIR FORCE SYSTEMS COMMAND

WRIGHT-PATTERSON AIR FORCE BASE, OHIO

NOTICES

When Government drawings, specifications, and other data are used for any purpose other than in connection with a definitely related Government procurement operation, the United State Government thereby incurs no responsibility nor any obligation whatsoever; and the fact that the Government may have formulated, furnished, or in any way supplied the said drawings, specifications or other data, is not to be regarded by implication or otherwise as in any manner licensing the holder or any other person or corporation, or conveying any rights or permission to manufacture, use or sell any patented invention that may in any way be related thereto.

This document is subject to special export controls and each transmittal to foreign Governments or foreign Nationals may be made only with prior approval of the Nonmetallic Materials Division, AFML/LN, Air Force Materials Laboratory, Wright-Patterson Air Force Base, Ohio 45433.

Copies of this report should not be returned unless return is required by security considerations, contractual obligations or notice on a specific document

Unclassified
Security Classification

DOCUMENT CONTROL DATA - R & D

(Security classification of title, body of abstract and indexing annotation must be entered when the overall report is classified)

1 ORIGINATING ACTIVITY *(Corporate author)* Case Western Reserve University	2a. REPORT SECURITY CLASSIFICATION Unclassified 2b. GROUP

3 REPORT TITLE
Interface and Mechanics Research in Fiber Reinforced Composites

4 DESCRIPTIVE NOTES *(Type of report and inclusive dates)*
Summary Technical Report May 1970-May 1971

5. AUTHOR(S) *(First name, middle initial, last name)*
Harry R. Nara

6 REPORT DATE March 1972	7a. TOTAL NO. OF PAGES 262 +xiii	7b. NO. OF REFS 130
8a. CONTRACT OR GRANT NO F33615-70-C-1016 b. PROJECT NO. ARPA Order No. 719 c. Program Code 9D10 d.	9a. ORIGINATOR'S REPORT NUMBER(S) AFML-TR-71-260 9b. OTHER REPORT NO(S) *(Any other numbers that may be assigned this report)*	

10 DISTRIBUTION STATEMENT
Approved for public release; Distribution unlimited

11. SUPPLEMENTARY NOTES	12. SPONSORING MILITARY ACTIVITY Air Force Materials Laboratory Wright-Patterson A F B, Ohio

13 ABSTRACT

Experimental and analytical investigations were performed to provide increased understanding of the fundamental behavior of fiber reinforced plastic composites. The research was conducted in a number of discrete tasks which were grouped into three principal categories, namely: materials research, mechanics of composites, and analysis and design of composite structures.

In the materials research category, information on the physical and chemical characteristics of graphite fiber surfaces was obtained using gas and liquid adsorption techniques and mass spectrometry. This information provides a new insight into the relationship between graphite fiber surface characteristics and their adhesion (or lack of adhesion) to plastic matrices. In an investigation targeted to develop composites having improved fiber-matrix adhesion and higher tougnness, graphite fiber-nylon 6 matrix composites were prepared by in-situ polymerization of nylon in a reaction vessel containing the fibers. The composites had promising mechanical behavior, but optimum engineering properties were not obtained due to difficulties in achieving high fiber content, good fiber alignment and low void content.

In the mechanics of composites category, four research tasks were completed. Exact analytical solutions were obtained for longitudinal shear deformation of composites. Analyses were performed to define the stress field in composites containing circular inclusions in various types of arrays. In an investigation using the scattered light photoelastic technique, apparatus was completed for investigating the stress distribution in composites while load is applied to the composite. An

(continued)

DD FORM 1 NOV 65 1473

Security Classification

14 KEY WORDS	LINK A ROLE	LINK A WT	LINK B ROLE	LINK B WT	LINK C ROLE	LINK C WT
Carbon Fibers						
Composites						
Surface Studies						
In-Situ Polymerization						
Photoelasticity						
Fracture Mechanics						
Inclusion Problems						
Plate Buckling						
Plates With Cut-Outs						
Large Displacements						
Ultimate Load						
Cylinder Buckling						

Abstract continued

experimental investigation was performed to relate fracture characteristics of unidirectional fibers reinforced plastic composites to specimen thickness, void content, and loading rate.

In research related to analysis and design of composite structures, a finite displacement analysis method was developed for laminated plates subjected to membrane compression, lateral pressure, and an arbitrary temperature distribution. The ultimate strength of buckled laminated plates and the effects of cutouts on the post-buckling response was investigated both analytically and experimentally. The exact solution was obtained for the buckling of anisotropic cylindrical shells.

INTERFACE AND MECHANICS RESEARCH IN FIBER REINFORCED COMPOSITES

H. R. NARA

CASE WESTERN RESERVE UNIVERSITY

TECHNICAL REPORT AFML-TR-71-260

March 1972

Approved for public release; distribution unlimited

Air Force Materials Laboratory
Air Force Systems Command
Wright-Patterson Air Force Base, Ohio

ic

FOREWORD

The work reported herein was performed under the sponsorship of the Advanced Research Projects Agency, Department of Defense, through Contract F33615-70-C-1016, ARPA Order No. 719, Program Code 9D10. Technical direction of the contract was performed by the Air Force Materials Laboratory, Nonmetallic Materials Division, Wright-Patterson Air Force Base, Ohio. Mr. H. S. Schwartz is the Air Force Program Manager.

This work is a follow-on to the effort under Contracts AF 33(615)-3110 which had covered the period May 17, 1965 to June 17, 1969 and F33615-68-C-1077 which covered the period May 17, 1969 to May 17, 1970.

The contractor is Case Western Reserve University, with Dr. H. R. Nara (phone 216-368-4414) as program supervisor.

This is the final report for the contract period May 17, 1970 to May 16, 1971.

This report was submitted by the author October 1971.

This report has been reviewed and is approved.

A. M. LOVELACE
Director
Air Force Materials Laboratory

ABSTRACT

Experimental and analytical investigations were performed to provide increased understanding of the fundamental behavior of fiber reinforced plastic composites. The research was conducted in a number of discrete tasks which were grouped into three principal categories, namely: materials research, mechanics of composites, and analysis and design of composite structures.

In the materials research category, information on the physical and chemical characteristics of graphite fiber surfaces was obtained using gas and liquid adsorption techniques and mass spectrometry. This information provides a new insight into the relationship between graphite fiber surface characteristics and their adhesion (or lack of adhesion) to plastic matrices. In an investigation targeted to develop composites having improved fiber-matrix adhesion and higher toughness, graphite fiber-nylon 6 matrix composites were prepared by in-situ polymerization of nylon in a reaction vessel containing the fibers. The composites had promising mechanical behavior, but optimum engineering properties were not obtained due to difficulties in achieving high fiber content, good fiber alignment and low void content.

In the mechanics of composites category, four research tasks were completed. Exact analytical solutions were obtained for longitudinal shear deformation of composites. Analyses were performed to define the stress field in composites containing circular inclusions in various types of arrays. In an investigation using the scattered light photoelastic technique, apparatus was completed for investigating the stress distribution in composites while load is applied to the composite. An experimental investigation was performed to relate fracture characteristics of unidirectional fiber reinforced plastic composites to specimen thickness, void content, and loading rate.

In research related to analysis and design of composite structures, a finite displacement analysis method was developed for laminated plates subjected to membrane compression, lateral pressure, and an arbitrary temperature distribution. The ultimate strength of buckled laminated plates and the effects of cutouts on the post-buckling response was investigated both analytically and experimentally. The exact solution was obtained for the buckling anisotropic cylindrical shells.

TABLE OF CONTENTS

SECTION

I. INTRODUCTION

II. SUMMARY

III. MATERIALS RESEARCH

A. Structure Analysis of Graphite Fiber Surfaces Through Low Temperature Inert Gas Adsorption and Mass Spectrometry

B. Adsorption from Solution onto "Thornel-50" Fiber Surfaces

C. Nylon Graphite Composites by In-Situ Polymerization

IV. MECHANICS OF COMPOSITES

A. Longitudinal Shear Deformation of Composites

B. Multiple Circular Inclusion Problems in Plane Elastostatics

C. Scattered Light Photoelasticity

D. An Experimental Study of the Fracture Properties of Unidirectional Composite Materials

V. ANALYSIS AND DESIGN OF COMPOSITE STRUCTURES

A. Finite Displacement Analysis of Laminated Composite Plates

B. Post-Buckling Strength of Anisotropic Plates

C. Buckling of Laminated Composite Plates with Cutouts

D. Buckling of Anisotropic Circular Cylindrical Shells

REFERENCES

LIST OF FIGURES

SECTION	FIGURE		PAGE
III-A	1	Microgravimetric Gas Adsorption Apparatus	
	2	Adsorption Apparatus and Measuring Equipment	
	3	Microbalance Cryostat	
	4	Total Gas Evolved on Vacuum Heat Treating "Thornel-50" Fibers	
	5	Composition of Gases Evolved on Vacuum Heat Treating "Thornel-50" Fibers	
	6	Evolution of CO, CO_2 and H_2O on Vacuum Heating "Thornel-50" Fibers	
	7	Scanning Electron Microscope Photograph of "Thornel-50" Fiber Surface	
	8	Scanning Electron Microscope Photograph Showing the Cross Section of "Thornel-50" Fibers	
	9	Adsorption Isotherm for Nitrogen, at 77.3°K, on "Thornel-50" Fibers Vacuum Heat Treated at 880°C.	
	10	Low Coverage Isotherm for Nitrogen at 77.3°K, on "Thornel-50" Fibers Vacuum Heat Treated at 880°C.	
	11	Extreme Low Coverage Isotherm for Nitrogen, at 77.3°K, on "Thornel-50" Fibers Vacuum Heat Treated at 880°C.	
	12	B.E.T. Plot, for Nitrogen at 77.3°K, on "Thornel-50" Fibers Vacuum Heat Treated at 590°C.	
	13	B.E.T. Plot, for Argon at 90.2°K, on "Thornel-50" Fibers Vacuum Heat Treated at 490°C.	
	14	Kagamer Plot, for Argon at 77.3°K and 90.2°K, on "Thornel-50" Fibers Vacuum Heat Treated at 490°C.	

SECTION	FIGURE		PAGE
	15	t-Plot, for Nitrogen at 77.3°K, on "Thornel-50" Fibers Vacuum Heat Treated at 880°C.	
	16	t-Plot, for Nitrogen at 77.3°K on "Thornel-50" Fibers Vacuum Heat Treated at 880°C.	
	17	Isosteric Heats and Differential Entropies of Adsorption for Nitrogen on "Thornel-50" Fibers Vacuum Heat Treated at 290°C, 325°C, 660°C and 880°C.	
	18	Isosteric Heats and Differential Entropies of Adsorption for Argon on "Thornel-50" Fibers Vacuum Heat Treated at 325°C.	
III-B	1	Liquid Chromatograph	
	2	Adsorption of Stearic Acid on Carbon	
	3	Adsorption of Octodecane on "Thornel-50"	
	4	Adsorption of Benzoic Acid on "Thornel-50"	
	5	Adsorption of Octadecane on "Thornel-50" Langmuir Plot	
	6	Adsorption of Stearic Acid on "Thornel-50" Langmuir Plot	
	7	Adsorption of Benzoic Acid on "Thornel-50" Langmuir Plot	
	8	Isosteric Heats of Adsorption on Stearic Acid on "Thornel-50"	
III-C	1	Sample 54A-1 x 500 Fracture Surface	
	2	Sample 54A-1 x 1000 Fracture Surface, Different Location	
	3	Sample 54A-1 x 5000 Fracture Surface, Center of Figure 2	
	4	Sample 54B-1 x 1000 Fracture Surface	

SECTION	FIGURE		PAGE
	5	Sample 54B-1 x 5000 Fracture Surface	
	6	Sample 67 x 1000 Fracture Surface	
	7	Sample 67 x 5000 Fracture Surface, Center of Figure 6	
	8	Sample 56C-2 x 1000, Fracture Surface	
	9	Sample 56B-2 x 1000, Fracture Surface	
IV-A	1	Arbitrary number of inclusions with radii R_i placed at the points a_i	
	2	Period Parallelogram for Regular Array of Inclusions	
	3	Ratio of Effective Shear Modulus to Matrix Shear Modulus versus Fiber Volume Content for Glass-epoxy Composite (μ_f/μ_o = 20 or K = 0.905) Based on Square Array Model	
	4	Ratio of Effective Shear Modulus to Matrix Shear Modulus versus Fiber Volume Content for boron-epoxy Composite (μ_f/μ_o = 120 or K = 0.9835) Based on Square Array Model	
	5	Typical Distribution of Inclusions Used for the Random Model of a Composite	
	6	Maximum Shearing stress σ_{rz} versus Fiber Volume Content for Glass-eposy (μ_f/μ_o = 20) and Boron-epoxy (μ_f/μ_o = 120) Composite Based on Square Array Model	
	7	Maximum Shearing Stress σ_{rz} versus Fiber Volume Content for Glass-epoxy Composite (μ_f/μ_o = 20) Based on Hexagonal Array Model	
	8	Representative Region for Computation of the Constant β	

SECTION	FIGURE		PAGE
IV-B	1	Inclusion of Radius R_i at Origin of Coordinates	
	2	N Inclusions with Radii R_i Placed at the Points a_i in an Unbounded Matrix	
	3	$\sigma_{\rho\rho o}$ at the Interface vs θ for $\gamma_i = 1$ and Discrete Values of v in Case of Uniaxial Tension	
	4	$\sigma_{\rho\theta o}$ at the Interface vs θ for $\gamma_i = 1$ and Discrete Values of v in Case of Uniaxial Tension	
	5	$\sigma_{\rho\theta o}$ at the Interface vs θ for $\gamma_i = 1$ and Discrete Values of v in case of Uniaxial Tension	
	6	σ_{xxo} on x = a vs y for $\gamma_i = 1$ and Discrete Values of v in case of Uniaxial Tension	
	7	$\sigma_{\rho\rho o}$ at the Interface vs θ for $\gamma_i = 1$ and Discrete Values of v for the Bending Case	
	8	$\sigma_{\rho\rho o}$ at the Interface vs θ for $\gamma_i = 1$ and Discrete Values of v for the Bending Case	
	9	$\sigma_{\rho\theta o}$ at the Interface vs θ for $\gamma_i = 1$ and Discrete Values of v for the Bending Case	
	10	σ_{xxo} at x = a vs y for $\gamma_i = 1$ and Discrete Values of v for the Bending Case	
	11	Arbitrary Array of Equal Inclusions	
	12	$\sigma_{\rho\rho o}$ at the Interface for Particular Inclusions from Figure 11 for $\gamma_i = 1$ in Case of Uniaxial Tension	

SECTION	FIGURE		PAGE
	13	$\sigma_{\theta\theta o}$ at the Interface for Particular Inclusions from Figure 11 for $\gamma_i = 1$ in Case of Uniaxial Tension	
	14	$\sigma_{\rho\theta o}$ at the Interface for Particular Inclusions from Figure 11 for $\gamma_i = 1$ in Case of Uniaxial Tension	
IV-C	1	Degree of Freedom of the Live Loading Fixture	
	2	Sequence of Orientations for Viewing Model	
	3	Ports for the Axial Load Actuator and Two Ports for the Torque Actuator	
	4	Exterior View of the Axial Load Actuator on the Base Plate	
	5.	Outer Shell and Axial Load Actuator Next to the Inside View of the Torque Tube	
	6	Assembled Hydraulic Actuator with the Cover Plate Off	
	7	Adjustable C-Frame	
	8	View Behind the Back Plate Showing the Tilting Mechanisms and the End of the Drive Shaft for the Height Adjusting Mechanism	
	9	Upside Down View of the Load Ring with the Concentrated Compression Load Applicator in the Load Ring. One of the Four Axial Load Sensing Elements is also Shown.	
	10	Partially Assembled Live-Load Loading Frame with the Model in Upright Position. Three Glass Plates and the Angle Frame to Hold the Glass Plates in Place are Missing	

SECTION	FIGURE		PAGE
	11	Partially Assembled Live-Load Loading Frame with the Model in Tilted Position	
IV-D	1	Specimen Showing Fatigue Crack (7x)	
	2	End View of Fracture Surface Showing Initial Crack Length	
	3	Fixture for Three Point Bend Test	
	4	Influence of Specimen Thickness on Stress Intensity Factor, Crack Length Ratio = 0.5 inch	
	5	Influence of Crack Length Ratio on Field Stress, Specimens 9100, Thickness = 0.1 inch	
	6	Influence of Crack Length Ratio on Field Stress, Specimens 9110, Thickness = 0.3 inch	
	7	Influence of Crack Length Ratio on Field Stress, Specimens 9120, Thickness = 0.5 inch	
	8	Influence of Crack Length Ratio on Field Stress, Specimens 9130, Thickness = 1.0 inch	
	9	Influence of Specimen Thickness on Normal Stress for all Specimens, Crack Length Ratio = 0.5 inch	
	10	Influence of Void Content on Stress Intensity Factors for Various Thicknesses	
	11	Influence of Loading Rate on Stress Intensity Factor, Specimens 8249	
	12	Load-Crack Opening Displacement Curve for Specimens 0-9100 - A,B,C, & D	
	13	Influence of Specimen Thickness on the Slope of the Log Field Stress versus Log Crack Length Ratio Curve	

SECTION	FIGURE		PAGE
V-A	1	Planform View of Laminated Plate	
	2	Solution to Problem Set #1	
	3	Solution to Problem Set #2	
	4	Solutions to Problem Set #3	
V-B	1	Post Buckling Load Distribution	
	2	Post Buckling Analysis Model	
	3	Schematic Diagram for Unbuckled Compression Testing Fixture without Deformation Measurement Attachment	
V-D	1	Shell Geometry and Layer Configuration	
	2	Stress Resultants and Stress Couples in Shell Element	
	3	Buckling Load for Case 1: Isotropic, Axial Compression, SS4, Flugge's Theory	
	4	Buckling Load for Case 2: 3(0,90,0) Radial Pressure, Cl, Flugge's Theory	
	5	Buckling Load for Case 3: 3(0,90,0) Axial Compression, Cl, Flugge's Theory	
	6	Buckling Load for Case 4: 3(0,90,0) Torsion, Cl, Flugge's Theory	
	7	Buckling Load for Case 5: 4(0,±22.5,90) Radial Pressure, SS4, Flugge's Theory	
	8	Buckling Load for Case 6: 4(0,±22.5,90) Axial Pressure SS4, Flugge's Theory	
	9	Buckling Load for Case 7: 4(0,±22.5,90) Axial Compression, SS1, Flugge's Theory	

SECTION	FIGURE		PAGE
	10	Buckling Load for Case 8: 4(0,±22.5,90) Torsion, SS4, Flugge's Theory	
	11	Buckling Load for Case 9: 4(0,±22.5,90) Radial Pressure, SS4, Donnell's Theory	
	12	Buckling Load for Case 10: 4(0,±22.5,90) Axial Compression, SS4, Donnell's Theory	
	13	Buckling Load for Case 11: 4(0,±22.5,90) Torsion, SS4, Donnell's Theory	
	14	Buckling Load for Case 12: 4(0,±22.5,90) Combined Radial Pressure and Torsion, SS4, Donnell's Theory	
	15	Buckling Load for Case 12: External Pressure Portion Enlarged	
	16	Buckling Load for Case 13: 4(0,±22.5.90) Combined Radial Pressure and Torsion, SS4, Flugge's Theory	
	17	Buckling Load for Case 14: 4(0,±22.5,90) Combined Axial Pressure and Torsion, SS4, Flugge's Theory	
	18	Buckling Load for Case 15: 4(0,±22.5,90) Combined Axial Compression and Radial Pressure, SS4, Flugge's Theory	
	19	Buckling Load for Case 16: 4(0,±22.5,90) Hydrostatic Pressure, SS4, Flugge's Theory	
	20	Buckling Load for Case 17: 4(0,±22.5,90) Hydrostatic Pressure, SS4, Donnell's Theory	

LIST OF TABLES

SECTION	TABLE	TITLE	PAGE
III-A	I	Supplier's Analyses of Absorbate Gases	
	II	Absorbate Molecular Cross Sectional Areas in $Å^2$	
	III	Specific Surface Areas, $A^{sp}(m^2gm)$ of Vacuum Heat Treated "Thornel-50" Graphite Fibers	
	IV	Comparison of A^{sp} - Determined with N_2 and Ar	
III-B	I	Measurement of Dead-Volume	
III-C	I	Comparison of Co-Catalysts	
	II	Test Data for Composites	
IV-D	I	Material Properties and Summary of Results	
V-B	I	List of Specimens Tested	
	II	Summary of Results: Unbuckled Compression Tests	
	III	List of Plates Tested	
	IV	Critical Load, Predicted and Observed Post Buckled Ultimate Strengths	
V-D	I	Classification of Numerical Results	
	II	Buckling Loads and Circumferential Wave Numbers	
	III	Classification of Numerical Examples	

SECTION I

INTRODUCTION

The program, "Integrated Research on Carbon Composite Materials," was initiated in May 1965 under a contract through the Air Force Materials Laboratory. Union Carbide Corporation was the prime contractor with Bell Aerosystems and Case Western Reserve University as subcontractors. The work conducted under these initial contracts can be found in the Annual Reports AFML-TR-66-310, Parts I, II, III, IV and V. In May 1970, Case Western Reserve University continued the work initiated under these contracts through a new contract (F33-615-70-C-1016).

This is the final report prepared under this new contract. All of the projects reported herein were initiated under the original contracts. The reader is referred to the previously published Annual Reports for the definition of individual projects. This report is divided into three sections:

(a) Materials Research

(b) Mechanics of Composites

(c) Analysis and Design of Composite Structures

Projects which were completed at the end of the contract period are reported in self contained sections including an individual Abstract, Introduction, References, etc. Projects which were incomplete at the end of the contract period are reported with only a summary report.

SECTION II

SUMMARY

Materials Research

A. Structure Analysis of Graphite Fiber Surfaces Through Low Temperature Inert Gas Adsorption and Mass Spectrometry

A study was made of the surface properties of unsized vacuum heat treated "Thornel 50" graphite fibers. The techniques used were low temperature inert gas adsorption by microgravimetry, and mass spectrometry. The experiments showed that graphite fiber specific surface area was low - on the order of 1 m^2/g. This specific surface first decreased and then increased as the fibers were heated to higher and higher temperatures. The shape of the adsorption isotherms, the calculated differential thermodynamics of adsorption, comparison of adsorption data for fibers heat treated to different temperatures, analysis of the mass spectra of gases evolved during heating, and the known dimensions of the graphite crystallites provided strong evidence for three kinds of adsorption site patches on the fiber. These were identified as the tops, edges, and oxidized edges of oriented graphite crystallites in the fiber surface. The fractions of the fiber surface composed of these three patch types were ca. 0.67, ca. 0.26 and ca. 0.07. Vacuum heat treatment decreased the oxidized edge and increased the unoxidized edge surface. Lack of adsorption hysteresis at high relative pressures suggested a negligible number of large pores opening to the outside of the fiber. However, presence of a relatively large number of micropores was indicated. Comparison of the BET surface area obtained with nitrogen at 77°K with a calculation based on scanning electron microscopy indicated a fiber roughness factor of 3.

B. Adsorption from Solution onto "Thornel-50" Fiber Surfaces

The adsorption of stearic acid, octadecane, and benzoic acid - from solution in cyclohexane onto "Thornel-50" fiber surfaces - was studied by continuous flow column chromatography. Fiber surface area, and the energetics of solute adsorption as a function of surface coverage, were evaluated from the adsorption data. All three solutes were shown to form adsorbed close packed monolayers of horizontally oriented molecules when surface saturation was achieved. The specific surface area of the fibers calculated from the saturation adsorption values was ca. 1.3 m^2/gram. Affinities of the solutes for the fiber surface increased in the order

octadecane < benzoic acid < stearic acid. Isosteric heat calculations, made for the coverage range of 25 to 100 percent, indicated weak (physical) adsorption of stearic acid and suggested that any active adsorption sites present comprise only a small fraction of the fiber surface area.

C. Nylon 6/Graphite Fiber Composites by In Situ Polymerization

The in situ polymerization of caprolactam to Nylon 6 was investigated as a method for making graphite fiber composites. It was necessary to find a co-catalyst (using sodium caprolactam as catalyst) which could be mixed at about 100°C and where the final mixture had a long enough pot life to allow for mixing and application to the fibers. The temperature could then be raised to 200°C to initiate rapid polymerization.

Co-catalysts tested were all esters as these had earlier been shown to have appropriate lifetimes. They were phenyl acetate, benzyl acetate, benzyl benzoate, t-butyl acetate and ε-caprolactone. Benzyl derivatives gave brittle polymerizates, while the others gave tough materials. Phenyl was excluded as potentially reacting too rapidly. t-Butyl gave good polymers at 190°C but expanded into a foam when heated to 210° due to volatilization of the t-butanol. ε-Caprolactone initiated well and produced no residues, so it was chosen as the major co-catalyst.

Jigs were designed on which graphitic fiber could be wound at various tensions. These were put in tubes containing precatalyzed monomer at 100°C. The whole was degassed several times and then heated to 200°C for polymerization.

Several samples of composites were made with fiber densities of 25 to 40 volume % using "Thornel" 50S and 75S fibers. The samples still had some voids due to lack of complete penetration of monomer. The samples varied widely in their tensile strengths and moduli due mainly to variations in fiber density, but also to voids. The best samples achieved about 70% transfer of properties. This is a respectable figure when one considers that these are the first samples made at these fiber densities.

Mechanics of Composites

A. Longitudinal Shear Deformation of Composites

An exact analytical solution is given for the problem of antiplane shear loading of a unidirectional composite containing randomly distributed fibers of arbitrary radii and shear moduli. An expression for the effective shear modulus is developed. For the

case of a regular array this expression gives results that are virtually identical with the numerical solutions presented earlier. In the case of a random distribution of fibers, results that are essentially in agreement with the conclusions of Adams and Bai are obtained. Finally, the results are used to discuss the visco-elastic behavior of a composite.

B. Multiple Circular Inclusion Problems in Plane Elastostatics

The general representation, has been modified to give a more straightforward solution of the elastic boundary value problem for an unbounded matrix containing a single circular inclusion. Using these results, the problem of an unbounded matrix containing an arbitrary number of elastic inclusions (which can have any radii and elastic properties) has been solved for uniform and in-plane bending stress fields.

As the first application of the general results to composites, transverse loading of a single ply for the case of fibers having the same shear modulus as the matrix has been considered.

C. Scattered Light Photoelasticity

In the scattered-light photoelastic technique stresses are found to be proportional to the slope of the fringe order (taken with respect to distance along the light beam path). For transmitted light work stresses are proportional to the fringe order itself. Hence the scattered light technique is inherently less accurate than the transmitted light method. The potential for a full three-dimensional stress analysis without slicing or destroying the model provides compelling reason to seek ways to overcome the difficulties of obtaining high accuracy with scattered light. One promising approach which has been successfully followed, is to develop numerical techniques which will help to get the most out of the fringe data by "preventing" the derivative from becoming too erratic. A recently completed Master's degree thesis "Smoothed Spline Functions - Applications to Experimental Mechanics" (P. Shankar) summarizes this work. The techniques which have been developed are also applicable to experimental problems other than scattered light photoelasticity.

A great deal of effort has been expended in the design and fabrication of a scattered light polariscope, and recently a live loading fixture to use with that polariscope.

D. An Experimental Study of the Fracture Properties of Unidirectional Composite Materials

It has been shown by experimentation that (1) the load crack opening displacement curves give inconclusive results for the thin (0.1 inch) specimen but that the larger specimen (0.3, 0.5, and 1.0 inch) specimens appear to be close to satisfying the requirements of linear elasticity, (2) the square root singularity will be satisfied for the thin specimens, (3) the nominal stress in the specimens at fracture will be below the yield stress of the material, and (4) the value of the stress intensity factor will be a minimum for thin specimens, giving conservative results. These last three points indicate that thin specimens should be used to determine the unidirectional composite fracture toughness. The actual thickness requirement is less than the smallest thickness tested in this study because of lateral specimen stability problems in the bend test for very thin specimens. Therefore, an alternate specimen should be used, possibly a center or edge cracked tensile specimen or the recently promoted compact specimen. In fact, the work often mentioned here by Wu and Reuter (11) used a center cracked tensile specimen and is a valid test for composite fracture toughness. With the alternate specimens for which fixture nonlinearities will not exist, the load-crack opening displacement records should be further studied.

Analysis and Design of Composite Structures

A. Finite Displacement Analysis of Laminated Plates

A method of analysis for the large displacement behavior of laminated plates subjected to membrane compression, lateral pressure and the arbitrary temperature distribution is developed based on an extension of the work completed earlier by Chan. This analysis method will be used subsequently in an optimum design procedure.

B. Buckling of Laminated Composite Plates with Cut Outs

The buckling strength and post buckling behavior of laminated square plates with a centrally located circular hole were studied both experimentally and analytically. The analysis was based on the work of Chan and the experimental program used both aluminum and fiberglass specimens.

C. Post Buckling Strength of Anisotropic Plates

An approximate analysis was performed to obtain formulae for predicting the post-buckling strength of orthotropic and anisotropic

material plates under unidirectional edge compression. The theoretical predictions were verified by tests on fiberglass-epoxy composite plates. Excellent agreement is obtained between the theoretical predictions and test data.

An accurate fixture for the post-buckling testing of rectangular plates was designed incorporating a number of novel ideas. The fixture can be used for both buckling and post-buckling tests up to failure with accurately maintained boundary conditions.

A test method has been developed for the unbuckled compression stress-strain and strength determination of plates and sheets. The corresponding fixture has been used to test aluminum and fiberglass plates down to .030 inch thick. Accurate results are obtained and failure is obtained in the gage section.

D. Buckling of Anisotropic Circular Cylindrical Shells

The numerical results in this section have shown that this method of solution presented in this study can be successfully applied to predict the buckling load of a general anisotropic cylindrical shell. The buckling analysis takes into consideration the following conditions:

(a) The loading condition can be any combination of the radial pressure, the axial force, and the torsional force.

(b) Eight sets of boundary conditions include four simple supports, SS1 -- SS4, and four clamped supports C1 -- C4.

(c) L/r ratio can be any value.

The analysis uses both Flugge's and Donnell's theories. A total of 20 different cases of shell buckling has been investigated.

The great success in the buckling analysis involving the axial compression resulted from the appropriate arrangement of the characteristic roots. An improper arrangement can cause the false change of signs of the boundary determinant, and hence the incorrect buckling loads are obtained.

For the cases studied, the range of differences between Donnell's and Flugge's results is from 9.2% to 38.5% for the cases with the circumferential wave number n = 2, and the deviation is less than 2.5% for the cases with n = 6 or higher. The cause for this deviation is correlated with the inaccuracy of the characteristic roots obtained from Donnell's equations with n = 2,3.

The boundary conditions have significant effects on the buckling

loads for short cylinders, but it has little effect on the long cylinders. As indicated through the numerical comparison, the buckling loads with SS1 boundary conditions are only 46.4% to 54.8% of those with SS4 boundary conditions for short cylinders of isotropic material. For long cylinders, there is only a 5% difference beween SS1 and SS4 buckling loads. For the orthotropic case the effects of the boundary condition are insignificant, less than 5% difference. The boundary effect for the anisotropic case is moderate. It ranges from 75% for the very short cylinder ($L/r = 0.5$) to 99.8% for the very long cylinder ($L/r > 100$).

SECTION III

MATERIALS RESEARCH

During this last year of the contract, three projects on materials research were conducted. In the first project, the surface characteristics of graphite fibers were studied through both low temperature gas adsorption, and mass spectrometry. These experiments provided data on the specific surface area, the evidence of three kinds of adsorption sites, and an indication of the presence of a large number of micropores with relatively few large pores. In a series of related experiments to characterize the graphite fiber surface through adsorption from solution additional data on the specific surface area as well as surface adsorption energetics were obtained.

The third series of experiments on materials research dealt with the in-situ polymerization of nylon-6 with graphite fibers to obtain void free composites with improved fiber-matrix bond characteristics.

A. Structure Analysis of Graphite Fiber Surfaces Through Low Temperature Inert Gas Adsorption and Mass Spectrometry

(Prof. T. Fort, and Preben J. Moller)

Introduction

Production of "Thornel" fibers involves taking a rayon precursor through a series of progressively higher temperature pyrolysis, carbonization and graphitization steps.(1) The last of these steps is a rapid "hot stretch" in a nitrogen atmosphere at temperatures approaching 3000°C, which treatment causes a high degree of preferred orientation of graphite layers parallel to the fiber axis. The oriented graphite fibers so produced are very strong, and may exhibit a Young's modulus in excess of 50 million p.s.i.(2) This characteristic, coupled with lightness and high temperature resistance, has led to the use of "Thornel" fibers as a favored reinforcement for polymer matrices in advanced, high performance composite structures.

A problem with these (and other) graphite fibers, however, has been their poor adhesion to the polymer matrix which surrounds them.(3) Attempts to improve this adhesion have led to various treatments of the fiber to produce a more bondable surface. While some gains have been made (4-6), most work has been empirical. Real optimization of adhesion (and interfacial shear) awaits thorough characterization of the fiber surface. The objective of this research has been to make such a characterization, and to predict the effects of present (and future) surface treatments on fiber surface properties.

This effort consists of a study of the surface of "as received" and vacuum heat treated "Thornel 50" fibers. The techniques used are low temperature inert gas adsorption by microgravimetry, and mass spectrometry. From the first is derived information about fiber surface area, energy and heterogeneity. The second gives information about materials volatilized from the fiber surface during vacuum heat treatment. A special effort is made to relate these surface analyses to what is known about the bulk structure of "Thornel 50", and to the bulk and surface properties of other graphitic carbons.

EXPERIMENTAL

A. Materials

1. Adsorbent: The absorbent was, in all experiments, "Thornel-50" graphite fiber obtained from the Union Carbide Corporation Technical Center in Parma, Ohio. This specially prepared, unsized fiber was identified as Lot 10018 74E and had a tensile strength of 287 x 10^3 p.s.i. and a Young's modulus of 51.2 x 10^6 p.s.i. A typical density for "Thornel-50" is 1.63 g./cm^3 as measured by the liquid immersion method.

2. Adsorbates: All adsorbates were research grade gases obtained from Matheson Gas Products, Joliet, Illinois. Manufacturer's specifications for the nitrogen, argon, and helium used are listed in Table 1. These gases were used without further purification.

B. Apparatus

1. Balance and Pumps: The measurement system as shown in Figures 1 and 2 consists of a Cahn Model RG, High Vacuum, Electrobalance (Ventron Instruments, Paramount, California) mounted in a vacuum system largely assembled from standard Varian (Varian Associates, Palo Alto, California) parts. The balance chamber is connected to the gas manifold through vibration damping bellows, and the entire assembly is mounted on a heavy metal table permanently bolted to the concrete floor of an air conditioned room. The system is pumped by a Varian Model 941-6001 Vac Sorb cryogenic sorption pump and a Varian Model 912-6000 50-liter-per-second ion pump. The system attains a base pressure of 10^{-8} torr after the balance chamber is baked out at 100°C and the pumps and gas manifold are baked out at 250°C.

2. Pressure Measurement: System pressures below 10^{-4} torr are measured with a Varian U.H.V. ion gage. This same pressure range is also covered by a G.E. Minitube ion gage (General Electric Company, Schenectady, New York) which can, in addition, function at

pressures up to 10^{-2} torr if operated at very low (10μ A) emission currents. Pressures between 10^{-3} and 1 torr are determined with a Hastings Model VT-6 thermocouple gage (Hastings-Raydist, Inc., Hampton, Virginia) and from 0.6 torr to 760 torr with a Kern spiral gage (Electronic Space Products, Inc., Los Angeles, California) which is operated as a null device. Null is detected by noting the position of a spot of light reflected from a mirror mounted on the spiral gage to a calibrated scale. The reference side of the spiral gage is pumped by mechanical and mercury diffusion pumps. Pressure on the reference side is measured with a wide bore (27 mm. i.d.) manometer read by a precision cathotometer (Ealing Corporation, Catalog Number 11-5279, Cambridge, Massachusetts) with an accuracy of ± 0.01 torr. Low pressure measurements are corrected for thermal transpiration effects according to the equation of Liang (7). All manometer pressures are corrected to 0°C.

3. Gas Handling, Analysis and Control: The adsorbate gases are admitted to the manifold through a Matheson ultra pure transfer regulator (Matheson Scientific Instruments, Joliet, Illinois) to a Granville-Phillips Series 203 variable leak valve (Granville-Phillips Corporation, Boulder, Colorado). The composition of the gas atmosphere over the fiber sample is monitored by a Veeco SPI-10 Monopole Spectrometer (Veeco Instruments, Plainview, New York).

4. Sample Container and Support: The sample is contained in a 15 mm. diameter, blown, pear-shaped thin walled quartz pan suspended from a 56 cm. long and 0.003 cm. diameter platinum wire. The pan and wire assembly is suspended inside a 25 mm. inner diameter quartz hangdown tube connected through graded seals to a standard Varian flange. The hangdown tubes are internally coated with SnO_2 in the bottom and Pd near the metal flanges to aid in removal of static electrical charges. Coating of the sample pan with SnO_2 was shown to have no effect on mass measurements. The sample itself is grounded through the suspension wire.

5. Temperature Control: Sample temperature during an experiment is controlled either by direct contact of the hangdown tube with liquid nitrogen or liquid oxygen (for experiments at 77 and 90°K) or by a cryostat constructed as shown in Figure 3. Sample temperatures of 90°K to 300°K may be maintained with the unit as described.

The basic parts of the cryostat are heated copper block contained in an evacuated chamber surrounded by cooling liquid. The heater block (of high heat capacity) is a cylindrical piece of copper 6 cm. in diameter and 16 cm. high with vertical holes drilled to accommodate two series connected 75 watt cylindrical heating elements and the sample hangdown tube. This block fits an evacuatable glass jacket sealed to the upper part of the hangdown tube. The sample pan is immersed 14 cm. below the top of the temperature controlled

block. A Dewar of cooling fluid surrounds the jacket.

Temperature of the copper block is controlled to ± 0.01°C by a Melabs Model CTC-1A Proportional Temperature Controller (Melabs Inc., Palo Alto, California). Current through the heaters may be varied with a control rheostat. Temperatures are measured with a Rosemount Model 108J1C platinum resistance thermometer (Rosemount Engineering Company, Minneapolis, Minnesota) read by a L. & N. Model K-4 Potentiometer (Leeds and Northrup Company, Philadelphia, Pennsylvania).

Cryogenic temperatures are obtained by admitting nitrogen gas (helium avoided because of its ability to diffuse through quartz) into the cryostat jacket and filling the outer Dewar with liquid nitrogen. Liquid nitrogen level is maintained constant (± 1 mm) with a (special) fluidic principle sensor.* After sufficiently low temperatures are obtained, the cryostat is pumped to pressures in the 10^{-4} torr region as measured on a Pirani gage (Consolidated Vacuum Corporation, Rochester, New York). The temperature of the sample at a given cryostat condition is determined by making blank runs with a thermocouple suspended inside the hangdown tube.

Vacuum heat treatments of the fibers are effected through use of a high temperature Lindberg Hevi Duty Mini Mite Tube Furnace (Lindberg Hevi Duty, Watertown, Wisconsin).

6. Data Recording: Sample mass changes, outputs from the ion gage pressure sensors, and the mass spectrometer are all recorded simultaneously and serve as a permanent record of the experiments.

7. Precision and Accuracy: With the very thin and annealed platinum hangdown wire a sensitivity of ± 0.05 μg is achieved at pressures up to 300 torr. Noise level increases at higher pressures due to aerodynamic forces and sensitivity is ± 10 μg at 760 torr.** This noise level is a function of tube diameter and temperature and can be reduced through use of baffles in the tube.

---

* Designed by E. Samuels of this department.

** The factor limiting precision at high relative pressures is the ability to maintain constant coolant level around the hangdown tube.

The mass readings are taken at approximately the same hours as the blank runs in order to compensate for small daily fluctuations in building conditions. Small instrument drifts are compensated for by extending the blank run time to the same interval as the experiment time.

C. Procedure

Samples - ca. 0.57 g - of the rather "springy" graphite fiber are pushed into the quartz sample pan without any previous surface treatment being applied. The sample pan is then mounted on the balance and the system sealed and pumped down to ca. 10^{-7} torr. The apparatus, excluding the hangdown tube, is baked out for ca. 10 hours and then allowed to cool to room temperature. Vacuum heat treatment (VHT) is then started, increasing temperature in increments small enough to maintain the total pressure of the system below 10^{-6} torr for low vacuum heat treatment temperatures (VHTT) and below 10^{-7} torr for the high VHTT. When the desired final temperature is reached, VHT is continued until sample weight is constant and system pressure is below 6×10^{-8} torr. This requires 3 days for 240°C VHTT and 15 hours for 880°C VHTT. Mass spectra are recorded regularly during VHT, and are obtained simultaneously with measurements of system pressure and sample weight. The flow of gas through the manifold is calculated for each pressure range using specifications supplied by the valve and pump manufacturers.

At the conclusion of each VHT the sample is allowed to cool to room temperature. System pressure drops to ca. 2×10^{-8} torr. The sample is then cooled to the desired adsorption temperature either by surrounding the hangdown tube with liquid nitrogen or oxygen or through use of the cryostat. After ca. 5 hours the pump is isolated from the rest of the system and the first dose of adsorbate gas immediately leaked in. Sample weight is monitored continuously. When equilibrium is achieved a second dose of gas is leaked into the system. Equilibrium times are very long - up to 6 or 8 hours for each experimental point - and the kinetics of adsorption and desorption on graphite fibers will be subject of a later report.

Conversion of the raw data into measurements of adsorbed gas molecules requires correction for the buoyancy on the sample pan, hangdown wire and sample of the gas inside the vacuum system. Correction must also be made for thermomolecular forces caused by the fact that the enclosed gas is not everywhere at the same temperature. Temperature gradients exist across the sample, along the wire, and near the lamp. Corrections for these temperature gradients may be made if the effect, on apparent sample weight, of a nonadsorbing gas is known. Helium at liquid nitrogen temperatures has been used for this purpose but was found unsuitable in the present experi-

ments* because it penetrated micropores in the graphite fiber surface which were not available to nitrogen and argon.(8)

The corrections are therefore made in two parts. Thermomolecular force effects and buoyancy effects on the sample pan, hangdown wire and balance beam are approximated from experiments (blank runs) with a sample of quartz rod placed on the balance pan in place of the fiber sample. The very low surface area of this rod, which is of the same weight as the sample, minimizes adsorption effects. These measurements are made at various pressures and temperatures with each gas investigated. Thermomolecular effects cause significant ($> \pm 0.1$ μg) apparent weight increases at pressures between 10^{-4} torr and 2 torr with the maximal effect noted at ca. 10^{-2} torr. Buoyancy effects increase with gas pressure. The counterweight, a piece of quartz, is held unchanged at room temperature throughout all experiments.

Apparent sample weight decreases due to buoyancy of the samples are determined in two ways:

(1) A series of experiments is made with nitrogen and argon at temperatures (25-200°C) sufficiently high that it can be assumed no adsorption occurs. Buoyancy at a given pressure is then plotted vs. reciprocal temperature and the effect at the adsorption temperature determined by extrapolation.

(2) The weight change due to buoyancy (Δw_{buoy}) is calculated using the reported sample density of 1.63 g/cm^3 to determine the volume of the sample and estimating the densities of the non-ideal low temperature adsorbate gases from tabulations of second virial coefficients (Hirschfelder, Curtiss and Bird).(9) The true weight change, Δw, is then obtained from the expression:

$$\Delta w = \Delta w' - \Delta w_{blank} - \Delta w_{buoy}$$

where $\Delta w'$ is read directly as the equilibrium weight at the recorder and Δw_{blank}, due to adsorption on the balance pan, etc., is measured at each temperature with each adsorbate as previously described. The two methods for detemining buoyancy check reasonable well, and the second is used in most actual calculations.

---

*Another difficulty with helium is that it caused burnout of a diode in the electrobalance, apparently by arcing at approximately 3 torr helium pressure. The problem was solved by relocating the diode outside the vacuum system.

After each adsorption -desorption cycle is completed, the sample is degassed at a temperature slightly lower than the VHTT before proceeding. Background for the mass spectra is determined during blank runs.

RESULTS

A. Fiber Weight Loss During Vacuum Heat Treatment

The fibers were subjected to vacuum heat treatments at progressively higher temperatures. Equilibrium fiber weight was determined at the conclusion of each VHT step. VHT was carried out at temperatures in addition to those later investigated by adsorption studies. Small weight losses were found to occur. A total weight loss of 0.16 percent, based on initial sample weight, was found when a given fiber sample was given VHT to 900°C.

C. Gas Evolution During Vacuum Heat Treatment

Calculations based on the continuous total pressure recordings and weight readings made during vacuum heat treatment showed (Figure 4) that most gas was evolved at approximately 270°C and 680°C, and that a tendency toward increasing gas evolution occurred as temperature was raised above 770°C.

The composition of the gases evolved over the VHTT range 200°C-880°C was obtained with the mass spectrometer. Results, corrected for background spectra, are shown in Figure 5. A variety of gases were evolved. These were mainly CO, CO_2, H_2O, H_2, N_2, NH_3 and hydrocarbons (principally CH_4 and C_2H_6). It was found (Figure 6) that after having passed through an initial maximum at approximately 300°C, the evolution of CO is increased steadily with VHTT while the evolution of CO_2 reached a maximum at approximately 670°C. H_3O, H_2 and NH_3 were evolved in decreasing amounts as VHTT was increased to 700°C. Evolution of CH_4 and C_2H_6 reached a VHTT maximum at approximately 415°C.

C. Observations with the Scanning Electron Microscope

Scanning electron microscope (SEM) photographs were obtained of fiber samples after subjecting them to vacuum heat treatments of 400°C and 800°C as well as of samples of untreated fiber. Pictures were taken at 5000 and at 20000 magnifications with a Materials Analysis Co., Model 700 high resolution scanning electron microscope.

The SEM analysis showed (Figures 7 and 8) that the fiber diameter was approximately 7.4 μ . This diameter corresponds to a geometric surface area of 0.33 m^2/g. if the fibers had been smooth cylinders with length >> diameter. No significant differences in surface appearance were noted with SEM after various VHT.

D. Gas Adsorption Isotherms

Adsorption and desorption isotherms were obtained with nitrogen and argon as adsorbates at temperatures of 77.3°K, 90.2°K, 92.4°K and 103.3°K at pressures varying from $2x10^{-5}$ torr to approximately 760 torr for fibers vacuum heat treated (VHT) at 240°C, 290°C, 325°C, 490°C, 590°C, 695°C and 880°C. Typical data obtained are shown in Figures 9 through 11. Low coverage isotherms are inserted in the graphs.

The isotherms all had a characteristic shape. Adsorption increased rapidly at low relative pressures, then more slowly and in linear steps as pressure increased. At high relative pressures the rate of adsorption increase with pressure increased again. For most fiber samples the amount (moles) of nitrogen and argon adsorbed at a given relative pressure was nearly the same.

Desorption data showed that there was little or no adsorption-desorption hysteresis at high surface coverage. Some hysteresis was observed at low coverage for all samples but lack of a sufficient number of data points made it difficult to characterize this completely.

The multilayer region was analyzed for nitrogen isotherms according to the Frenkel-Halsey-Hill equations (10-14); the log-log plots of Δw vs. log p_0/p, FHH-plots, were found to give straight lines for relative pressures above approximately 0.017.

E. Fiber Surface Area Calculations

Fiber surface areas were calculated from the adsorption data by applying the Brunauer, Emmett and Teller theory (15), the "point B" method (16), the Kagamer method (17) and, for nitrogen, from Pierce's n-values (18) and Lippens-Linsen-de Boer t-values (19) for statistical layers. These methods provide different ways of estimating the number of gas molecules adsorbed when the surface is covered by one statistical monolayer of adsorbed material. Surface areas may then be calculated if the area occupied by each adsorbed gas molecule is known. Adsorbate molecule cross sectional areas are usually estimated from bulk adsorbate densities. Areas used in this work are listed in Table 2.

Examples of adsorption data plotted according to each of the above methods are shown in Figures 12 to 16, and the surface area results are summarized in Table 3. This summary shows that:

(1) A^{SP} for "Thornel-50" graphite fibers is low and on the order of 1 m^2/g.

(2) Vacuum heat treatment first reduced, then increased, A^{SP}. The lowest specific surface area was effected by VHT at 600°C.

(3) Surface areas calculated from nitrogen and argon adsorption experiments at different adsorption temperatures were in fairly good agreement when adsorption data at low relative pressures (0.01-0.10) were used to calculate A^{SP}. A comparison of N_2 and Ar results is given in Table 4.

(4) For VHTT below 300°C, significant differences in A^{SP} as measured at 77°K and 90°K were observed. For VHTT above 300°C, the A^{SP} values agree fairly well.

(5) The difference pointed out in (4) was larger for Ar than for N_2.

(6) The B.E.T. specific surface area (A^{SP}) for the lowest investigated VHTT is 1.17 $\pm$ 1.17 $\pm$ 0.03 m^2/g. as measured with N_2 at 77.3°K.

(7) The specific surface areas calculated from the different adsorption models are in reasonable agreement, although the areas determined from the t-plot were all lower than those from the other models.

Reproducibility of a given A^{SP} determination on a given sample at given conditions and for a given adsorbate was $\pm$ 2 percent. The A^{SP} values obtained may be compared with a specific surface area of 1.3 m^2/g. obtained by Didchenko (20) who used a volumetric gas adsorption method to characterize "Thornel 40" fiber surfaces.

F. Thermodynamics of Adsorption

The isosteric heat of adsorption, q_{ST}, was calculated from the expression

$$q_{ST} = RT^2 \left(\frac{\partial \ln P}{\partial T}\right)_{\eta_s} = R \frac{T_1 T_2}{T_1 - T_2} \left(\ln \frac{P_1}{P_2} \right)_{\eta_s} .$$

Here R is the gas constant, T_1 and T_2 a pair of absolute adsorption temperatures, P_1 and P_2 the respective adsorbate pressures and n_s is the number of moles of adsorbed gas.

The differential entropy of adsorption referred to the liquid state was calculated as suggested by Hill (14,21,22) and Everett (23) from the expression

$$\bar{S}_s - S_L' = -(S_G - \bar{S}_s) + \frac{E_L}{T} - R\ln\frac{P}{P_o}$$

$$= \frac{-q_{ST}}{T} + \frac{E_L}{T} - R\ln\frac{P}{P_o} \quad .$$

Here $\bar{S}_s$ is the differential entropy

$$\bar{S}_s = \left(\frac{\partial S_s}{\partial n_s}\right)_{P,T,A} \quad ,$$

S_L' is the molar entropy of the liquid at temperature T and pressure P_o , S_G is the molar entropy of unadsorbed gas and P is the absorbate pressure calculated as the mean

$$P = (P_1 P_2)^{1/2} \quad .$$

The temperature T was calculated from the expression

$$\frac{1}{T} = \frac{1}{2}\left(\frac{1}{T_1} + \frac{1}{T_2}\right) \quad ,$$

and E_L is the heat of liquefaction. The adsorbate is assumed inert.

The isosteric heats and differential entropies of adsorption were plotted as functions of coverage, θ , and results are shown in Figures 17 to 18. $\theta = 1$ is the B.E.T. monolayer value taken from Table 3. For nitrogen, it was found (Figure 17) that q_{ST} initially decreased to a minimum at approximately 7 percent surface coverage, then passed through a maximum at approximately 30 percent coverage followed by a decrease to E_L at $\theta = 1$. q_{ST} at the lowest measurable coverage was ca. 4.2 kcal/mole and this value decreased with

increasing VHT. The maximum value of q_{ST} (at $\theta \approx 0.30$) was ca. 5.7 kcal/mole for VHTT = 290°C. This maximum decreased to ca. 3.5 kcal/mole as VHTT was increased to 660°C, then rose to 5.3 kcal/mole for VHTT = 880°C. For VHTT = 660°C a maximum in q_{ST} was observed at $\theta = 0.16$, but a peak at $\theta = 0.3$ was still seen. The differential entropies mirrored the isosteric heat data. Maxima in the differential entropy plots were observed at $\theta = 0.07$ and minima at $\theta = 0.30$.

The isosteric heat data for argon exhibited maxima of 5.5 kcal/mole at $\theta \approx 0.16$ and 3.7 kcal/mole at $\theta \approx 0.30$ for fibers VHT at 325°C. A third maximum of 3.6 kcal/mole was observed at $\theta \approx 1.0$. The respective differential entropies decreased from initial high (low coverage) values to minima at $\theta = 0.6$, $\theta = 0.27$, and $\theta = 0.90$ (Figure 18).

DISCUSSION

"Thornel" filaments differ in structure from the graphitized carbon blacks which have been subjects of so many surface chemical adsorption investigations (e.g. 24-28). The latter materials are composed of polyhedral crystallites with the faces of the polyhedra formed by the basal planes of the graphite lattice.(29) High temperature treated blacks such as Graphon have very few oxidized surface sites, and the distorted packing of carbon atoms along the contact lines of the basal planes in Graphon comprises only a very small fraction of the total surface. High temperature treated blacks thus provide an extremely uniform low energy surface for adsorption.

In "Thornel" fibers, on the other hand, the structure consists of long ribbon-shaped crystallites with the basal planes of these crystallites oriented with the fiber axis. (30-31) X-ray studies (32) have shown the crystallites to be stacks of 8 to 10 layers. Laser excited Raman spectroscopy has indicated the width of the crystallites, in "Thornel-50", to be 155 Å. (33) Density determinations indicate porosity of "Thornel" filaments is ca. 30 percent. Investigations have shown these pores to be needle-like, with diameters in the range of 10-20Å and lengths of 200-300Å. (34) The pores are preferentially oriented parallel to the fiber axis. Part of the pores are inaccessible and comprise a true internal surface.

All these structural characteristics might be expected to influence adsorption on "Thornel-50"surfaces. Thus, these surfaces should contain both "faces" and "edges" of graphite crystallites. The exposed edges should be likely sites for adsorption, both because of their inherently higher (in comparison to the faces) energy and because they are probable loci for oxidized surface adsorption sites. Accessible pores may also serve as "traps" for gas molecules.

With these facts in mind, consider the typical adsorption isotherm shown in Figures 9 to 11. This isotherm is of the general Type II shape in theB.E.T. (15) classification, but exhibits a series of straight line segments below monolayer coverage. Some indications of steps above monolayer coverage are also observed. (35) If the low coverage straight lines correspond to adsorption on different regions of the fiber surface then, expanding on an idea of Graham (36), the intercepts of the various straight lines with the $P/P_0 = 0$ axes give information about the percentage of surface of different kinds. Extrapolation of the straight line isotherm segments in Figures 10 and 11 yields intercepts at 30 and 3 percent coverage for fibers vacuum heat treated at 880°C. Similar extrapolations of isotherms obtained for fibers vacuum heat treated at 325°C and 590°C yield intercepts at 26 and 27, and at 7 and 6, percent coverage. Lines, with zero intercept, drawn parallel to the straight line segments of the isotherms which intercept the $P/P_0 = 0$ axes at 26-30 percent coverage would then indicate the low coverage adsorption on one type of surface site. Similarly, a line drawn parallel to the 7-3 percent coverage isotherm segment and passing through the origin would indicate adsorption on a second type of surface site. Since gas molecules will adsorb preferentially on high energy surface sites, the above reasoning suggests that the "Thornel-50" surface is composed of from 7-3 percent "high" energy sites, 26-30 percent "medium" energy sites, with the remainder being sites of "low" energy.

It is now postulated that, in the present experiments, adsorption occurs preferentially on oxidized sites at the edges of the stacks of basal planes (high energy sites), then on the nonoxidized edges of the stacks of basal planes (medium energy sites), and finally on the tops of the stacks of basal planes (low energy sites) in the oriented graphite crystallites in "Thornel-50". This interpretation is aided by the isosteric heat and differential entropy calculations. Reference to Figures 17 and 18 shows maxima in isosteric heats of adsorption at surface coverages below 7, at 27-30, and at 100, percent. The first maximum is caused by adsorption on the oxidized edge surfaces. By analogy to adsorption studies made on homogeneous graphitized carbon black surfaces (24), the second and third maxima may be interpreted as being caused by lateral interactions of adsorbate molecules on patches of homogeneous nonoxidized edge, and homogeneous face, surface in the graphite crystals. These ideas are reinforced by the differential entropy data which indicate restricted mobility of adsorbed molecules at surface coverages corresponding to completion of adsorption on the edges and on the faces of the exposed graphite crystallites.

The postulated surface character is also reinforced by a simple calculation of the relative areas of these surfaces in these fibers based on data of Ruland (32) and Koenig (33). It is first assumed that the crystallites, though oriented with the fiber axis, are randomly rotated around this axis. Then, if the crystallites are

considered as ribbons 155 Å wide (33) and 60 Å high (32) (the interlayer spacing in graphite is ca. 6.69 Å and there are 8-10 layers in a stack in "Thornel-50"), the fraction of the surface which is side is

$$\frac{60}{155+60} = 0.28$$

and the fraction of the surface which is face is

$$\frac{155}{155+60} = 0.72 \quad .$$

These calculations check the calculations based on the adsorption isotherms amazingly well.

Further confirmation of the ratios of face to edge area is found by comparing the adsorption isotherms obtained on fibers subjected to various vacuum heat treatments (Figure 9 to 11) along with the mass spectra of gases evolved during these treatments (Figures 5 and 6). Low temperature VHT effects release of physically adsorbed (principally water and nitrogen) and trapped (principally hydrogen and hydrocarbons) gases from the "Thornel-50" fibers. At intermediate VHTT the diameter of small pores in the fibers increases a little because of thermal expansion of the fiber;* physically adsorbed and trapped gases have more thermal energy, and more are released. At higher VHTT, oxidized surface groups are replaced by hydrogen and this leads to evolution of CO and CO_2 (Figures 4 and 5). Similar behavior is found for natural graphite (38), various graphitized carbons (39) and polyacrylonitrile based graphite fibers (40), though the quantities and ratios of these gases are different. If the oxidized surface sites are, as postulated, on the edges of the stacks of basal planes, changes in these sites should be reflected in changes in the adsorption isotherms. Figures 9 to 11 show that the fraction of the "Thornel-50" surface thought to be unoxidized edge increases from 0.26 to 0.30 as vacuum heat treatment temperature is increased from 290°C to 880°C. This increase is exactly balanced by a decrease from 0.07 to 0.03 in the fraction of the surface thought to be oxidized edge.

Evolution of trapped materials can also explain the changes in A^{SP} effected by vacuum heat treatment. VHT temperatures up to 660°C

---

* The transverse thermal expansion coefficient of the fiber increases from ca. 9.8×10^{-6} to 12×10^{-6} in./in./°C (37) as fiber temperature is raised from 300°C to 600°C.

reduces A^{SP} . This reduction may be caused by blocking of narrow pores (leading in to the larger pores parallel to the fiber axis) by material released from the interior of the fiber.* Above 660°C this material is oxidized and released as CO and CO_2 , which opens up the narrow pores again.

Fiber surface areas were calculated by a number of methods because B.E.T. plots of the data sometimes yielded more than one straight line. It was found that if the straight line found in a B.E.T. plot in the relative pressure range 0.01-0.10 was used to calculate surface areas, these areas agreed reasonably well with A^{SP} determined by most of the other methods. However, the A^{SP} values determined from the Lippens-de Boer t-plot are relatively low. It has been noted previously (41) that the Lippens-de Boer method does not apply to carbon surfaces. The deviation from linearity at low relative pressures in the Frenkel-Halsey-Hi/l plots indicate the presence of micropores, while the linearity at higher relative pressures indicate the absence of capillary condensation. There are probably very few accessible macropores (little or no adsorption hysteresis was observed at high relative pressures) but a large number of micro- and ultra-micropores in the "Thornel-50" surface.

Finally, a surface roughness factor (r) calculation was made based on the geometric area calculated from the scanning electron microscope photographs and the B.E.T. nitrogen areas measured at 77°K. This calculation shows that r decreases from a "fiber as received" value of 4 to a minimum value of 2 after vacuum heat treatment of 660°C, then slowly increases again.

IMPLICATIONS FOR ADHESION

Strong evidence has been presented for the existence of three types of adsorption site patches on "Thornel-50" fiber surfaces. These are identified as the tops, edges, and oxidized edges of oriented (with respect to the fiber axis) graphite crystallites. The patches occupy approximately 67, 26 and 7 percent of the fiber surface, respectively. The percentage of oxidized edge is reduced by vacuum heat treatment which effectively deactivates the surface. The fibers have a low specific surface area and a roughness factor of 2-4.

The surfaces thus characterized are not optimum for adhesion. Improvements should be realized if fiber surface area and energy

---

* The high temperature graphitization of the fibers is achieved by passing them through a hot tube. Heating time is very short and complete degassing of the fibers is probably not accomplished.

could be increased. The best means of achieving surface area increases without adversely affecting other fiber properties is probably through a post-processing chemical etch treatment. Chemical etching might also increase the fraction of surface which is oxidized and thus also increase surface energy. A large opportunity exists here because only one-third of the existing edge surface is presently composed of active oxidized sites. Though these sites have not been identified, they are almost certainly hydroxyl and carboxyl groups. Known techniques for graphite oxidation, if applied to "Thornel 50" filaments and limited to the surface of the fibers, should yield significant improvements in "Thornel-50" based composite performance.

TABLE I

SUPPLIER'S ANALYSES OF ADSORBATE GASES

	Purity (%)	Impurity Analysis (ppm)*							
		O_2	H_2	Ar	He	Ne	CO_2	N_2	Hydrocarbons
Nitrogen	99.9990	<1	<1	<5	<1	<1	<0.5		<0.5
Argon	99.9995	<1	<1				<0.5	<5	<0.5
Helium	99.9995	<0.1	N.D.	N.D.		<0.2	N.D.	<5	N.D.

* Dew point determinations indicated H_2O in N_2 to be below 1 ppm and H_2O in Ar to be below 0.63 ppm.

TABLE II

ADSORBATE MOLECULAR CROSS SECTIONAL AREAS* IN $Å^2$

ADSORBATE	ADSORPTION TEMPERATURE (°K)			
	77.3	90.2	94.2	103.3
N_2	16.2	17.0	17.2	17.8
Ar	13.8	14.4	14.6	15.0

* The cross sectional areas at 94.2°K and 103.3°K were obtained by linear extrapolation of the data at 77.3°K and 90.2°K.

TABLE III

SPECIFIC SURFACE AREAS, A^{SP} (m^2/g),
OF VACUUM HEAT TREATED "THORNEL-50" GRAPHITE FIBERS

VHTT (°C)	Adsorbate	Ads. Temp. (°K)	A^{SP}_{BET}	$A^{SP}_{Point\ B}$	$A^{SP}_{Kagamer}$	$A^{SP}_{Pierce,\ for\ p/p_o=0.4}$	$A^{SP}_{t\text{-}plot}$***
240	N_2	77	1.17	1.21	1.18	1.22	0.79
		90	1.21	1.32		1.43*	
290	N_2	77	0.76	0.75	0.67		0.52
		90	0.78	0.78	0.76		
	Ar	77	0.83		0.97		
		90	1.41	1.49	1.69		
325	N_2	92	0.67	0.67	0.80		
		103		0.80	0.93		
	Ar	94	0.67	0.65			
		103	0.78	0.75			
400	N_2	77	1.04	1.13	1.18	1.06	0.68
490	Ar	77	0.67	0.73	0.76		
		90	0.60	0.71	0.73		
590	N_2	77	0.72	1.06	0.80	1.19	0.70
		90		1.04	1.00	1.12**	
695	Ar	77	0.58	0.65	0.67		
		90		0.64	0.72		
880	N_2	77	0.80	0.80	0.80		0.52
		90	0.76	0.81	0.84		

*p/p_o = 0.25

**p/p_o = 0.2

***Only for N_2 at 77°K

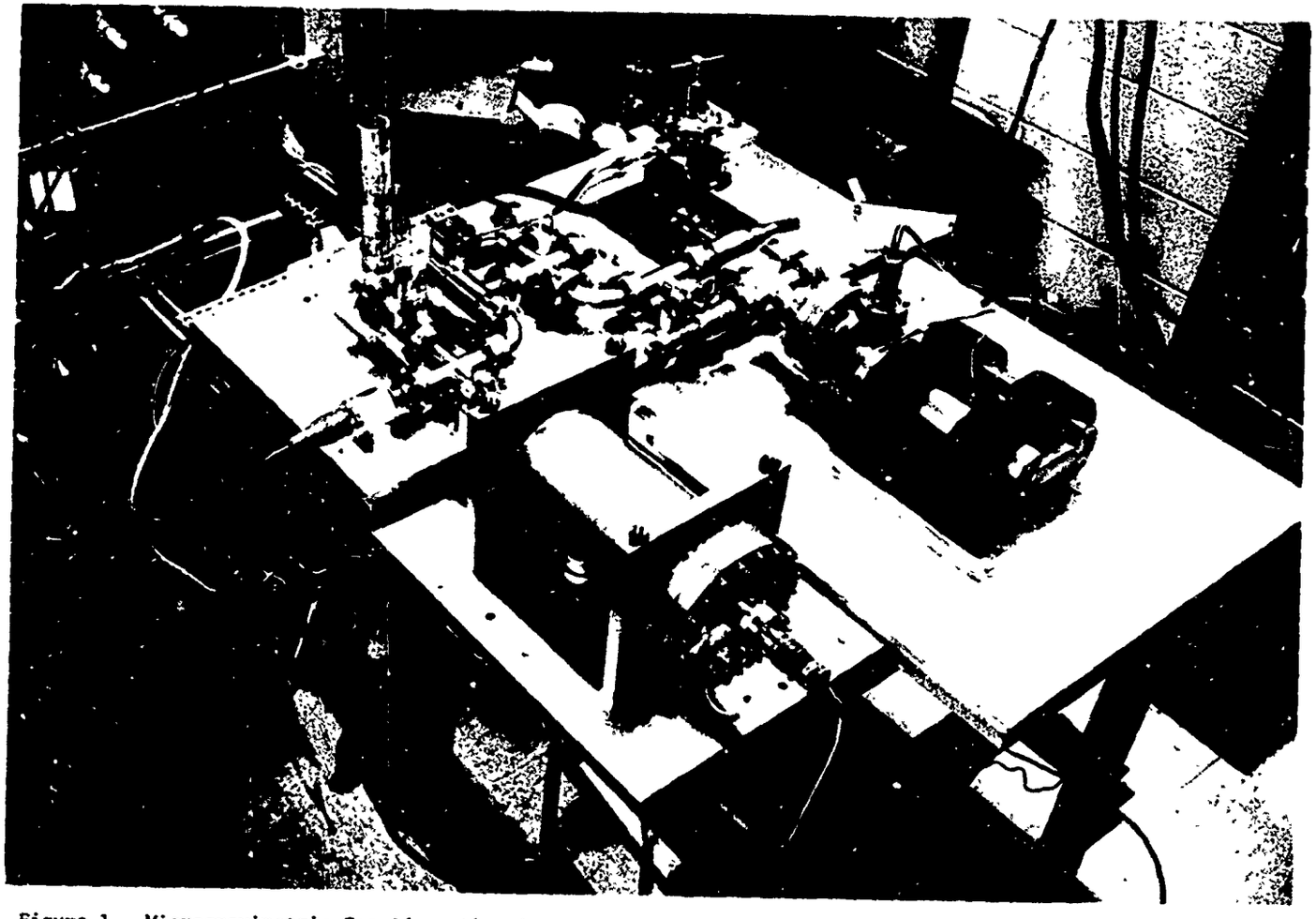

Figure 1 - Microgravimetric Gas Adsorption Apparatus.

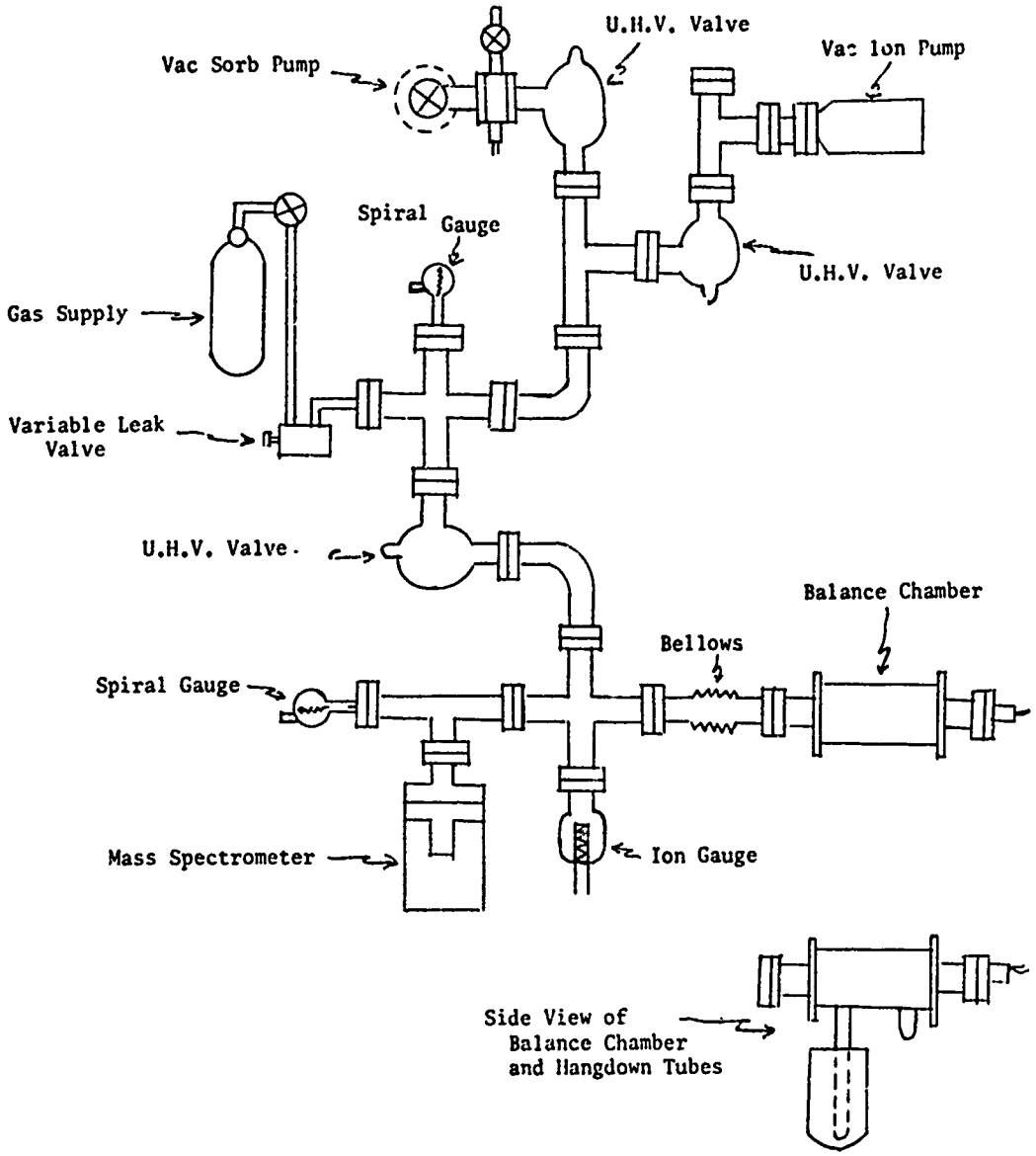

Figure 2 - Adsorption Apparatus and Measuring Equipment.

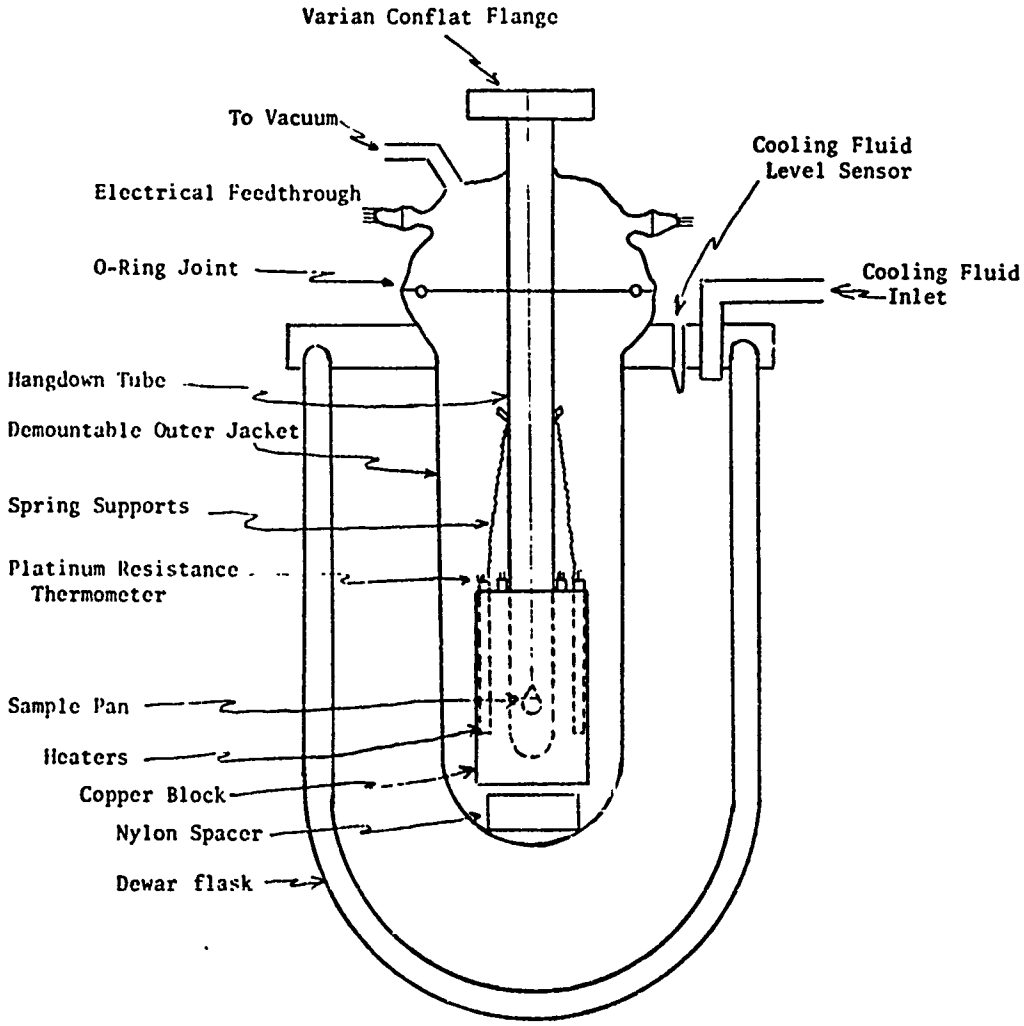

Figure 3 - Microbalance Cryostat

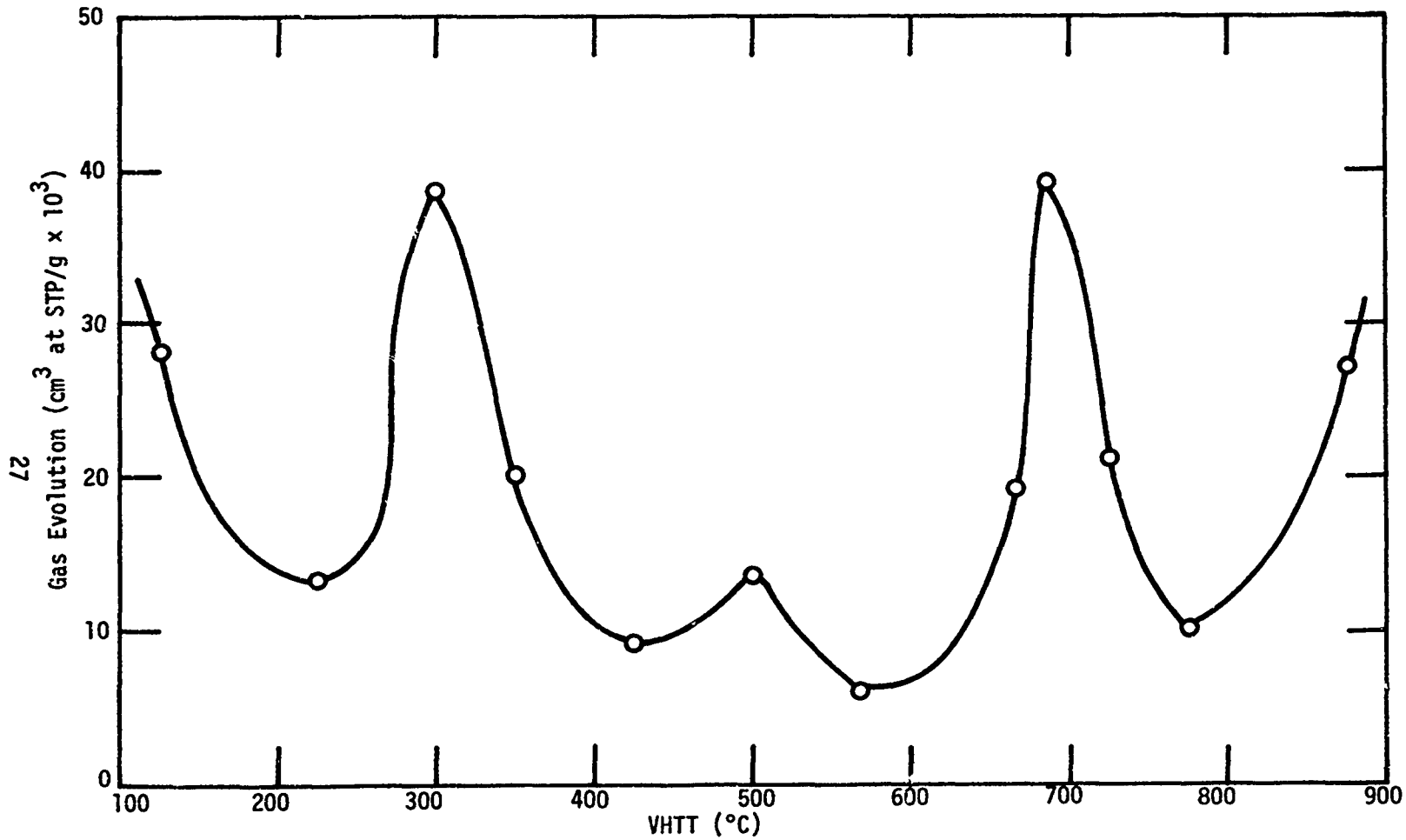

Figure 4. Total Gas Evolved on Vacuum Heat Treating Thornel-50 Fibers.

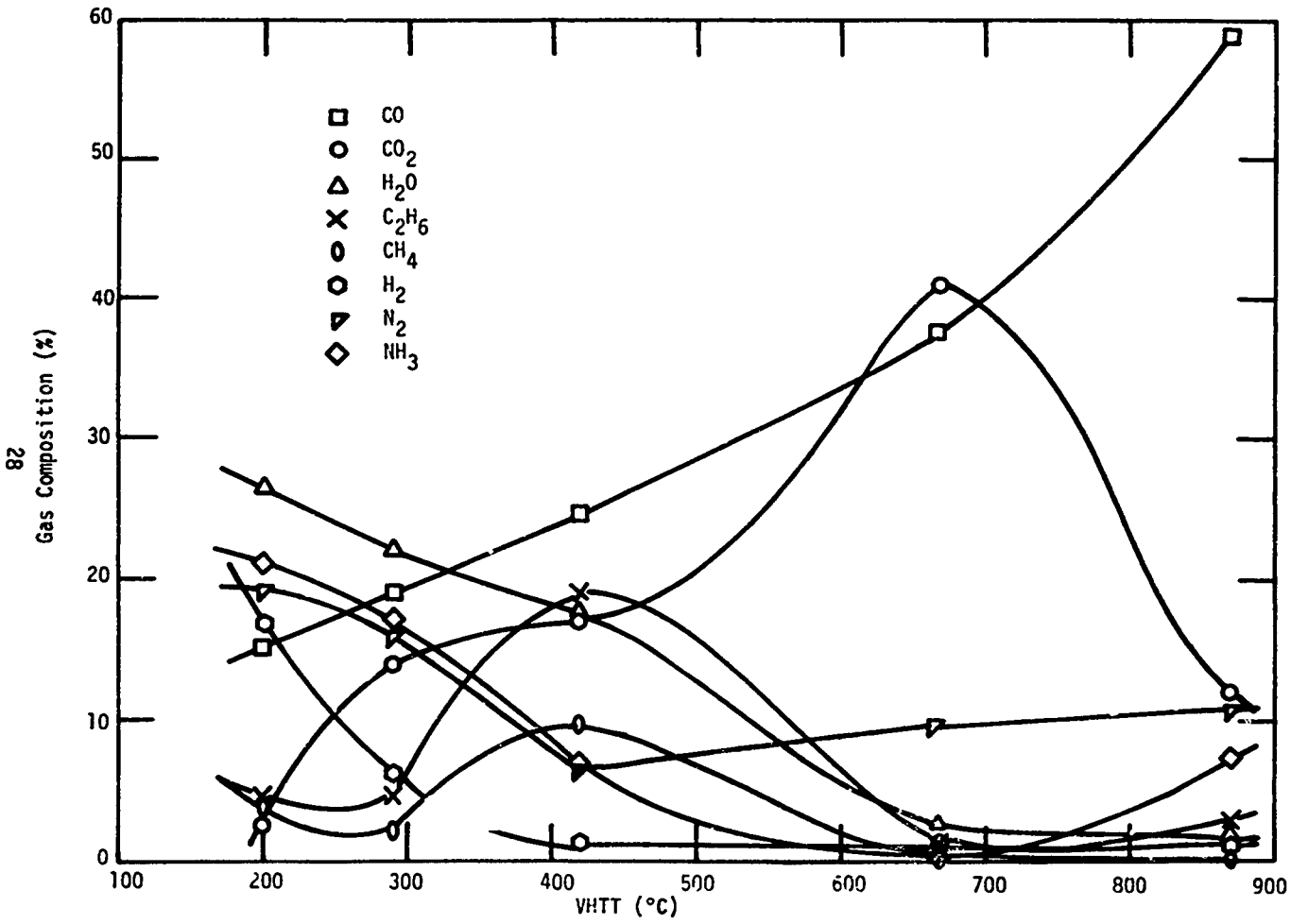

Figure 5. Composition of Gases Evolved on Vacuum Heat Treating Thornel-50 Fibers.

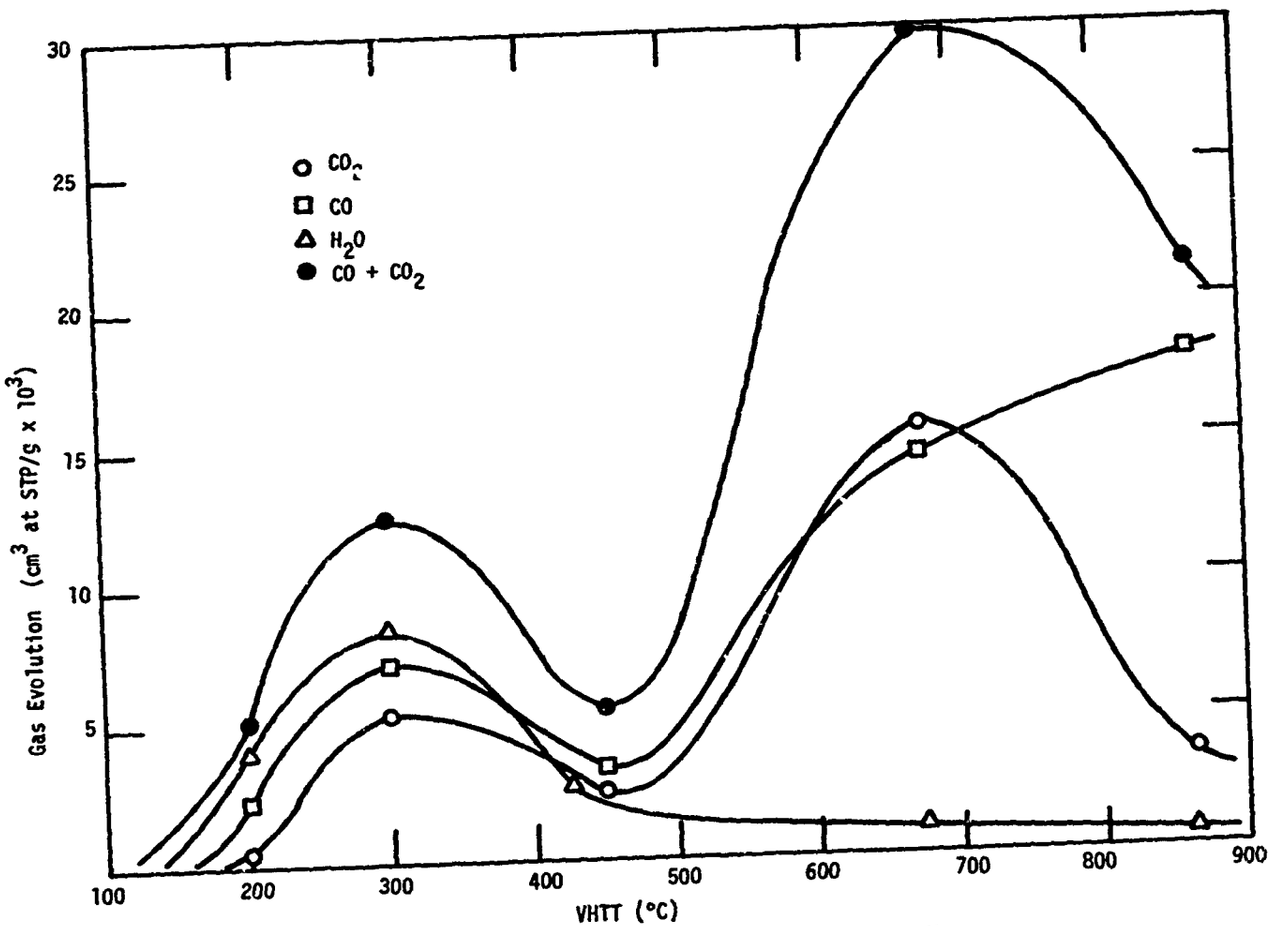

Figure 6. Evolution of CO, CO_2, and H_2O on Vacuum Heating Thornel-50 Fibers.

Figure 7 - Scanning Electron Microscope Photograph of Thornel-50 Fiber Surfaces.

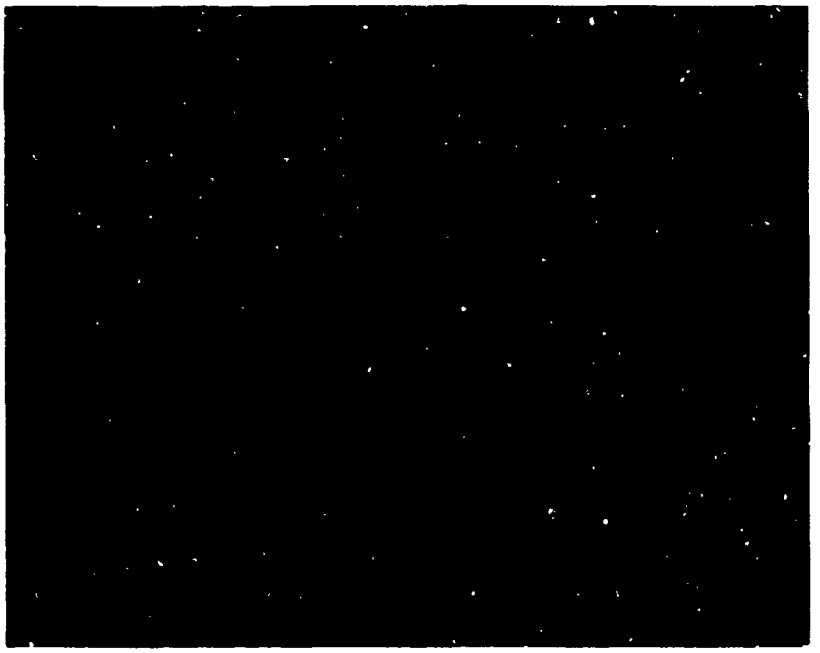

Figure 8 - Scanning Electron Microscope Photograph Showing the Cross Section of Thornel-50 Fibers.

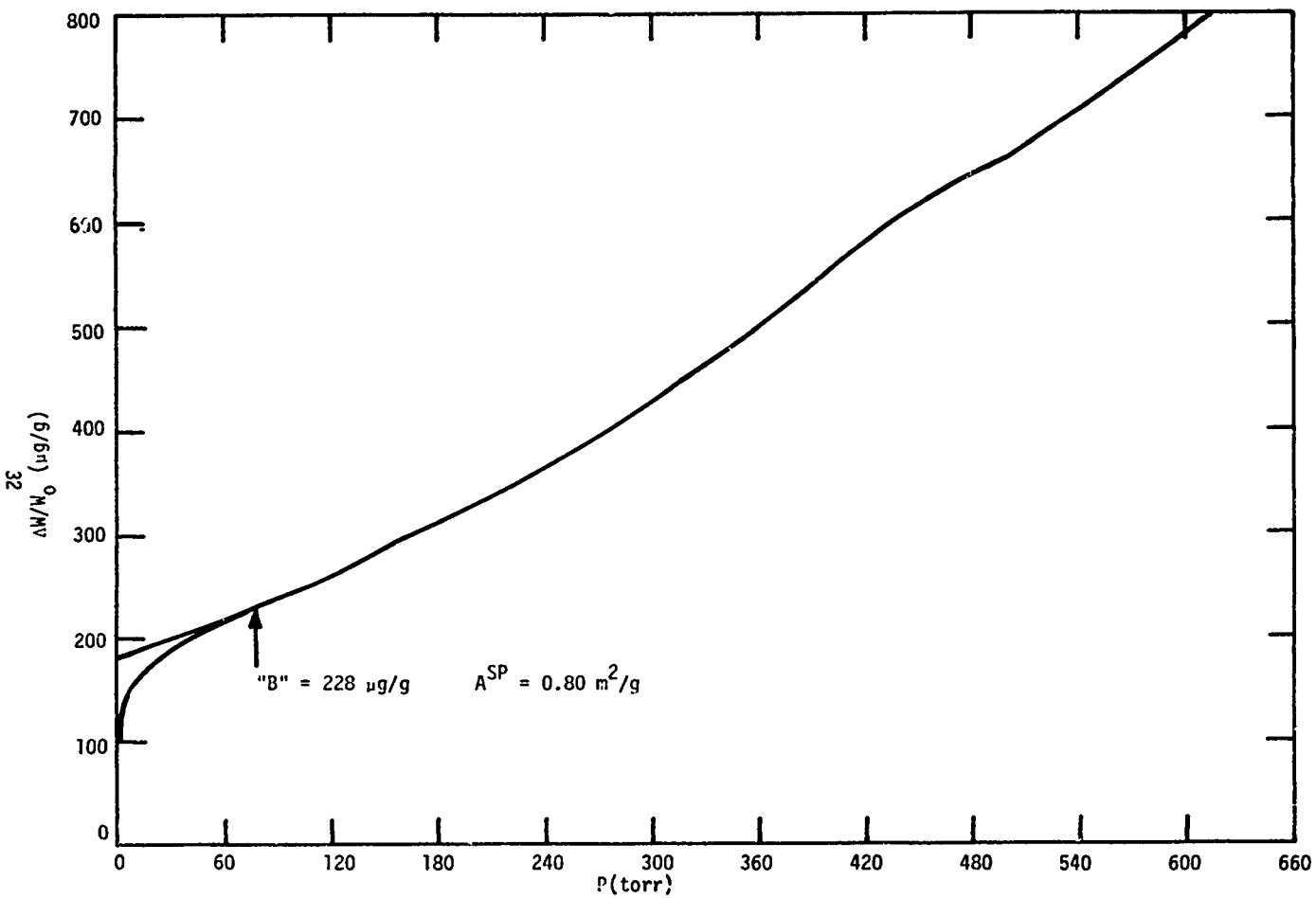

Figure 9. Adsorption Isotherm for Nitrogen, at 77.3°K, on Thornel-50 Fibers Vacuum Heat Treated at 880°C. Point "B" is marked on the Graph.

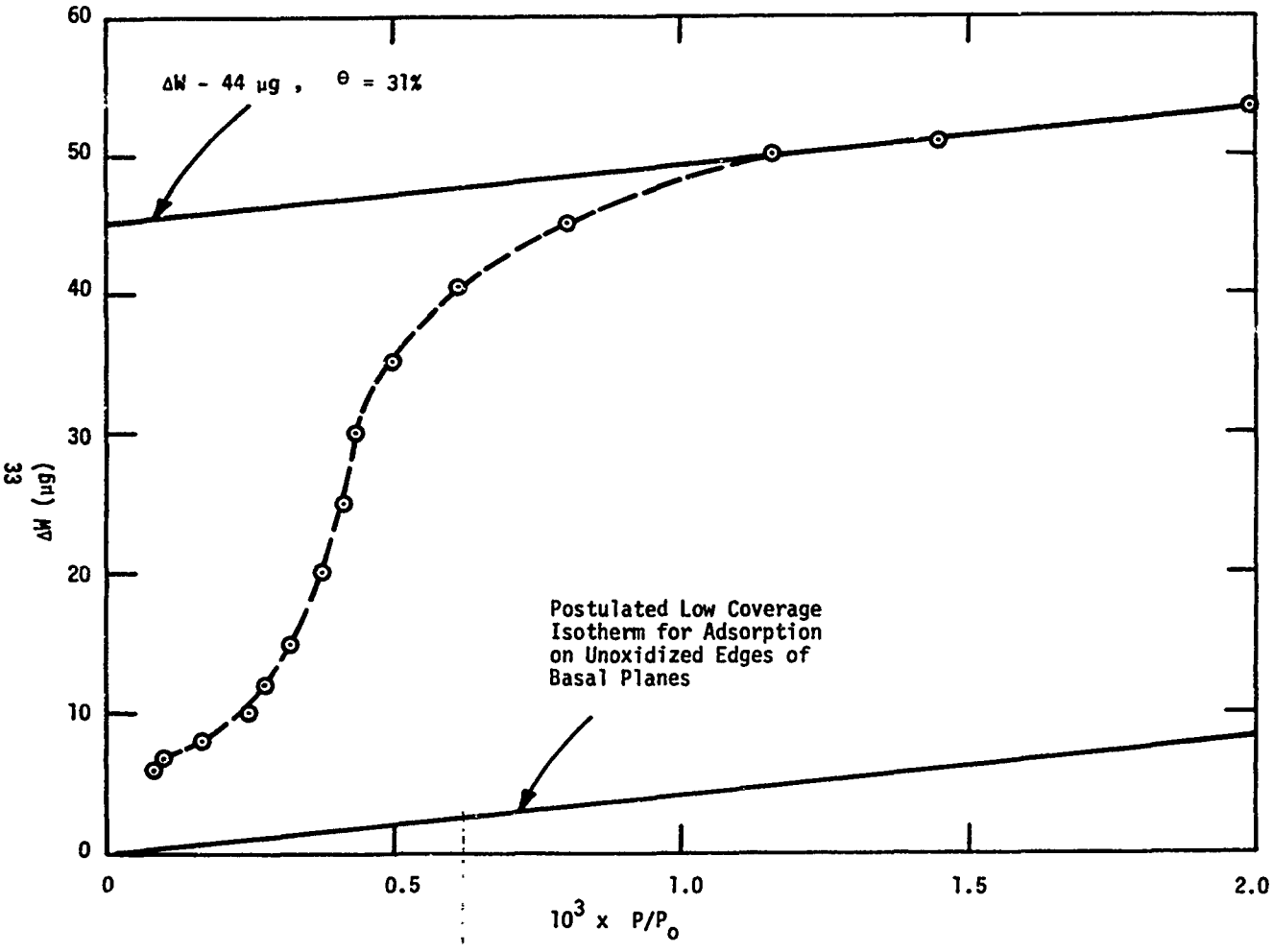

Figure 10. Low Coverage Isotherm for Nitrogen at 77.3°K, on Thornel-50 Fibers Vacuum Heat Treated at 880°C.

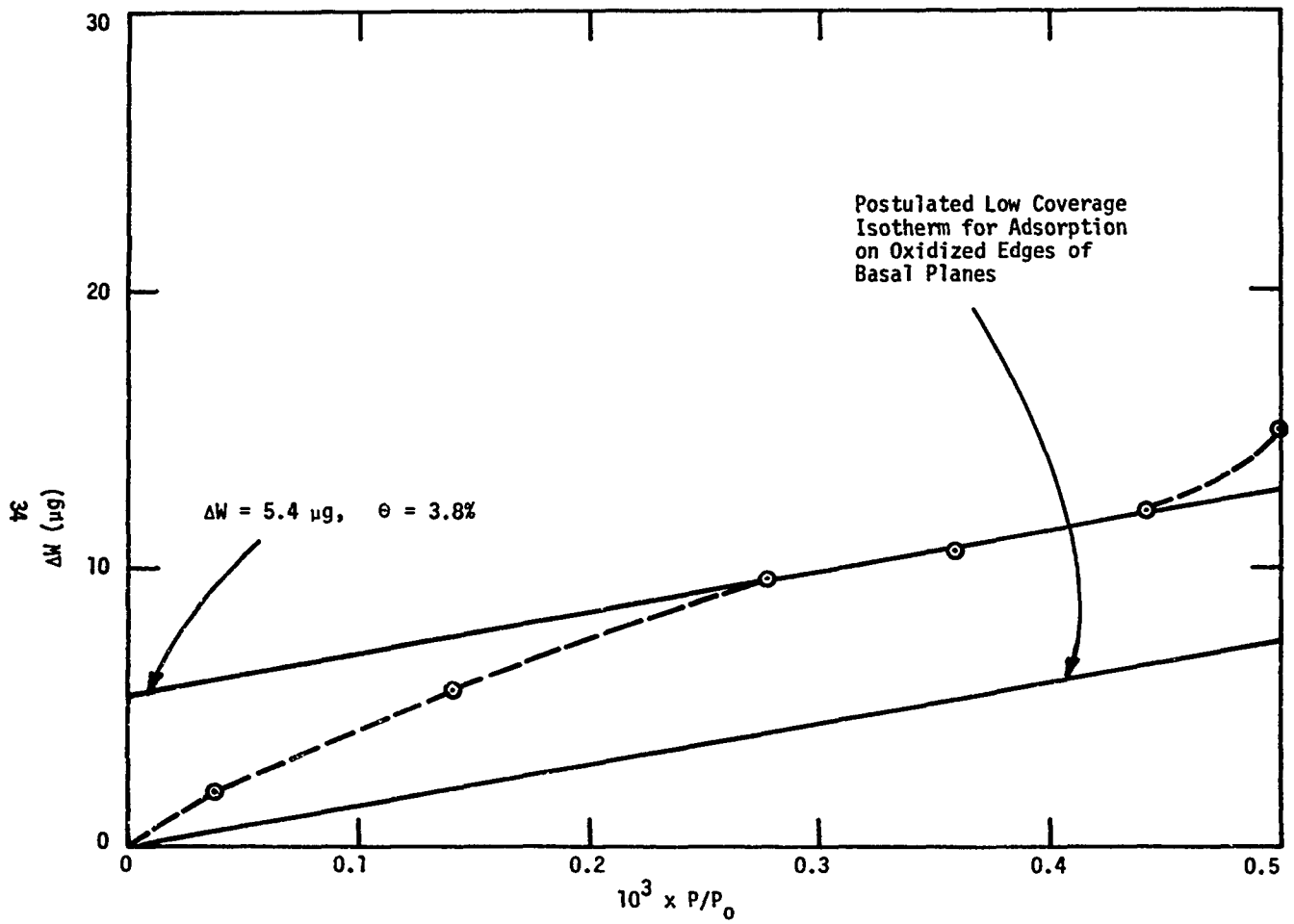

Figure 11. Extreme Low Coverage Isotherm for Nitrogen, at 77.3°K, on Thornel-50 Fibers Vacuum Heat Treated at 880°C.

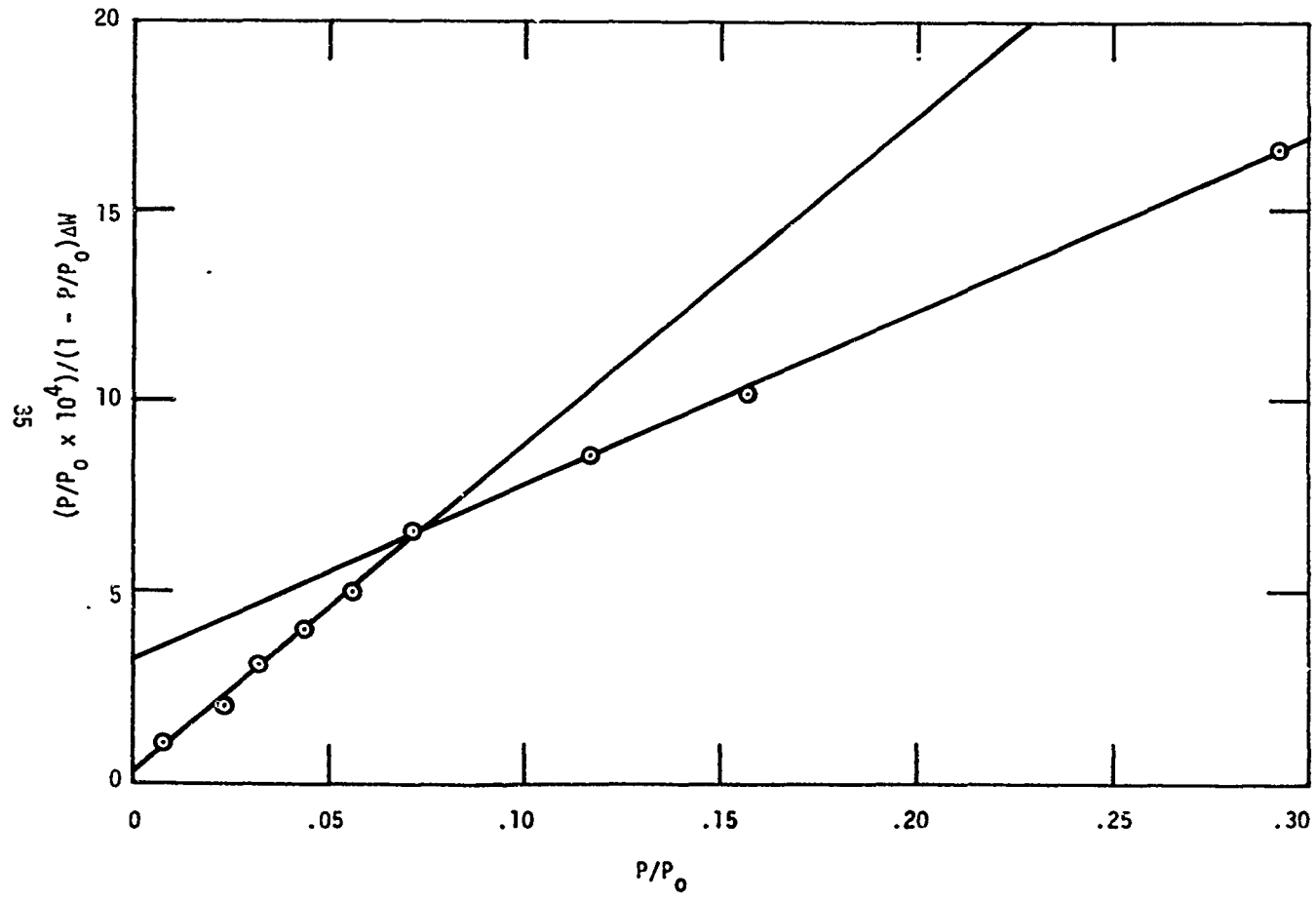

Figure 12. B.E.T. Plot, for Nitrogen at 77.3°K, on Thornel-50 Fibers Vacuum Heat Treated at 590°C.

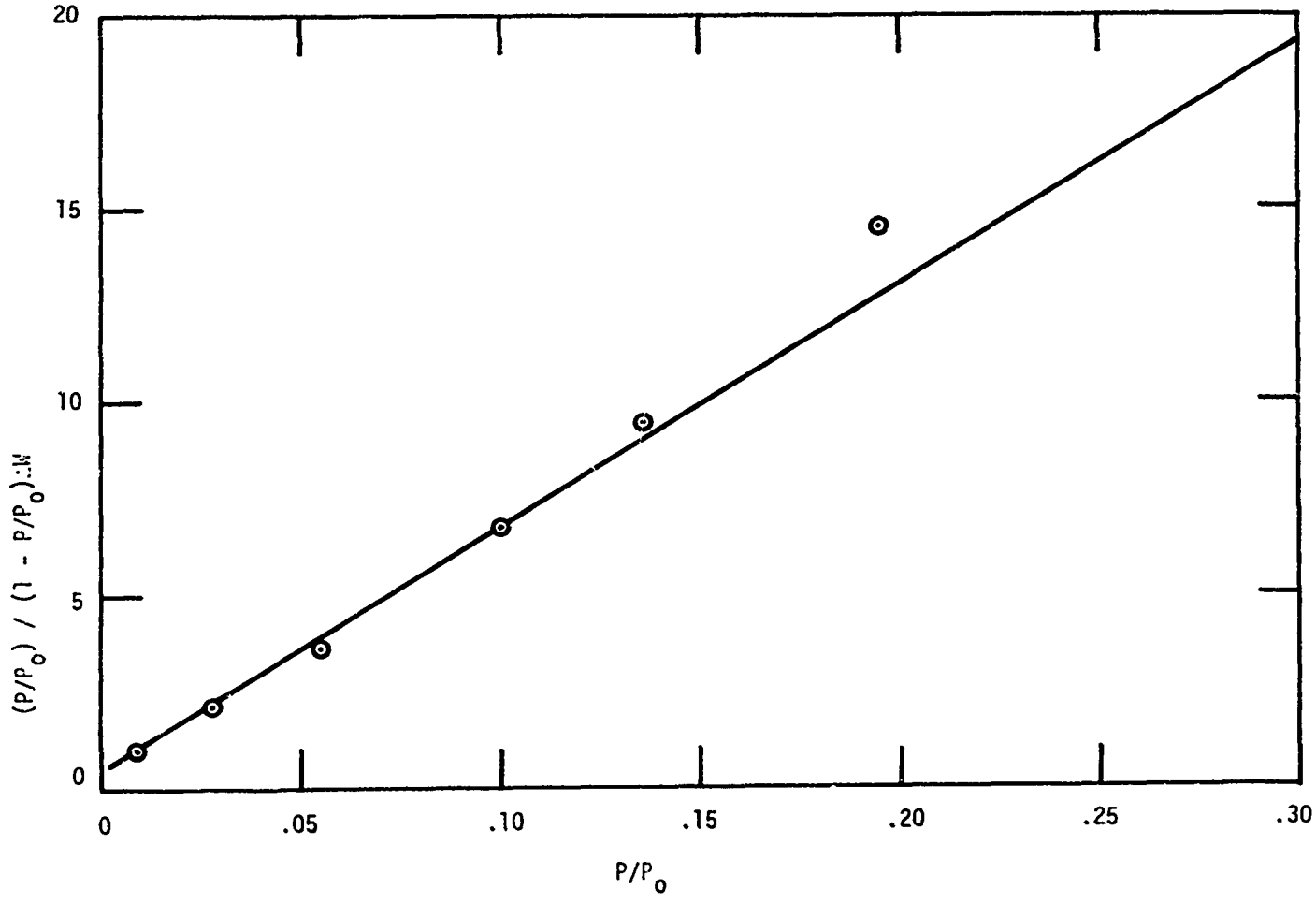

Figure 13 - B.E.T. Plot, for Argon at 90.2°K, on Thornel-50 Fibers Vacuum Heat Treated at 490°C.

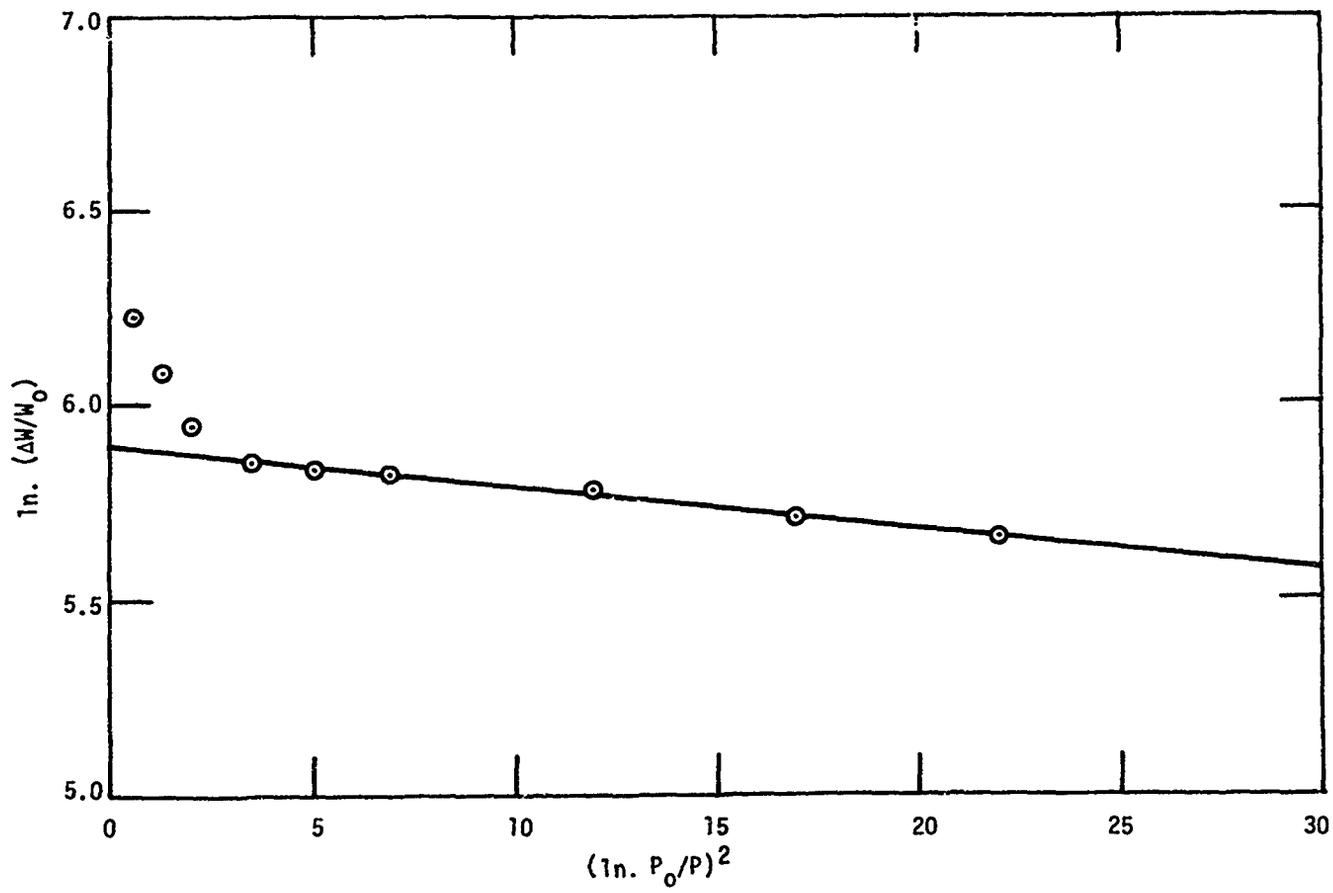

Figure 14 - Kagamer Plot, for Argon at 77.3°K and 90.2°K, on Thornel-50 Fibers Vacuum Heat Treated at 490°C.

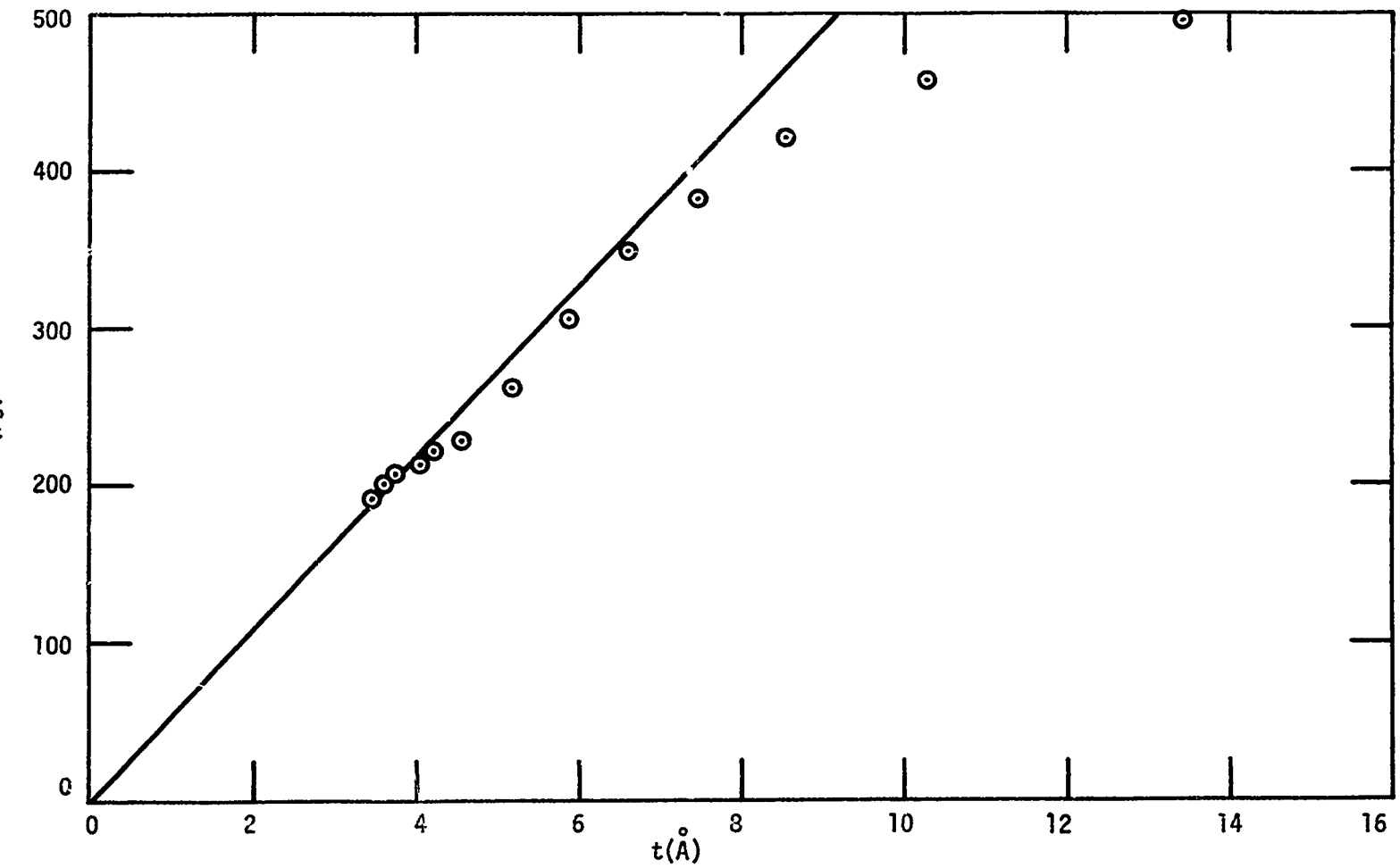

Figure 15. t-Plot, for Nitrogen at 77.3°K, on Thornel-50 Fibers Vacuum Heat Treated at 880°C.

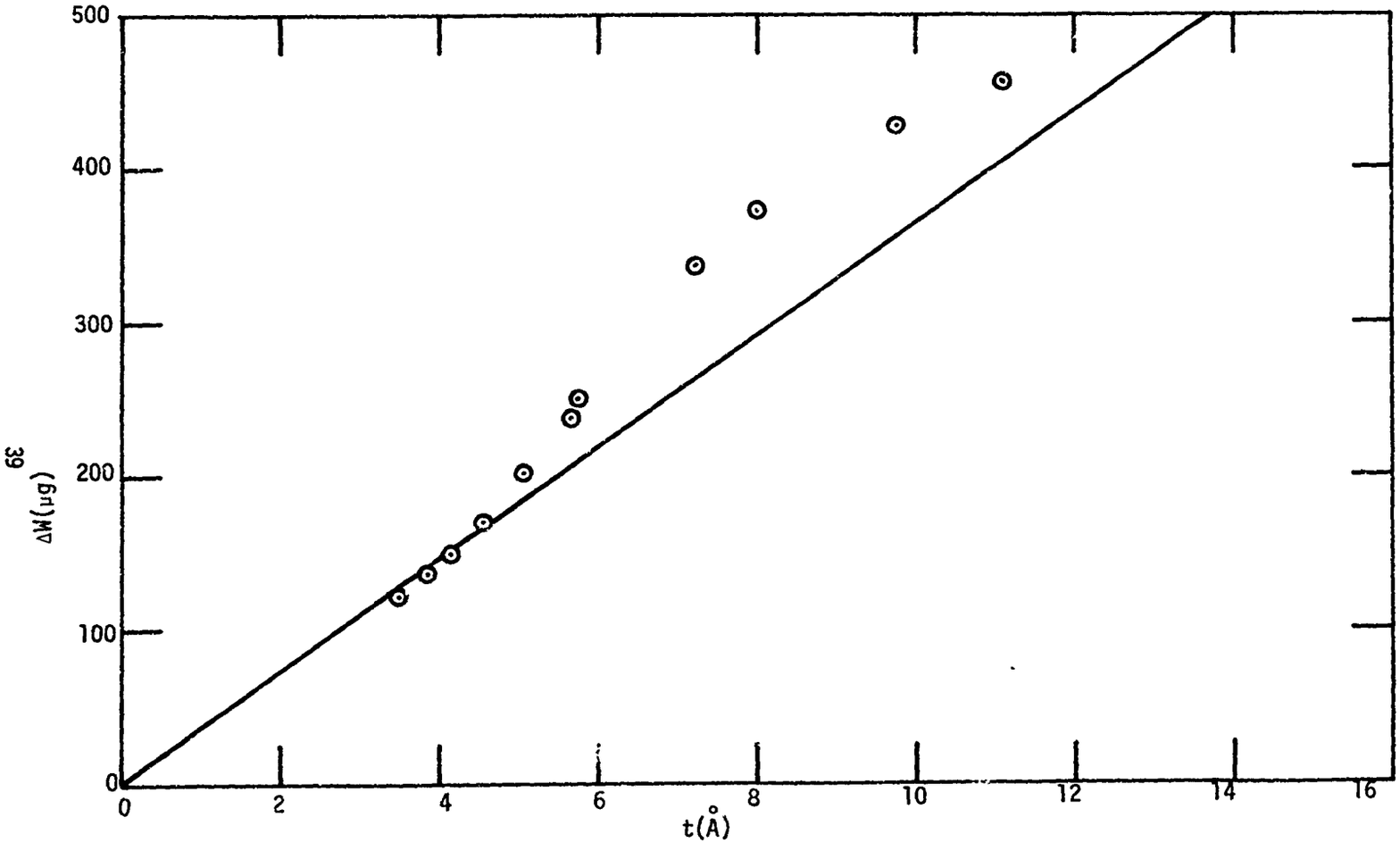

Figure 16. t-Plot, for Nitrogen at 77.3°K, on Thornel-50 Fibers Vacuum Heat Treated at 880°C.

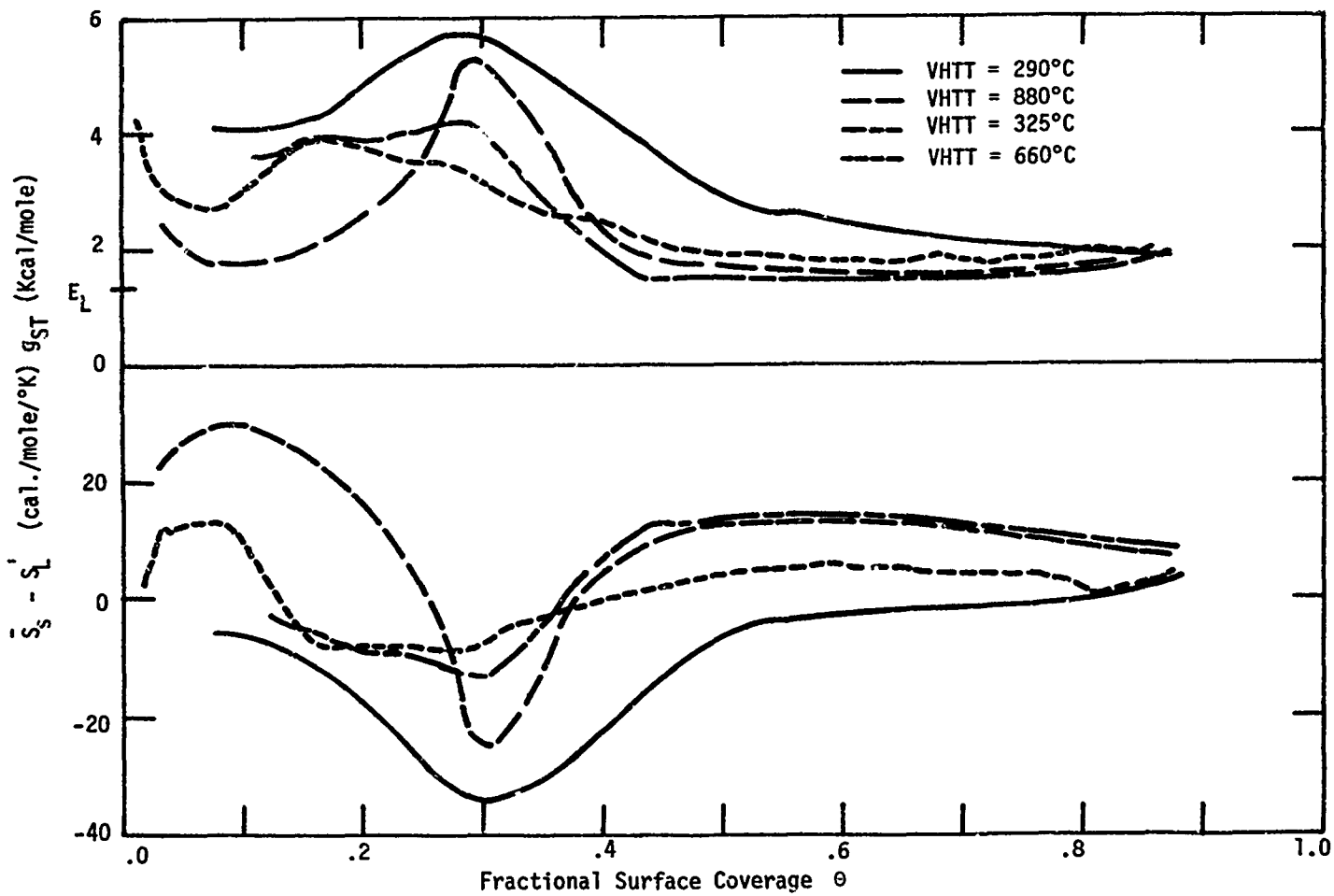

Figure 17. Isosteric Heats and Differential Entropies of Adsorption for Nitrogen on Thornel-50 Fibers Vacuum Heat Treated at 290°C, 325°C, 660°C and 880°C.

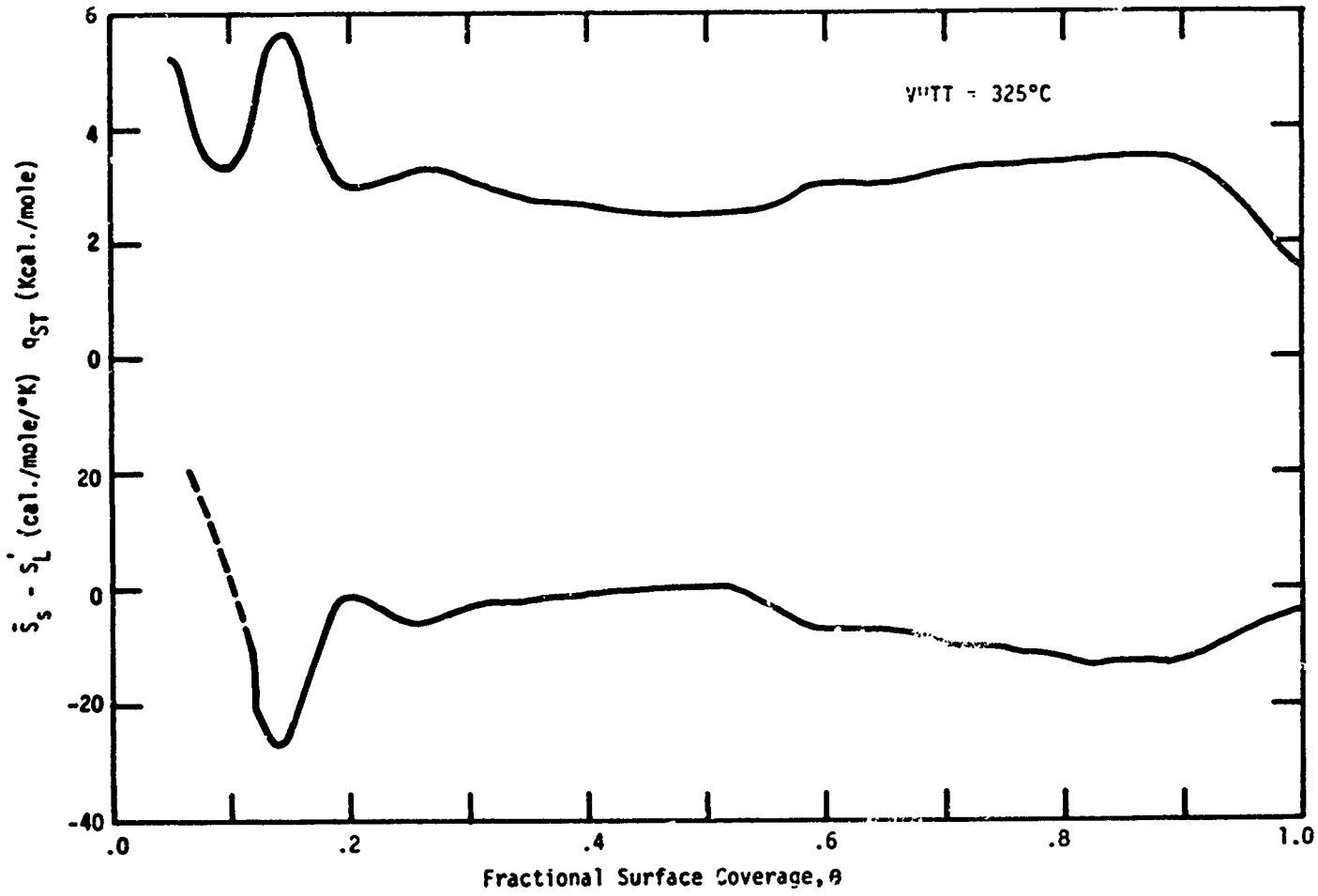

Figure 18. Isosteric Heats and Differential Entropies of Adsorption for Argon on Thornel-50 Fibers Vacuum Heat Treated at 325°C.

TABLE IV

COMPARISON OF A^{SP} - DETERMINED WITH N_2 and Ar

BET - Areas (in m^2/g)

VHTT (°C)		325	
Adsorption Temperature T(°K)		92.4	103.3
Absorbate	N_2	0.67	0.80
	Ar	0.67	0.78

B. Adsorption from Solution onto "Thornel-50" Fiber Surfaces (Prof. T. Fort and Satish C. Sharma)

Introduction

A considerable interest has been shown during the last decade in the development of high-strength, high-temperature resistant carbon-graphite fibers as reinforcing materials for polymer matrices to produce high strength composite materials. As a result of these developments graphite fibers with Young's modulus of up to 100 million psi and tensile strengths of over 300,000 psi along the fiber axis have been available. However, their use as reinforcing materials for polymer matrices has achieved only limited success because of poor adhesion between the fiber surface and the polymer matrix surrounding it. Studies [1] have shown that the interfacial shear strength achieved in most such composites is much lower (usually an order of magnitude) then the theoretically predicted maximum work of adhesion. While some improvements have been made [2-4] to increase the interfacial shear strength through various treatments administered to the fiber surface, not enough is yet known about the effect of these treatments on the surface characteristics of graphite fibers. Only limited correlations are available between fiber surface characteristics and the properties of graphite fiber reinforced composite materials. In order to systematically optimize the properties of such composites a knowledge of the interfacial characteristics of the composites and their variation with the nature of the fiber surface and the polymer matrix is necessary.

The objective of the present work is to determine information

about the surface properties (surface area, surface chemistry, and surface heterogeneity) which affect bonding of "Thornel-50" fiber to polymer matrices. This information is derived from studies of the adsorption of several organic solutes, from solution in cyclohexane, onto the "Thornel-50" graphite fiber surface. The solutes studied are stearic acid, octadecane, and benzoic acid. The technique used to follow adsorption is continuous flow column chromatography.

Experimental

A. Materials

1. "Thornel-50" Graphite Fibers: The graphite fibers were obtained from the Union Carbide Corporation Technical Center in Parma, Ohio. These specially prepared, unsized, fibers were used without any pretreatment except washing with pure cyclohexane which was also the solvent for the adsorption studies.

2. Solvent: Cyclohexane was chosen to be the solvent for all adsorption experiments. Because of its non-polar, non-planar nature, it was expected not to compete significantly with the solutes for sites on the "Thornel-50" surface.

The cyclohexane was obtained from the Matheson Scientific Company, Cleveland, Ohio. This 99+ mole percent chromatoquality material was shown by gas chromatographic analysis to be 99.88 percent cyclohexane. The solvent was further purified by fractional distillation.

3. Adsorbates

Stearic Acid: Stearic acid (99.5 percent) was obtained from Lachat Chemicals, Chicago, Illinois, and used as received.

Octadecane: Octadecane (99.5 percent) was obtained from Lachat Chemicals, Chicago, Illinois, and used as received.

Benzoic Acid: Fisher Certified ACS benzoic acid was obtained from the Fisher Scientific Company, Cleveland, Ohio, and used as received.

B. Equipment

1. Introduction

"Thornel-50" graphite fibers have a very low ($\sim 1\ m^2/gm.$) specific surface area. Classical techniques to study adsorption from solutions on high surface area powdered solids could not, therefore, be applied to obtain quantitative adsorption data on these fibers. After consideration of other available experimental techniques to

study adsorption from solutions, it was decided to use continuous flow column chromatography. This technique has been used in the past [5,6] to study adsorption of gases [5] and vapors, [5,6] on activated carbon powders [5] and other materials [6]. The present work is, however, the first time that it has been used to study adsorption from solutions onto fiber surfaces. A schematic of the equipment constructed for this purpose is shown in Figure 1.

2. Column: "Thornel-50" graphite fibers are wound in a spiral manner around an 8 mm diameter glass rod and the fiber-wound rod is packed tightly in a column made of stainless steel. The column is 39.4 cm long and has an inner diameter of 1.71 cm. This method of packing is expected to minimize channeling and give a uniform and reproducible packing.

3. Oven: The chromatographic column along with the temperature equilibration coils is mounted inside a 22 in. x 15 in. x 30 in. (LxWxH) thermostat constructed from 2-in. thick "Marinite." The system can be baked to temperatures of about 300°C and the adsorption temperature can be controlled between 25°C and 100°C. There is provision for evacuating the system and for purging it with nitrogen while simultaneously heating to clean the fiber surface.

4. Temperature Controller: The temperature of the column during an adsorption run can be controlled with an accuracy of better than ± 0.5°C with the help of an on-off temperature controller. A Fisher (Fisher Scientific Company, Cleveland, Ohio) temperature control unit Model 15-445-44 along with thermoregulator Model 15-445-30 is used for this purpose. The temperature is controlled by air circulation along with electric heaters.

5. Pumps: Two identical, Model 196-31, Milton Roy Minipumps (Milton Roy Pump Company, Chemical Pump and Equipment Corporation, Bedford, Ohio) are used to pump the solvent and solutions through the chromatographic column. These pumps are capable of delivering constant flow rates of 16 to 160 ml/hr with an accuracy of ± 0.3%. Both the pumps were calibrated and the calibrations agreed very well with the manufacturer's specifications.

6. Detector: The eluent from the chromatographic column is continuously monitored for concentration changes using a differential refractive index method. A Model 1103 LDC Refractomonitor supplied by Laboratory Data Control Co., Danbury, Connecticut is used for this purpose. It is capable of detecting refractive index differences of $\pm 10^{-7}$ R.I. units.

7. Recorder: The output from the detector is recorded using a Model E11CTS Esterline Angus Speedservo Recorder supplied by Esterline Angus Division of Esterline Corporation, Indianapolis, Indiana.

C. Procedure:

1. Measurement of "Dead Volume": The dead volume between the point of switch from solvent to solution (and vice-versa) and the detector must be accurately known before the amount absorbed at different solute concentration can be calculated. Dead volume was estimated by calculating the volume of tubing and fittings and adding this volume to the void volume of the column. The dead volume was also determined experimentally by running the solvent through the dry column at known flow rates and noting the time required for it to pass through the dead volume region.

2. Measurement of Adsorption Isotherms: After the temperature has stabilized in the system, the solvent is pumped through the column at a fixed desired flow rate. With solvent flowing through the reference chamber of the detector the output from the column is monitored until a steady baseline is obtained on the recorder chart. After obtaining a steady baseline and making it coincide with the recorder zero the column inlet is switched from solvent to a solution of known concentration flowing at the same rate as the solvent. With pure solvent flowing through the reference chamber the column effluent is continuously monitored for concentration changes. The signal changes because of the emergence of the solute front and after some time reaches another constant value signifying the establishment of adsorption equilibrium inside the column. After the signal has remained unchanged for at least two hours, the run is considered complete and the amount of solute adsorbed can be calculated by material balance for the solute. By repeating this procedure with different solute concentrations and at different temperatures, adsorption isotherms are developed.

Results

A. Dead Volume

Table I lists the estimated and experimental dead volume found for the "Thornel-50" packed adsorption column. The two sets of values agree reasonably well. The difference may result from error in the fiber density (1.63 gm./cc.) used in the estimations, or to small amounts of channeling in the column during the experiments. Agreement was considered sufficiently good to proceed with the adsorption experiments.

B. Adsorption Isotherms

In Figure 2 are shown isotherms for the adsorption of stearic acid from cyclohexane solution onto "Thornel-50" at 22°C and at 45°C. Also shown in Figure 2 is data of Kipling and co-workers [7] for the adsorption of stearic acid from cyclohexane onto Graphon. Adsorption

increases as stearic acid solution concentration is increased to 6×10^{-4} mole fraction, then remains constant as solution concentration is further increased. Adsorption from a given solution concentration, below 6×10^{-4} mole fraction, is greater at 22°C than at 45°C.

Data for the adsorption of octadecane from cyclohexane solution onto "Thornel-50" at 25°C is shown in Figure 3. The adsorption isotherm has the same general shape as those for stearic acid, except that a higher solution concentration, 20×10^{-4} mole fraction, is required to achieve surface saturation.

Figure 4 shows data for adsorption of benzoic acid from cyclohexane solution onto the "Thornel-50" surfaces. The adsorption isotherm has a more complex shape than those found for stearic acid and octadecane in that there is some suggestion of two adsorption plateaus. Surface saturation is finally achieved at a solution concentration of 10×10^{-4} mole fraction benzoic acid.

C. "Thornel-50" Surface Area

The specific surface area of the "Thornel-50" filaments was estimated from the adsorption isotherms shown in Figures 2-4, with the assumption that the adsorption plateaus corresponded to close packed, horizontally oriented monolayers of solute molecules on the fiber surface. The area occupied by each adsorbed stearic acid molecule was taken to be 114 $Å^2$ [7]. The area occupied by each adsorbed octadecane molecule was taken to be 98 $Å^2$ [8], and that occupied by each adsorbed benzoic acid molecule was taken to be 70 $Å^2$ (calculated from molecular models). With these estimates, the surface area of the "Thornel-50" filaments was calculated to be 1.39 m^2/gm., 133 m^2/gm. and 1.36 m^2/gm., respectively.

D. Langmuir Adsorption Isotherms

The form of the adsorption isotherms suggested applications of the Langmuir adsorption equation to the experimental data. The convenient form of this equation is

$$\frac{c}{\Gamma} = \frac{1}{b\Gamma_m} + \frac{1}{\Gamma_m} c \quad ,$$

where

c = concentration of solute in solution ($\frac{\text{gms. solute}}{\text{100 mls. soln.}}$)

Γ = concentration of solute adsorbed at solution concentration c ($\frac{\text{mgm. solute}}{\text{gm. adsorbent}}$)

Γ_m = concentration of solute adsorbed at monolayer coverage ($\frac{\text{mgm. solute}}{\text{gm. adsorbent}}$)

and

b = constant .

If the Langmuir adsorption model is obeyed, graphs of $\frac{c}{\Gamma}$ vs. c should yield straight lines with slopes of $\frac{1}{\Gamma_m}$ from which the surface area may be evaluated. The adsorption data for octadecane did yield a good straight line (Figure 5) from which a fiber surface area of 1.48 m^2/cm. was calculated. The stearic acid data from experiments at moderate to high solution concentrations yielded fair straight lines (Figure 6) from which fiber surface areas of 1.51 and 1.55 m^2/gm. were calculated. The benzoic acid data did not yield a straight line Langmuir plot (Figure 7).

E. Isosteric Heat of Adsorption

The isosteric heat of adsorption (Q_{ST}) for stearic acid from cyclohexane onto "Thornel-50" was calculated from the data in Figure 2 and the equation

$$Q_{ST} \cong -R \left(\frac{\partial \ln c}{\partial (1/t)} \right)_\theta$$

Here,

Q_{ST} = isosteric heat ($\frac{\text{calories}}{\text{gm. mole}}$)

R = gas constant ($\frac{\text{calories}}{\text{gm. mole °K}}$)

C = concentration of solute in solution ($\frac{\text{moles}}{\text{liter}}$)

and

T = absolute temperature (°K).

The calculated values of the isosteric heat of adsorption are plotted as a function of surface coverage in Figure 8. Q_{ST} is seen to be small (2.8-2.9 k cal/mole) and to vary only 0.1 k cal/mole as fractional surface coverage is increased from 0.25 to 1.0. The values

of isosteric heat shown in Figure 8 were calculated from the smoothed-out adsorption isotherms plotted in Figure 2.

Discussion

A. Surface Area of "Thornel-50"

The specific surface areas of "Thornel-50" fibers calculated from the adsorption plateau heights in Figures 2, 3, and 4 were 1.39, 1.33 and 1.36 m^2/gm., respectively. The agreement between these values is excellent, even though they have been derived from adsorption data for three different molecules. This fact tends to confirm the validity of each individual measurement, and also the postulated surface area orientation of molecules in the adsorbed films.

No comparative surface area values for "Thornel-50" , obtained from solution, are available. Brooks and Scola [9] obtained 0.55 m^2/gm. by krypton adsorption on "Thornel-50" at 77°K. A value of 0.8 m^2/gm was obtained by Brooks and Scola [9] by nitrogen adsorption on "Thornel-25" at 77°K while Didchenko [10] obtained 1.6 m^2/gm. for the same material. Other experiments in our laboratory [11] yield 1.3-1.4 m^2/gm. for "Thornel-50" from argon and nitrogen adsorption experiments at 90°K.

A specific surface area of 1.3 m^2/gm. represents a roughness factor of approximately 3.0 for "Thornel-50" surfaces if each filament is assumed to be a smooth cylinder 6 microns in diameter.

B. Langmuir Adsorption Isotherms

Of the three solutes investigated, only octadecane gave a good linear Langmuir plot. Deviation from linearity for stearic acid and benzoic acid may probably be ascribed to dimerization of these solutes in cyclohexane, which would change their effective solution concentration, or possibly to heterogeneity of the "Thornel-50" surface which would make the energy of acid adsorption a function of surface coverage (contrary to the Langmuir model). Both these possibilities are being investigated.

C. Energy of the "Thornel-50" Surface

Comparison of the solute concentrations required to achieve surface saturation suggests that increasing order of solute affinities for the "Thornel-50" is octadecane < benzoic acid < stearic acid. These affinities refer to the gross surface and not specific attraction to active sites. This gross surface is probably quite similar to that of Graphon, as evidenced (Figure 2) by the similar adsorption of stearic acid from cyclohexane onto "Thornel-50" and this graphitized

TABLE I

MEASUREMENT OF DEAD-VOLUME

I. CALCULATED VALUE = 38.86 c.c.

II. EXPERIMENTAL

FLOW RATE (c.c./Minute)	TIME (Minutes)	DEAD VOLUME (c.c.)
0.935	39.7	37.12
0.935	40.2	37.59
0.530	69.9	37.10
0.935	39.6	37.04
1.335	27.9	37.26
	Average =	37.22 c.c.

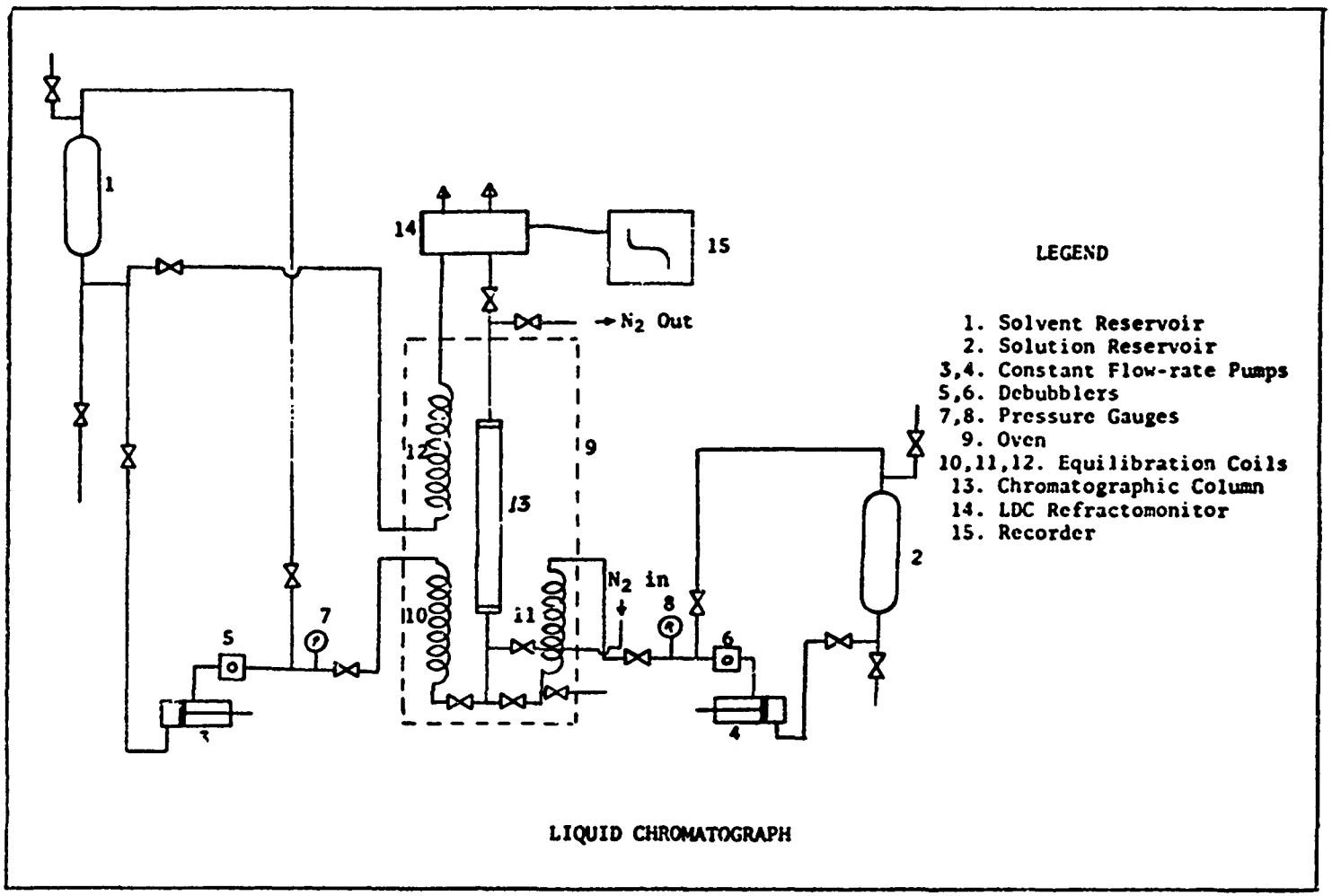
1
2
3
4
5
6
7
8
9
10
11
12
13
14
15
N_2 Out
N_2 in
LEGEND
1. Solvent Reservoir
2. Solution Reservoir
3,4. Constant Flow-rate Pumps
5,6. Debubblers
7,8. Pressure Gauges
9. Oven
10,11,12. Equilibration Coils
13. Chromatographic Column
14. LDC Refractomonitor
15. Recorder
LIQUID CHROMATOGRAPH

Figure 1

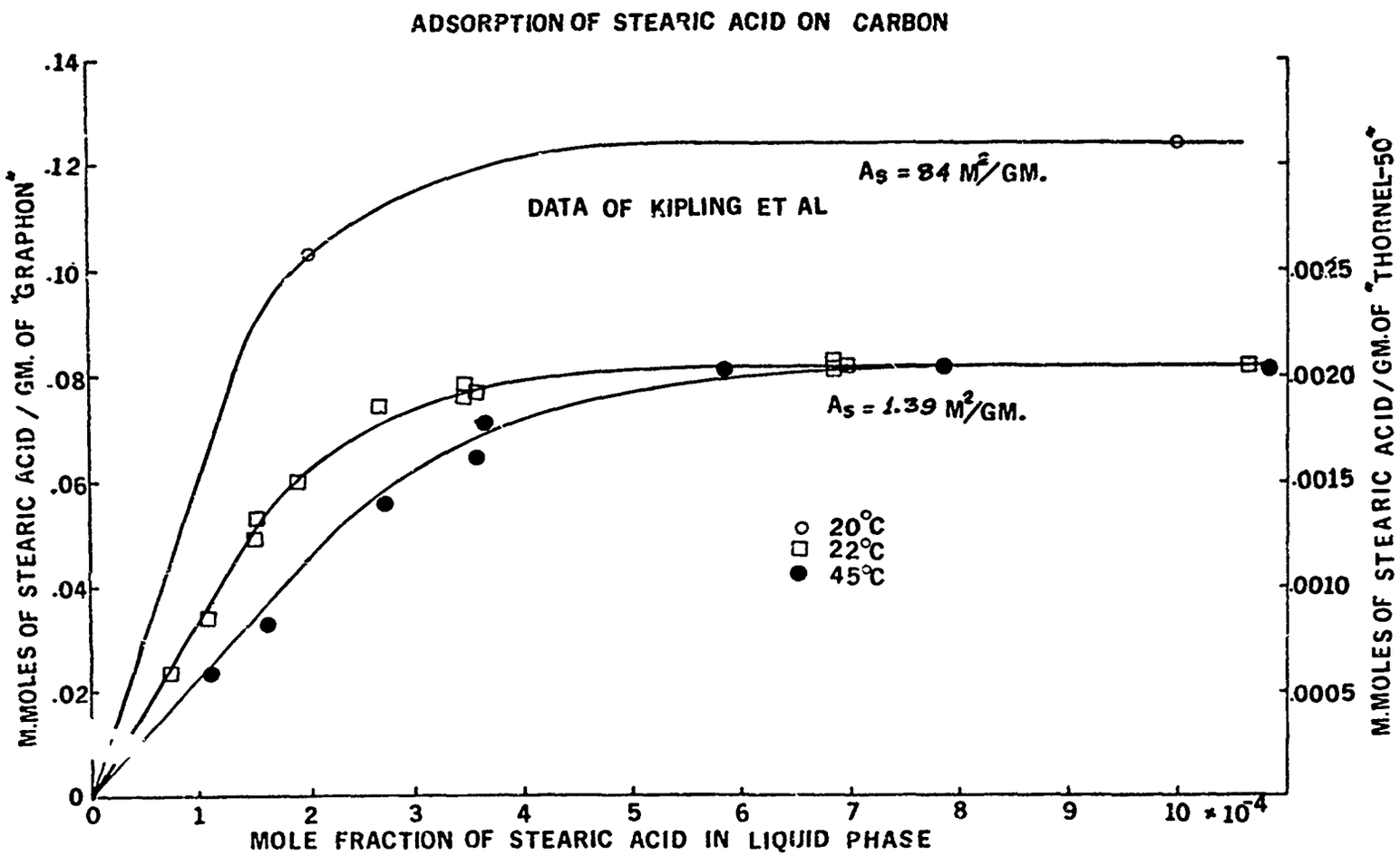
ADSORPTION OF STEARIC ACID ON CARBON
M.MOLES OF STEARIC ACID / GM. OF "GRAPHON"
M.MOLES OF STEARIC ACID / GM. OF "THORNEL-50"
MOLE FRACTION OF STEARIC ACID IN LIQUID PHASE
A_S = 84 M^2/GM.
DATA OF KIPLING ET AL
A_S = 1.39 M^2/GM.
20°C
22°C
45°C
.14
.12
.10
.08
.06
.04
.02
0
.0025
.0020
.0015
.0010
.0005
0 1 2 3 4 5 6 7 8 9 10 × 10^{-4}

Figure 2

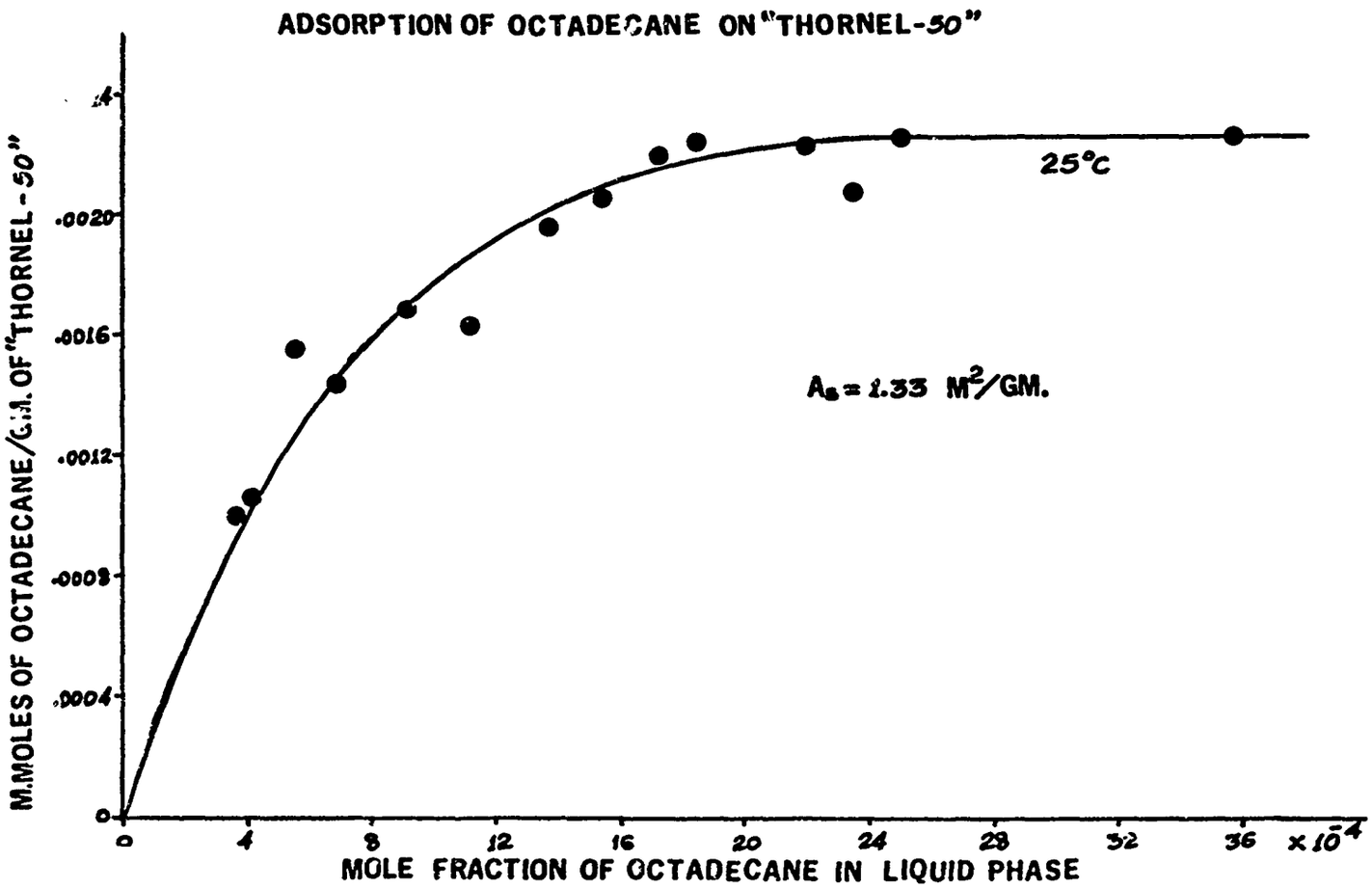
ADSORPTION OF OCTADECANE ON "THORNEL-50"
M.MOLES OF OCTADECANE/GM. OF "THORNEL-50"
.0020
.0016
.0012
.0008
.0004
0
0
4
8
12
16
20
24
28
32
36
x 10⁻⁴
MOLE FRACTION OF OCTADECANE IN LIQUID PHASE
25°C
A_s = 1.33 M²/GM.

Figure 3

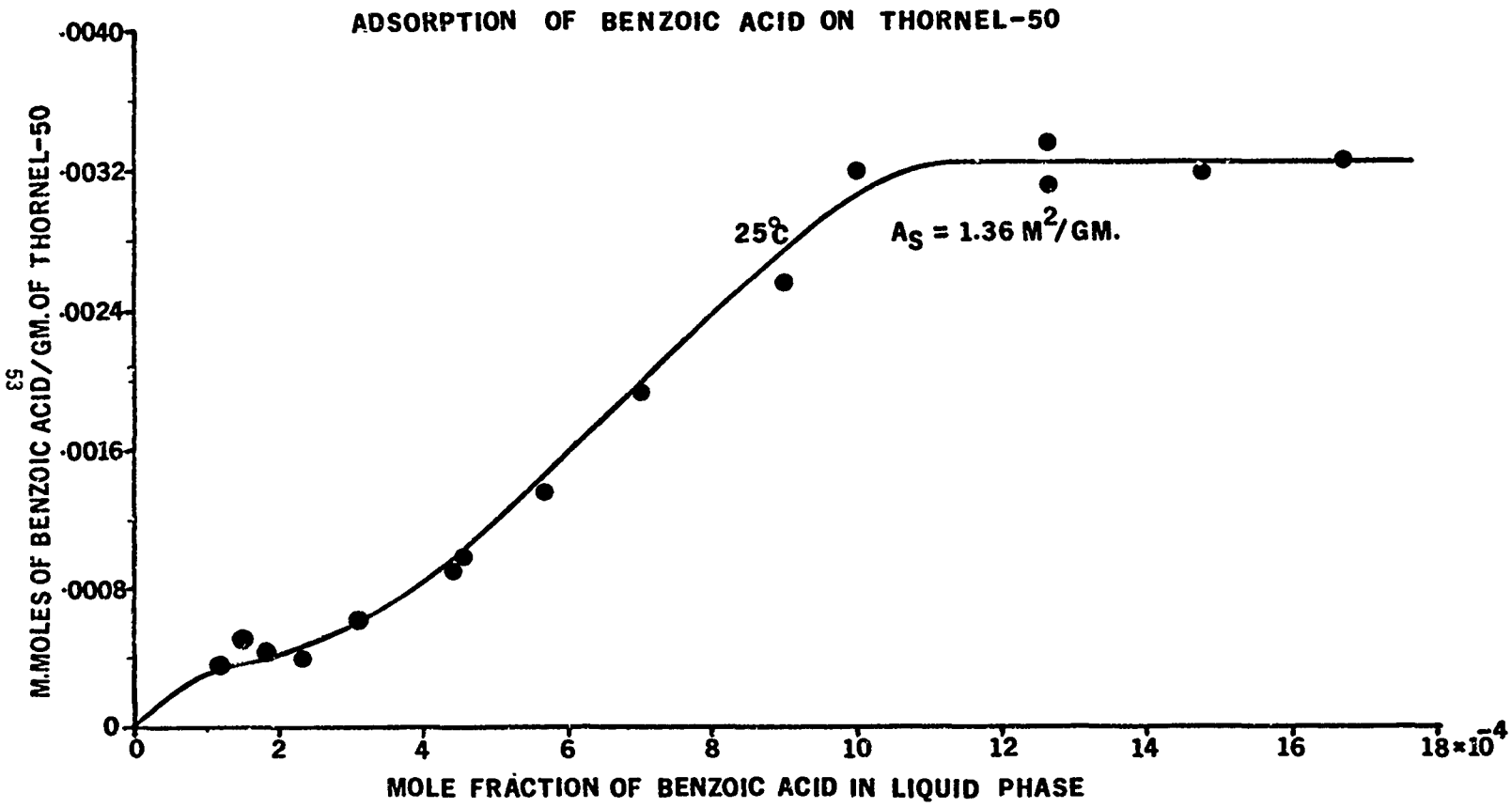
ADSORPTION OF BENZOIC ACID ON THORNEL-50
M.MOLES OF BENZOIC ACID/GM.OF THORNEL-50
·0040
·0032
·0024
·0016
·0008
0
25°C
A_S = 1.36 M^2/GM.
0
2
4
6
8
10
12
14
16
18×10⁻⁴
MOLE FRACTION OF BENZOIC ACID IN LIQUID PHASE

Figure 4

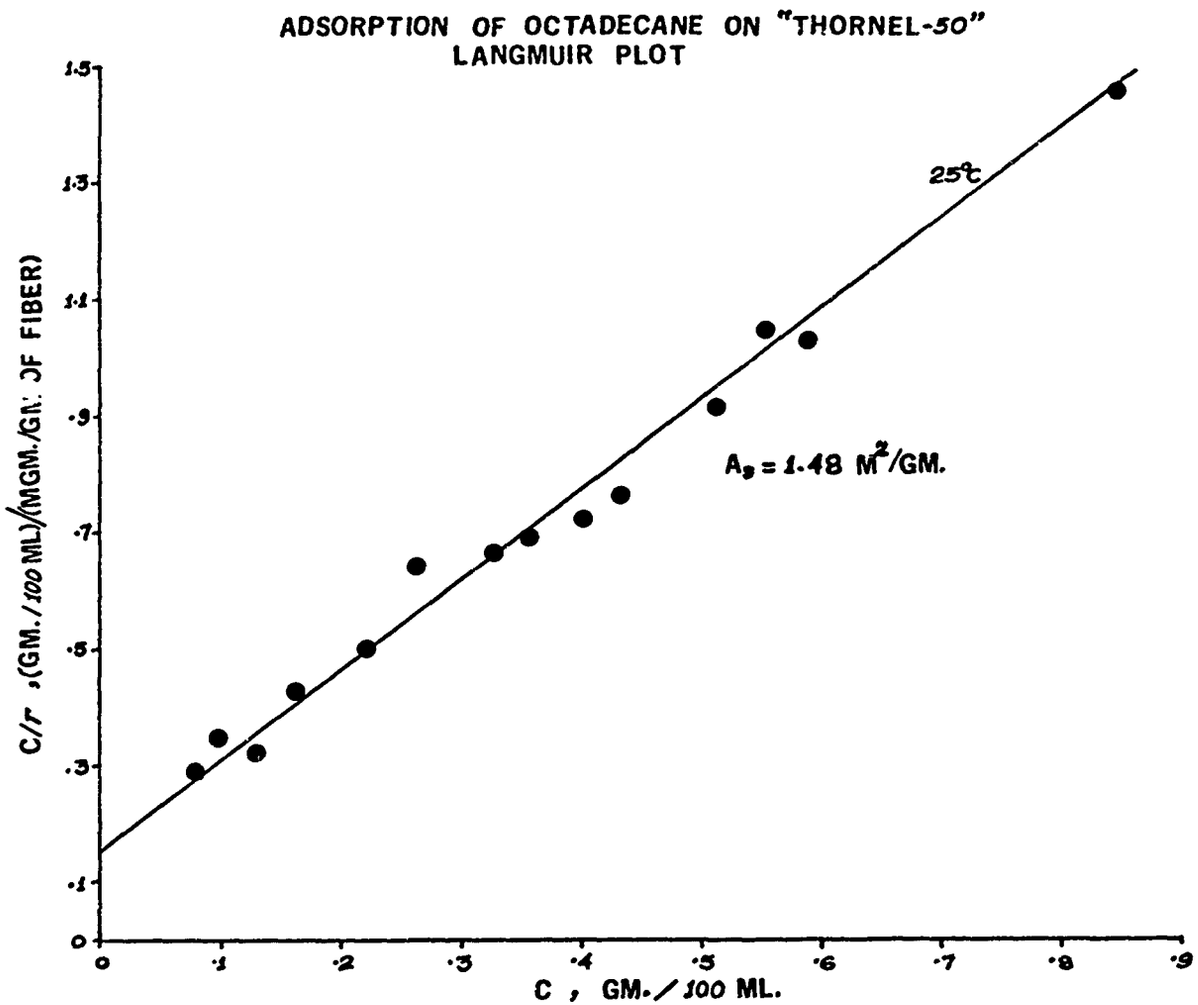
ADSORPTION OF OCTADECANE ON "THORNEL-50"
LANGMUIR PLOT
25°C
$A_s = 1.48\ M^2/GM.$
C/r s (GM./100 ML)/(MGM./GM. OF FIBER)
C , GM./100 ML.
0
.1
.2
.3
.4
.5
.6
.7
.8
.9
1.1
1.3
1.5

Figure 5

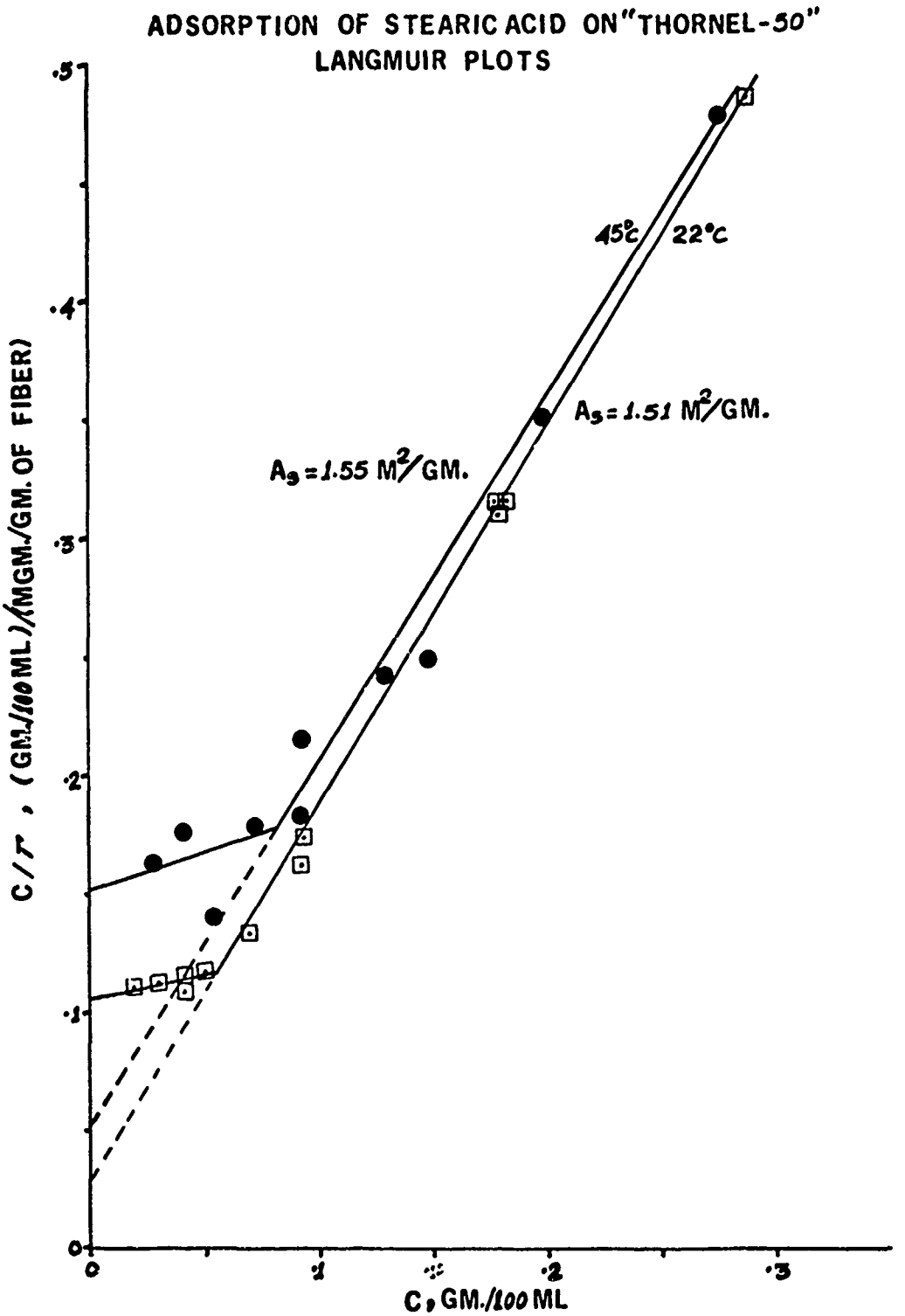
ADSORPTION OF STEARIC ACID ON "THORNEL-50"
LANGMUIR PLOTS
45°c
22°c
$A_s = 1.51\ M^2/GM.$
$A_s = 1.55\ M^2/GM.$
C/Γ , (GM./100 ML)/(MGM./GM. OF FIBER)
C, GM./100 ML
0
·1
·2
·3
·4
·5

Figure 6

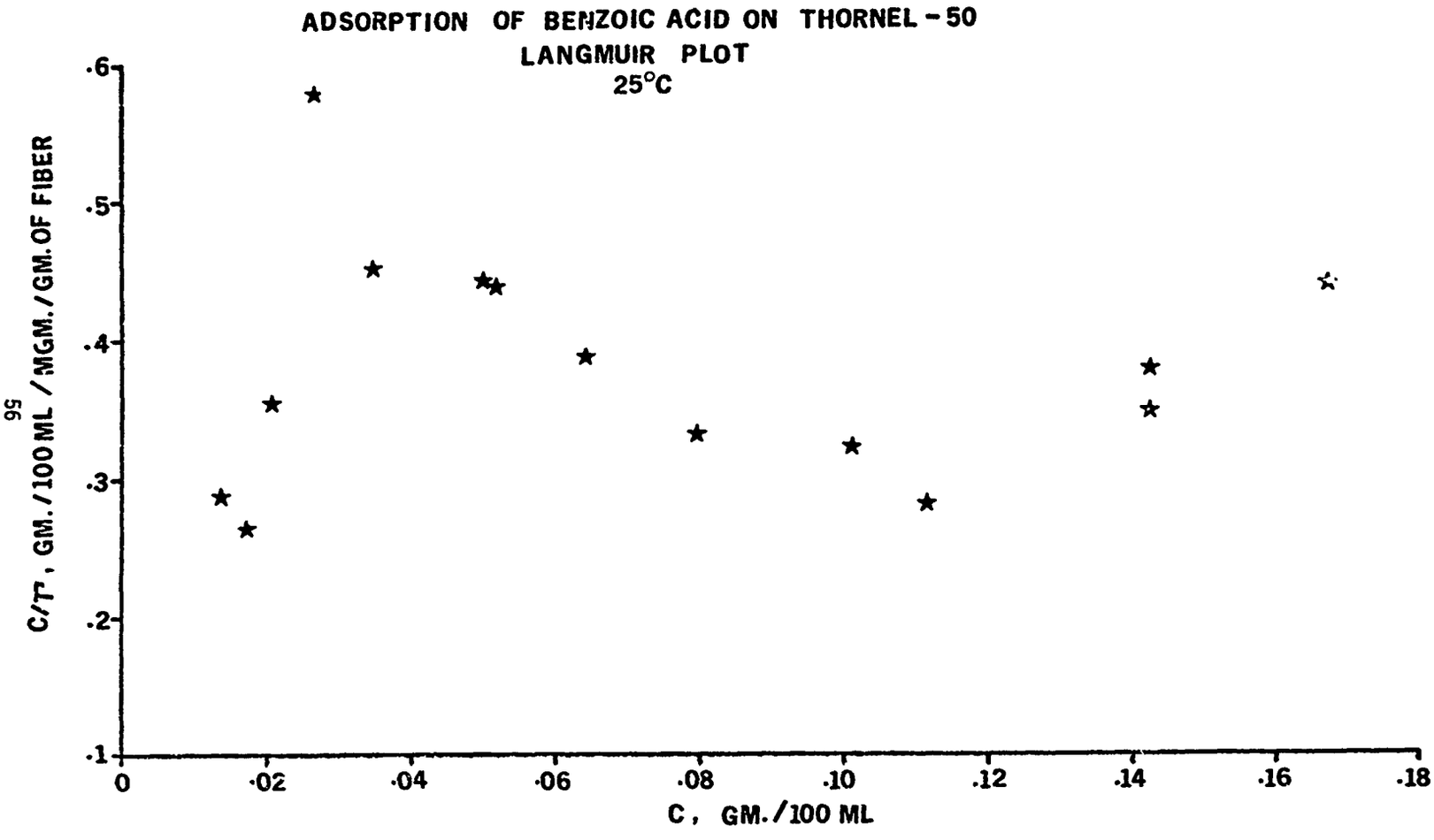
ADSORPTION OF BENZOIC ACID ON THORNEL-50
LANGMUIR PLOT
25°C
C/Γ, GM./100 ML /MGM./GM. OF FIBER
.6
.5
.4
.3
.2
.1
0
.02
.04
.06
.08
.10
.12
.14
.16
.18
C, GM./100 ML

Figure 7

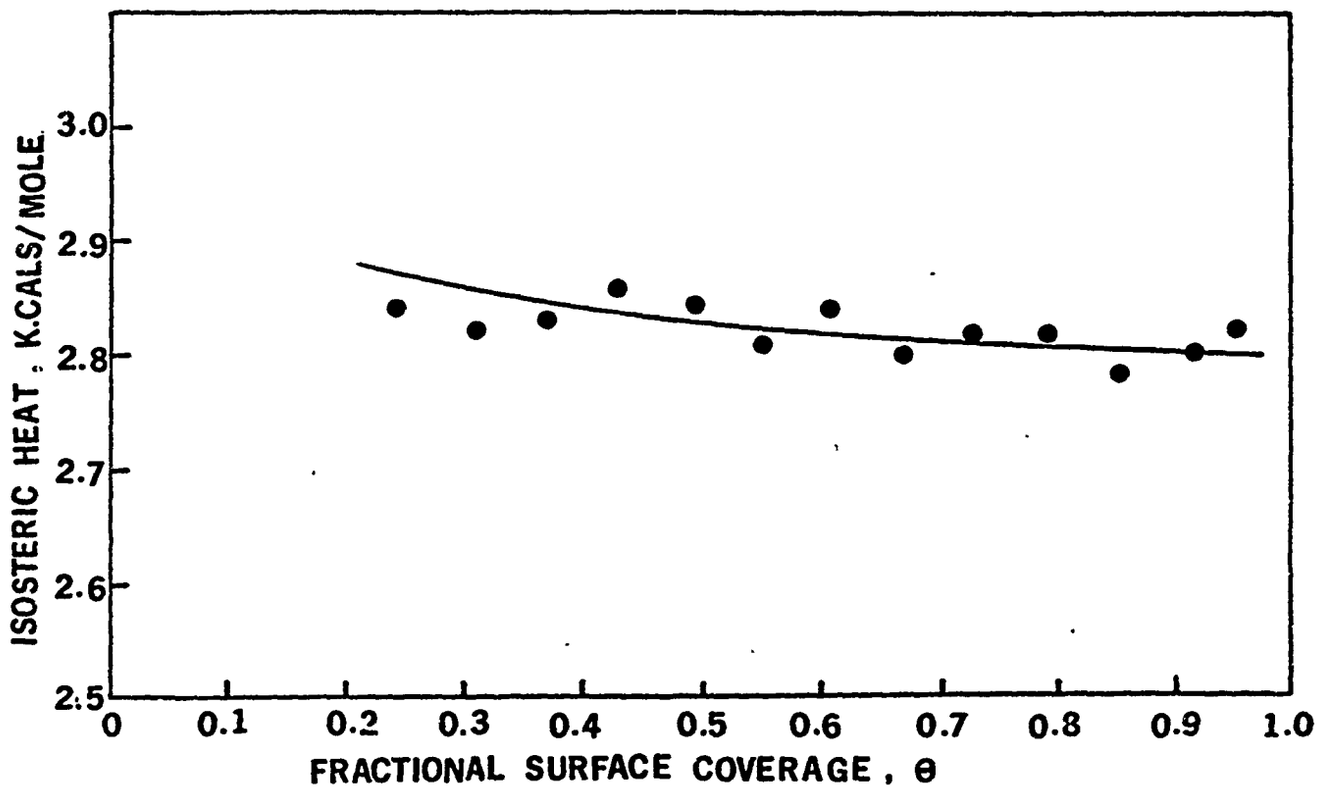

ISOSTERIC HEATS OF ADSORPTION FOR STEARIC ACID ON "THORNEL-50"

Figure 8

carbon black.

The general homogeneity of the "Thornel-50" surface is also evidenced by the nearly surface coverage independent isosteric heats of stearic acid adsorption shown in Figure 8. The low values (2.8-2.9kcal/mole) of these heats indicate weak (physical) adsorption of the acid to the low energy fiber surfaces.

It should be emphasized that the sensitivity of the differential refractometer used to sense adsorption only permits measurements, with stearic acid, down to a surface coverage of 25 percent. Measurements of benzoic acid adsorption, now in progress, may be carried down to a surface coverage of about 1 percent. These measurements will, it is expected, confirm a small number of active sites on the "Thornel-50" fiber surface.

C. Nylon-Graphite Composites by In-S Polymerization
(Prof. Morton Litt and Allan W. Brinkman)

Introduction

It was the objective of this research to make Nylon 6 graphite fiber composites by in-situ polymerization. Composites made by this approach were expected to be void-free and show improved matrix bonding to the fiber surfaces. Wetting problems experienced with other matrix systems are avoided by employing monomeric reagents instead of low molecular weight polymeric reagents. Thus, improved wetting would lead to void-free composites. Also, bonding was expected to improve because fibers initiate crystallization and polymerization might occur at the fiber surface.

To begin, it was necessary to design and integrate three aspects leading to a composite:

A. A co-catalyst had to be selected.

B. Molds and jigs had to be designed and made.

C. The polymerization and testing procedures had to be developed.

A. Selection of co-catalyst

Benzyl acetate, benzyl benzoate, phenyl acetate, and ε-caprolactone were compared to tert-buytl acetate. The basis for comparison was defined by reaction velocity, polymer quality and void content.

Caprolactone created no voids due to vapors from residue leaving groups since it did not form leaving groups, but did create crazed voids in bulk matrix due to polymer adhesion to glass. Benzyl acetate and benzyl benzoate produced very slow reactions and very low grade polymer products; however, no voids due to vaporized residue were observed. Tert-butyl acetate produced rapid reactions and a very tough product, but created many voids due to vaporized t-butanol. Phenyl acetate produced a fast reaction with good polymer product, but it can terminate the reaction if used in excess.

TABLE I

Comparison of Co-catalysts

Co-catalyst	Rate of Polymerization	Properties	Voids
Tert-butyl acetate	Fast	Tough	Many
ε-caprolactone	Moderate	Tough	Few
Benzyl benzoate	Slow	Brittle	None
Benzyl acetate	Slow	Brittle	None
*Phenyl acetate	Fast	Tough	Few

* Phenoxy radical can terminate amide anion.

Caprolactone was selected as the catalyst which offered the best compromise between void content, reaction velocity, and polymer quality.

B. Mold and Jig Designs

Jigs

Rod jigs in combination with glass tubes can be used to obtain composites containing approximately 25 - 20% v/v fiber. Ladder jigs and "H" bar jigs allow greater fiber compaction because they are stiffer than the rod jig and so allow greater fiber tension during winding. However, at higher than 25 - 30% v/v fiber, the monomer doesn't penetrate completely between fibers under the degassing conditions used.

The ladder jig is the most versatile because it can be used in any of the three mold designs. Also, it contains the fibers well, limiting fiber wash. The rod jig is best used in glass tubes. It is undesirable in any of the other molds. The "H" bar is undesirable because only very light fiber densities can be employed as the monomer doesn't penetrate rapidly.

Molds

Glass molds (test tubes) had the advantages of being readily available, inexpensive, and allowed work to begin without delay. However, in using them, entrapped air was difficult to remove since

little or no manipulation of the wetted fibers is possible. Furthermore, caprolactone bonds strongly to the glass, making voids when the nylon shrinks.

A three-plate mold with a ladder jig and compression bar were used to make composites. This design allowed moderately high vacuum to be applied to loosely-wound fibers - a combination which improved degassing- after the fibers were covered with reactive caprolactam. The mold had to be reopened and a compression bar added. On closing, the fibers were compressed to obtain higher fiber content composites. The mold then had to be transferred to an oven at 240°C for twenty hours. It is not known why heating for twenty hours is required. The reaction was expected to occur within one hour. In comparison to glass, the all-aluminum cavity eliminated matrix bonding to the walls.

Finally, a match die type mold employing a ladder jig was designed. This mold allowed very rapid heat-up. All six sides of the cavity could be heated to 220°C. within eleven minutes. This mold cavity might also be changed to accommodate 1/16 to 1/2 inch thick specimens. In addition, it could allow vacuum operations and compression operations on the fibers. A bulk polymerization was performed successfully in this mold; however, every time composites were attempted, no reaction or only partial reactions occurred in 30 - 40 minutes at 220° $\pm$ 5° C. It is not known why polymerization rates are inhibited.

C. Procedure

Outline of Procedure

The process leading to a composite involved two separate and parallel procedures. The first procedure was the preparation of the monomer anion solution. The other procedure was preparation of the fibers. These two procedures combined at the last step where a catalyzed monomer solution was combined with the fiber jig to cast the composite. The cast composite was then cut by means of saws, milling machine, and routers. The resulting coupon specimens were then tested.

Procedure Details

Monomer was sublimed-distilled at 90°C. at approximately .5 mm Hg for twenty hours. Sodium methoxide (1/100 mole ratio) was added to the monomer and sublimed-distilled again. This solution was transferred to clear dry test tubes and stored. This constituted the preparation of the monomer anion solution.

For fiber preparation, two to five grams of graphite fibers were wound on the selected jig. Approximately one to two ounces tension was maintained during winding. The fibers were then extracted with hot methy ethyl ketone in a soxhlet extractor approximately

twenty hours. The fibers were then removed from the extraction and dried. Drying was performed in two steps. The bulk of the solvent was removed by a stream of dry air. This required approximately twenty minutes. The second drying step was performed in a vacuum oven (90°C house vacuum), for twenty hours. This concluded fiber preparation.

The composite was cast by adding co-catalyst (usually caprolactone) to the catalyzed (1/100 mole ratio) monomer anion solution and pouring this over the jig and fibers in a test tube. The monomer/fiber system was degassed at 100°C and the solution was heated to polymerization temperature, which ranged in this work between 195°C and 220°C. After polymerization was complete, the composite was removed from the tube and machined for testing. Machining was performed by sawing specimens to approximate dimensions and then milling specimens to 4 1/2" x 1/2" x 1/16". Tensile specimens were further routed to a consistent shape with a template. These were then tested.

Testing constituted a tensile test to obtain modulus of elasticity, the ultimate tensile strength, and ultimate strain. Strain measurements were obtained by means of strain gauges. Specific gravity and calculated void volume was obtained on the same tensile specimens. The nature of the fracture and the fracture surface were observed with a scanning electron microscope.

Results and Discussion

The stress-strain test data for the samples and comparison with the component values are given in Table II.

TABLE II

Test Data for Composites

Sample	Young's Modulus (E) × 10^{-6} psi	U.T.S. × 10^{-3} psi	% Strain at Failure	SP.G	E(Calc) × 10^{-6} psi
Cast Nylon 6	.40 ± .05	12.5 ± 1	> 100	1.16 ± .01	
Thornel,T50S[a]	57	279	.49[b]	1.67	
Thornel,T75S[a]	77	327	.42[b]	1.86	
Nylon 6/T50S					
54A-1[c]	15.3	45.5	.35	1.31[e]	17[e]
54B-1	12.7	36.4	.29	1.25	10
54B-2	13.3	37.4	.32	1.28	13
67[d]	10.8	30.8			
Nylon 6/T75S					
56C-1[c]	29.6	51.2	.19	1.36	22
56C-2	27.7	71.6	.28	1.37	23
56B-1	18.5	53.4	.30	1.35	21
56B-2	17.7	38.2	.22	1.32	18
56A-1	24.8	43.4	.22	1.32	18

a. Manufacturer's data.
b. Calculated assuming Hookean behavior.
c. Co-catalyst in series was caprolactone.
d. Co-catalyst was t-butyl acetate.
e. Material for Sp.G. determination taken from point near failure. However, due to lack of homogeneity, modulus and Sp.G. do not correlate too well.

Several facts are apparent. First the samples vary widely in their elongation and strength at failure. This is true even for samples cut from the same piece, e.g. 56B-1 and 56B-2 through their moduli are the same. We feel that this is an artifact of the measurement. [The strain gauges were first glued to the sample and the leads then soldered to the gauge.] The best samples, though still probably low, are therefore more representative of the composite. In these, we have achieved about 70% translation of fiber modulus into composite modulus based on the rule of mixtures with 28% and 36% volume percent fibers for samples 54A-1 and 56C-2 respectively. Considering that these are the first reasonable fiber density composites made with Nylon 6, this is quite promising. Flexural and shear strength should be measured, and will be if more samples are made.

The sample made using t-butyl acetate, 67, was polymerized at 190°C, where no volatiles are liberated. It too showed good tensile

strength relative to its modulus; one can estimate about 70% retention of fiber properties.

Using our present technique, penetration of fibers by monomer becomes difficult above fiber densities of 35%, and voids remain. A vacuum press would be needed to make samples of higher density. The same effect could be achieved by impregnating a loose skein of fibers and then stretching or twisting with compression while polymerizing.

Of the three successful sets of polymerizations, 67 and 54 polymerized rapidly, within ten minutes, while 56 polymerized over a one hour period, and crystallized from solution. Thus one would expect the following: Runs 67 and 54 would show good ductility of the nylon during deformation while run 56 would tend to be brittle. On the other hand, run 67 contains t-butyl alcohol liberated from the co-catalyst. This could make the adhesion of nylon to fiber weaker than when caprolactone is the co-catalyst. Scanning electron microscope photographs of the fracture surfaces were taken to examine for the above possibilities. Where available, photos from high strength (relative to fiber density) and low strength composites were examined. The photo are shown below.

Figs. 1, 2, 3 show the fracture surface of a strong composite using caprolactone initiator and "Thornel" 50S. The major factor noticeable is the tremendous working of the surface and lack of any single strand pullout. Fig. 2 shows a region with multiple fracture, which always increases the energy absorption. Fig. 3, an enlargement of Fig. 2 shows the nylon adhesion to the fiber and the tremendous distortion of the nylon. In general, there is little evidence of separation at the nylon/fiber interface of the phases. To sum up, for the most characteristic nylon/fiber composites, the nylon adheres well to the graphite, distorts and pulls out as the crack front propagates and thus causes multiple crack propagation. All these processes lead to high energy absorption.

Figs. 4 and 5 show the same system for another jig of carbon fiber, where the composite had poor properties. Fig. 4 shows extensive pull-out of the fibers. Fig. 5 shows the separation between fiber and matrix, with the high ductility of the matrix. Obviously there is some adhesion, but much less than in sample 54A.

Figs. 6 and 7 are of a composite made with t-butyl acetate co-catalyst. One can again see pull-out, but much better adhesion than in Fig. 5. The cups around the fibers may be due to the ductility of the matrix. They may also be due to adsorption of t-butanol on the fiber surface, preventing adhesion. However, most fibers have a ductile area with much material adhering to them, (e.g., lower middle right of Fig. 6), thus indicating reasonable adhesion before drawing.

Figs. 8 and 9 compare a good and poor sample of composite using

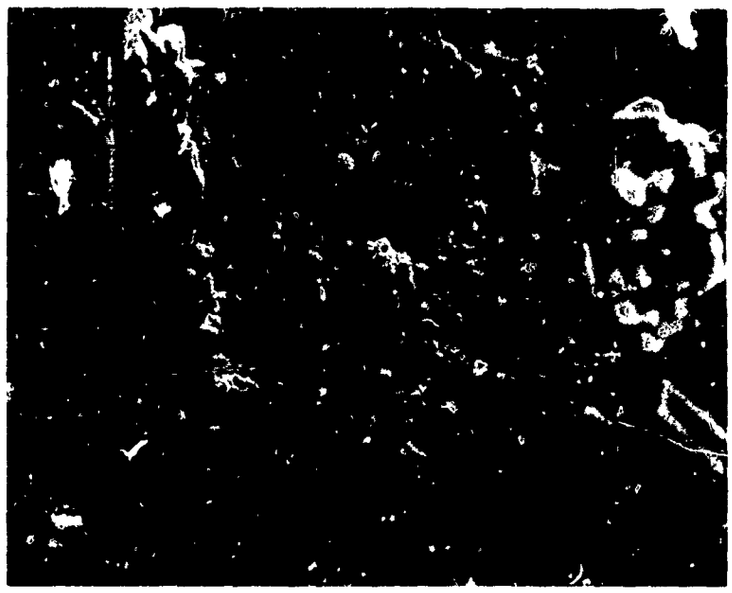

Fig. 1. Sample 54A-1 × 500 Fracture Surface.

Fig. 2. Sample 54A-1 × 1000 Fracture Surface, different location.

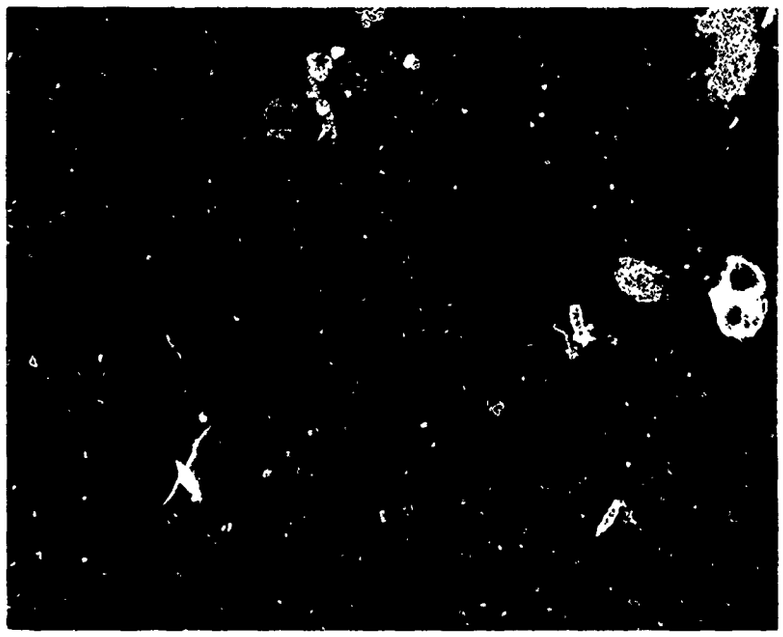

Fig. 3. Sample 54A-1 × 5000 Fracture Surface - Center of Fig. 2

Fig. 4. Sample 54B-1 × 1000 Fracture Surface.

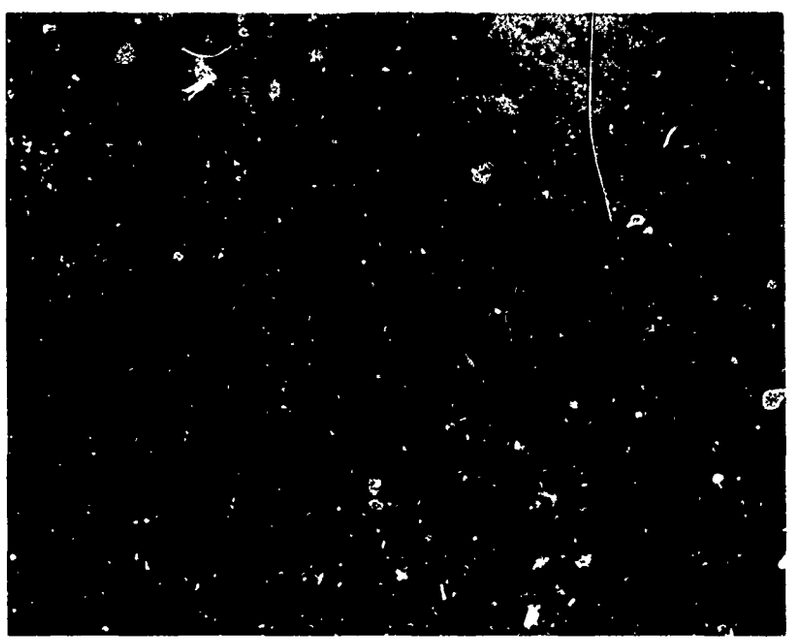

Fig. 5. Sample 54B-1 × 5000 Fracture Surface.

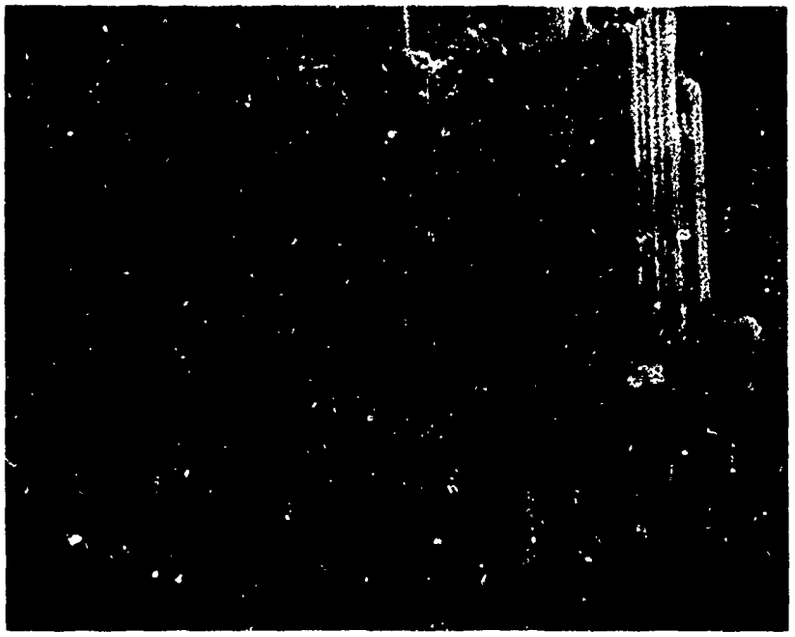

Fig. 6. Sample 67 × 1000, Fracture Surface.

Fig. 7. Sample 67 × 5000, Fracture Surface, Center of Fig. 6.

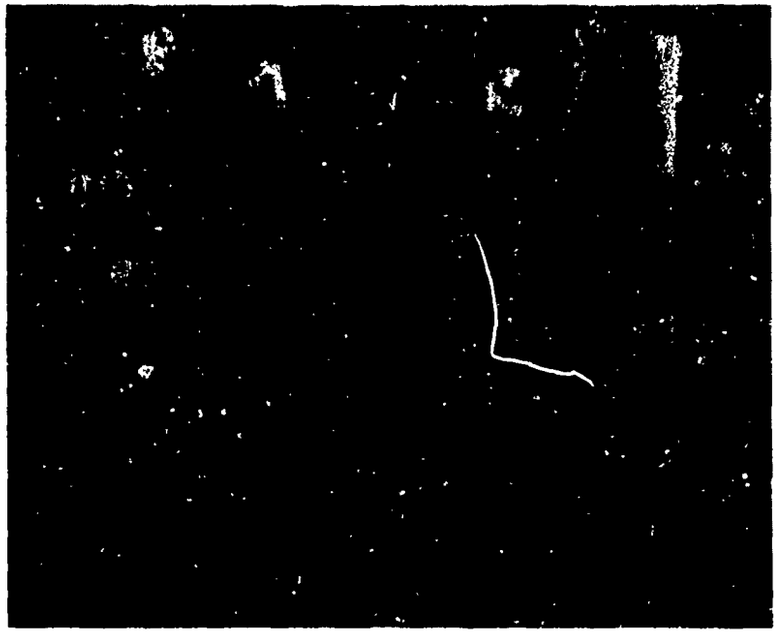

Fig. 8. Sample 56C-2 × 1000, Fracture Surface.

Fig. 9. Sample 56B-2 × 1000, Fracture Surface.

"Thornel" 75S.Here the polymers formed very slowly and precipitated on the fibers, rather than polymerizing rapidly to where monomer is insignificant. Even the good sample, 56C-2, shows no multiple fracture and no ductile behavior of the matrix. It does show reasonable adhesion as there are very few pull-outs. Fig. 9 corroborates the poor sample behavior by showing extensive pull-out, as well as no matrix ductility. Over-all, the sample behavior followed the predictions,except that t-butyl acetate samples were better than expected.

Within the limits of the experimental observations, we can sum up as follows. There are still many uncontrolled variables in this system - both in composite preparation and in experimental testing. Some samples however, in spite of the lack of control, show the promise of the system. In the best samples the nylon adhered well to the fiber, deforming during rupture and eventually leading to multiple fracture of the composite. The major problems seem to be solved in that respectable composite has been made.

We can extrapolate to the properties of a properly made composite from this. Such a material would have no voids, and little or no monomer remaining. Monomer would have been polymerized rapidly over highly degassed fibers using ε-caprolactone as co-catalyst. We would expect this composite to show complete transfer of fiber properties and perhaps, due to multiple fracture, absorb much energy during the fracture process. (Impact testing would be needed to find out about this.) Shear strength should be high due to the good adhesion, though no higher than for other matrices.

Better control of properties and better properties could be obtained using a polymer which is not in equilibrium with its monomer. Nylon 7 is such a one, as is poly(2,2-dimethyl β-alanine). Here adhesion will be better, as no low molecular weight species will be present. In addition, both polymers have higher melting points than Nylon 6, giving better properties at elevated temperatures.

SECTION IV

MECHANICS OF COMPOSITES

A total of four projects on the Mechanics of Composites were completed during the year. A study of the longitudinal shear deformation of composites with randomly distributed fibers lead to an exact analytical solution based upon work completed earlier in the program. The basic work used for this solution was continued and results were obtained for multiple circular inclusions under an arbitrary loading.

The live loading fixture for studying fiber composites with the scattered light polariscope was recently completed. A study of stress and strain distribution in fiber composite models will be conducted.

An experimental study of the fracture properties of unidirectional composite materials provided results to indicate the effects of specimen thickness, crack length ratio, void content and loading rate on the stress intensity factor.

A. A Longitudinal Shear Deformation of Composites (Prof. G. P. Sendeckyj)

Introduction

It is well known that the filaments in unidirectional fiber reinforced composites are randomly distributed and have randomly varying radii and elastic properties. This occurs not by intent but due to the difficulty encountered in controlling the spacing between fibers, their radii and elastic properties. In boron reinforced composites (in which the fibers have relatively large and uniform diameters) the spacing can be controlled at an increase in fabrication costs. Variations in elastic properties occur in the manufacturing of the fibers and there is no way of controlling them. A consistent manufacturing process would give fibers having a small variation in the moduli.

In the case of glass fiber reinforced composites, the variation in radii tends to be rather large (as can be seen from micrographs of typical composite cross sections). This is due to the small radii of the fibers and the resulting difficulties in controlling them. Furthermore, the elastic moduli can also be expected to vary within some range of values.

A model of the composite to be realistic must reflect its

morphology; this is, it must take into account the random spacing of the fibers, random variation of the radii and the range in elastic moduli. With the exception of some recent work by Adams and Tsai [1,2], no attempts have been made to treat the problem in its full complexity. The exact analyses that have been performed assume the fibers to have the same radii and moduli and to be distributed in regular [3-5] and diamond [5-8] arrays. (It should be noted that the square and hexagonal arrays are special cases of the rectangular and diamond ones). The results vary considerably, with the square array giving higher predicted moduli than the hexagonal one for the same fiber volume content.

A variational formulation (one that implicitly takes into account the random fiber spacing and random radii) has been adopted by Hill [9] and Hashin [10]. Unfortunately, the resulting bounds on the effective composite moduli are rather far apart for composite systems of interest. Furthermore, the variational approach gives no information about the stress distribution within the composite.

In the present work, an attempt is made to remedy the deficiencies of the analysis based on variational principles and on the assumption of regular spacing of fibers. The problem in its full generality is considered and solved for the case of longitudinal shear loading of the composite; that is, an exact analytical solution is given for the problem of antiplane shear loading of a unidirectional composite containing randomly distributed fibers of arbitrary radii and shear moduli. After some preliminaries, the solution is presented in Section 3. An expression for the effective shear modulus is developed in Section 4. For the case of a regular array this expression gives results that are virtually identical with the numerical solutions of [3,4,6-8]. In the case of a random distribution of fibers, results that are essentially in agreement with the conclusions of [1,2] are obtained. Finally, the results are used to discuss the viscoelastic behavior of a composite.

2. Preliminary Results

Consider a fiber reinforced composite containing aligned fibers. If the composite is loaded by shearing stresses parallel to the fiber axes, the resulting deformation is of antiplane type [11]. In this case one has

$$u = v = 0 \quad , \quad w = w(x,y), \tag{1}$$

where u,v,w are displacements along the coordinate axes (with w being the displacement parallel to the fiber axis). The nonzero displacement and stress components are given, in terms of an analytic function F(z) of the complex variable z = x + iy, by

$$\mu\, w(x,y) = \mathrm{Re}\,\{F(z)\}\ , \tag{2}$$

$$\sigma_{xz} - i\sigma_{yz} = \frac{dF}{dz}\ , \tag{3}$$

where Re { } is used to denote the real part of the function in the brackets and μ is the shear modulus. In terms of polar coordinates, (3) becomes

$$\sigma_{rz} - i\,\sigma_{\theta z} = e^{i\theta}\,\frac{dF}{dz}\ . \tag{4}$$

Now let us turn to determining the stress distribution within the composite.

3. General Solution

Consider an unbounded matrix containing N (N could be infinite) circular cylindrical inclusions. Let subscripts "o" and "i" (i=1,2,...,N) on elastic field quantities refer to the matrix and inclusions, respectively. Let R_i and a_i denote the radius and position of the center of the ith inclusion (as shown in Figure 1). Assuming the interface between the matrix and inclusions to be perfectly bonded, the boundary conditions for the ith inclusion are

$$\left.\begin{aligned} w_o &= w_i \\ \sigma_{rzo} &= \sigma_{rzi} \end{aligned}\right\} \quad \text{on } |z-a_i| = R_i\ , \tag{5}$$

where σ_{rz} is the "radial" shearing stress expressed in terms of a local polar coordinate system with origin at the center of the ith inclusion. Letting the stress state at infinity be $\sigma_{xz}^{\infty} = 1$, $\sigma_{yz}^{\infty} = 0$, it is required to determine the elastic fields near the inclusions.

By using the method of [12], it can be readily shown that the desired complex potentials are

$$F_o(z) = z - \sum_{m=1}^{\infty}\sum_{n=1}^{P_m} K_{m,n}\,\frac{C_{m,n}}{z-\zeta_{m,n}} \tag{6}$$

$$F_i(z) = (1 + K_i) \quad z - \sum_{m=1}^{\infty} \sum_{n=1}^{P_m *} K_{m,n} \frac{C_{m,n}}{z-\zeta_{m,n}} \tag{7}$$

where

$$P_m = N(N-1)^{m-1} \tag{8}$$

$$K_n = (\mu_n-\mu_0)/(\mu_n+\mu_0) \quad , \quad K_{1,n} = K_n \quad , \tag{9}$$

$$C_{1,n} = R_n^2 \quad , \quad \zeta_{1,n} = a_n \quad (n=1,2,\ldots,N) \tag{10}$$

and, in general,

$$K_{m,n} = K_{m-1,k} K_i \quad , \tag{11}$$

$$\zeta_{m,n} = a_i + R_i^2 / (\bar{\zeta}_{m-1,k} - \bar{a}_i) \quad , \tag{12}$$

$$C_{m,n} = \bar{C}_{m-1,k} \; R_i^2 \, [\bar{\zeta}_{m-1,k} - \bar{a}_i]^{-2} \quad , \tag{13}$$

if $|\zeta_{m-1,k} - a_i| \geq R_i$; otherwise the terms are not computed. The calculations indicated by (11) to (13) are to be carried out for all m; $k = 1,2,\ldots,P_{m-1}$; $n = 1,2,\ldots,P_m$; and $i = 1,2,\ldots,N$. The asterisk on the summation symbol in (7) denotes that terms that are singular within the inclusion under consideration are to be omitted from the sum.

If all the inclusions have identical shear moduli μ_f , then

$$\begin{aligned} K_n &= K = (\mu_f - \mu_0)/(\mu_f + \mu_0) \quad , \\ K_{m,n} &= K^m \quad , \end{aligned} \tag{14}$$

and the general solution, Eqs. (6) and (7), reduces to the results given in [12].

4. Effective Shear Modulus

Consider an unbounded elastic matrix containing aligned, randomly distributed fibers. Assume that the fibers have arbitrary radii that

lie within a fixed range of values. That this assumption is necessary can be seen from examining micrographs of typical composite cross sections. Also, let the fibers have randomly varying shear moduli. The necessity of this assumption follows from experimental data on mechanical properties of single fibers. It is required to determine the effective shear modulus of the composite.

The problem in its full generality is sufficiently difficult that no universally valid results (with the possible exception of bounds) can be expected. If certain restrictions on the variation of the variables (spacing, radii and shear moduli) are imposed then theoretically rigorous results can be derived. By a well known energy theorem in elasticity it follows that the effective shear modulus μ can be bounded from above by letting all the fibers have the shear modulus of the stiffest fiber. Similarly μ can be bounded from below by letting all the fibers have the shear modulus of the most flexible fiber. Hence one can write

$$\mu^- \leq \mu \leq \mu^+ \quad , \tag{15}$$

where μ^- and μ^+ are derived values of the effective modulus based on the least and greatest stiffness of the fibers. If the variation in fiber shear moduli is small, these bound will be rather close.

In what follows, the fibers will be assumed to have the same moduli. The effect of variation in modulus from fiber to fiber can be recovered by using bounds (15).

In a fundamental paper, Hill [13] developed exact expressions for the effective moduli of multiphase media. In the case under consideration the pertinent expression may be written as

$$\mu = \mu_0 + vB\,(\mu_f - \mu_0) \tag{16}$$

where μ_f, v and B are the assumed constant shear modulus of the fibers, volume fraction of fibers in the composite, and the average strain concentration in the fibers, respectively. The use of (16) requires knowledge of the average strain concentration factor in the fibers, which can be obtained from the general solution as follows: Consider a typical fiber (inclusion) with the origin of coordinates being put at its center. The stresses within the inclusion are

$$\sigma_{xz} - i\sigma_{yz} = (1+K)\left[1 + \sum_{m=1}^{\infty} K^m \sum_{n=1}^{P_{m*}} \frac{C_{m,n}}{[z-\zeta_{m,n}]^2}\right] , \tag{17}$$

where K is given by (14). It should be noted that the fibers have

been assumed to have identical shear moduli. Since all the singularities are outside the inclusion, the stresses can be expanded in a Taylor series about the center of the inclusion to give

$$\sigma_{xz} - i\sigma_{yz} = (1+K)\left[1 + \sum_{m=1}^{\infty} K^m \sum_{n=1}^{P_{m*}} \frac{C_{m,n}}{\zeta_{m,n}^2}\left(1 + \frac{2z}{\zeta_{m,n}} + \frac{3z^2}{\zeta_{m,n}^2} + \ldots\right)\right] . \quad (18)$$

Terms with z^k (k=1,2,3,...) yield stresses that depend on cosine and sine of $k\theta$. Hence, upon averaging over the inclusion, these give a zero contribution. Thus one has

$$\tau_{xz} - i\tau_{yz} = (1+K)\left[1 + \sum_{m=1}^{\infty} K^m \sum_{n=1}^{P_{m*}} \frac{C_{m,n}}{\zeta_{m,n}^2}\right] = (1+K)\,(A_x+iA_y) \quad (19)$$

for the averaged complex stress combination $\tau_{xz} - i\tau_{yz}$. The quantities A_x and A_y are real. To complete the evaluation of B in (16), the averaged complex stress combination has to be averaged over all the inclusions. This can be done rather easily in the case of a regular array of fibers; but in the general case, approximations have to be introduced at this point. If the fiber distribution is statistically homogeneous (a standard assumption in statistical and variational formulations of the problem), the average over all the fibers can be expected to be closely approximated by the averaged stress concentration within a typical fiber. This implies that $A_y = 0$ and, hence

$$\tau_{xz} = (1+K)\,A_x \quad . \quad (20)$$

The validity of using τ_{xz} as the averaged stress in all the inclusions can be checked by computing τ_{yz} and comparing its value with zero. Using τ_{xz}/μ_f as the average strain in the fibers it follows that (16) can be written as

$$\frac{\mu}{\mu_o} = 1 + 2v\,KA_x \quad . \quad (21)$$

This includes the correction due to the fact that (6) and (7) are for finite number of inclusions and we have an infinite number. Eq. (21) is the desired expression for the effective shear modulus of the composite. It should be realized that in using (21) an infinite series

has to be summed. This is rather difficult to do due to the slow convergence of the general solution [12]. The series can be transformed into a rapidly converging one for the case of a regular array of equal inclusions. This is done next.

Regular Arrays of Inclusions. Consider a composite reinforced by a regular array of equal fibers arranged as shown in Figure 2. The inclusion centers are put at the points

$$z = \omega_{m,n} = 2(m + nce^{i\alpha})\, a \qquad (m,n \text{ integers}) \tag{22}$$

where c, a, α are parameters giving the spacing of the fibers in the array (as shown in the figure)*. For the sake of convenience, the radius of the inclusion is taken equal to unity. Then the fiber volume fraction is related to the parameters a, c and α by

$$v = \frac{\pi}{4\, a^2 c \sin\alpha} \,. \tag{23}$$

The array becomes rectangular for $\pi/2$. If also c = 1, the array is square. $\alpha = \frac{\pi}{3}$, c = 1 corresponds to a hexagonal array. Other combinations of α and c give all the possible regular arrays.

For the regular array of fibers with period parallelogram specified by (22), it can be shown after some rather tedius computations that

$$\begin{aligned} A_x - iA_y = \frac{1}{1-KS_2} &+ \frac{3K^2S_4^2}{(1-KS_2)^2[(4a^2)^2-S_4^2\,K^2]} \\ &+ \frac{5K^2S_6^2}{(1-KS_2)^2[(4a^2)^4-S_6^2\,K^2]} \\ &+ \frac{7K^2S_8^2}{(1-KS_2)^2[(4a^2)^6-S_8^2\,K^2]} + \cdots \,, \end{aligned} \tag{24}$$

---

* The array is taken to be symmetrical about the x-axis.

where

$$S_{2K} = \sigma_{2k}/4a^2 \quad , \tag{25}$$

$$\sigma_{2k} = \sum_{\substack{n=-\infty \\ m=-\infty}}^{\infty}{}' \; [m + nce^{i\alpha}]^{-2k} \quad . \tag{26}$$

The prime on the summation symbol in (26) indicates that the summation is to be carried out for all integer values of m and n with the exception of n = m = 0. The series σ_{2k} occur in the theory of the Weierstrass elliptic functions [14]. They can be transformed into extremely rapidly converging series by classical methods (for example, see the derivations for a rectangular period parallelogram given in [15]). Thus

$$\sigma_2 = \frac{\pi^2}{3} + 2\pi^2 \sum_{n=1}^{\infty} \frac{1}{\sin^2\phi} \quad ,$$

$$\sigma_4 = \frac{\pi^4}{45} + 2\pi^4 \sum_{n=1}^{\infty} \left[\frac{1}{\sin^4\phi} - \frac{2}{3\sin^2\phi} \right] \quad ,$$

$$\sigma_6 = \frac{2\pi^6}{945} + 2\pi^6 \sum_{n=1}^{\infty} \left[\frac{2}{15\sin^4\phi} - \frac{1}{\sin^4\phi} + \frac{1}{\sin^6\phi} \right] \tag{27}$$

$$\sigma_8 = 2.008115 + 2\pi^8 \sum_{n=1}^{\infty} \left[\frac{1}{\sin^8\phi} - \frac{420}{315\sin^6\phi} + \right.$$

$$\left. + \frac{126}{315\sin^4\phi} - \frac{4}{315\sin^2\phi} \right] ,$$

where

$$\phi = n\pi c\,(\cos\alpha + i\sin\alpha) \; . \tag{28}$$

As an example, for a rectangular array, $\alpha = 90°$ and $\sin\phi = \sinh n\pi c$; hence, only the first few terms are needed to get six place accuracy. For other arrays, the convergence is almost as fast.

The ratio of effective shear modulus to matrix shear modulus was computed for a square array of fibers in the cases of glass-epoxy (μ_f/μ_o = 20) and boron-epoxy (μ_f/μ_o = 120) composites. The results are shown versus the fiber volume fraction in Figures 3 and 4. In both figures, the solid line is based on the derived expression (Eqs. (21) and (24)); while, the dotted line corresponds to using only the first term in (24). For the sake of comparison points from curves by Doner and Adams [3] and Chen [4] are shown as squares and triangles in the figures.

From the figures it is obvious that the presently derived expressions are in excellent agreement with the various numerical solutions for commonly encountered fiber volume fractions ($v < 0.7$). For higher fiber volume fractions the agreement becomes poor. This is attributed to the difficulties in convergence of the numerical results in this range. No comparison with experimental data is made since that aspect has been discussed sufficiently elsewhere. Similar comparisons can be made for hexagonal arrays; but the lack of space prevents us from presenting those results here.

It so happens that $S_2 = v$ and $S_4 \simeq v$ for the square arrays. This suggests replacing S_2 and S_4 by v and neglecting the remaining terms in (24) to give

$$\frac{\mu}{\mu_o} = 1 + 2Kv \left[\frac{1}{1-Kv} + \frac{3K^2v^2}{(1-Kv)^2[(4a^2)^2-K^2v^2]} \right] \tag{29}$$

for the ratio of effective shear modulus to the matrix shear modulus. It should be noted that if only the first term in the brackets in (29) is retained, the expression for the effective shear modulus reduces to the approximate ones given by Van Fo Fy [5], Kilchinskii [16], Hashin [17] and others. This expression is plotted as a dashed line in Figures 3 and 4. From the figures it is seen that the simplified expression (29) gives excellent agreement with the more exact one. Hence it can be adopted for slide rule computation of the effective shear modulus.

Finally, it should be noted that expressions (21) and (24) for the effective shear modulus are based on a rigorous analytical derivation and are valid for all regular arrays. Hence they can be used for assessing the effect of viscoleastic phases as is indicated below.

An exact expression for the effective shear modulus of a composite containing randomly spaced fibers with randomly varying radii

was derived above. Its use is restricted by the slow convergence of the infinite series that has to be summed. This can be seen from the following example.

Consider a composite containing a random distribution of equal fibers. To expedite the computations the composite was modelled by 37 inclusions in an unbounded matrix. If the inclusions are spaced in a regular hexagonal array, a value of interfiber spacing equal to six radii gives stresses on the center inclusion in excellent agreement with results for an infinite array [12]. Hence this model is expected to give accurate results. Starting with the hexagonal array, the inclusions were displaced along the coordinate axes by a random distance (< one radius in magnitude) while the inclusion at the origin was constrained to remain at the origin. This gave a random distribution of inclusions, an example of which is shown in Figure 5. For this random distribution of inclusions, the series for A_x was summed and the result substituted in (21) to give a value for the effective shear modulus. A computer program was written to perform the summation. Unfortunately, due to slow convergence of the series, it takes approximately ten minutes on the UNIVAC 1108 to obtain one value for the effective shear modulus for a fiber volume fraction of 0.1. Due to the long computation time and low volume fraction only one value of μ/μ_0 was computed and it is shown in Figures 3 and 4 by a solid circle. This value corresponds to the array shown in Figure 5. Since the computer run time increases rapidly with increasing v (due to the need of taking more terms in the series and more inclusions in the model), no other results were generated.

If the fibers are distributed in a doubly periodic array, the series for A_x can be summed to give expression (24). Results based on using (24) in (21), when compared with numerical solutions and approximate expressions lead to the following conclusions:

(1) The agreement with the results of Chen [4] is excellent. The results due to Doner and Adams [3] give poorer agreement. This is to be expected since the later results are suspect as was pointed out by Quackenbush and Thomas [18] and Symm [19]. Furthermore, the approximate expression, equation (29), is in excellent agreement with the exact expression.

(2) Eqs. (21) and (24) are valid for all regular arrays. This is in marked contrast to the numerical results which are restricted to rectangular and hexagonal arrays. Furthermore, these equations are readily adopted to predicting the viscoelastic shear modulus as has been indicated in Section 4.

(3) Upon comparing (21) and (24) with the expression based on the self-consistent model [16,17] it is seen that the self-consistent model gives an effective shear modulus that is a lower bound on the exact results for square and hexagonal arrays. Finally, it should be noted that the present results are obviously superior to the approximate expression (obtained by curve fitting the results of Doner and Adams) given by Hewitt and de Malherbe [20].

5. Stress Distribution

For a regular array of fibers, with period parallelogram specified by [22] the series in [17] can be summed* to give

$$\sigma_{xz} - i\sigma_{yz} = \beta^{-1} \sum_{n=0}^{\infty} F_{2n+1} \left[z^{2n} + Kz^{-2n-2} \right], \qquad (30)$$

The coefficients F_{2n+1} are given by

$$F_1 = D_1 + K \sum_{n=1}^{\infty} (2n+1)(4a^2)^{-n} S_{2(n+1)} D_{n+1}, \qquad (31)$$

$$F_{2n+1} = K \sum_{m=n}^{\infty} (2m+1)\binom{2m}{2m-2n}(4a^2)^{-m} S_{2(m+1)}[D_{m-n+1} + E_{m-n}], \qquad (32)$$

* For details of the summation see Section 8.

where $E_o = 0$ and $\binom{2m}{2r}$ are binomial coefficients. Furthermore,

$$E_n = \frac{K}{1-KS_2}\left[(4a^2)^{-n} S_{2(n+1)} + K \sum_{m=1}^{\infty} \binom{2m+2n+1}{2m}(4a^2)^{-2m-n} S_{2(m+1)}S_{2(m+n+1)}\right], \quad (33)$$

$$D_{n+1} = \sum_{b=2}^{\infty} \sum_{e=2}^{b} \sum_{m=0}^{\infty} \binom{b+1}{b}\binom{b}{e}\binom{2n+m-1}{m}(4a^2)^{-b-m-n} S_{2+b+m} S_{2+e} S_{2(1+n)+b-e+m}$$

$$+ \sum_{b=0}^{\infty} \sum_{e=0}^{b} \sum_{m=0}^{\infty} \sum_{\ell=1}^{\infty} \binom{b+1}{b}\binom{b}{e}\binom{2n+m-1}{m}\binom{m+2\ell-1}{2\ell}(4a^2)^{-b-m-n-2\ell} \times$$

$$\times S_{2(1+\ell)+b+m} S_{2(1+\ell)+e} S_{2(1+n)+b-e+m}, \quad (n > 0) \quad (34)$$

and

$$D_1 = \frac{1}{1-KS_2} + \frac{K^2}{(1-KS_2)^2}\left[\sum_{n=1}^{\infty} (2n+1)(4a^2)^{-2n} S^2_{2(n+1)}\right.$$

$$\left. + K \sum_{m=2}^{\infty} \sum_{n=0}^{\infty} (2m-1)\binom{2m+2n-1}{2n}(4a^2)^{-2n-2m+2} S_{2m} S_{2(m+n)}S_{2(n+1)}\right], \quad (35)$$

where

$$S_{2k} = (4a^2)^{-1} \sum_{\substack{m=-\infty \\ n=-\infty}}^{\infty}{}' [m + nce^{i\alpha}]^{-2k} \quad (36)$$

The prime on the summation symbol in (36) indicates that the summation is to be carried out for all integer values of m and n with the exception of $n = m = 0$. The series for S_{2k} can be transformed into rapidly converging series as has been done above but it is much more convenient to evaluate them by using the results given in Section 9. It should be noted that the series for E_n and D_n are only approximate expressions as can be seen from the derivations given in Section 8. More arrucate expressions for E_n and D_n can be obtained; but the required effort is too great to be justified since the expressions given above seem to give sufficient accuracy. Finally, the coefficient β is given by

$$\beta = [1 + \frac{K}{a^2 b}] F_1 + \frac{(3 - c^2)(a^6 b^3 + K)}{3a^4 b^3} F_3$$

$$+ \frac{(5 - 10c^2 + c^4)(a^{10} b^5 + K)}{5a^6 b^5} F_5$$

$$+ \frac{(7 - 35c^2 + 21c^4 - c^6)(a^{14} b^7 + K)}{7a^8 b^7} F_7$$

$$+ \frac{(9 - 84c^2 + 126c^4 - 36c^6 + c^8)(a^{18} b^9 + K)}{9a^{10} b^9} F_9 + \ldots, \tag{37}$$

where $b = 1 + c^2$, for a rectangular array and

$$\beta = F_1 + [(1 - b^2)a^2 + \frac{K(-2 + 12b^2 - b^4 - b^6)}{b^6(1+b^2)a^4}] \frac{F_3}{3}$$

$$+ [(1 - b^2 + b^4)ba^4 + \frac{K(1 - b^2)}{a^6 b^4}] \frac{F_5}{5}$$

$$+ [(1 - b^2 + b^4 - b^6)a^6 - \frac{K(1 + b^6)}{(b^2 + 1)a^8 b^6}] \frac{F_7}{7}$$

$$+ [(1 - b^2 + b^4 - b^6 + b^8)a^8 + \ldots] \frac{F_9}{9} + \ldots, \tag{38}$$

where $b = \tan \alpha$, for a diamond array.

6. Discussion of Stress Distribution

The results of the previous section were used to compute the maximum shearing stresses at the inclusion-matrix interface. The computations were carried out using only the leading terms (terms with S_{2n} , $n \geq 6$ being neglected) of the solution. The magnitude of the maximum shearing stress (σ_{rz}) at the interface was found and the results are shown in Figs. 6 and 7 for the cases of square and hexagonal array. For comparison purposes, the numerical results of Foy [8] and points from curves given by Van Fo Fy and V.V. Klyavlin [21] are shown as hollow and solid circles in the figures.

From Fig. 6, it is seen that the present results, with terms containing S_{2n} ($n \geq 6$) being neglected, are in excellent agreement with the results due to Foye [8] and Van Fo Fy and V. V. Klyavlin [21]. It should be noted that the points due to Foye seem to give a bit of scatter with some falling below and some above the presently derived curves. The points due to Van Fo Fy are in good agreement with the derived results. Furthermore, it should be realized that the material properties used by those authors are slightly different from the ones assumed in the present paper. This does not effect the comparison since the solution is rather insensitive to small variations in elastic moduli as can be seen by comparing the curves for glass-epoxy and boron-epoxy composites.

The maximum shearing stress exhibits the following trend: The stress undergoes a slight initial increase as the fiber volume content v increases from zero; then the stress decreases and finally increases again for large values of v. This trend is also evident in the rules of Foye, but does not appear in the curves given by Van Fo Fy and Klyavlin.

For the hexagonal array, the agreement between the present results and those of [8,21] is not as good (see Figure 4) with the curves being in better agreement with the results of [21]. The discrepancy can be traced to the approximations introduced by arbitrarily neglecting terms with S_{2n} ($n \geq 6$) since for a hexagonal array $S_2 = v$, $S_4 \approx S_8 \approx S_{10} \approx 0$, $S_6 \neq 0$. Thus, in effect, the curves are based on the leading two terms of the solution. Hence it is not surprising that poor agreement is obtained.

The solution given in Section 5, can be used to generate results for other regular arrays of inclusions. Unfortunately, for $\alpha \neq 90°$ or $60°$, S_4 and S_6 can have relatively large negative values leading to the necessity of taking a large number of terms. Thus the results, based on neglecting S_{2n} for $b \geq 6$, are not valid. Furthermore, the

accuracy of the expressions for E_n and D_n becomes questionable. From the structure of the solution, it is known that the leading terms were neglected in the expressions for E_n and D_n are of the order $(4a^2)^{-4}S_4^4$ $(4a^2)^{-8}S_6^4$, etc. Thus, if the volume fraction of inclusions is small, the neglected terms are small. As the volume fraction v increases $(4a^2)$ goes to 4 and these terms can no longer be neglected. Thus the results can be expected to be accurate for small values of v (< 0.3). Under this restriction, we have that the maximum stress in the matrix is less than two. On the basis of the above discussion, we can conclude (albeit imperfectly) that for small fiber volume content, the stress concentration effect of the inclusions is small (less than two).

7. Evaluation of Series

Summation of the double series in (19) to give (24) for the case of a regular array of equal fibers is rather involved. A brief outline of the procedure is given below.

When the fibers form a regular array whose period parallelogram is given by (22), the combination A_x and $i\,A_y$ can be written as

$$A_x + i\,A_y = 1 + K\,g_1 + K^2\,g_2 + k^3\,g_3 + \ldots \tag{39}$$

where

$$g_1 = \sum_{n,m=-\infty}^{\infty}{}' \,[2a\,(m + nce^{i\alpha})]^{-2} \,, \tag{40}$$

$$g_2 = \sum_{n,m,k,\ell=-\infty}^{\infty}{}' \,[4a^2(m + nce^{i\alpha})\,(k + \ell ce^{i\alpha}) + 1]^{-2} \tag{41}$$

$$g_3 = \frac{1}{4a^2} \sum_{k,\ell,m,n,s,t=-\infty}^{\infty}{}' \,[4a^2(k+\ell ce^{i\alpha})(m+nce^{i\alpha})(s+tce^{i\alpha}) + (k + \ell ce^{i\alpha}) + (s + cte^{i\alpha})]^{-2} \,, \tag{42}$$

etc. Upon recalling the definition of S_2, it follows that $g_1 = S_2$.

Summation of series in (41) and (42) is considerably more difficult but not impossible. They can be summed by the elementary trick of expanding the terms in the series g_n in a binomial series, rearranging them and resumming the series. This gives

$$g_2 = \sum_{n=0}^{\infty} (an+1)\,(4a^2)^{-2n}\, S^2_{2(n+1)} \quad , \tag{43}$$

$$g_3 = S_2^3 \sum_{n=1}^{\infty} (an+1)\,(4a^2)^{-2n}\, S_{2(n+1)} \sum_{m=0}^{n} \binom{2n}{2m} S_{2(m+1)}\, S_{2(n+1-m)}, \tag{44}$$

$$g_4 = S_2^4 + \sum_{k=1}^{\infty} (2k+1)\,(4a^2)^{-2k} \sum_{\ell=0}^{k} \binom{2k}{2\ell} \sum_{m=0}^{\ell} \binom{2\ell}{2m} \sum_{n=0}^{k-\ell} \binom{2k-2\ell}{2n} \times$$

$$\times\, (4a^2)^{-2n}\, S_{2(k+1-\ell)}\, S_{2(k+1-\ell+m)}\, S_{2(\ell+1+n)}\, S_{2(\ell+1+n-m)} \quad , \tag{45}$$

etc. where $\binom{n}{k}$ are binomial coefficients. The convergence rate of these series is very rapid since $S_{2n} < 1$ and $a > 1$. Substituting these series for g_n into (30) and again rearranging terms, allows one to sum the resulting series to give (24) which is the desired result.

8. Evaluation of Series for the Stresses

Summation of series (17) to give (30) for the case of a regular array of equal fibers is rather involved. A brief description of the procedure is given below.

When the fibers form a regular array whose period parallelogram is given by (22), the stresses can be written as

$$\sigma_{xz} - i\sigma_{yz} = 1 + \sum_{n=1}^{\infty} K^n A_n \tag{46}$$

where

$$A_1 = p(z) + S_2 \quad , \tag{47}$$

$$A_2 = \sum_{m,n}' \omega_{m,n}^{-2}\, p(z - \omega_{m,n}^{-1}) + S_2^2 \quad , \tag{48}$$

$$A_3 = \sum_{k,\ell}' \sum_{m,n}' [\omega_{m,n}\, \omega_{k,\ell} + 1]^{-2} \left[p\left(z - \frac{\omega_{k\ell}}{\omega_{m,n}\, \omega_{k,\ell} + 1}\right) + S_2^3 \right] , \tag{49}$$

$$A_4 = \sum_{k,\ell}' \sum_{m,n}' \sum_{s,t}' [\omega_{k,\ell}\, (\omega_{m,n}\, \omega_{s,t} + 1) + \omega_{s,t}]^{-2} \times$$

$$\times \left[S_2 + p\left(z - \frac{\omega_{m,n}\, \omega_{k,\ell} + 1}{\omega_{k,\ell}(\omega_{m,n}\, \omega_{s,t} + 1) + \omega_{s,t}}\right) \right] , \tag{50}$$

etc., where the prime on the summation symbol indicates that the summation is to be carried out for all integer values, positive and negative, of m and n (or k & ℓ or s & t), with the exception of $n = m = 0$. Furthermore, $p(z)$ is the Weierstrass elliptic function and S_{2n} are series defined by (30). Some useful relations between the Weierstrass elliptic function and the series S_{2n} are given in Section 9.

Series (46) follows immediately from (17) if one takes into account the double-perodicity of the assumed distribution of fibers. Further summation is achieved by (i) expanding the Weierstrass p function in a Laurant series (see Section 8), (ii) expanding terms in the resulting series, whenever necessary, in binomial series, (iii) rearranging terms and resumming. This gives

Series (46) follows immediately from (17) if one take into account the double-perodicity of the assumed distribution of fibers. Further summation is achieved by (i) expanding the Weierstrass p function in a Laurant series (see Appendix II), (ii) expanding terms in the resulting series, whenever necessary, in binomial series, (iii) rearranging terms and resumming. This gives

$$A_1 = S_2 + z^{-2} + \sum_{n=1}^{\infty} (2n+1)(4a^2)^{-n} S_{2(n+1)} z^{2n} , \tag{51}$$

$$A_2 = S_2^2 + S_2 z^{-2} + \sum_{n=1}^{\infty} (2n+1)(4a^2)^{-n} S_{2(n+1)} z^{-2(n+1)}$$
$$+ \sum_{n=2}^{\infty} c_n \sum_{m=1}^{n-1} \binom{2n-2}{2m} (4a^2)^{-m} S_{2(m+1)} z^{2(n-m-1)} , \tag{52}$$

$$A_3 = S_2 \sum_{n=1}^{\infty} (2n+1)(4a^2)^{-2n} S_{2n+2}^2$$
$$+ \sum_{m=1}^{\infty} z^{-2m} \sum_{n=0}^{\infty} \binom{2n+2m-1}{2n} (4a^2)^{-2n-m+1} S_{2(n+1)} S_{2(n+m)}$$
$$+ \sum_{k=2}^{\infty} c_k \sum_{m=0}^{k-2} \binom{2k-2}{2m} z^{2k-2m-2} \sum_{n=0}^{\infty} \binom{2m+2n+1}{2n} \times$$
$$\times (4a^2)^{-2n+m} S_{2(m+n+1)} S_{2(n+1)} , \tag{53}$$

$$A_4 = S_2^4 + S_2 \sum_{n=1}^{\infty} \frac{2n+1}{(4a^2)^{2n}} S_{2(n+1)} \sum_{m=0}^{n} \binom{2n}{2m} S_{2(m+1)} S_{2(n+1-m)}$$
$$+ \left[z^{-2} \sum_{n=0}^{\infty} (2n+1) z^{-2n} + \sum_{r=2}^{\infty} c_r \sum_{n=0}^{r-1} \binom{2r-2}{2n} z^{2(r-1-n)} \right] \times$$
$$\times \sum_{b=0}^{\infty} \sum_{e=0}^{b} \sum_{m=0}^{\infty} \sum_{\ell=0}^{\infty} \binom{b+1}{b} \binom{b}{e} \binom{2n+m-1}{m} \binom{m+\ell-1}{\ell} \times$$
$$\times (4a^2)^{-(b+m+\ell+n)} S_{2+b+m+\ell} S_{2+e+\ell} S_{2+2n+b+m-e} , \tag{54}$$

etc., where c_n is defined by (59) in Section 9. Eq. (46), with A_n given by (51) to (54), can be considered as a series in z with coefficient which in turn are complicated infinite series. The coefficient of z^{2n} (for fixed n) can be looked upon as a series in S_2. Upon summing the series in S_2 whenever possible, it follows that the coefficient of z^{2n} is given by F_{2n+1} (which is defined by (31) and (32)). Similar consideration for terms with z^{-2n-2} give the result that F_{2n+1} is also the coefficient z^{-2n-2}. Thus (46), when summed, becomes (30) with $\beta = 1$. This result is <u>not</u> the correct solution for a composite.

A little reflection on the formulation of the problem is enough to convince one that this is to be expected. The problem was initially formulated for the case of a finite number of inclusions in an unbounded matrix. That is the problem solved by (17). In going over to the case of a doubly-periodic array of inclusions, the finite number of inclusions was assumed to form a regular array and the number of inclusions in the array was increased to infinity. As such, (30) with $\beta = 1$ is the solution of the problem of an infinite array of fibers occupying a region that is infinite in extent and yet finite in comparison to the unbounded extent of the matrix. Hence, (30) with $\beta = 1$ is not the desired solution for a composite material.

The results have to be corrected. The infinite array of fibers has the effect of a single inclusion in an infinite matrix and, hence, the effective loading on the composite (array of inclusions and the matrix in their vicinity) is higher than the imposed stress at infinity (due to the stress concentrating nature of inclusions). This indicates the necessary correction; that is, the effective stress in the composite region has to be used as the loading function in the results for a doubly periodic array of fibers. Since this is impossible to do from the above considerations, the correction has to be arrived at in a different manner.

It can be made by considering a representative region of the composite, computing the net stresses transmitted across its boundaries and using the net stresses as the loading condition on the composite. Thus consider the representative regions of the composite shown in Figure 8. Two distinct cases have to be considered, namely, the rectangular array (Fig. 8a) and the diamond array (Fig. 8b). The stresses on the surface of the representative region are given by (30) with $\beta = 1$, upon taking the appropriate values of z. Integrating over the boundary of the representative volume, one gets that the net traction in the x-direction is β and that the y-direction is zero. The expressions for β in the two cases are given by (37) and (38). Dividing (30), with $\beta = 1$,

by β gives the desired correct solution.

Since the series, (34) and (35), defining the coefficient D_{n+1} are rather complicated, the leading terms are recorded below:

$$D_1 = \frac{1}{1 - KS_2} + \frac{K^2}{(1 - KS_2)^2} \; [\; 3(4a^2)^{-2}\, S_4^2 + 5(4a^2)^{-4}\, S_6^2$$

$$+ 7(4a^2)^{-6}\, S_8^2 + \ldots + 30(4a^2)^{-4}\, KS_4^2 S_6 + 210(4a^2)^{-6}\, KS_4 S_6 S_8 + \ldots],$$

$$D_2 = K^3 \; [\; 3(4a^2)^{-3}\, S_4^2 + 81(4a^2)^{-5}\, S_4 S_6^2$$

$$+ (4a^2)^{-7}\, [518\, S_4 S_8^2 + 250\, S_6^8 S_8\;] + \ldots\;] \;,$$

$$D_3 = K^3 \; [\; 3(4a^2)^{-4} S_4^2 S_6 + (4a^2)^{-6}\, [5\, S_6^3 + 146\, S_4 S_6 S_8\;]$$

$$+ (4a^2)^{-8}\, [1686\, S_4 S_8 S_{10} + 478\, S_6 S_8^2\;] + \ldots\;] \;,$$

$$D_4 = K^3 \; [\; 3(ea^2)^{-5}\, S_4^2 S_8 + (4a^2)^{-7}\, [5\, S_6^2 S_8 + 240\, S_4 S_6 S_{10}\;]$$

$$+ (4a^2)^{-9}\, [775\, S_6 S_8 S_{10} + 7\, S_8^3\;] + \ldots\;] \;,$$

$$D_5 = K^3 \; [\; 3(4a^2)^{-6}\, S_4^2 S_{10} + 5(4a^2)^{-8}\, S_6^2 S_{10} + 7(4a^2)^{-10}\, S_8^2 S_{10}$$

$$+ \; 9(4a^2)^{-12}\, S_{10}^3 + \ldots\;] \;.$$

9. Some Useful Relations

The Weierstrass p function is defined [22] as

$$p(z) = z^{-2} \sum_{m,n}{}' \; [z - \omega_{m,n}]^{-2} - \sum_{m,n}{}' \; \omega_{m,n}^{-2} \tag{55}$$

where $\omega_{m,n}$ is the period parallelogram, which in our case is given by (55). The prime on the summation symbol is used to denote summation over all integer (positive and negative values of m and n with exception of m = n = 0. Upon using definition (36), Eq. (55) can be written as

$$p(z) = z^{-2} + \sum_{m,n}' [z - \omega_{m,n}]^{-2} - S_2 . \tag{56}$$

The Weierstrass p function can be expanded in a Laurant series as

$$p(z) = z^{-2} + \sum_{n=2}^{\infty} c_n z^{2n-2} \tag{57}$$

where

$$c_2 = 3(4a^2)^{-1} S_4 , \qquad c_4 = 5(4a^2)^{-2} S_6 \tag{58}$$

and

$$c_n = \frac{3}{(2n+1)(n-3)} \sum_{m=2}^{n-2} c_m c_{n-m} , \quad (n \geq 4) . \tag{59}$$

In this form all the coefficients in (57) can be written in terms of S_4 and S_6 .

Alternately, we have

$$p(z) = z^{-2} + \sum_{m,n}' \omega_{m,n}^{-2} [1 - \frac{z}{\omega_{m,n}}]^{-2} - S_2$$

$$= z^{-2} + \sum_{n=1}^{\infty} (2n+1)(4a^2)^{-n} S_{2(n+1)} s^{2n} . \tag{60}$$

Comparison of (57) and (60) gives

$$c_{n+1} = (2n+1)(4a^2)^{-n} S_{2(n+1)} . \tag{61}$$

which relates $S_{2(n+1)}$ to S_4 and S_6 . Thus the series S_{2n} can be evaluated rather simply once the values of S_4 and S_6 have been computed.

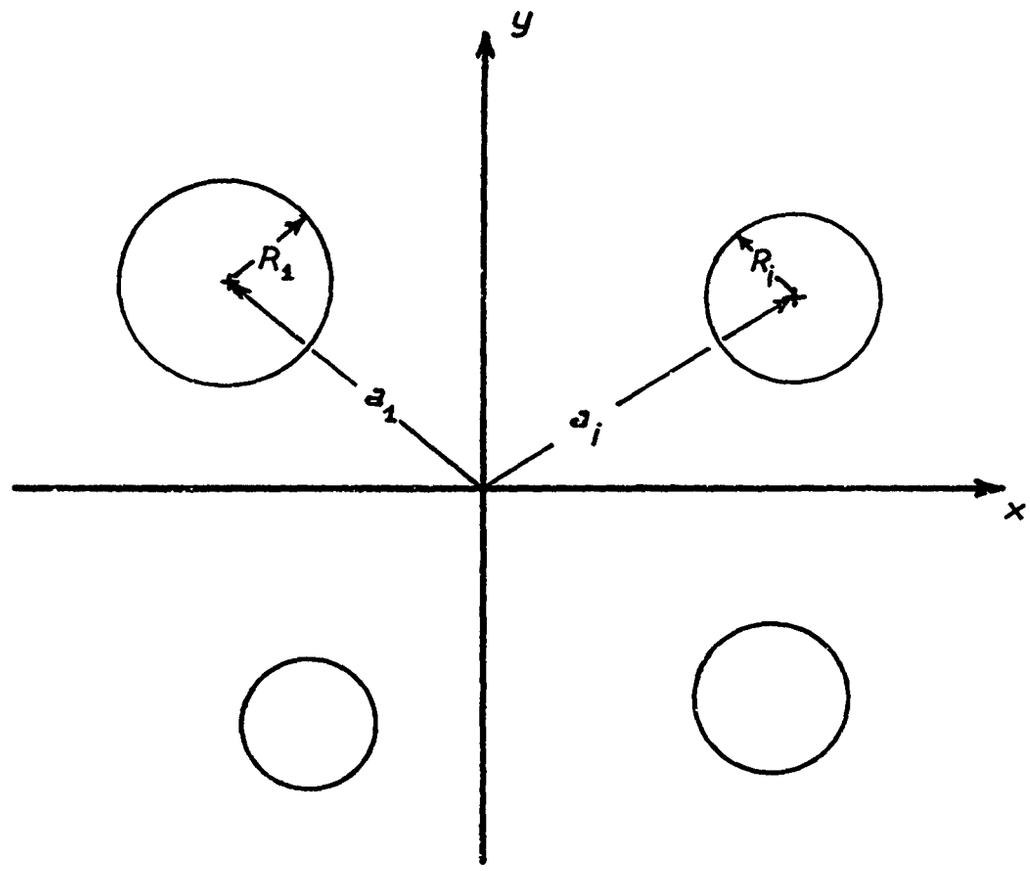

Figure 1. Arbitrary Number of Inclusions with Radii R_i plated at the points a_i

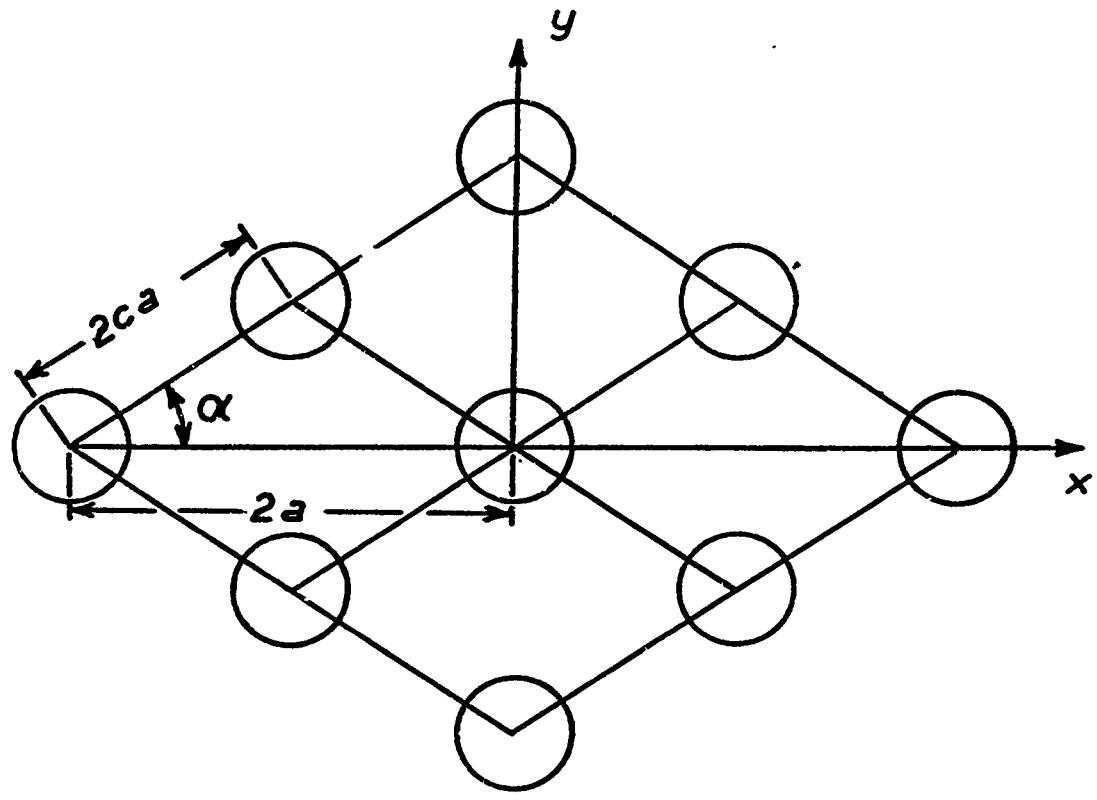

Figure 2. Period Parallelogram for Regular Array of Inclusions

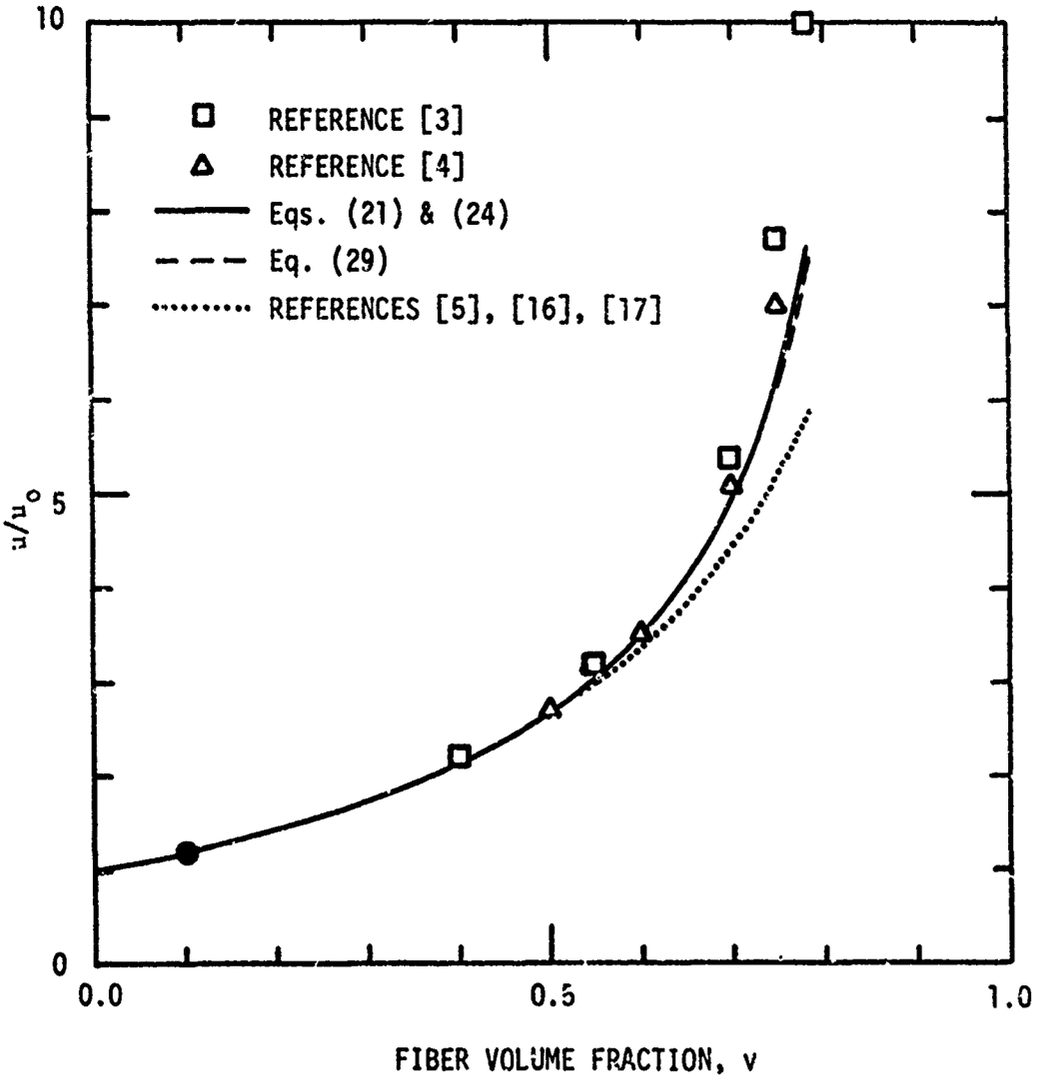

Figure 3. Ratio of effective shear modulus to matrix shear modulus versus fiber volume content for glass-epoxy composite (μ_f/μ_o = 20 or K = 905) based on square array model.

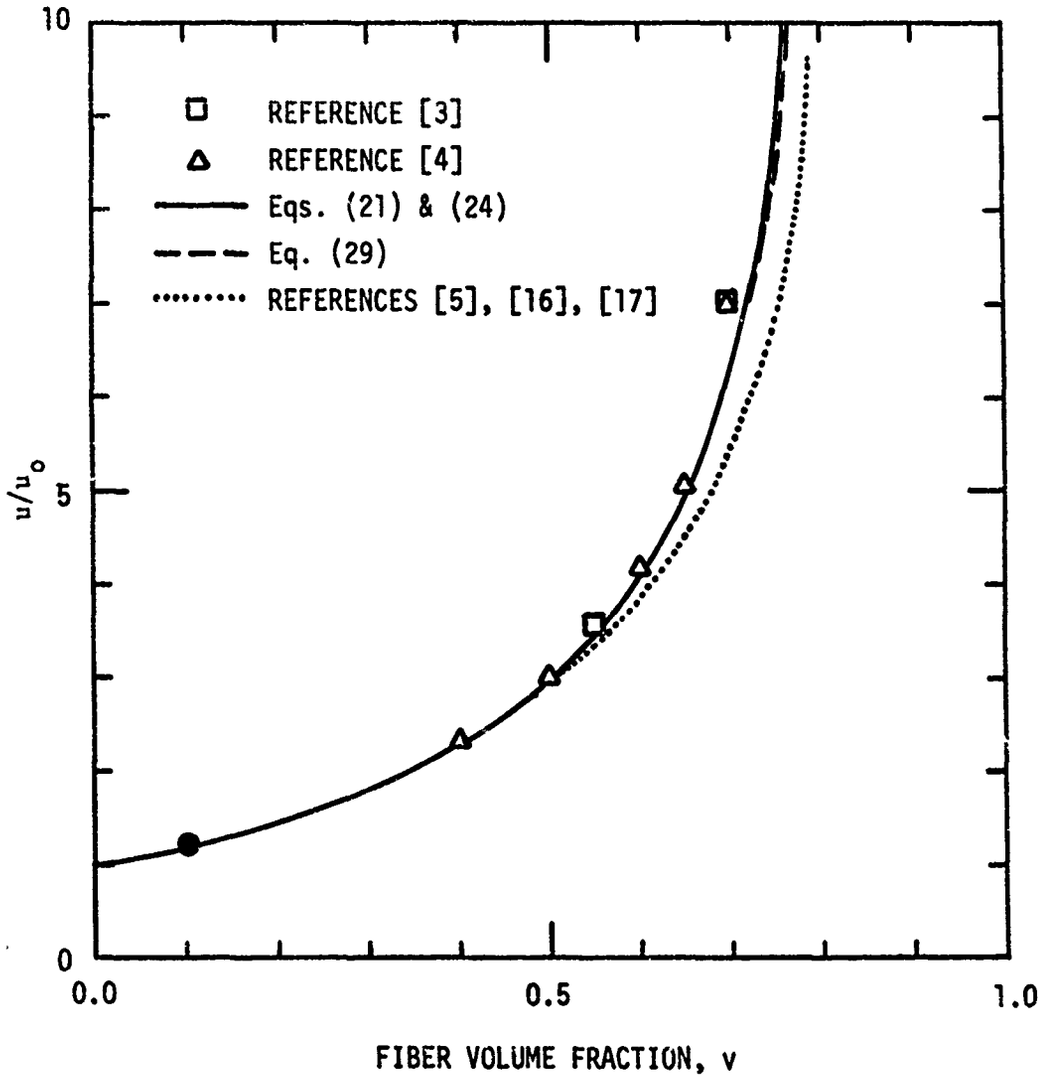

Figure 4. Ratio of effective shear modulus to matrix shear modulus versus fiber volume content for boron-epoxy (μ_f/μ_o = 120 or K - .9835) based on square array model.

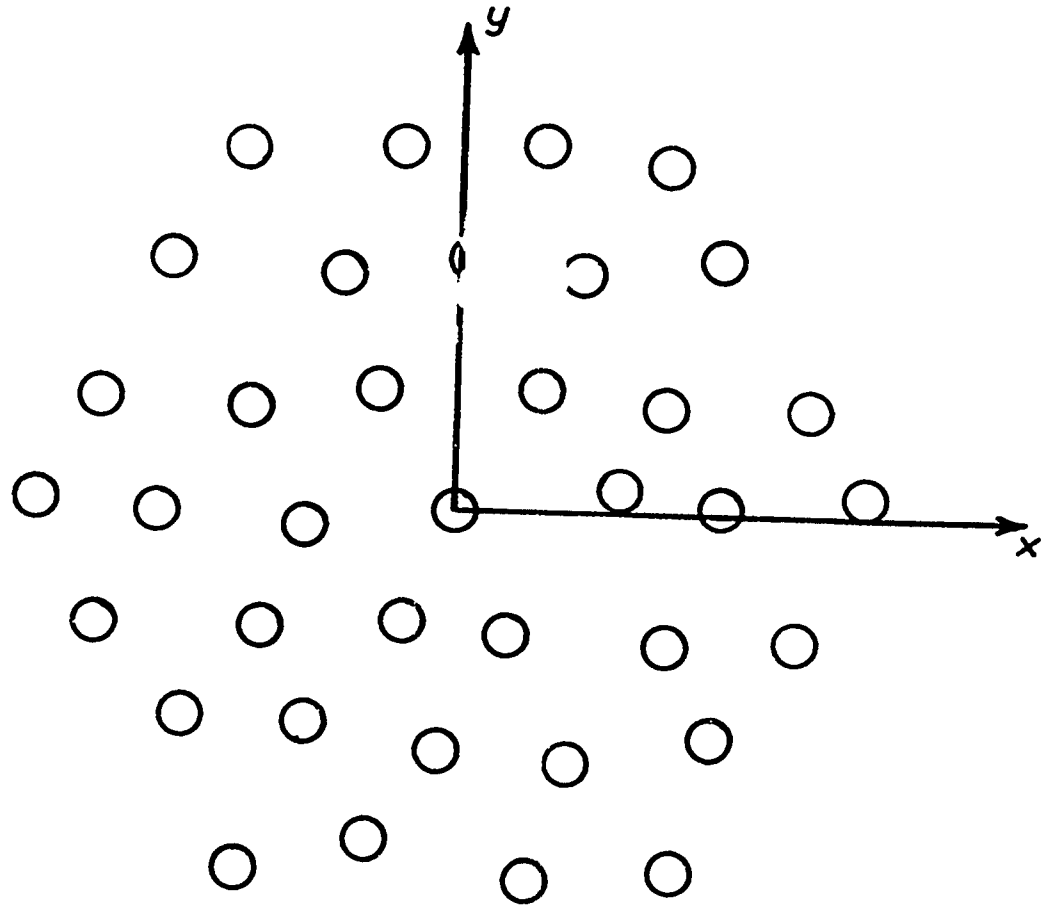

Figure 5. Typical Distribution of Inclusions used for the Random Model of a Composite

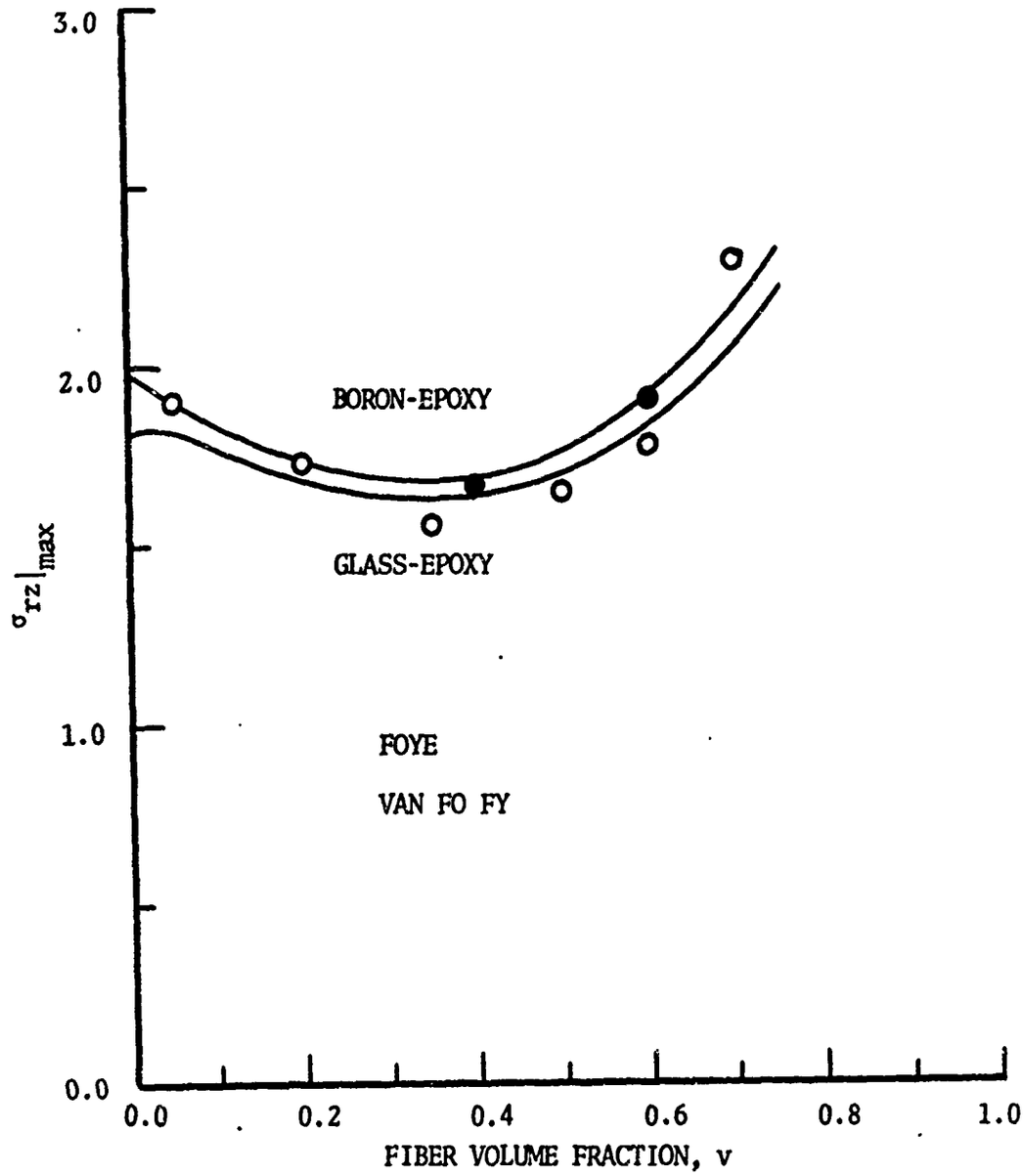

Figure 6. Maximum shearing stress τ_{rz} versus fiber volume content for glass-epoxy (μ_f/μ_0 = 20) and boron-epoxy (μ_f/μ_m = 120) composite based on square array model.

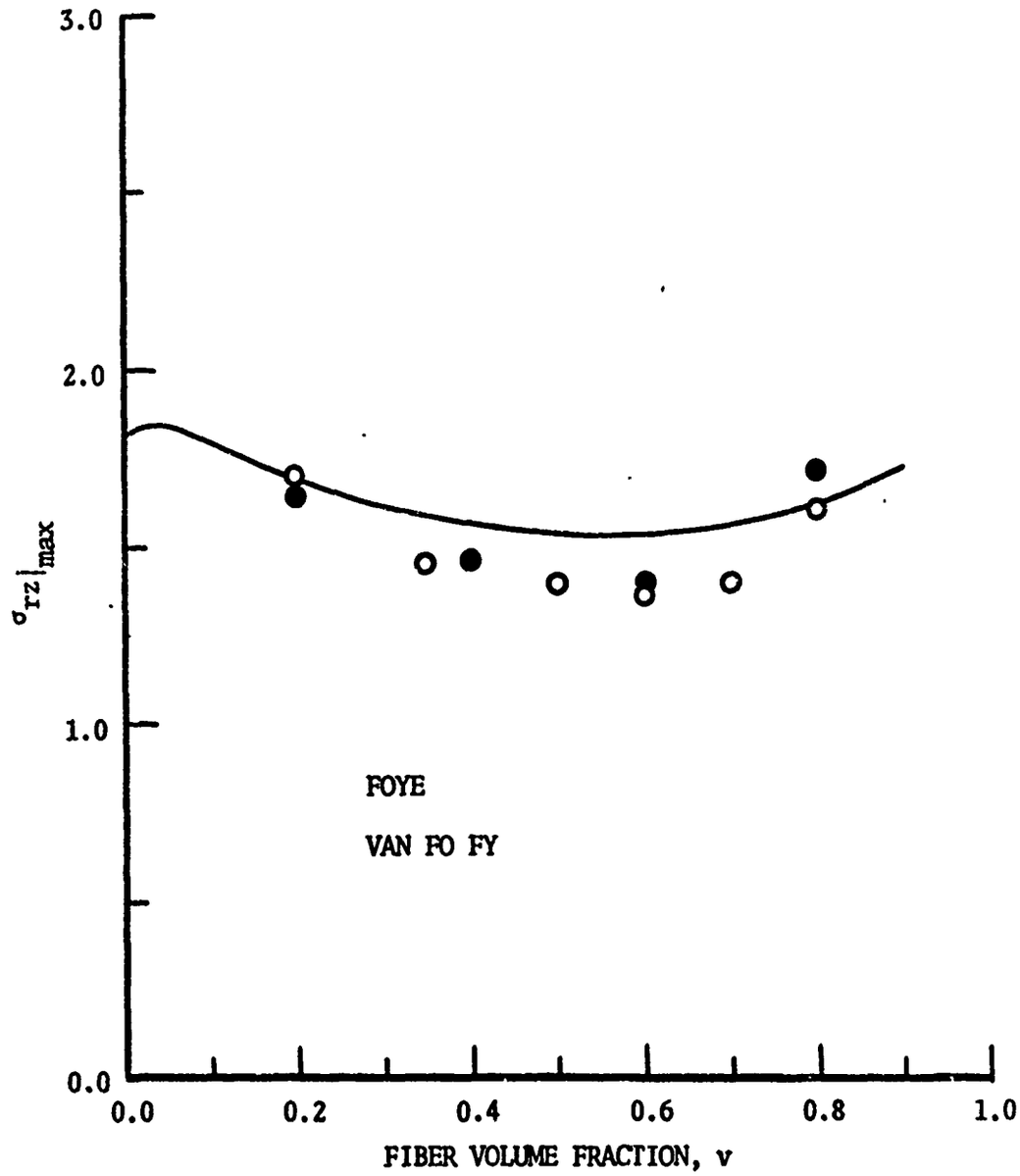

Figure 7. Maximum shearing stress τ_{rz} versus fiber volume content for glass-epoxy composite (μ_f/μ_o = 20) based on hexagonal array model.

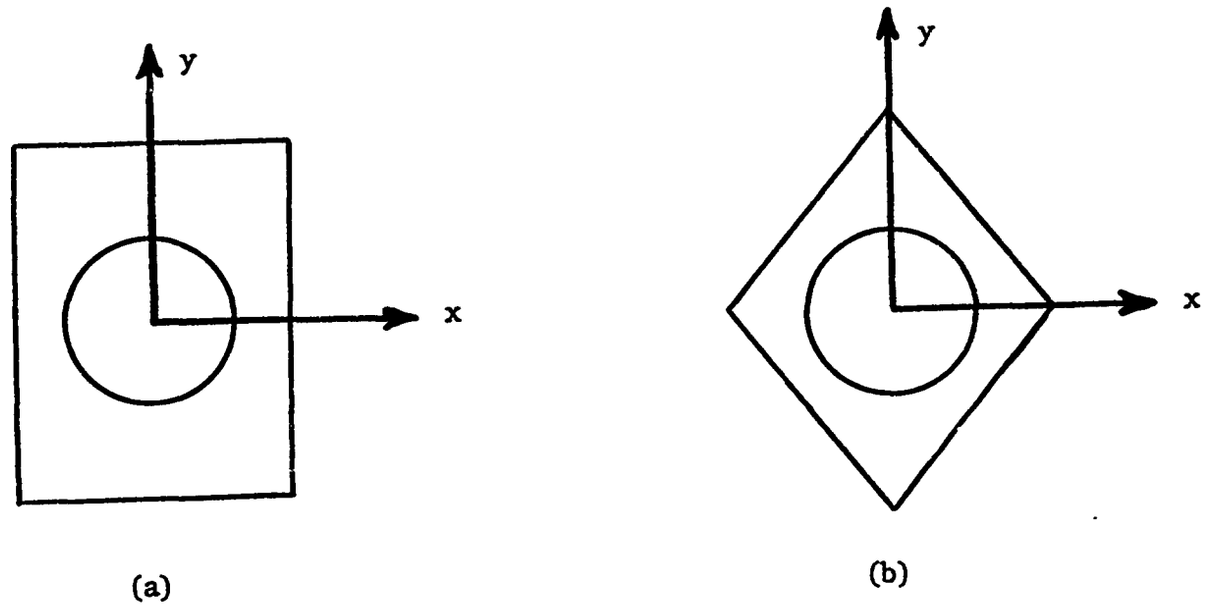

Figure 8. Representative region for computation of the constant B.

B. Multiple Circular Inclusions Problems in Plane Elastostatics (Professor G. P. Sendeckyj and Dr. Ing-Wu Yu)

During the period covered by this report, work on the multiple circular inclusion problem has been continued. The general representation, given by Sendeckyj [1], has been modified to give a more straightforward solution of the elastic boundary value problem for an unbounded matrix containing a single circular inclusion. Using these results, the problem of an unbounded matrix containing an arbitrary number of elastic inclusions (which can have any radii and elastic properties) has been solved for uniform and in-plane bending stress fields. Since these results are given in considerable detail in [2,3] only a brief summary is given here (see Sections 2 and 3).

As the first application of the general results to composites, transverse loading of a single ply for the case of fibers having the same shear modulus as the matrix has been considered. A paper containing these results has been prepared and submitted for publication [4]. The main features of this paper are summarized in Sections 4 through 6. Directions for future work are indicated in the last section.

1. Basic Formulas. Consider an isotropic solid in a state of plane deformation parallel to the x,y plane. As is well known [5], the displacements and stresses in the plane of deformation can be written in terms of two analytic functions, $\phi(z)$ and $\psi(z)$, of the complex variable $z = x + iy$ as

$$2\mu(u + iv) = \kappa\,\phi(z) - z\,\overline{\phi'(z)} - \overline{\psi(z)}$$

$$\sigma_{xx} - i\,\sigma_{xy} = \phi'(z) + \overline{\phi'(z)} - \bar{z}\,\phi''(z) - \psi'(z)\,, \qquad (1)$$

$$\sigma_{xx} + \sigma_{yy} = 2\,[\phi'(z) + \overline{\phi'(z)}\,]\,,$$

where a prime on a function denotes differentiation with respect to its argument and

$$\kappa = \begin{cases} 3-4\nu & \text{for plane strain,} \\ (3-\nu)/(1+\nu) & \text{for (generalized) plane stress.} \end{cases} \qquad (2)$$

2. General Solutions of Single Circular Inclusion Problems

Now let us consider an infinite elastic matrix containing a circular inclusion of radius R_i placed as shown in Figure 1. Letting subscripts "o" and "i" on elastic field quantities refer to the matrix and inclusion respectively, the boundary conditions corresponding to a perfect bond at the interface are

$$\left.\begin{aligned} u_o + i\, v_o &= u_i + i\, v_i \\ \sigma_{\rho\rho o} - i\, \sigma_{\rho\theta o} &= \sigma_{\rho\rho i} - i\, \sigma_{\rho\theta i} \end{aligned}\right\} \quad \text{at } \rho = R_i \qquad (3)$$

It is required to find a representation of the solution satisfying boundary conditions (3). A number of such representations are possible depending on the conditions that are imposed at infinity. If no conditions are imposed at infinity, we have

Representation I [1]: The general form of the solution satisfying (3) can be written as

$$\phi_o(z) = f(z) - \frac{\beta_i - \alpha_i}{1 - \beta_i}\, z\, \bar{f}'(R_i^2/z) - \frac{\beta_i - \alpha_i}{1 + \beta_i}\, \bar{h}(R_i^2/z) \quad , \qquad (4a)$$

$$\psi_o(z) = \frac{2\beta_i}{1 - \beta_i}\, \frac{R_i^2}{z}\, f'(z) + \frac{\beta_i - \alpha_i}{1 - \beta_i}\, \left[\frac{R_i^2}{z}\, \bar{f}'(R_i^2/z) - \frac{R_i^4}{z^2}\, \bar{f}''(R_i^2/a) \right]$$

$$+ \frac{\alpha_i + \beta_i}{1 - \beta_i}\, \bar{f}(R_i^2/z) + h(z) - \frac{\beta_i - \alpha_i}{1 + \beta_i}\, \frac{R_i^4}{z^3}\, \bar{h}'(R_i^2/z) \quad , \qquad (4b)$$

$$\phi_i(z) = \frac{1 + \alpha_i}{1 - \beta_i}\, g(z) \quad , \qquad (4c)$$

$$\psi_i(z) = \frac{1 + \alpha_i}{1 + \beta_i}\, h(z) \quad , \qquad (4d)$$

where

$$\alpha_i = [\Gamma_i(\kappa_o + 1) - (\kappa_i + 1)]/[\Gamma_i(\kappa_o + 1) + \kappa_i + 1] \quad ,$$

$$E_i = [\Gamma_i(\kappa_0 - 1) - (\kappa_i - 1)]/[\Gamma_i(\kappa_0 + 1) + \kappa_i + 1] \quad ,$$

$$\Gamma_i = \mu_i/\mu_0 \tag{5}$$

are the contractions suggested by Dundurs [6], $\bar{f}'(R_i^2/z) = \overline{f'(R_i^2/\bar{z})}$ $f(z)$, $h(z)$ are arbitrary functions of z.

Since no restrictions have been placed on the singularities of $f(z)$ and $h(z)$, this representation admits singularities in the matrix and/or the inclusion. Furthermore, one has no control over the elastic fields at infinity. For example, if for $f(z)$ and $h(z)$ one takes the singularity for a concentrated force applied at some point in the matrix, then (4) gives a constant stress at infinity. The correct solution follows upon eliminating the constant stress by again using (4).

Even though Representation I can be used to solve all conceivable problems for a single inclusion, it is convenient for our purposes to introduce a somewhat more restricted representation which is given below:

<u>Representation II</u>: If the singularities of $f(z)$ and $h(z)$ occur only in the matrix ($|z|>R_i$) and if the stresses at infinity are to be those corresponding to $f(z)$ and $h(z)$ in a homogeneous matrix, then the solution satisfying boundary conditions (3) is given by

$$\phi_0(z) = f(z) - D_i[z\bar{f}'(R_i^2/z) + \bar{h}(R_i^2/z) - \bar{f}'(0)z] \quad , \tag{6a}$$

$$\begin{aligned}\psi_0(z) = {} & h(z) - E_i\,\bar{f}(R_i^2/z) - D_i[-(R_i^2/z)\,\bar{f}'(R_i^2/z) \\ & + (R_i^4/z^2)\,\bar{f}''(R_i^2/z) + (R_i^4/z^3)\,\bar{h}'(R_i^2/z)] \\ & + \{G_i[f'(0) + \bar{f}'(0)] + J_i[f'(0) - \bar{f}'(0)]\}(R_i^2/z) \quad ,\end{aligned} \tag{6b}$$

$$\phi_i(z) = (1-E_i)\{f(z) + [K_i(f'(0) + \bar{f}'(0)) + L_i(f'(0) - \bar{f}'(0))]z\}, \tag{6c}$$

$$\psi_i(z) = (1 - D_i)\{h(z) - M_i[f'(z) - f'(0)](R_i^2/z)\} \quad , \tag{6d}$$

where

$$
\begin{aligned}
D_i &= (\beta_i - \alpha_i)/(1 + \beta_i) \ , \\
E_i &= -(\beta_i + \alpha_i)/(1 - \beta_i) \ , \\
G_i &= \beta_i(1 + D_i + 4K_i)/(1 - \beta_i) \ , \\
J_i &= \beta_i(1 + \alpha_i)/(1 - \beta_i^2) \ , \\
K_i &= (\beta_i - \alpha_i)/]\!(1 - 2\beta_i + \alpha_i) \ , \\
L_i &= -(\beta_i - \alpha_i)/]\!(1 - \alpha_i) \ , \\
M_i &= 2\beta_i/(1 - \beta_i)
\end{aligned}
\tag{7}
$$

and $f'(0)$ denotes $f'(z)$ evaluated at $z = 0$.

This representation is readily derived from (4),[2]. It has the advantage over Representation I that if the functions $f(z)$ and $h(z)$ are the solution for a homogeneous matrix with singularities outside $|z| = R_i$, then (6) gives immediately the solution for an infinite matrix containing a circular inclusion. In this sense, it is a generalization of the results for a cavity or rigid inclusion given by Green and Zerna [7].

Even though Representation II is appropriate when singularities are specified in the matrix, it cannot be used when singularities are specified within the inclusion. Hence it is more restricted than Representation I, which can be used to solve problems in which singularities are given within the inclusion.

Finally, it is convenient to write $\phi_0(z)$ and $\psi_0(z)$ in both representations as

$$
\begin{aligned}
\phi_0(z) &= f(z) + F(z) \ , \\
\psi_0(z) &= h(z) + H(z) \ .
\end{aligned}
\tag{8}
$$

The functions $f(z)$ and $h(z)$ will be called loading functions; while,

$F(z)$ and $H(z)$ will be called reflexive functions in what follows.

3. Inclusion Disturbing a Uniform and/or Bending Stress Field

Consider an unbounded matrix containing n distinct circular inclusions. Let R_i and a_i denote the radius and position of the center of the ith inclusion. Let subscripts "o" and "i" ($i = 1,2,\ldots,N$) on elastic quantities refer to the matrix and the ith inclusion, respectively. Assuming that the inclusions are perfectly bonded to the matrix, we have that boundary conditions (3), where the displacements and stresses are given in terms of local polar coordinates with origins at the centers of the inclusions, have to be satisfied at each inclusion-matrix interface. It is required to find the solution if an arbitrary elastic field, with no singularities in $|z - a_i| < R_i$, is applied to the matrix.

This problem can be readily solved by using the Schwarz alternating method [5], . For a discussion of the method and details of the solution the reader is referred to [1,2]. The present section contains results only.

Let the applied stress field by a combined uniform and in-plane bending loading. Referring to Fig. 2 and using the notation of the previous sections, the complex potentials for a homogeneous matrix corresponding to a combined uniform and bending stress field are

$$\begin{aligned} \phi^o(z) &= f(z) = A_1 z + A_2 z^2 , \\ \psi^o(z) &= h(z) = B_1 z + B_2 z^2 , \end{aligned} \tag{9}$$

where

$$\begin{aligned} A_1 &= (p_o + q_o)/4 , \qquad A_2 = (q_1 - i\, p_1)\, e^{-i\upsilon}/8 , \\ B_1 &= (q_o - p_o)e^{-2i\upsilon}/2 , \qquad B_2 = (q_1 + i\, p_1)e^{-3i\upsilon}/8 , \end{aligned} \tag{10}$$

and p_o, q_o, p_1, q_1, υ are specified constants for the assumed stress field.

Upon using $f(z)$ and $h(z)$, defined by (9), as the loading functions and applying the Schwarz method of successive approximations for a number of cycles, it becomes evident that the solution

can be written as

$$\phi_o(z) = A_1 z + A_2 z^2 + \sum_{m=1}^{\infty} \sum_{i=1}^{N} \sum_{k=1}^{P_m} \sum_{n=1}^{m+2} B_{imkn} [z - \zeta_{imk}]^{-n} , \quad (11)$$

$$\psi_o(z) = B_1 z + B_2 z^2 + \sum_{m=1}^{\infty} \sum_{i=1}^{N} \sum_{k=1}^{P_m} \sum_{n=1}^{m+3} E_{imkn} [z - \zeta_{imk}]^{-n} , \quad (12)$$

$$\phi_i(z) = F_{i1} z + F_{i2} z^2 + \sum_{m=1}^{\infty} \sum_{j=1}^{N_*} \sum_{k=1}^{P_m} \sum_{n=1}^{m+2} D_{ijmkn} [z - \zeta_{jmk}]^{-n}, \quad (13)$$

$$\psi_i(z) = H_{i1} z + H_{i2} z^2 + \sum_{m=1}^{\infty} \sum_{j=1}^{N} \sum_{k=1}^{P_m} \sum_{n=1}^{m+3} G_{ijmkn} [z - \zeta_{jmk}]^{-n}, \quad (14)$$

where B_{imkn}, E_{imkn}, F_{i1}, F_{i2}, H_{i1}, H_{i2}, D_{ijmkn} and G_{ijmkn} are unknown coefficients depending on the radii, spacing and elastic moduli of the inclusions and

$$\zeta_{i11} = a_i , \quad (15)$$

$$\zeta_{i,m+1,\ell} = a_i + F_i^2 [\bar{\zeta}_{jmk} - \bar{a}_i]^{-1} \quad \text{for } i \neq j , \quad (16)$$

where

$$\ell = \begin{cases} (j - 1) P_m + k & \text{if } j < i , \\ (j - 2) P_m + k & \text{if } j > i , \end{cases} \quad (17)$$

$$P_m = (N - 1)^{m-1} . \quad (18)$$

The commas in the subscripts in (16) and subsequently are used to separate the indices whenever confusion can arise. Furthermore, the asterisk on the summation symbol denotes that terms with $j = i$ are omitted from the sums.

The complex potentials are singular at the points $z = \zeta_{imk}$ which can be given a simple geometrical interpretation. The points $z = \zeta_{i11} = a_i$ are the positions of the centers of the inclusions; while, the points $z = \zeta_{imk}$ ($m \geq 2$, $k \geq 1$) are the result of successive inversion of $z = \zeta_{i11}$ with respect to the inclusion boundaries, which is the operation indicated by (16).

Recursion formulas for the unknown coefficients in (11) to (14)

can be found as follows: Choose any inclusion and decompose complex potentials (11) and (12) into loading and reflexive functions. The loadings functions are the ones with no singularities inside the inclusion; while, the reflexive ones are those with singularities within the inclusion. Application of Representation II to this inclusion immediately gives the coefficients of the reflexive functions in terms of the coefficients of the loading functions. Repeating this for all the inclusions yields the required recursion formulas. Since the derivation of the recursion formulas is rather lengthy, it will not be presented here. The interested reader is referred to [2] for details of the derivation. Only the results will be presented here. For $i = 1,2,\ldots,N$

$$
\begin{aligned}
B_{i111} &= -D_i R_i^2 (\bar{B}_1 + 2\,\bar{a}_i \bar{B}_2 + 2\,a_i \bar{A}_2) \;, \\
B_{i112} &= -D_i R_i^4 \bar{B}_2 \;; \qquad\qquad (19) \\
B_{i113} &= 0 \;,
\end{aligned}
$$

$$E_{i111} = R_i^2 \left[(D_i - E_i + 2\,G_i)\,A_1 + 2\,(G_i + J_i)\,a_i\,A_2\right.$$

$$\left. + 2\,(D_i - E_i + G_i - J_i)\,\bar{a}_i\,\bar{A}_2\right] + \sum_{m=2}^{\infty} \sum_{j=1}^{N}{}^{*} \sum_{k=1}^{P_{m-1}} \Big\{ D_i\,\bar{E}_{j,m-1,k1}$$

$$+ \sum_{n=1}^{m+1} (-1)^n\, n\, R_i^2 \left[(G_i + J_i)(\bar{\zeta}_{im\ell} - \bar{a}_i)^{n+1}\, R_i^{-2(n+1)}\, B_{j,m-1,kn}\right.$$

$$\left. + (G_i - J_i)(\zeta_{im\ell} - a_i)^{n+1}\, R_i^{-2(n+1)}\, \bar{B}_{j,m-1,kn}\right] \Big\} \quad , \qquad (20)$$

$$\left.\begin{aligned} E_{i112} &= -\,R_i^2 \left[E_i\, R_i^2\, \bar{A}_2 + D_i\, \bar{a}_i\, (\bar{B}_1 + 2\,\bar{a}_i\,\bar{B}_2 + 2\,a_i\,\bar{A}_2)\right] \quad , \\ E_{i113} &= -\,D_i\, R_i^4\, (\bar{B}_1 + 4\,\bar{a}_i\,\bar{B}_2 + 2\,a_i\,\bar{A}_2) \quad , \\ E_{i114} &= -\,2\,D_i\, R_i^6\, \bar{B}_2 \quad , \end{aligned}\right\} \qquad (21)$$

$$F_{i1} = (1 - E_i)\left[(1 + 2K_i)A_1 + 2(K_i + L_i)a_iA_2 + 2(K_i - L_i)\bar{a}_i\bar{A}_2\right]$$

$$- \sum_{m=2}^{\infty} \sum_{j=1}^{N}{}^{*} \sum_{k=1}^{P_{m-1}} \sum_{n=1}^{m+1} n(1 - E_i)\left[(K_i + L_i)(\bar{a}_i - \bar{\zeta}_{im\ell})^{n+1}\, B_{j,m-1,kn}\right.$$

$$\left. + (K_i - L_i)(a_i - \zeta_{im\ell})^{n+1}\, \bar{B}_{j,m-1,kn}\right] R_i^{-2(n+1)} \quad , \qquad (22)$$

$$F_{i2} = (1 - E_i)\, A_2 \quad , \qquad (23)$$

$$\left.\begin{aligned} H_{i1} &= (1 - D_i)(B_1 + 2\,\bar{a}_i\, A_2) - 2(1 - E_i)\,\bar{a}_i\, A_2 \quad , \\ H_{i2} &= (1 - D_i)\, B_2 \quad , \end{aligned}\right\} \qquad (24)$$

For $m = 2,3,\ldots,\infty$; $j = 1,2,\ldots,N$ $(j\neq i)$; $k = 1,2,\ldots,P_{m-1}$ and ℓ given by (23) we have

$$B_{im\ell r} = \sum_{\substack{n=r-1\\(n\neq 0)}}^{m+1} (-1)^{n+1} nD_i\left[(\zeta_{im\ell}-a_i)\binom{n+2}{r+1} + \binom{n+1}{r}a_i\right](\zeta_{im\ell}-a_i)^{n+r+1}R_i^{-2(n+1)}\overline{B}_{j,m-1,kn}$$

$$+ \sum_{n=r}^{m+2}(-1)^{n+1}D_i\binom{n}{r}(\zeta_{im\ell}-a_i)^{n+r}\, R_i^{-2n}\, \overline{E}_{j,m-1,kn}$$

$$r = 1,2,\ldots,m+2 \quad , \tag{25}$$

$$E_{im\ell 1} = \sum_{n=1}^{m+1} (-1)^{n+1} n(E_i-D_i)(\zeta_{im\ell}-a_i)^{n+1}R_i^{-2n}\, \overline{B}_{j,m-1,kn} - D_i\overline{E}_{j,m-1,k1} \quad , \tag{26}$$

$$E_{im\ell 2} = D_i(\zeta_{im\ell}-a_i)\overline{E}_{j,m-1,k1} + \sum_{n=1}^{m+1} (-1)^{n+1}\Bigg[\binom{n}{2}E_i + D_i n\{1$$

$$+ \overline{a}_i R_i^{-2}[\binom{n+2}{2}(\zeta_{im\ell}-a_i) + (n+1)a_i]\}\Bigg](\zeta_{im\ell}-a_i)^{n+2}R_i^{-2n}\, \overline{B}_{j,m-1,kn}$$

$$+ \sum_{n=1}^{m+2}(-1)^{n+1}\, D_i\, n\, \overline{a}_1\, (\zeta_{im\ell} - a_i)^{n+1}\, R_i^{-2n}\, \overline{E}_{j,m-1,kn} \quad , \tag{27}$$

$$E_{im\ell r} = \sum_{n=r-2}^{m+1}(-1)^{n+1}\Bigg[\binom{n}{r}E_i + D_i n\{-\binom{n}{r-1} + (n+1)\Big[\binom{n}{r-2} + \binom{n-1}{r-3}a_i(\zeta_{im\ell}-a_i)^{-1}\Big]$$

$$+ (r-1)\overline{a}_i R_i^{-2}\,[(\zeta_{im\ell} - a_i)\binom{n+2}{r} + \binom{n+1}{r-1}]\}\Bigg](\zeta_{im\ell}-a_i)^{n+r}R_i^{-2n}\overline{B}_{j,m-1,kn}$$

$$+ \sum_{n=r-1}^{m+2}(-1)^{n+1}D_i n\Big[\binom{n-2}{r-3} + \binom{n-1}{r-2}\overline{a}_i(\zeta_{im\ell}-a_i)R_i^{-2}\Big](\zeta_{im\ell}- a_i)^{n+r-2}\times$$

$$\times R_i^{-2(n-1)}\overline{E}_{j,m-1,kn} \quad , \quad r = 3,4,\ldots,m+3 \quad , \tag{28}$$

$$D_{ij,m-1,kr} = (1 - E_i)\, B_{j,m-1,kr}\,, \quad r = 1,2,\ldots,m+1\,, \tag{29}$$

$$G_{ij,m-1,kr} = (1 - D_i)\, E_{j,m-1,kr} + (r-1)(D_i - E_i)\, \bar{a}_i\, B_{j,m-1,k,r-1}$$
$$- \sum_{n=r-1}^{m+1} n\, M_i\, (1 - D_i)(\bar{\zeta}_{im\ell} - \bar{a}_i)^{n-r+2}\, R_i^{-2(n-r+1)}\, B_{j,m-1,kn}, \tag{30}$$

where $\binom{m}{n}$ are binomial coefficients; $\binom{m}{n} = 0$ if $n > m$ or $n < 0$ and $\binom{0}{0} = 1$. Furthermore, terms with any subscript equal to zero are identically zero.

The computation procedure, when using recursion formulas (19) to (30), is as follows:

1^0 Set $m = 1$ and use (19)-(21) to compute B_{i11r} and E_{i11r}

2^0 Set $m = 2$ and

(a) use (25)-(28) to compute $B_{i2\ell r}$ and $E_{i2\ell r}$;

(b) use (20) to recompute E_{i111} .

3^0 For $m = M \geq 3$,

(a) use (25) to recompute $B_{ip\ell r}$ for $p = 2,3,\ldots,M-1$ and $r = 1,2,\ldots,M-1$;

(b) use (26)-(28) to recompute $E_{ip\ell r}$ for $p = 2,3,\ldots,M-1$ and $r = 1,2,\ldots,M-1$;

(c) use (25)-(28) to compute $B_{iM\ell r}$ and $E_{iM\ell r}$;

(d) use (20) to recompute E_{i111} .

4^0 Increase M by one and repeat step 3.

5^0 Use (22)-(24), (29) and (30) to compute the coefficients for the complex potentials for the inclusions.

The computations indicated above can be terminated when E_{i111} converges to a limit of desired accuracy.

If $E_{i111} \equiv 0$, then the computation procedure simplifies con-

siderably. In this case, the coefficients are found immediately from steps 1, 2a, 3c, 4 and 5. This situation is encountered when the inclusions lie on the x-axis and the applied stresses are specified by $\sigma_{xx} = \text{const.} \times y$, $\sigma_{xy} = \sigma_{yy} = 0$ at large distances from the inclusions.

Finally, if the inclusions have the same shear modulus as the matrix,

$$\alpha_i = \beta_i = (\kappa_0 - \kappa_i)/(2 + \kappa_0 + \kappa_i) \tag{31}$$

and the solution becomes

$$\begin{aligned}
\phi_0(z) &= A_1 z + A_2 z^2 , \\
\psi_0(z) &= B_1 z + B_2 z^2 + \sum_{i=1}^{N} \frac{2\beta_i}{1-\beta_i} \{2 R_i^2 [A_1 + a_i A_2 \\
&\quad + \bar{a}_i \bar{A}_2] \frac{1}{z - \zeta_{i11}} + \frac{R_i^4 \bar{A}_2}{(z - \zeta_{i11})^2} \} , \\
\phi_i(z) &= [(1 + \beta_i)/(1 - \beta_i)] [A_1 z + A_2 z^2] , \\
\psi_i(z) &= [B_1 - \frac{4\beta_i}{1-\beta_i} \bar{a}_i A_2] z + B_2 z^2 \\
&\quad + \sum_{j=1}^{N*} \frac{2\beta_j}{1-\beta_j} \{2 R_j^2 [A_1 + a_j A^2 + \bar{a}_j \bar{A}_2] \frac{1}{z-\zeta_{j11}} + \frac{R_i^4 \bar{A}_2}{(z-\zeta_{j11})^2} \}
\end{aligned} \tag{32}$$

The structure of solution (32) is extremely simple. The complex potentials for the matrix are singular inside the inclusions; while, those for the ith inclusion are singular in all inclusions except the ith one.

Now let us consider the application of solution (32) to a composite containing a square array of identical fibers of unit radius. Let ν_i denote the Poisson's ratio of the fibers. Let the centers of the fibers be put at the points

$$z = \omega_{m,n} = 2a(m + in) \ , \ (m,n = 0,\pm 1,\pm 2,\ldots) \ , \tag{33}$$

where a gives the spacing between the fibers. The fiber volume fraction is given in terms of a by

$$V = \pi/4a^2 \ . \tag{34}$$

Since the smallest center to center distance between fibers occurs for $a = 1$, the maximum fiber volume fraction is $\pi/4 = 0.7854$.

4. Square Array of Fibers Disturbing a Uniaxial Stress Field

As the first example, consider the case in which the macroscopic stress field, applied to the composite, is given by

$$\bar{\sigma}_{xx} = 1 \ , \quad \bar{\sigma}_{xy} = \bar{\sigma}_{yy} = 0 \ . \tag{35}$$

In this case,

$$A_2 = B_2 = 0 \ , \quad A_1 = P/4 \ , \quad B_1 = -P/2 \tag{36}$$

and the solution becomes

$$\begin{aligned} \phi_0(z) &= \frac{P\,z}{4} \ , \quad \psi_0(z) = -\frac{P\,z}{2} + \frac{P}{2}\gamma_i\, A(z) \ , \\ \phi_i(z) &= (1 + \gamma_i)Pz/4 \ , \quad \psi_i(z) = -Pz/2 + \frac{P}{2}\gamma_i\,[A(z) - 1/z] \ , \end{aligned} \tag{37}$$

where

$$P = 1/(1 + V\,\gamma_i) \ , \qquad \gamma_i = (\kappa_0 - \kappa_i)/(1 + a_i) \tag{38}$$

$$A(z) = \sum_{m,n=-\infty}^{\infty} [z - \omega_{m,n}]^{-1} \ . \tag{39}$$

The stresses, in terms of polar coordinates with origin at the center of any inclusion, can be found by using well known formulas. In the matrix,

$$\begin{aligned} \sigma_{\rho\rho 0} + \sigma_{\theta\theta 0} &= P \\ \sigma_{\rho\rho 0} - i\,\sigma_{\rho\theta 0} &= \frac{P}{2}\{1 + e^{2i\theta}\,[1 - \gamma_i\, A'(z)]\} \ , \end{aligned} \tag{40}$$

where

$$A'(z) = - \sum_{m,n=-\infty}^{\infty} [z - \omega_{m,n}]^{-2} \quad . \tag{41}$$

Series $A'(z)$ can be written as

$$A'(z) = -v - p(z) \quad , \tag{42}$$

where $p(z)$ is the Weierstrass p function [8,9]. Expanding $p(z)$ in a Laurant series [9] and substituting this result into (40), we get at the interface:

$$\begin{aligned} \sigma_{\rho\rho o} &= \frac{P}{2} \{1 + \gamma_i + \frac{\cos 2\theta}{P} + \gamma_i \sum_{n=2}^{\infty} c_n a^{-2n} \cos 2n\theta\} \quad , \\ \sigma_{\rho\theta o} &= - \frac{P}{2} \{ \frac{\sin 2\theta}{P} + \gamma_i \sum_{n=2}^{\infty} c_n a^{-2n} \sin 2n\theta \} \quad , \end{aligned} \tag{43}$$

where $c_2 = 0.590852$, $c_3 = 0$ and

$$c_n = \frac{3}{(2n + 1)(n - 3)} \sum_{m=2}^{n-2} c_m c_{n-m} \quad , \quad (n \geq 4) \quad . \tag{44}$$

Series (43) for the stresses are extremely rapidly convergent with twelve terms being sufficient to give six place accuracy.

The stresses at the interface are shown in Figures 3 through 5 for discrete values of v and $\gamma_i = 1$, which is the largest admissable positive value of γ_i. This value of γ_i corresponds to $\nu_o = 0.0$ and $\nu_i = 0.5$ which implies that the Young's modulus at the fibers is 1.5 times the Young's modulus of the matrix. The general trend of the results is that the stresses get smaller as the fiber volume fraction increases. This is in qualitative agreement with the results of Van Fo Fy (first nine Chapters of [10] and Foye [11]). It should be noted that, while this trend has been observed by Van Fo Fy and Foye for certain combinations of elastic constants, it does not hold in general. Other results by these investigators indicate steadily increasing stresses as v increases. Thus the present results cannot be applied directly to real composites.

Now let us derive an alternate expression for the stresses by introducing a different representation for the series $A'(z)$. By

using the result [12].

$$\frac{1}{\sin^2 z} = \sum_{\lambda=-\infty}^{\infty} [z - \pi\lambda]^{-2} , \tag{45}$$

the series for $A'(z)$ can be summed once to give

$$A'(z) = -\frac{\pi^2}{4a^2} \sum_{n=-\infty}^{\infty} \csc^2 \pi\left(\frac{z}{2a} - in\right)$$

$$= -\frac{\pi^2}{4a^2} \left\{ \csc^2 \frac{\pi z}{2a} + \sum_{n=1}^{\infty} \left[\csc^2 \pi\left(in - \frac{z}{2a}\right) + \csc^2 \pi\left(in + \frac{z}{2a}\right)\right]\right\} \tag{46}$$

Upon using trigonometric identities, it follows that

$$\csc^2 \pi\left(in \pm \frac{z}{2a}\right) = \left[i \sinh \pi n \cos \frac{\pi z}{2a} \pm \cosh \pi n \sin \frac{\pi z}{2a}\right]^{-2} \tag{47}$$

and it is seen that (46) is a rapidly converging series. Furthermore, each term in the series corresponds to a single row of fibers parallel to the x-axis. Thus this indicates that it is sufficient to take a small number of rows of fibers to develop the same stress distribution as occurs in the case of doubly periodic array. This is in agreement with the recent results due to Hulbert and Rybicki[12].

Upon substituting (39), with $A'(z)$ given by (46), into (1) and evaluating the resulting expressions on $z = a$, we get

$$\sigma_{xxo}\Big|_{x=a} = P \left\{1 + \frac{\pi^2 \gamma_i}{8\, a^2} \left[\operatorname{sech}^2 \frac{\pi y}{2a} + \sum_{n=1}^{\infty} \left(\operatorname{sech}^2 \pi\left(n - \frac{y}{2a}\right) + \operatorname{sech}^2 \pi\left(n + \frac{y}{2a}\right)\right)\right]\right\} , \tag{48}$$

$$\sigma_{yyo}\Big|_{x=a} = P - \sigma_{xxo}\Big|_{x=a} \qquad \sigma_{xyo}\Big|_{x=a} = 0 .$$

The x-component of stress on $z = a$ is shown in Figure 6 for $\gamma_i = 1$

and discrete values of v . It should be noted that the area under each curve is equal to $2a$ which is the force transmitted across $x = a$, $|y| \leq a$. Finally, it is readily shown that the x-component of the displacement is constant on $z = a$ for all values of y .

5. Square Array of Fibers Disturbing an In-plane Bending Stress Field

As the second example, consider the case in which the macroscopic stress field, applied to the composite, is given by

$$\bar{\sigma}_{xx} = y \ , \quad \bar{\sigma}_{xy} = \bar{\sigma}_{yy} = 0 \ . \tag{49}$$

In this case, which corresponds to pure transverse bending of the ply,

$$A_1 = B_1 = 0 \ , \quad A_2 = -\, i/8 \ , \quad B_2 = i/8 \tag{50}$$

and the solution becomes

$$\begin{aligned}
\phi_0(z) &= -\frac{i}{8} z^2 \ , \\
\psi_0(z) &= \frac{i}{8} z^2 + \gamma_i [\hat{}(z) + C(z)] \ , \\
\phi_i(z) &= -\frac{i}{8} (1 + \gamma_i) z^2 \ , \\
\psi_i(z) &= \frac{i}{4} \gamma_i \bar{\omega}_{m,n} z + \frac{i}{8} z^2 + \gamma_i [B(z) + C(z) - z^{-2}] \ ,
\end{aligned} \tag{51}$$

where $\omega_{m,n}$ is defined by (11) and

$$\begin{aligned}
B(z) &= \sum_{m,n} an[z - \omega_{m,n}]^{-1} \ , \\
C(z) &= \frac{i}{8} \sum_{m,n} [z - \omega_{m,n}]^{-2} \ .
\end{aligned} \tag{52}$$

The stresses, in terms of polar coordinates with origin at the center of any inclusion on the x axis, can be found by using well known formulas. In the matrix,

$$\sigma_{\rho\rho o} + \sigma_{\theta\theta o} = \rho \sin\theta$$

$$\sigma_{\rho\rho o} - i\,\sigma_{\rho\theta o} = \frac{1}{2}\{\rho \sin\theta + e^{2i\theta}\,[\rho \sin\theta - 2\gamma_i(B'(z) + C'(z))]\} \tag{53}$$

where

$$B'(z) = -\sum_{m,n} a\,n\,[z - \omega_{m,n}]^{-2} ,$$

$$C'(z) = -\frac{i}{4}\sum_{m,n} [z - \omega_{m,n}]^{-3} . \tag{54}$$

Even though $C'(z)$ can be expressed as a derivative of the Weierstrass $\wp$ function, $B'(z)$ cannot be written in terms of elliptic functions. Series (54) for $B'(z)$ and $C'(z)$ can be summed once in terms of complex trigonometric functions by using (45) and

$$\frac{\cos z}{\sin^3 z} = \sum_{m=-\infty}^{\infty} [z - m\pi]^{-3} , \tag{55}$$

which follows from (45) by differentiation with respect to z. Thus upon using (45) and (55) in (54), we get

$$B'(z) = -\frac{\pi^2}{4a}\sum_{n=1}^{\infty} n\,[\csc^2\pi(in - \frac{z}{2a}) - \csc^2\pi(in + \frac{z}{2a}] , \tag{56}$$

$$C'(z) = -\frac{i\,\pi^3}{32a^3}\{\frac{\cos\frac{\pi z}{2a}}{\sin^3\frac{\pi z}{2a}} + \sum_{n=1}^{\infty}[\frac{\cos\pi(in + \frac{z}{2a})}{\sin^3\pi(in + \frac{z}{2a})}$$

$$- \frac{\cos\pi(in - \frac{z}{2a})}{\sin^3\pi(in - \frac{z}{2a})}]\} . \tag{57}$$

These series converge very rapidly. Furthermore, each term in the series gives the contribution of a row of fibers. This indicates that it is sufficient to take a small number of rows of fibers to develop the same stress distribution as occurs in the case of a doubly periodic array. This is in agreement with the recent results due to

Hulbert and Rybicki [13].

The stresses at the interface were computed from (53), with $A'(z)$ and $B'(z)$ given by (56) and (57), for discrete values of the fiber volume fraction and $\gamma_i = 1$. They are plotted in Figures 7 through 9. As can be seen from these figures, the dependence of the stresses on v is more complicated than in the case of uniaxial loading. The point of maximum radial stress moves from $\theta = 45°$ for $v = 0$ to $\theta \approx 30°$ for $v = 0.7$. Furthermore, the maximum value of $\sigma_{\rho\rho}$ decreases initially and then increases as the fiber volume increases from zero to 0.7. The tangential stress exhibits a similar dependence on v. For low values of v, the maximum $\sigma_{\theta\theta}$ occurs at $\theta = 90°$; while for high values of v, $(\sigma_{\theta\theta})_{max}$ occurs at $\theta = 70°$. The shearing stress increases with v.

Finally, it is convenient to have expressions for the stresses in cartesian coordinates. Substituting (51) into (1) gives

$$\sigma_{xxo} - i\,\sigma_{xyo} = y - \gamma_i\,[B'(z) + C'(z)] \quad , \tag{58}$$

where $B'(z)$ and $C'(z)$ are given by (34) and (35). On $z = a$,

$$\begin{aligned} \sin \pi(in \pm \tfrac{z}{2a}) &= \cosh \pi(n \pm \tfrac{y}{2a}) \quad , \\ \cos \pi(in \pm \tfrac{z}{2a}) &= \pm\, i \sinh \pi(n \pm \tfrac{y}{2a}) \quad , \end{aligned} \tag{59}$$

and

$$\begin{aligned} [\sigma_{xxo}]_{x=a} = y &+ \frac{\gamma_i \pi^2}{4a} \sum_{n=1}^{\infty} n[\operatorname{sech}^2\pi(n - \tfrac{y}{2a}) - \operatorname{sech}^2\pi(n + \tfrac{y}{2a})] \\ &+ \frac{\gamma_i \pi^3}{32a^3} \{ \sinh \tfrac{\pi y}{2a} \operatorname{sech}^3 \tfrac{\pi y}{2a} \\ &+ \sum_{n=1}^{\infty} [\sinh \pi(n + \tfrac{y}{2a}) \operatorname{sech}^3\pi(n + \tfrac{y}{2a}) \\ &- \sinh \pi(n - \tfrac{y}{2a}) \operatorname{sech}^3\pi(n - \tfrac{y}{2a})] \} \quad , \end{aligned} \tag{60}$$

$$[\sigma_{xyo}]_{x=a} = 0 \quad . \tag{61}$$

The variation of σ_{xxo} on $x=a$ is shown in Figure 10 for $\gamma_i = 1$ and discrete values of v .

6. Random Array of Fibers Let us consider the stress distribution around typical fibers in a composite containing a random array of identical fibers for the case of uniaxial tension. Assuming that the fibers have unit radius the complex potentials are given by (37) and (38) with

$$A(z) = \sum_n (z-a_n)^{-1} \quad , \tag{62}$$

where a_n is a complex number giving the location of the center of the nth inclusion. The stresses in the matrix near a typical fiber which is placed at the origin of coordinates, are given by (40)with

$$A'(z) = - \sum_n (z-a_n)^{-2} \quad , \tag{63}$$

Values of a_n , corresponding to a random distribution of fibers, can be generated by taking a regular array of fibers and randomly perturbing the position of the inclusions in this array. They can also be determined from direct measured on micrographs of typical composite cross sections.

Figure 11 shows a typical fiber distribution that is observed in glass reinforced composites. This figure was constructed from an actual composite cross section. The fiber volume content is approximately 0.46 for this case. Figures 12 through 14 show the stresses in the matrix at the interface of selected fibers. The fibers for which results are presented are indicated in Figure 11. As can be seen from these figures, randomness of the fiber distribution has some effect on the stress distribution; but, the effect is small. It should be remembered that these results are for a composite in which the fibers and matrix have the same shear modulus.

7. Future Work The results presented above indicate future work that can be pursued. The general solution can be used to generate results for a real composite (one in which the fibers have different shear moduli than the matrix.)

The method of solution can be also used for regions bounded by other curves. Thus for example, knowledge of the general representation for a straight boundary will allow one to solve problems for regions bounded by straight and circular boundaries.

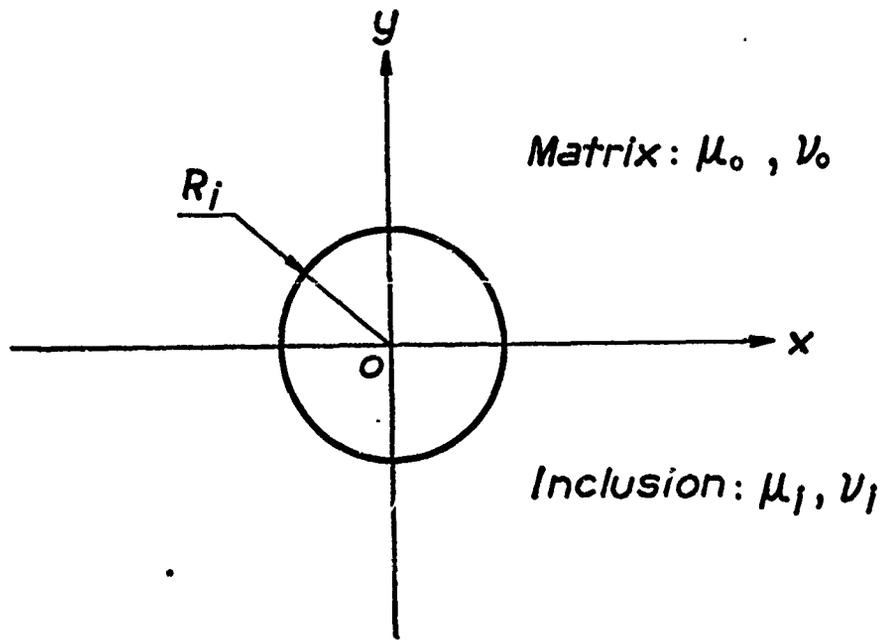

Figure 1. Inclusion of radius R_i at origin of Coordinates.

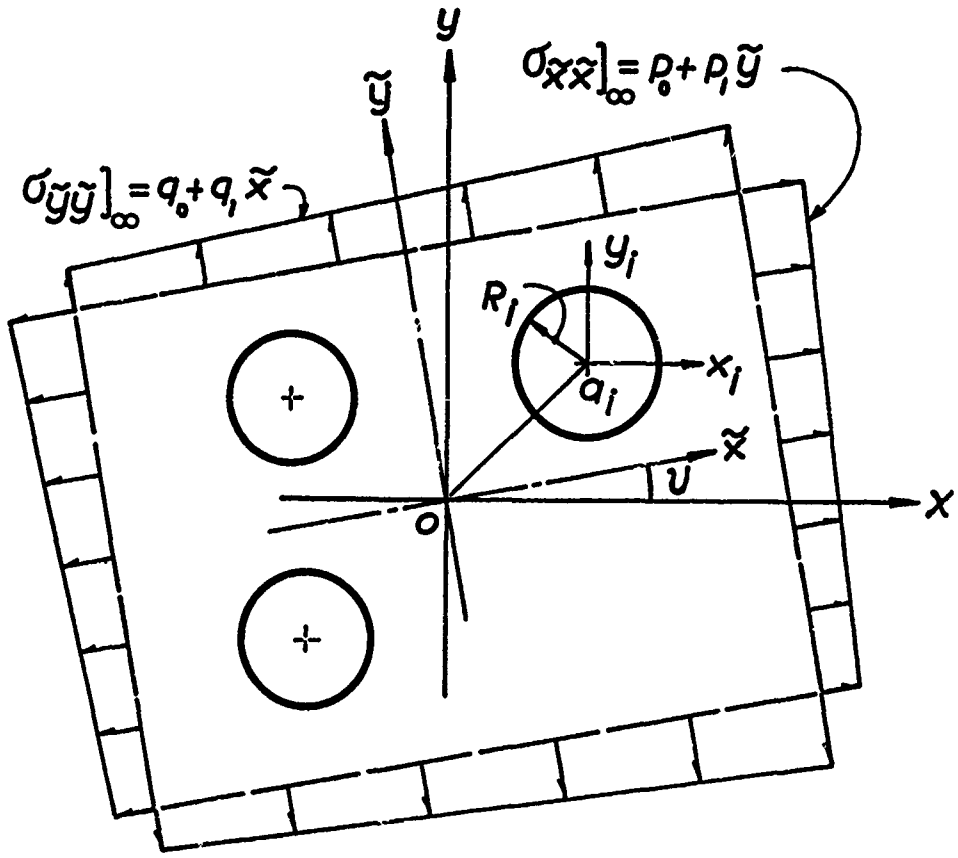

Figure 2. N inclusions with radii R_i placed at the points a_i in an unbounded matrix.

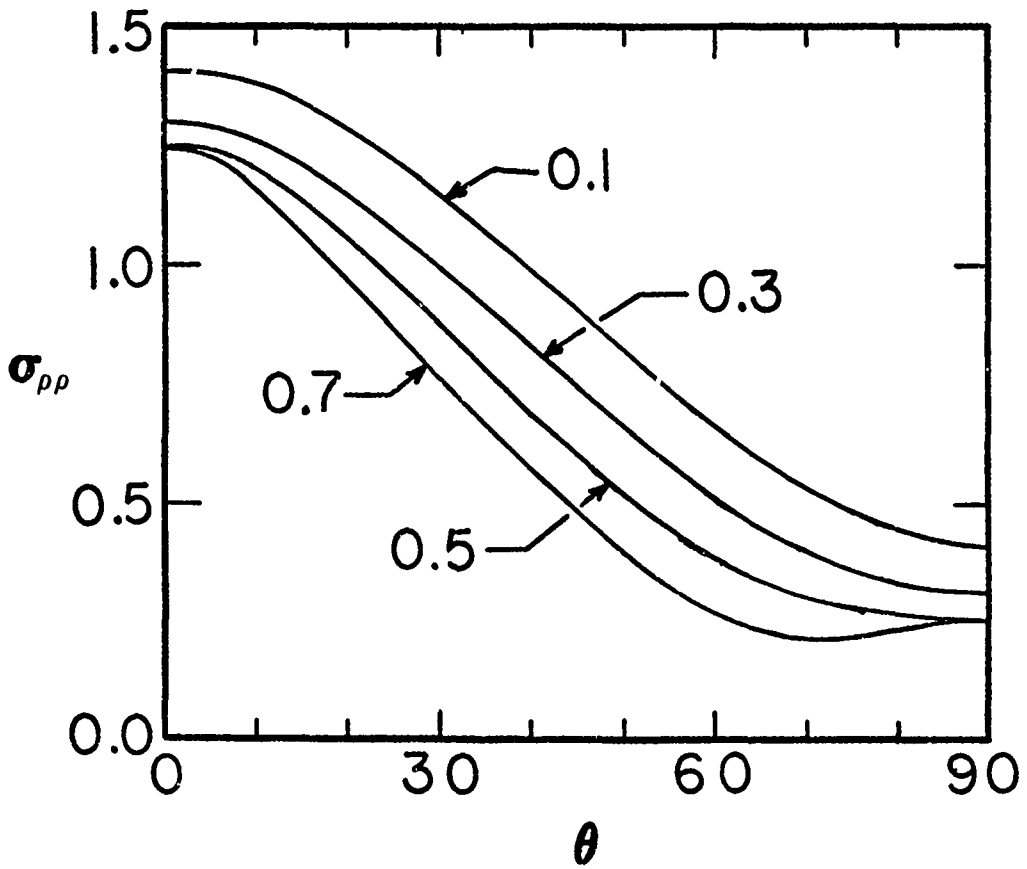

Figure 3. $\sigma_{\rho\rho o}$ at the interface versus θ for $\gamma_i = 1$ and discrete values of V in case of uniaxial tension.

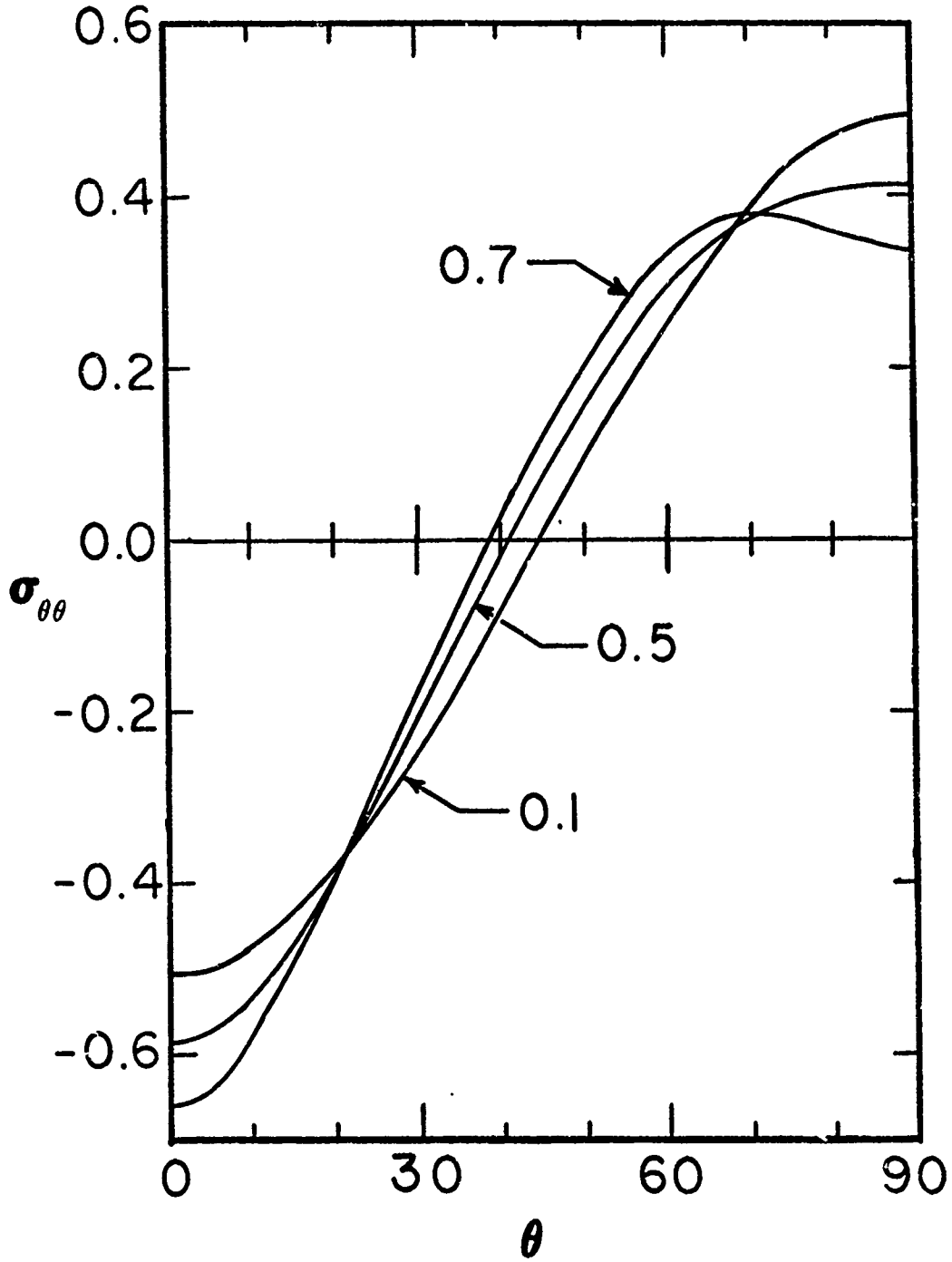

Figure 4. $\sigma_{\theta\theta o}$ at the interface versus Θ for $\gamma_i = 1$ and discrete values of V in case of uniaxial tension.

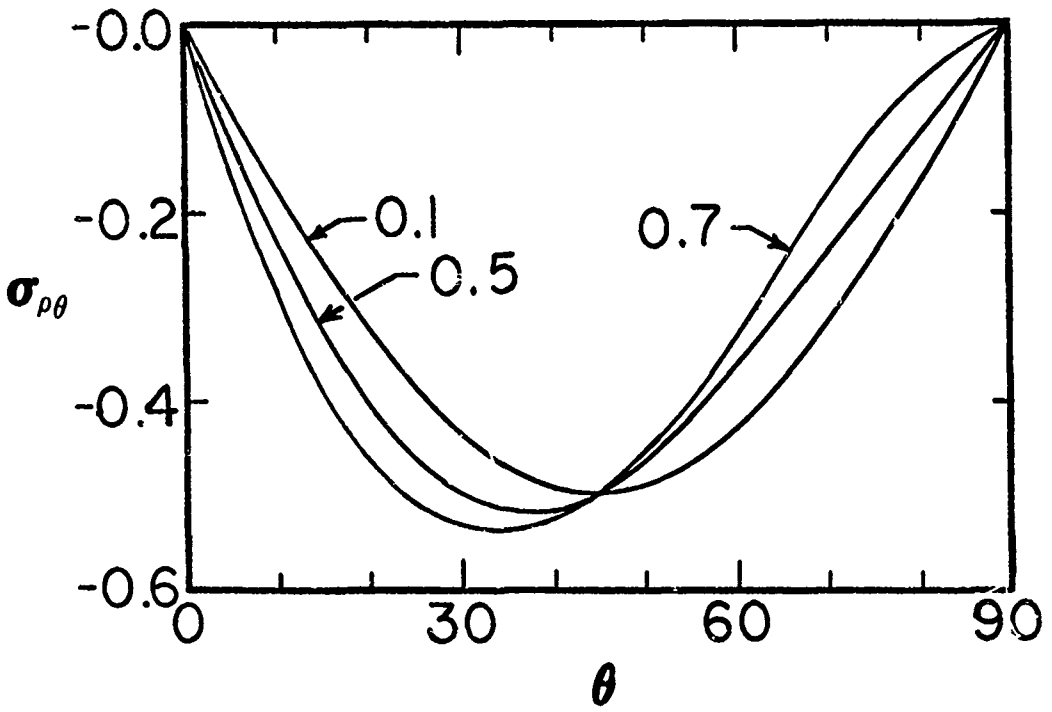

Figure 5. $\sigma_{\rho\theta o}$ at the interface versus Θ for $\gamma_i = 1$ and discrete values of V in case of unaxial tension.

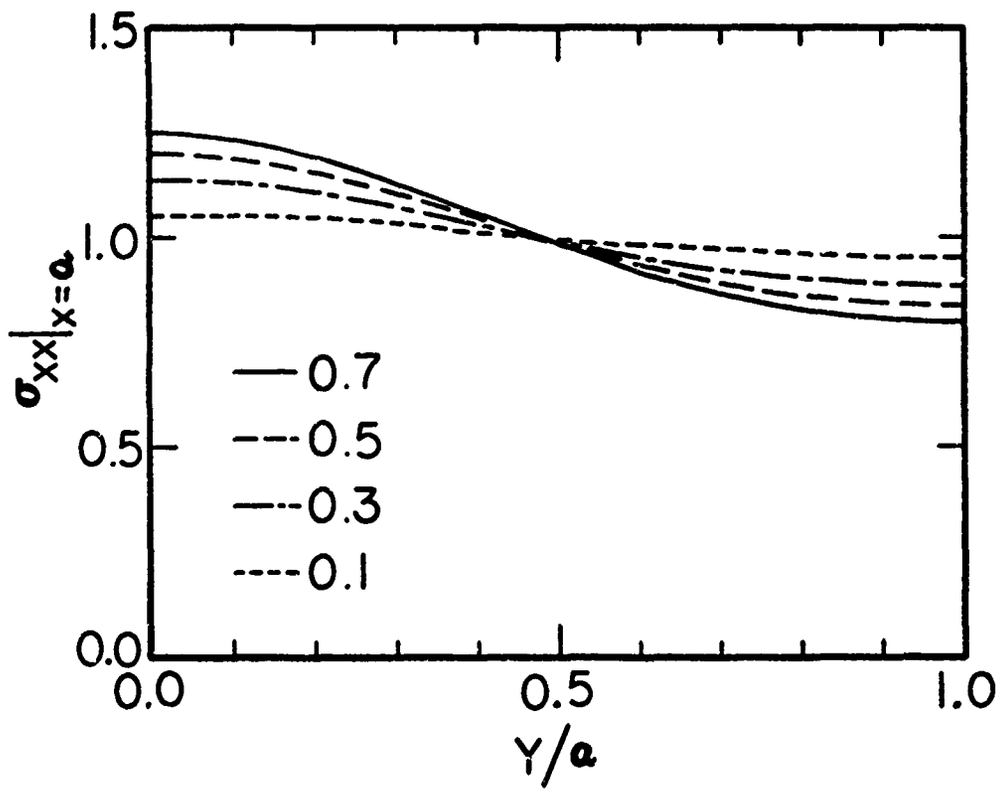

Figure 6. σ_{xxo} on X = a versus y for γ_i = 1 and discrete values of V in case of uniaxial tension.

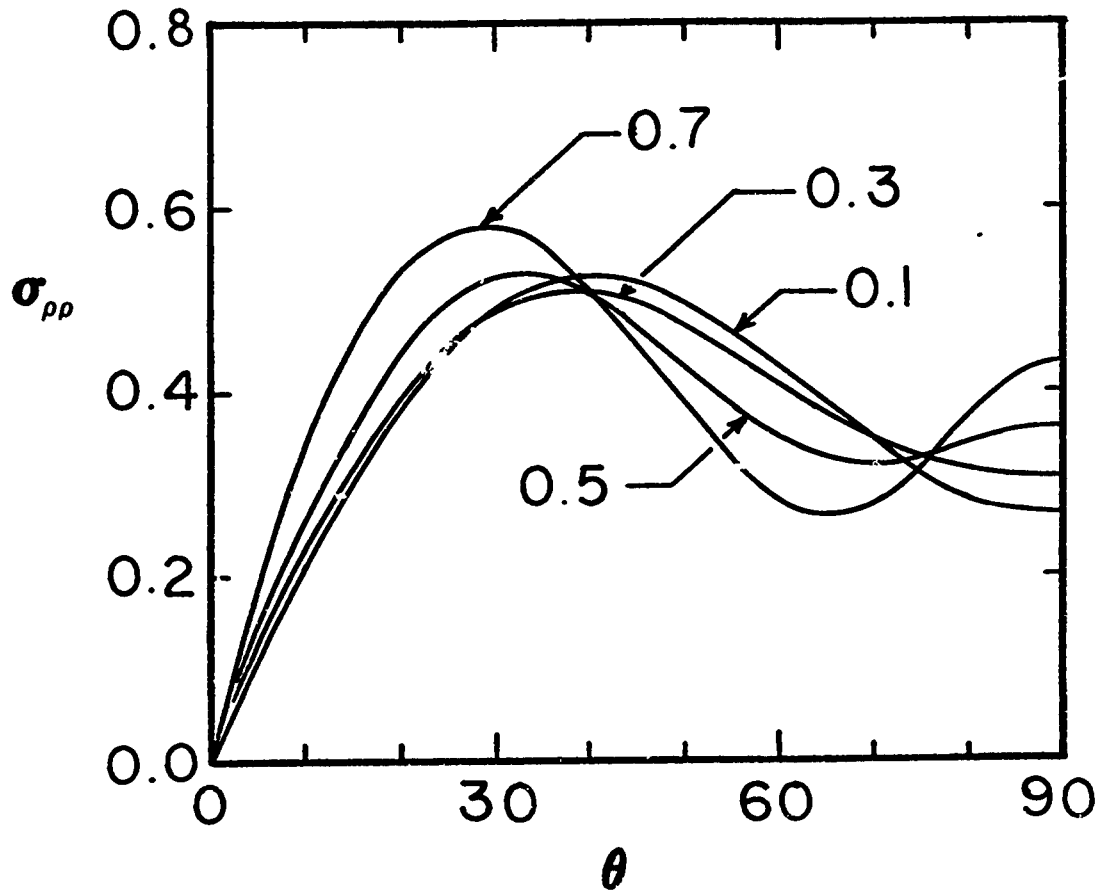

Figure 7. $\sigma_{\rho\rho o}$ at the interface versus Θ for $\gamma_i = 1$ and discrete values of V for the bending case.

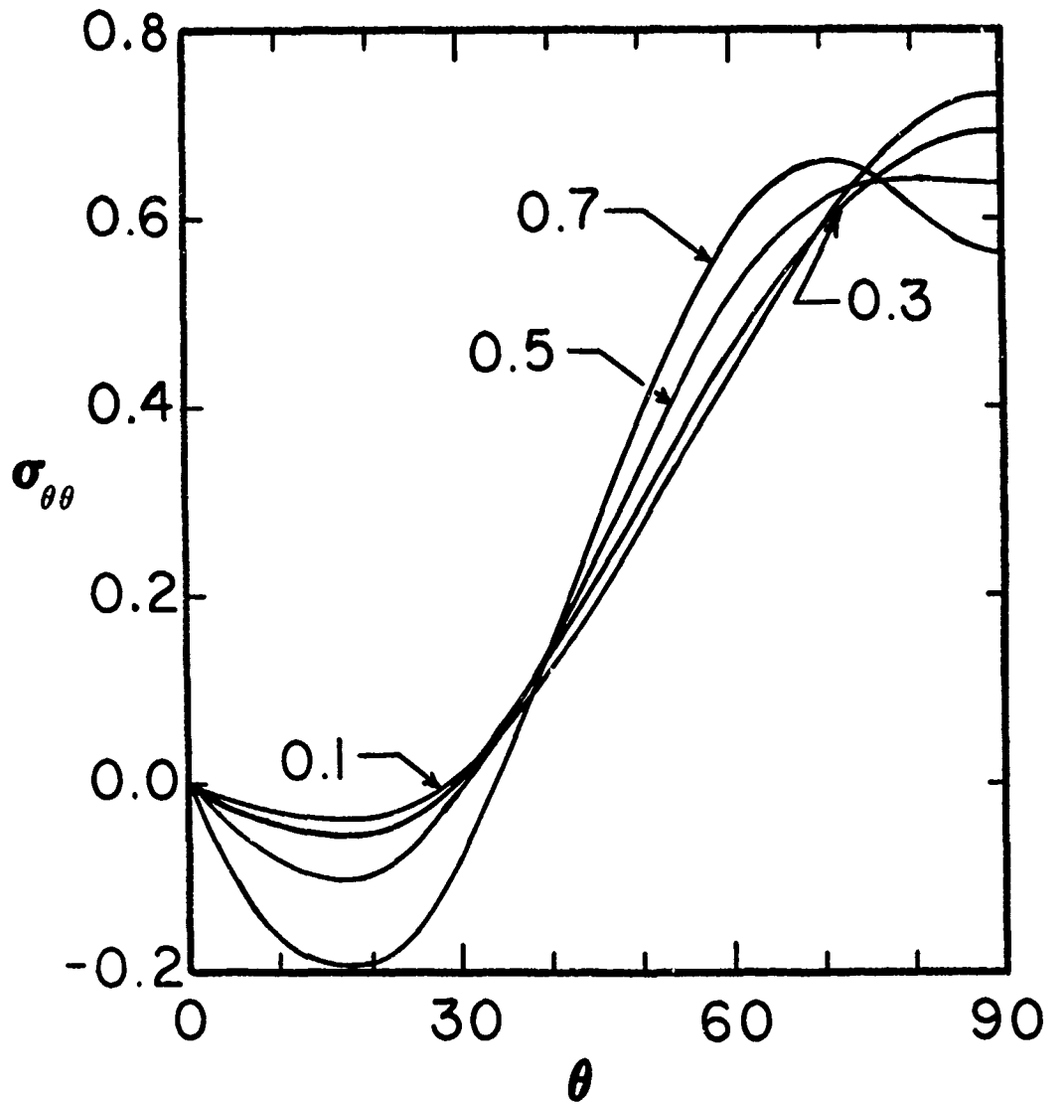

Figure 8. $\sigma_{\theta\theta o}$ at the interface versus Θ for $\gamma_i = 1$ and discrete values of V for the bending case.

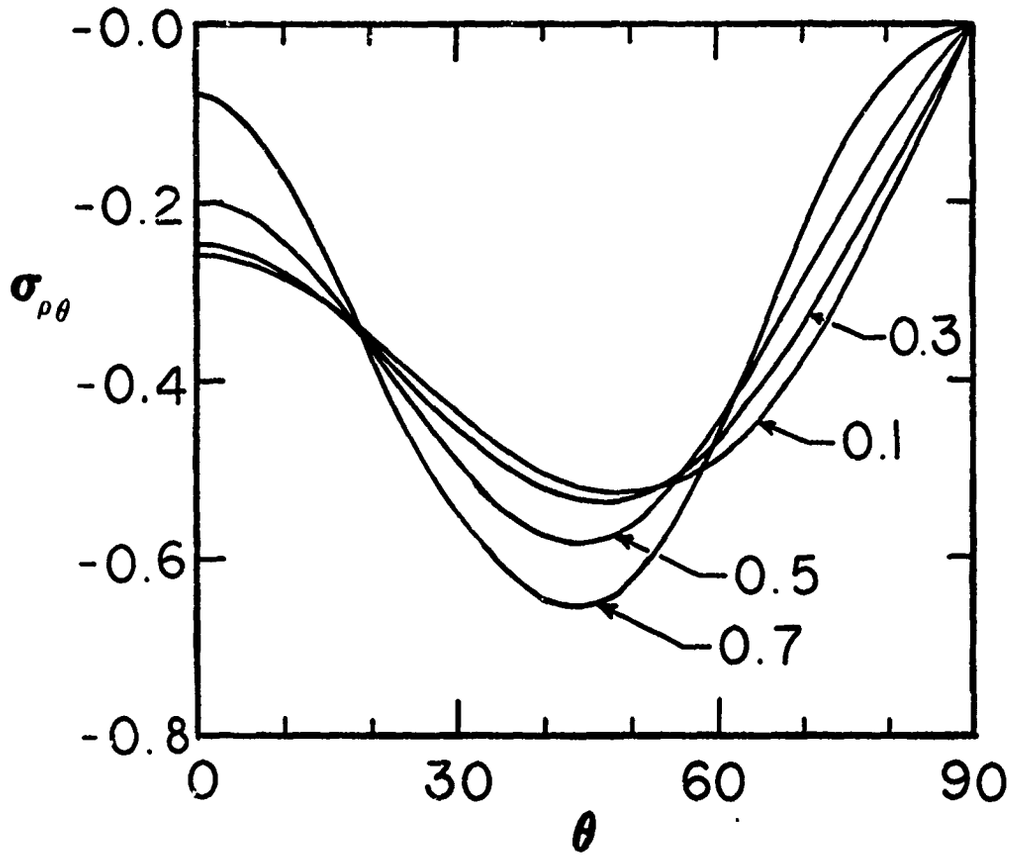

Figure 9. $\sigma_{\rho\theta o}$ at the interface versus θ for $\gamma_i = 1$ and discrete values of V for the bending case.

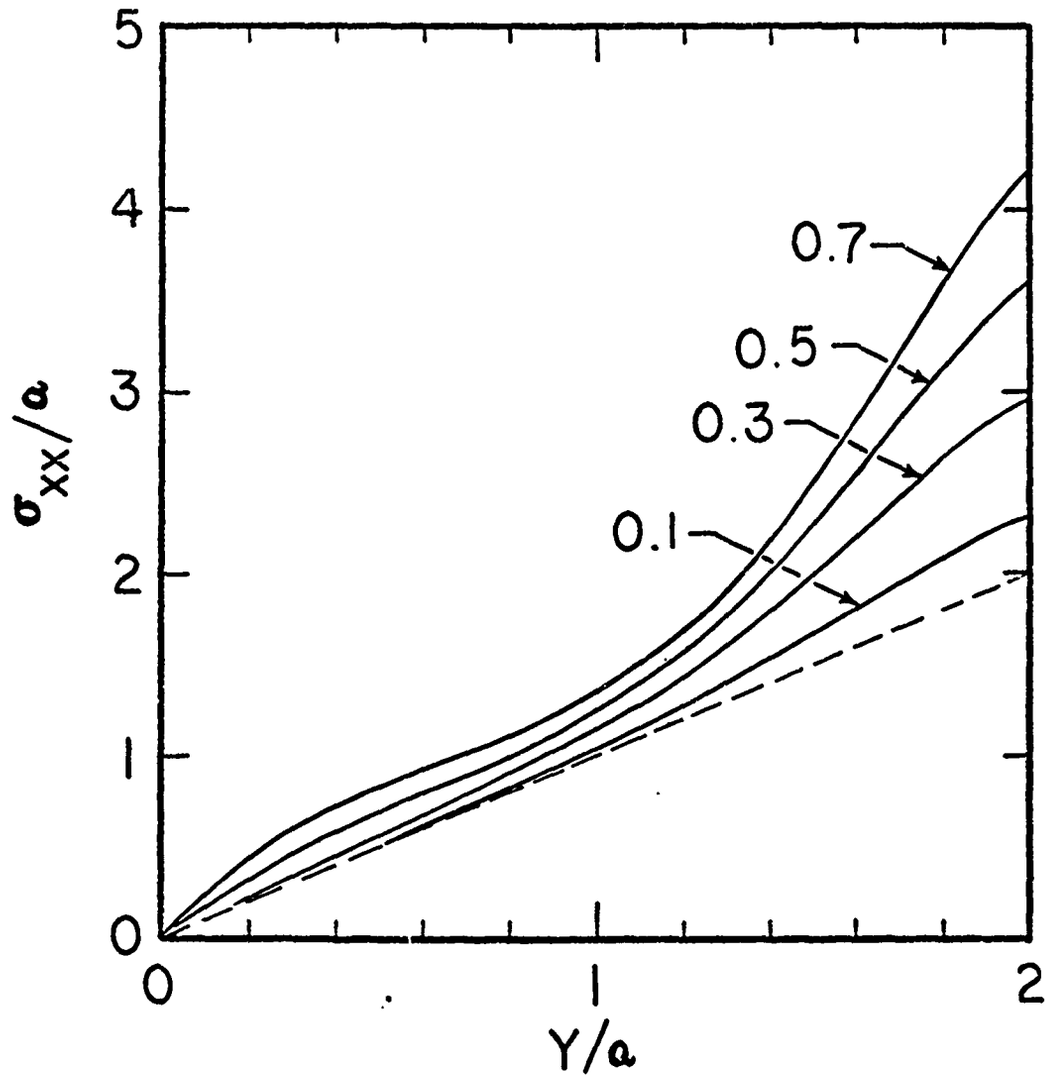

Figure 10. σ_{xxo} at X = a versus y for γ_i = 1 and discrete values of V for the bending case.

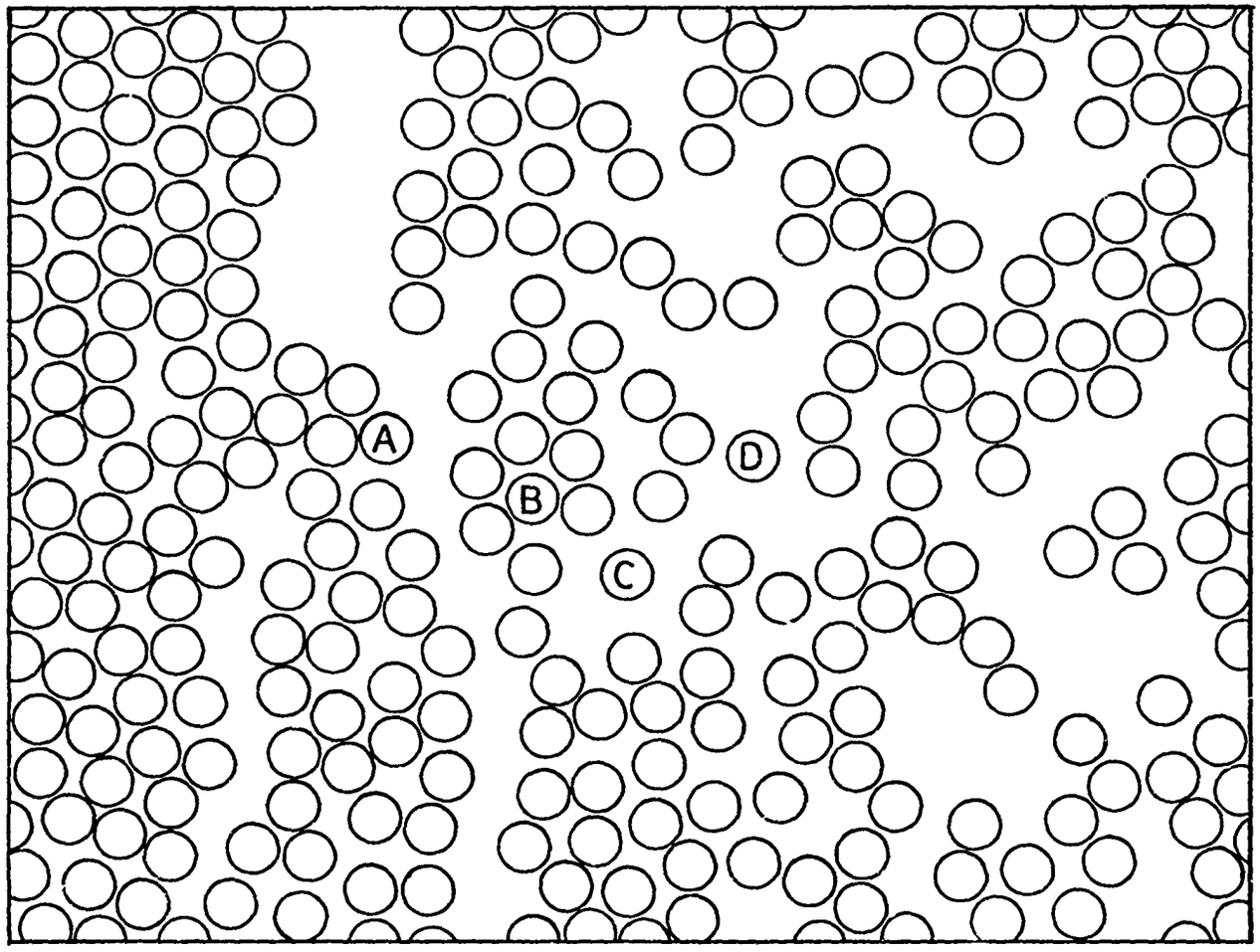

Figure 11. Arbitrary Array of Equal Inclusions

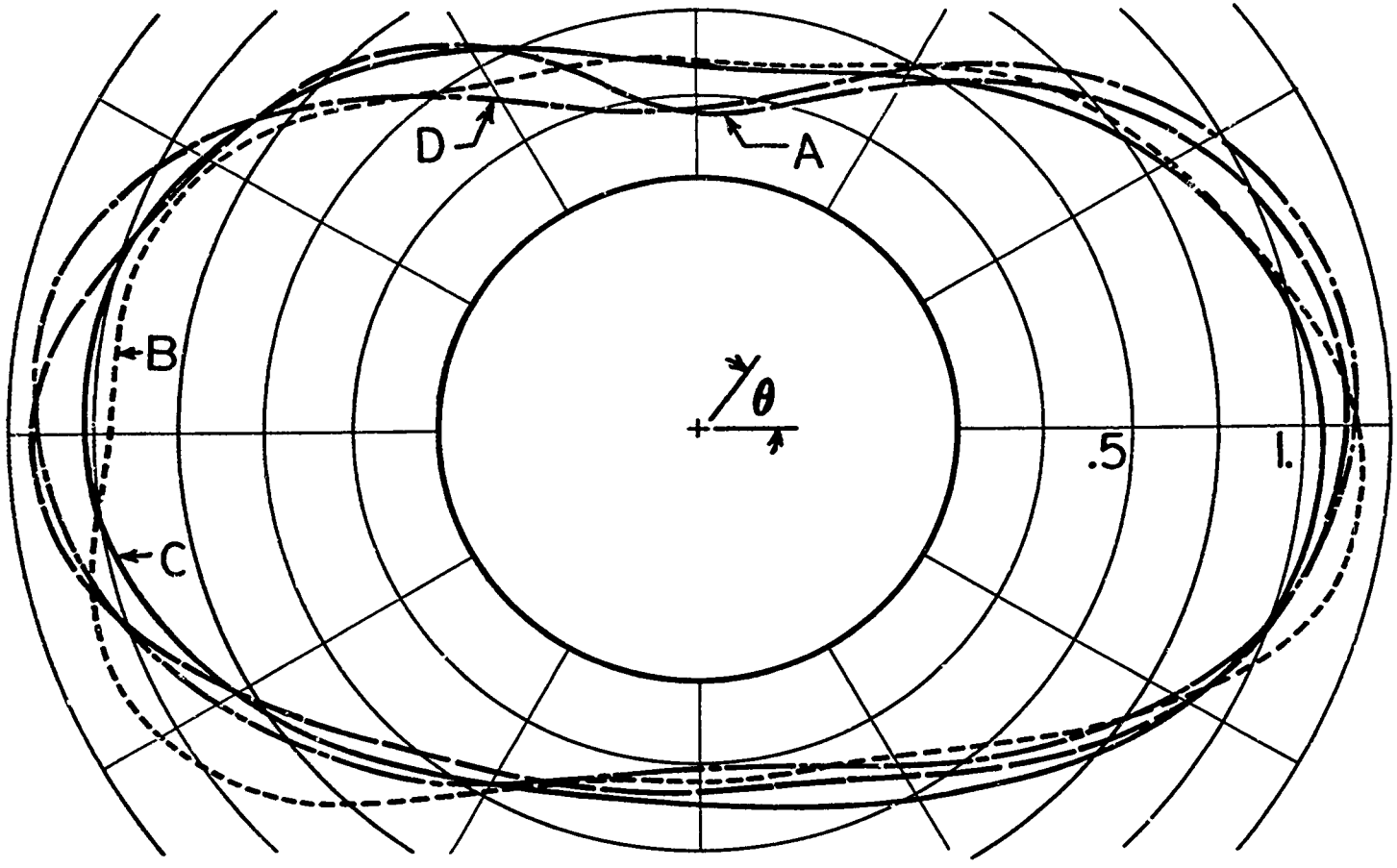

Figure 12. $\sigma_{\rho\rho o}$ at the interface for particular inclusions from Figure 11 for $\gamma_i = 1$ in case of uniaxial tension.

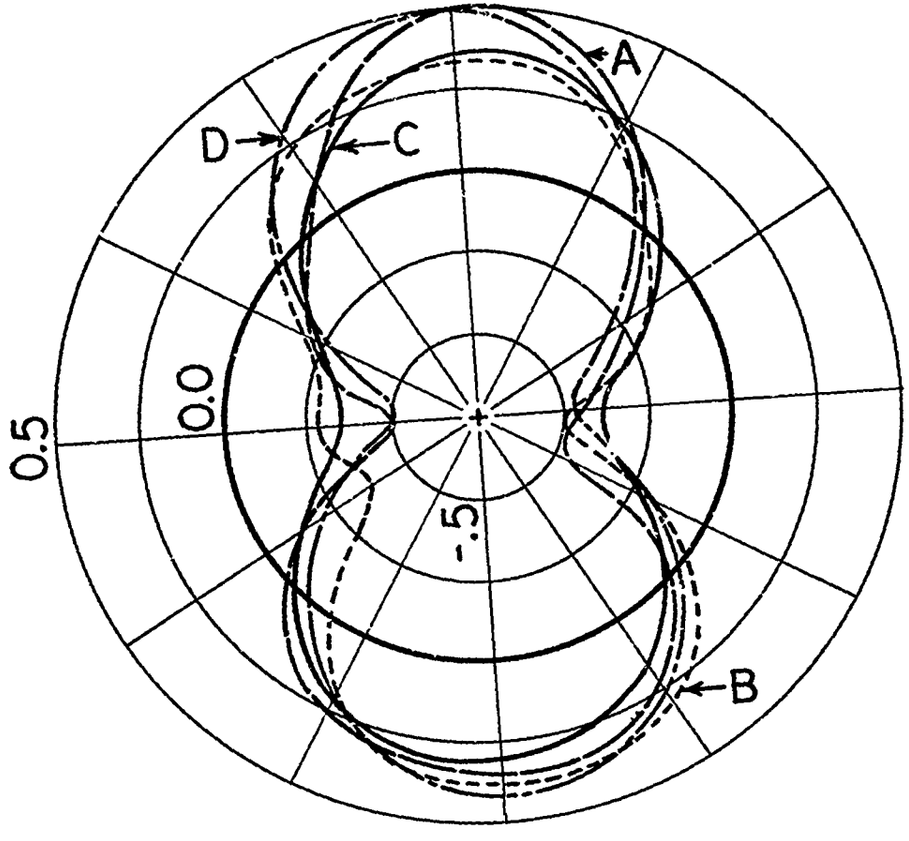

Figure 13. $\sigma_{\theta\theta o}$ at the interface for particular inclusion from Figure 11 for $\gamma_i = 1$ in case of uniaxial tension.

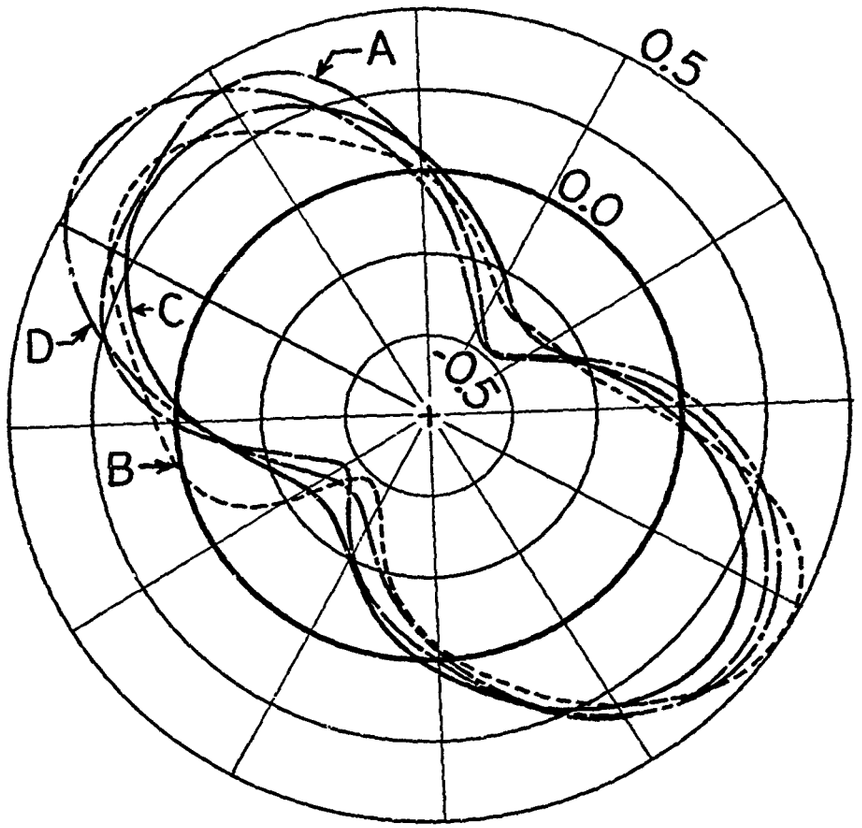

Figure 14. $\sigma_{\rho\theta o}$ at the interface for particular inclusion from Figure 11 for $\gamma_i = 1$ in case of uniaxial tension.

C. Scattered Light Photoelasticity
(Prof. J. Cannon, Mr. Choi, Mr. Shankar, Mr. Obaid)

Introduction

In the scattered-light photoelastic technique, stresses are found to be proportional to the slope of the fringe order (taken with respect to distance along the light beam path). For transmitted light, work stresses are proportional to the fringe order itself. Hence the scattered light technique is inherently less accurate than the transmitted light method. The potential for a full three dimensional stress analysis without slicing or destroying the model provides compelling reason to seek ways to overcome the difficulties of obtaining high accuracy with scattered light. One promising approach which has been successfully followed is to develop numerical techniques which will help to get the most out of the fringe data by "preventing" the derivative from becoming too erratic. A recently completed Master's degree thesis "Smoothed Spline Functions - Applications to Experimental Mechanics" (P. Shankar) summaries this work. The techniques which have been developed are also applicable to experimental problems other than scattered light photoelasticity.

A great deal of effort has been expended in the design and fabrication of a scattered light polariscope, and recently a live loading fixture to use with that polariscope. A statement of the main features of that work comprise the remainder of this report.

Scattered Light Polariscope

The recent development and availability of the Laser light source (concentrated, intense, monochromatic and coherent light beam) has enhanced the practical application of scattered-light photoelasticity which had been developed some twenty years earlier.

The polarized laser beam is passed through the photoelastic model after passing through the optical elements (polarizer and quarter wave plates) and stress fringes are viewed at the direction perpendicular to the light beam. In the scattered light polariscope, the model acts as the analyzer.

The potential advantages of scattered-light photoelasticity over conventional transmitted light photoelasticity are most pronounced in three dimensional problems.

In the conventional approach the stress frozen model must be made into slices for viewing in the transmission polariscope; whereas, in the scattered-light photoelasticity, the laser beam (1/32 inch dia. approximately) can be passed through the point of interest and the associated stress fringes can be obtained, thus eliminating the slicing (destruction) of the model.

Virtually all stress analysis studies carried out by the scattered-light photoelasticity to date have been made with frozen stress models, which have several inherent shortcomings.

1. Poisson's ratio of the photoelastic model material at the critical temperature (or stress freezing temperature) is nearly 1/2. This fact renders similitude between the model and prototype almost impossible. Another serious difficulty caused by this fact is that the deformation in the model at the critical temperature is nearly a constant volume deformation. Elastic deformation of common engineering materials is not a constant volume deformation.

2. It takes roughly two weeks of valuable time to complete the stress freezing cycle for a reasonable size of model and once the stress is frozen into a model the magnitude of stress and the type of loading cannot be changed without going through the stress freezing cycle again.

3. For a composite model of different materials or fiber reinforced composite model, the mismatch of material properties (mainly thermal expansion coefficients) of the materials induce large thermal stresses during the stress freezing cycle in addition to the stress due to the applied load.

There have been various ingenious schemes to circumvent these difficulties of the stress freezing method such as the use of two identical models; one loaded, the other not in order to separate the thermal stresses due to the stress freezing cycle and the stressed due to the applied load. However, the only way to eliminate the above mentioned shortcomings of stress frozen models is to develop a polariscope with live load capability. The advantages of the live-load approach with the scattered-light polariscope can easily be surmised from the above discussion.

The live-load loading fixture combined with scattered light photoelasticity has potential application in the analysis of three dimensional fiber reinforced composite models. In the fiber reinforced composite model with the fiber running in two perpendicular directions the model provides very restricted direction of view in that portion of stress fringes can be hidden behind the fibers. In addition to eliminating the inherent shortcomings associated with stress freezing, the live-load approach will enable one to deduce the fringes hidden behind the fibers and enable one to obtain complete stress fringes. The live-load loading frame may help to change scattered-light photoelasticity from a novelty to a practical everyday tool for the photoelastic stress analysis of three dimensional bodies.

II Design Criteria

The following design criteria were established for the loading fixture for the live loading of models for photoelastic stress analysis.

1. Overall dimensions of the loading frame should correspond approximately to a two-foot cube (i.e. extermal dimension of the immersion tank).

2. The load application portion of the loading frame (adjustable c-frame) must be located inside the two foot cube (approximate size) immersion tank.

3. Three sides of the immersion tank must be transparent (glass plates) for the viewing of model and stress fringes.

4. The loading frame must have x-y traverse with $\pm$ 5 inches from the midpoint in both x and y directions. (The milling machine table on which the immersion tank is to be mounted will provide this).

5. The loading frame must have the capability to rotate the model about the z-axis for ninety degrees one way and back under no applied load (see Fig. 1).

6. The loading frame must also have the capacility of tilting the model (rotation about x-axis) for a maximum of ninety degrees one way and returned to the original position.

7. The loading frame must be able to accommodate a model with maximum height (or length) of twelve inches and diameter (or diagonal of a square cross-section) of ten inches maximum.

8. Hydraulic means of applying load must be used.

9. The maximum axial load must be two thousand pounds and maximum torque must be three thousand inch-pounds. The stroke of the axial force actuator need not be more than one inch.

10. The hydraulic load actuator must have the capacility to actuate the axial load and torque independently of each other or simultaneously.

11. The hydraulic load actuator must not be larger than a six inch cube.

12. Means of measuring axial load and torque acting on the model must be provided. The measurements of the loads must be at the points external to the hydraulic actuator.

Some of the reasons for the above design criteria are as follows:

Overall size of the loading frame (2 feet cube) was arrived at because the milling machine table on which the loading frame will be mounted has a ten inch width. Also from the midpoint of the milling machine table cross motion to the edge of the milling machine frame is limited to 12 inches. The immersion tank is necessary to contain the immersion oil whose index of refraction matches that of the model, so that the oblique incidence of the laser (light) beam will not be refracted as the beam enters the model.

The rotation of the model (rotation about z-axis) provides the ease of stress fringe observation and enables one to pass the laser beam through any point of interest in the model (see Fig. 2).

The tilting of the model enables one to pass the laser beam along the direction perpendicular to the axis of the model All photoelastic materials creep under applied load. In order to maintain a constant load on the model for the duration of data acquisition, a hydraulic means of applying load was selected.

Photoelastic materials (polyester and epoxy of special formulation) have sensitivities (or stress fringe value) in range of 40 to 80 psi-inch/fringe and modulus of elasticity of approximately one half million pounds per square inch.

The magnitude of maximum axial load of 2,000 pounds was selected based on approximately four average stress fringes for ten square inch cross-section area. The axial force greater than 2,000 pounds will increase either the lateral dimension of the hydraulic load actuator or the required hydraulic pressure beyond reasonable limits

Maximum hydraulic actuator torque of 3,000 inch-pound was chosen based on two average stress fringes on the outer surface of a hollow cylindrical model of five inch outside diameter and one inch wall thickness.

In practice it is unusual to use a large diameter (diameter greater than six inches) model. If one uses a model with outside diameter greater than six inches, the wall thickness must be reduced to obtain reasonable number of stress fringes.

The axial deformation of the model will not be more than one percent of the model height (or length; 12 inches maximum height). The one inch stroke of the axial load actuator is more than adequate to accommodate this deformation. The increase of the stroke will increase the required total height of the hydraulic actuator by

by twice the stroke.

The rotation of the rotary actuator should be slightly more than 90° so that the model can be rotated 90° maximum and the torque can be continuously applied without repositioning the model.

The increase in the overall size of the hydraulic actuator will increase the overall height and lateral dimension of the loading frame correspondingly. It was thought that the 6 inch cube overall size of the hydraulic actuator will keep the overall size of the loading frame to approximately a two foot cube.

III Description of Components

1. Hydraulic Actuator and Hydraulic Circuit

As stated in the design criteria (10 and 11), the axial load actuator and the rotary (or torque) actuator must work either independently or simultaneously. The hydraulic actuator must be contained in a six inch cube.

Initially it was hoped that a unit of hydraulic actuator could be purchased from a commercial source. However, it was soon realized that no such unit was commercially available. Several commercial sources suggested that a linear (or axial force) actuator should be mounted on a rotary actuator or vice versa. Careful study quickly revealed that it was not possible to meet the previously stated design criteria by this arrangement. Thus, it was necessary to design and fabricate the hydraulic actuator.

The basic design of the hydraulic actuator was essentially mounting a linear (or axial force) actuator inside the rotary actuator (but not on the rotary actuator) and coupling the two by an integral piece of spline and a piston rod.

The torque tube with double rotating vane is constrained by a needle bearing at lower ends and by a ball bearing at the top and it is further constrained along the axial direction by a needle thrust bearing to rotate on the cylinder.

One serious problem was that there appeared to be no way of reaching the lower and upper compartment of the axial load actuator. Various schemes of connecting the cylinder to the hydraulic lines were considered. However, it was decided that the best way to reach the upper compartment of the cylinder is through a horizontal tunnel (3/16 inch dia.) in the base plate of the actuator and two vertical openings (diametrically opposite) from the tunnel and match the openings with the two vertical tunnels along the wall of the cylinder. The two tunnels in the wall of the cylinder were met by two holes drilled at an angle from inside the cylinder.

The lower compartment of the axial force actuator was reached again by another horizontal tunnel in the base plate of the actuator starting at the 30° from the first tunnel and ending slightly off the center of the base plate (Figure 3 shows the ports of the axial load actuator and two of the four ports of the torque actuator). The tunnel is met by a vertical opening 1/4 inch diameter. Figure 4 shows the exterior view of the piston rod, spline and cylinder assembled on the base plate. Figure 5 shows the housing of the torque tube ready for assembly. Figure 6 shows the assembled hydraulic actuator with cover plate off. A set of four Viton vane seals are also in view.

The hydraulic actuator is the heart of the live-load loading frame. The axial load actuator portion has been tested up to 1300 psi pressure without any difficulty. The testing and debugging of the torque actuator is presently in progress.

2. Specimen Length Adjustment, Tilting and Rotating Machines

Since the tilting of the model is required, natural choice here was to mount the adjustable C-frame (see Fig. 7) on a hollow cylindrical spindle, which will then rotate inside the spindle housing on two radial-thrust ball bearings. A worm gear (6 inch pitch diameter, single thread) is mounted at the back end of the spindle. The matching worm, which is mounted on the stiffener of the back plate of the immersion tank, will turn the worm gear causing the tilting (see Fig. 8).

In addition to tilting the model the worm and worm gear arrangement acts as a brake enabling one to hold the model at any tilted position without further holding arrangement. However, a locking arrangement has been built in for safety reasons.

The rotating of the model (rotation about z-axis) is accomplished by a ring worm gear (12 inch pitch diameter, single thread and machined into a ring) mounted on the outside of the load ring (see Fig. 9) which is turned by a matching worm mounted on the support ring anchor block. Again this worm and worm gear arrangement works as a rotary indexing device as well as brake resisting the torque applied by the torque actuator through the model. Since the worm is not easily accessible from the outside when the model is tilted to the horizontal position, a reversible gear motor (Bodine Type K, Model #733) is connected to the worm. This arrangement will allow one to rotate the model after tilting.

The height adjusting mechanism consists of a brass block riding on a one-inch diameter threaded rod which is rotated by a bevel gear and matching pinion. The drive shaft for the bevel pinion, and gear are placed inside the spindle and the threaded rod is hidden in the

rectangular-tube column.

The side plates of the support ring anchor block is bolted on to the brass block, which rides on the threaded rod. The brass block is guided by four cam rollers (McGill - CYR-1). The two wedges with the press down screws located in the support ring anchor block will clamp the support ring anchor block against the vertical column after the height adjustment is completed.

3. Load Measuring System

It was required that the axial load and torque applied to the model must be monitored excluding the influence of the friction in the hydraulic actuator. Strain gage transducers located at the exterior points of the hydraulic actuator can fulfill the requirements. It was then decided that the axial force strain gage transducer would be located in the load ring and the torque transducer would be positioned on spline-piston rod unit outside the hydraulic actuator but just below the loading platten connector.

The required outside diameter of the load ring of 11 inches and the required maximum axial load of 2,000 pounds made it impossible to adopt a commonly used form of axial load transducer - a hollow cylinder with appropriate wall thickness. With the above physical requirements, it was necessary to have the wall thickness of 1/16 inch or less in order to obtain a minimum acceptable sensitivity. Less than 1/16 inch wall thickness with 11 inch diameter ring would be very difficult to machine.

It was felt that the best approach would be to make the sensing elements of the transducer in the form of a beam subjecting the sensing equipment to bending stress due to the applied axial force.

In order to accommodate the sensing elements the load ring was cut into two rings, and the two rings were joined together by bolts with the curved beam (with 11" o.d. and 10" i.d. curvature) sensing elements between the rings. The load sensing elements will act as fixed end beams. It was necessary to undercut the edges of the rings across two perpendicular diameters to provide room for bolt heads and wrench. The loading sensing beam is shown in Fig. 9. Eight strain gages will be mounted, one on the top side and one on the bottom side of the sensing element and the strain gages will be connected to a full bridge circuit.

The torque transducer is the top straight shank portion of the spline-piston rod and four strain gages mounted at 45° with respect to the axis of the member will provide adequate sensitivity.

4. Model (or Specimen) Holder

It is not possible to provide one model holder that will work for all types of loading and all sizes and shapes of model to be used in the live-load loading frame. However, in the design of the unit it was intended to provide a basic and general attachment on which each user can mount a suitable holding device for a specific size and shape of chosen model. With this in mind, the lower end of the load ring was provided with six prongs equally spaced having a 8/16 UNC thread tapped hole through approximately the center of the prong.

A concentrated compressive load applicator is mounted on the load ring and is shown in Fig. 9. For example, a ten inch diameter 1" thick aluminum plate with either hexagonal or square opening of appropriate size having six 3/8 inch UNC tapped hole at midplane of the diameter will probably serve as a torque applicator. The hydraulic actuator end is provided with the loading button which can transmit torque and axial force simultaneously.

5. Immersion Tank

The immersion tank consists of two one inch thick steel plates at the base and back plate and three 3/8 inch thick glass plates. The glass plates will be fitted into the grooves at the bottom and the angle frames will support the top edges and the two vertical lines of joints.

The 7/16 inch wide grooves will provide the space for packing with Silastic adhesive (Dow Corning) which will seal against leaks and protect against glass breakage. The line of joints will also be sealed by the Silastic adhesive. The immersion tank will contain approximately twenty-five gallons of index matching immersion oil.

IV Concluding Remarks

This project is the first known attempt by anyone to design and fabricate a live-load loading frame for use in scattered light photoelasticity. Since the main emphasis was to design a compact and stiff system with small or negligible elastic deformation, many of the design problems faced by the designer were to devise a scheme or arrangement which would fulfill the function and meet the design criterion set forth for a particular part and then fit it in the available space. The partially assembled fixture is shown in Figures 10 and 11.

No efforts were made to minimize the total weight of the loading frame. On the contrary, heavier and thicker pieces of steel were

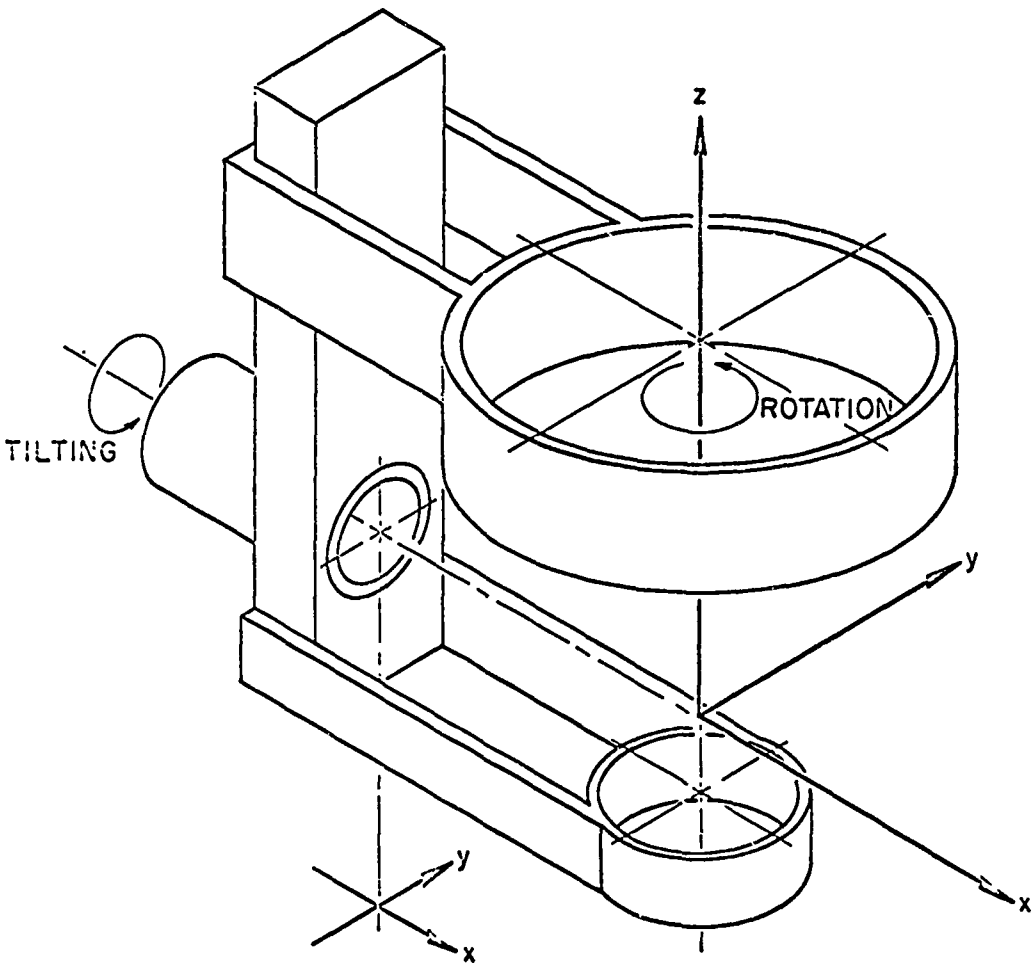

X-Y TRANSLATIONS ARE PROVIDED BY THE MILLING MACHINE TABLE.

FIGURE 1

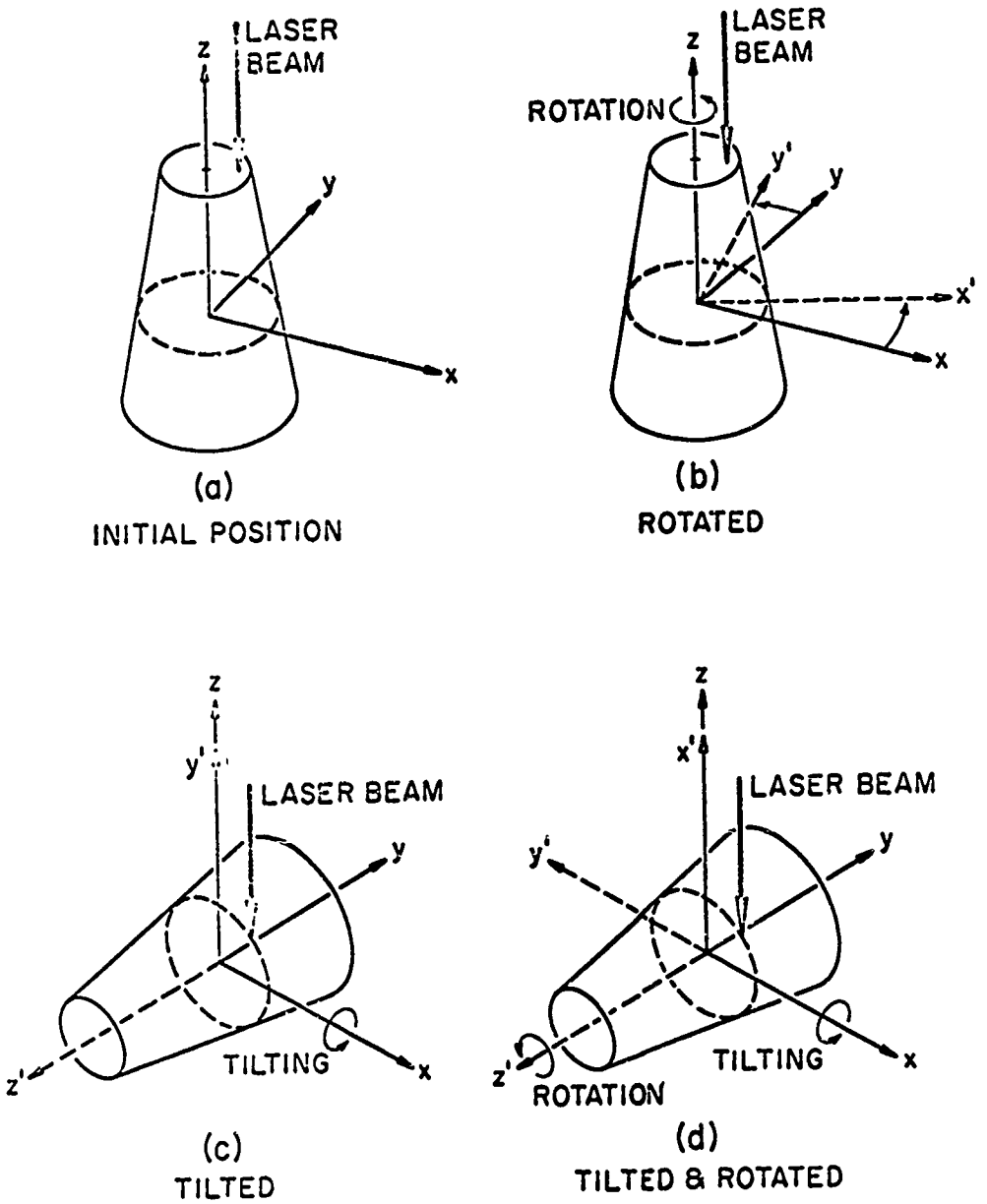
LASER BEAM
z
y
x
(a)
INITIAL POSITION
LASER BEAM
z
ROTATION
y'
y
x'
x
(b)
ROTATED
z
y'
LASER BEAM
y
z'
TILTING
x
(c)
TILTED
z
x'
LASER BEAM
y'
y
z'
ROTATION
TILTING
x
(d)
TILTED & ROTATED

FIGURE 2

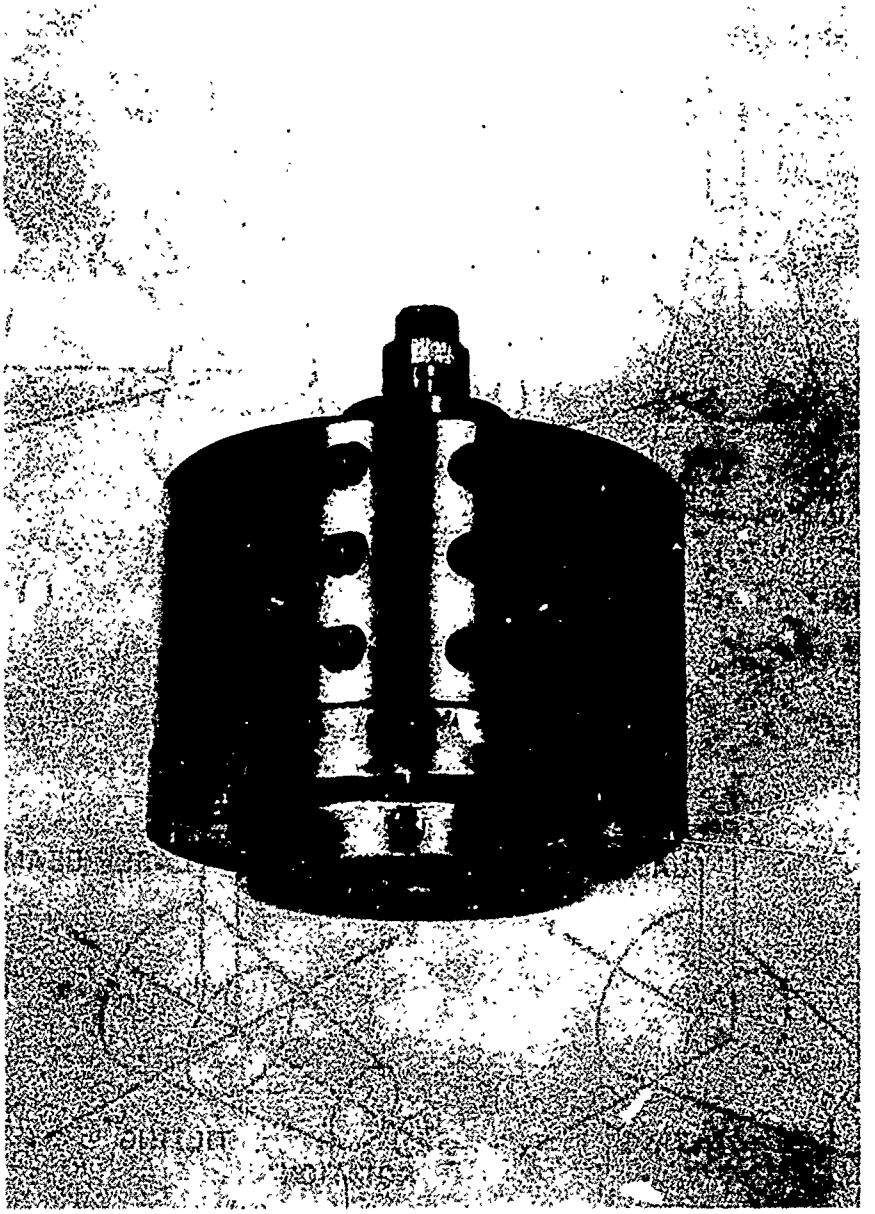

Figure 3 Ports for the axial load actuator and two ports for the torque actuator

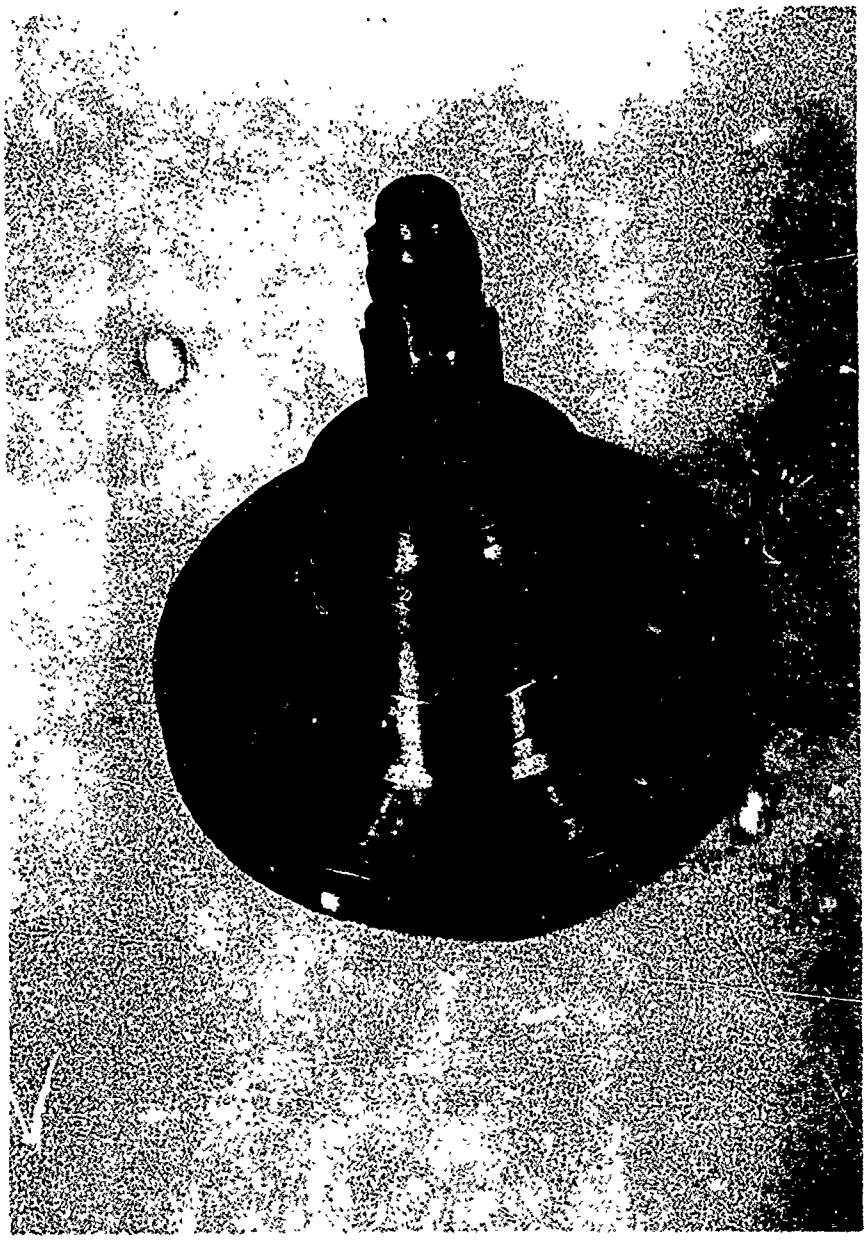

Figure 4 Exterior view of the axial load actuator on the base plate

Figure 5 Outer shell and axial load actuator next to the inside view of the torque tube

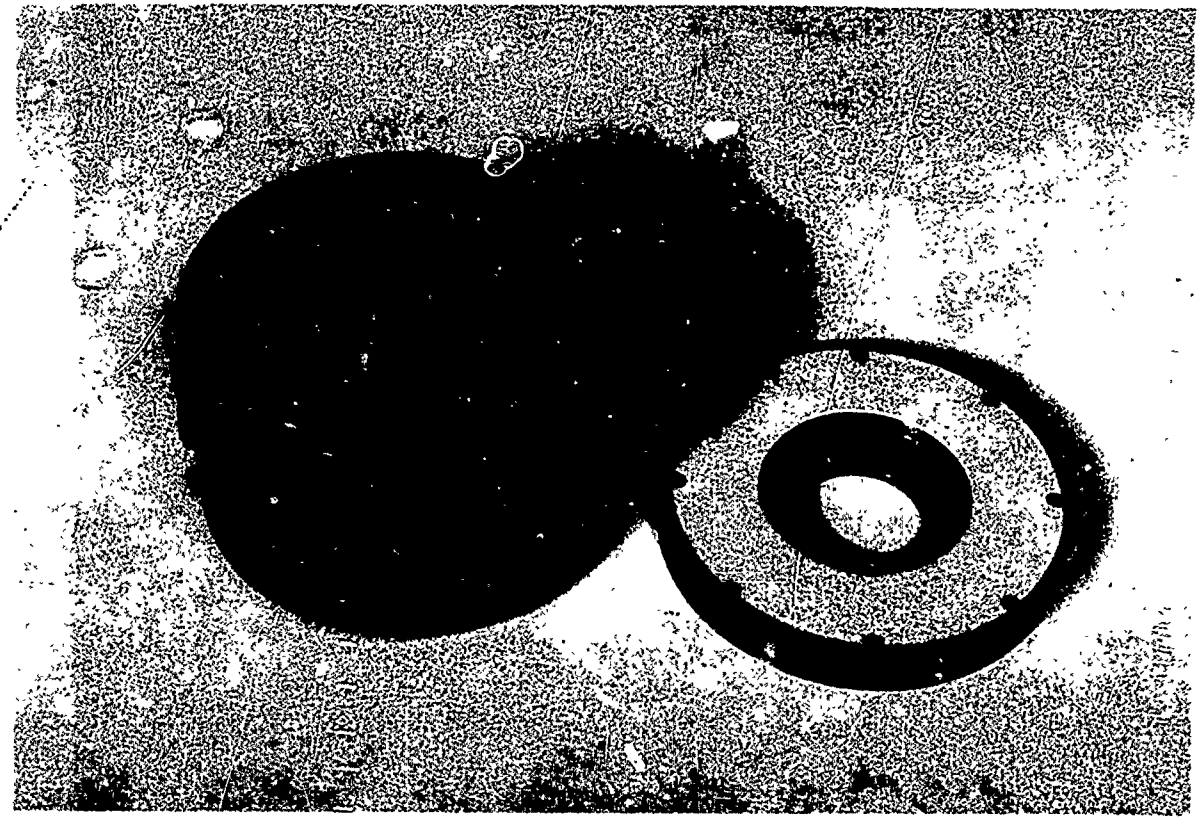

Figure 6 Assembled hydraulic actuator with the cover plate off

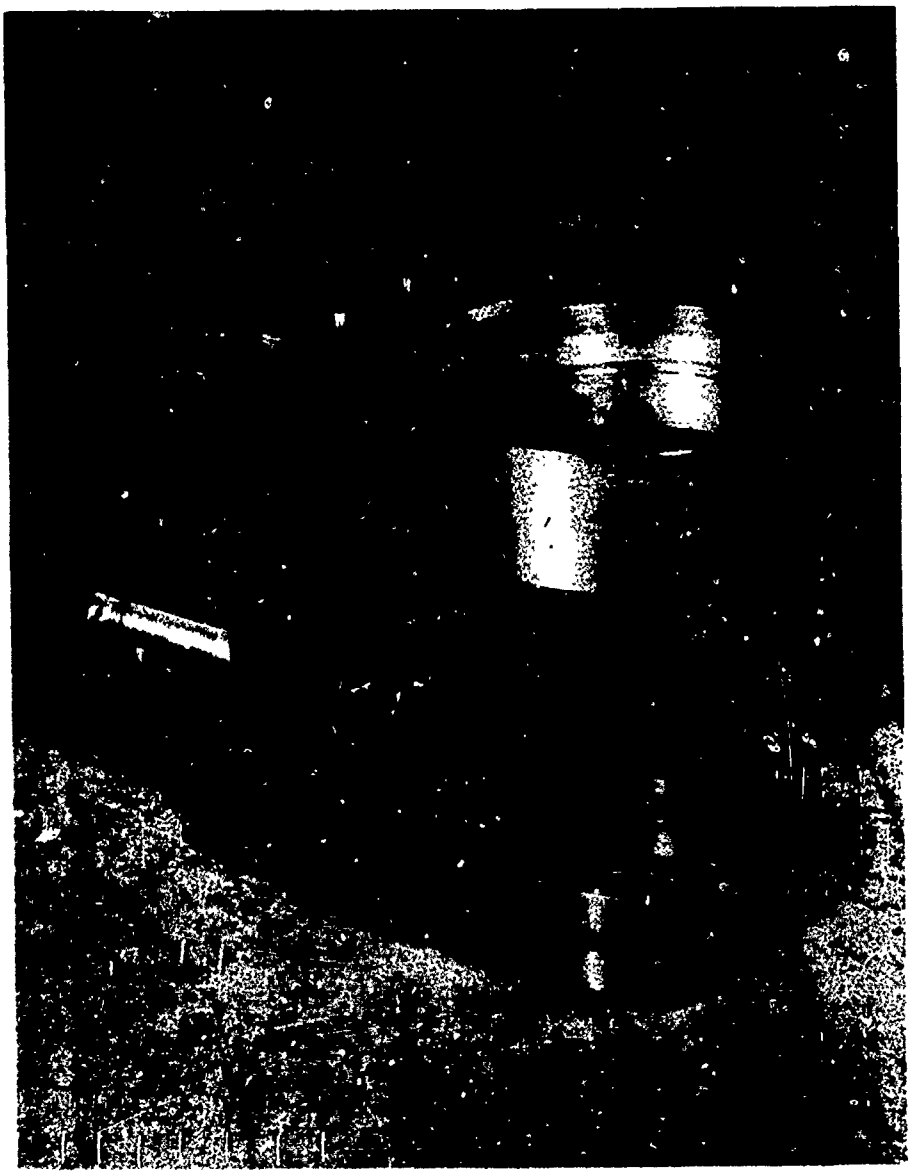

Figure 7 Adjustable C-frame

Figure 8 View behind the back plate showing the tilting mechanism and the end of the drive shaft for the height adjusting mechanism

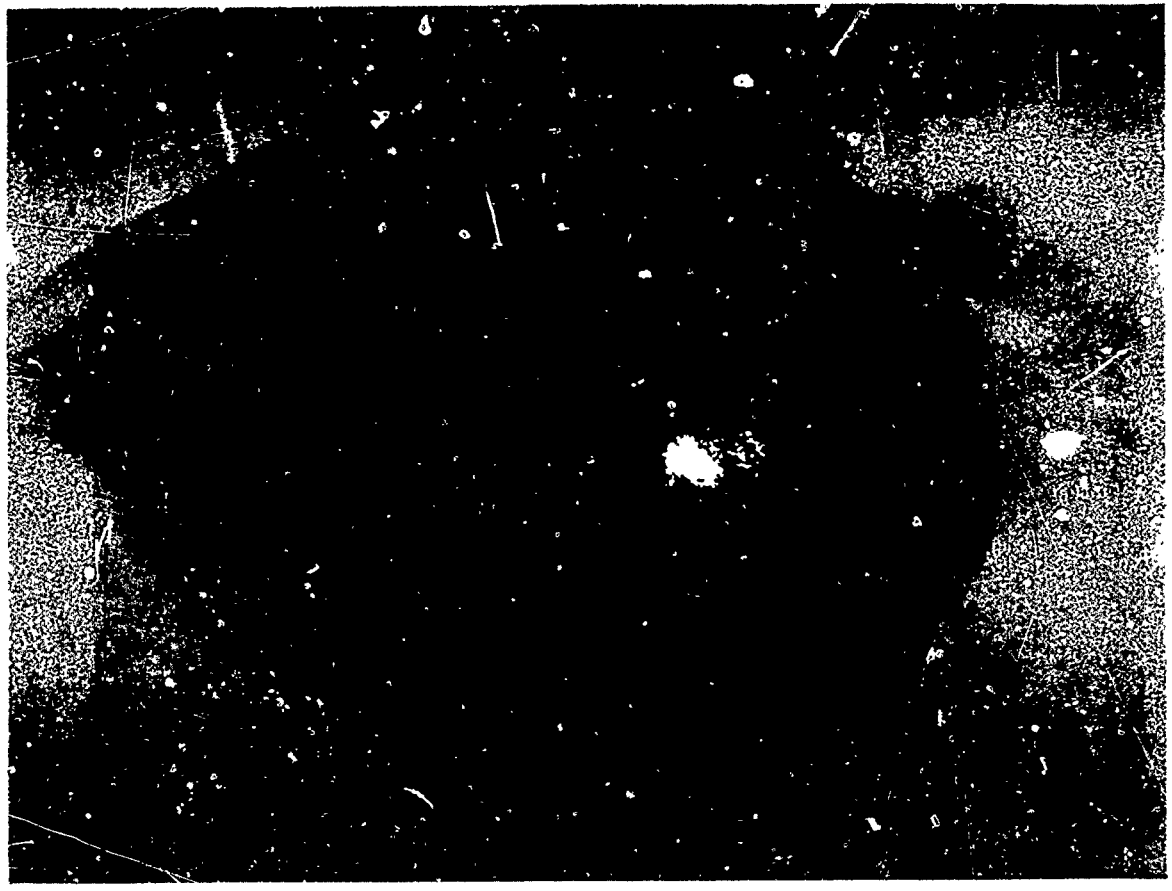

Figure 9 Upside down view of the load ring with the concentrated compression load applicator in the load ring.
One of the four axial load sensing element is also shown.

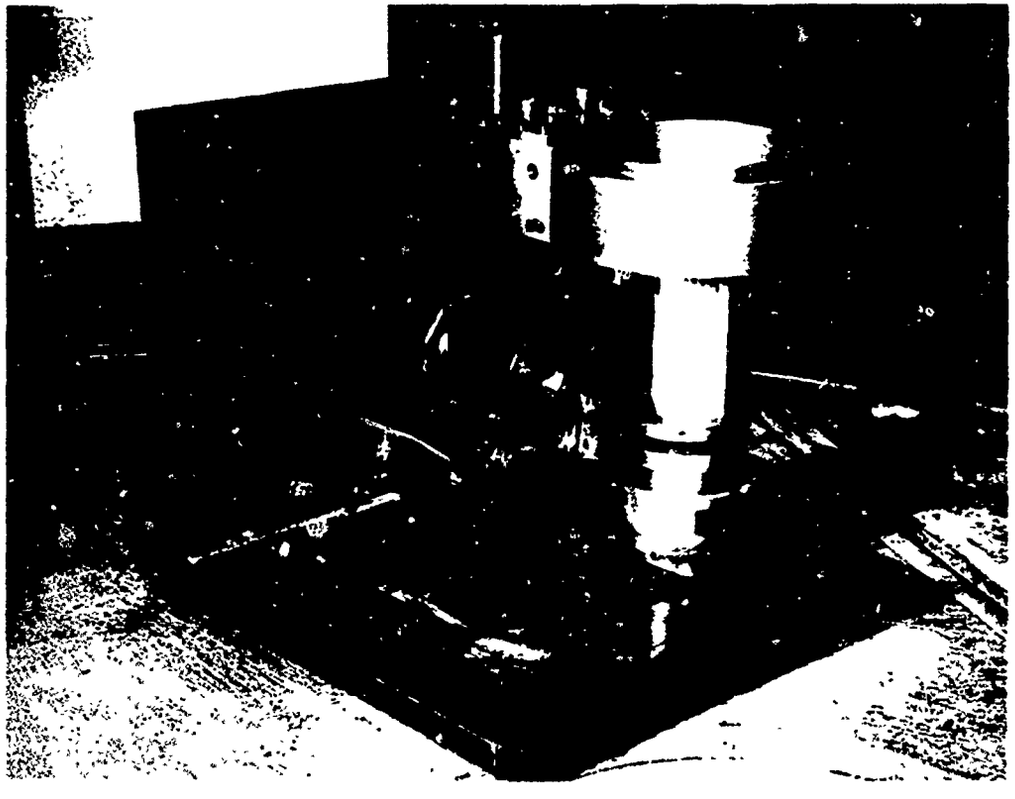

Figure 10 Partially assembled live-load loading frame with the model in up-right position. Three glass plates and the angle frame to hold the glass plates in place are missing.

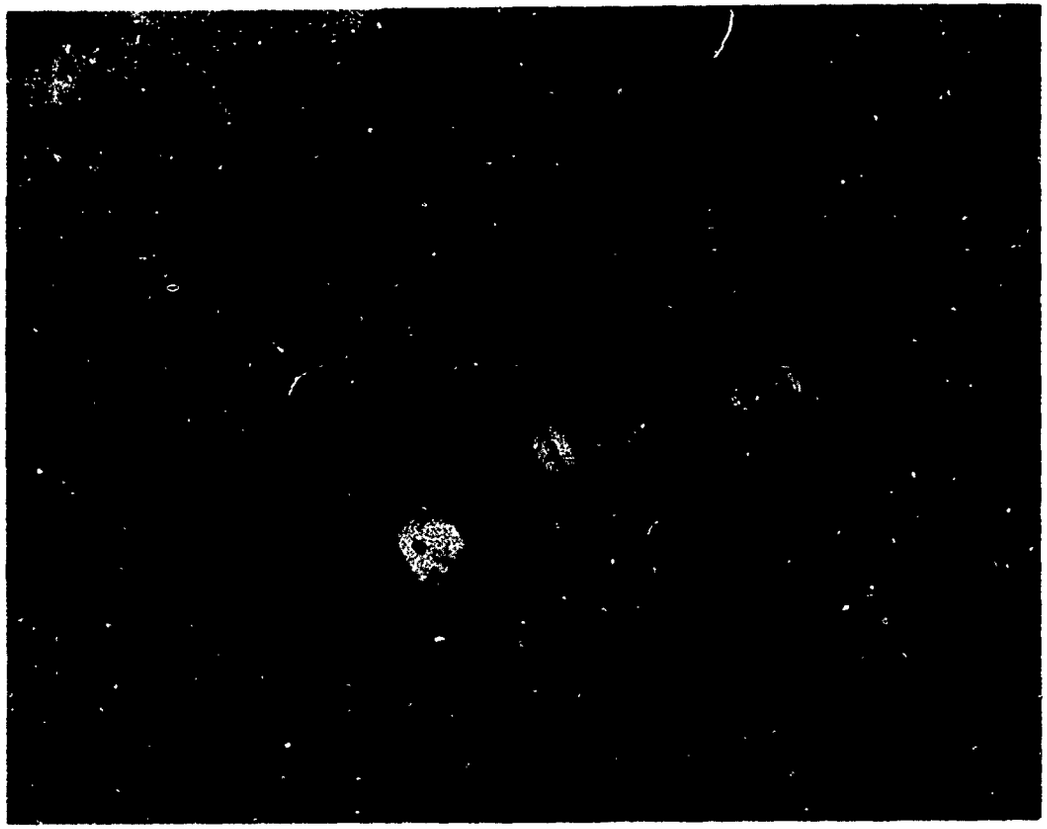

Figure 11 Partially assembled live-load loading frame with the model in tilted position.

chosen in order to obtain maximum stiffness whenever space permitted. For this reason only a few design calculations were made throughout the design. Design calculations made were for such items as the size of the sensing elements for the axial load and torque transducer, and pressures required for the hydraulic actuator, etc.

D. An Experimental Study of the Fracture Properties of Unidirectional Composite Materials

(Prof. T. P. Kicher and T. C. Esselman)

Introduction

The increased use of composite materials in structural applications has heightened the need for new design criteria and data, especially with regard to fracture mechanics. Composite materials, as with all other structural materials, have unavoidable inherent flaws which can cause catastrophic failure below the design stresses of the structure. Elimination of these catastrophic failures requires study and testing which will lead to a basic understanding of the failure mechanisms in composite materials. This understanding should complement design practice prevelant today based only on strength criteria. Although much work has been done on high strength metallic materials, the American Society for Testing and Materials sponsoring much of it, the applicability of the proposed testing recommendations has not yet been studied with respect to composite materials.

This study used the ASTM recommendations as a guideline and applied them to unidirectional glass fiber reinforced composites with an epoxy matrix. The stress intensity factors K were used for this work. Since the stress intensity factors in a unidirectional composite depend on the crack orientation, the orientations most interesting to designers are 1) the orientation in which flaws will most naturally occur, and 2) the orientation which will give the minimum crack resistance, or, in other words, the minimal value of the stress intensity factor. It is known that voids, through fabrication, tend to align themselves with the fibers, and that the minimum crack resistance occurs when the crack is aligned with the fibers. Therefore, the tests on the unidirectional composite were conducted with the crack in this preferred orientation.

The test used was the three point bend test. Isotropic analysis derived for this test was used to determine the stress intensity factors for the composite materials. A chevron notch with a fatigued crack was introduced into the specimen. During the test, a continuous plot of the applied load versus the brack opening displacement was recorded. This information was valuable in determining if linear elasticity applied to the specimens. The stress intensity factors for the unidirectional specimens were studied with respect to their

dependence on crack length, specimen thickness, rate of loading, and void content of the material.

2. Review of Theoretical Anisotropic Fracture Mechanics

Much of the work in analytical fracture mechanics has been directed to the stress and displacement distributions around finite cracks in continuous isotropic homogeneous materials. These analyses can be found in many references (for example, Reference 1). The elastic crack tip stresses in an anisotropic body has also been determined by several authors (2-8). Comparison of the stress states determined by the isotropic analyses and these determined by the anisotropic analyses leads to several conclusions.

The first is that the anisotropic stresses depend on the material constants while the relations for the isotropic media do not. The second similarity is that both solutions display a square root singularity of the order $r^{1/2}$. The third, and most important for this study, is that the parameter characterizing the crack size and the magnitude of the applied stress, the stress intensity factor, is defined in a similar manner for both the isotropic and the anisotropic case. Therefore, using stress considerations only, the strength of anisotropic bodies might be predicted in exactly the same way as isotropic bodies. The numerous solutions that have been generated for stress intensity factors for isotropic materials could be applied to anisotropic materials. However, Wu (9) points out that the displacement states in the anisotropic materials cannot be so easily compared to those from the isotropic materials. In general anisotropic materials, crack sliding accompanies crack opening, even in the case of a center crack plate with tension perpendicular to the crack at infinity. However, if a special crack orientation is used, namely, if the crack is oriented in one of the material principal directions, this inconsistency is eliminated. Wu (9) also points out that when the crack is oriented in one of the directions of elastic symmetry, the critical stress intensity factor should be either a maximum or a minimum. These cases are of the most practical interest. Therefore, the conclusion can be made that only when a crack is oriented in one of the material principal directions, can the isotropic analysis available be applied to an anisotropic plate.

The standard boundary collocation solution for an edge crack in a three point bend specimen was used to determine the stress intensity factor for the finite specimen. This is

$$K = \frac{3\,PL\,\sqrt{a}\,Y}{B\,W^2} \qquad (7)$$

where

$$Y = 1.93 - 3.07\,(a/W) + 14.53\,(a/W)^2 - 25.11\,(a/W)^2 + 25.80\,(a/W)^4 \,. \qquad (8)$$

K is the stress intensity factor, P is the applied load, L is the half length of the specimen, a is the crack length, B is the thickness and W is the depth of the specimen, and Y is the K calibration figure. However, the stress function used in the boundary collocation corresponding to the stresses existing at the tip of a crack in an isotropic homogeneous material. Therefore, the results from that boundary collocation procedure do not apply to the specimens in this study. However, since the stresses that exist at the tip of a crack in an orthotropic or anisotropic material are much more complicated, the collocation procedures have not yet been applied to these materials. Therefore, the results from the isotropic boundary collocation procedure will be used in this study. The analytical stress analyses also assume a homogeneous anisotropic solid to exist. However, since this study is considering only macrofracture properties, the composite, although microscopically heterogeneous, may be assumed homogeneous on the macro scale. Of course, a fairly uniform fiber packing density is necessary to make this assumption.

3. Experimental Determination of Fracture Properties

The experimental program was designed to characterize the fracture properties of glass fiber reinforced epoxies with respect to material and specimen variables. In order to achieve this goal, several things had to be accomplished.

(1) Specimens with suitable properties had to be fabricated and methods for characterizing material properties devised.

(2) Methods had to be found to prepare the specimens so that apparently "natural" cracks could be formed.

(3) Test procedures had to be adapted and analysis previously discussed applied.

Specimens for these tests were cut from either eight inch by eight inch or twelve inch by twelve inch fiberglass plates with thicknesses ranging from 0.100 to 1.00 inches. The plates were fabricated from 3M Scotchply* preimpregnated glass Type 1002 of either eight inch or twelve inch width.

---

* 3M Company, St. Paul, Minnesota.

The plates were fabricated by three different methods: 1) in a heated platen press, 2) in a heated platen press with the material and mold vacuum bagged, and 3) in an autoclave. Higher quality plates were sought using the second two methods of fabrication, but as the thickness of the plate became large (0.5 inch) the effect of the vacuum decreased. The vacuum was effective in removing voids for only thin plates. All methods were designed to achieve a constant fiber volume, which is controlled by the cured thickness per ply.

The material was characterized by determining the resin content, fiber content, and void content. The fiber and resin content by weight are found by using a resin burn-off technique in a muffle furnace at 800°F. The void content can then be related to these fiber and resin contents and the laminate specific gravity, which was determined by weighing the laminate suspended in water. The specific gravities of the pure resin and fiber must also be known. After the determination of the void content, the fiber and resin contents were converted to contents by volume.

The specimens needed for the three point bend test were rectangular beams with a chevron notch machined in one edge. The fiber configuration was unidirectional with the fibers aligned with the crack direction. The chevron notch facilitates introduction of a fatigue crack into the specimen. A cantilever beam type of fatigue machine was used to form the crack. The peak-to-peak displacement was varied to allow the cyclic stress to be varied. The crack was observed as it grew by placing a solution of ethylene glycol and black India ink at the tip of the chevron notch. This mixture follows the crack as the crack grows in the notch. To elminate any effect of the machined notch, the crack was allowed to grown past the end of the notch. Figure 1 shows a view of the chevron notch with a crack completely fatigued into it.

The initial crack length is necessary for the determination of the stress intensity factors. These are measured visually after fracture. The solution of ethylene glycol and black India ink that was injected into the crack to facilitate observing the fatigue crack also marks internally the distance the crack propagates during fatigue. The ink solution is allowed to dry before testing so that a permanent record remains. Figure 2 is an end view of a fracture surface showing the initial crack length markings.

The notched bend test was chosen for this study for several reasons: (1) the test requires a small amount of material in comparison to a center or edge crack tensile specimen, (2) the load requirement is very low, in a bend test high stresses can be attained with low applied loads, (3) the ASTM (14) has recommended the bend test as a standard for high strength metallic materials, adaptation of these recommended practices to composite materials would be important. An overall view of the test fixture with a specimen and

Figure 1. Specimen Showing Fatigue Crack (7x)

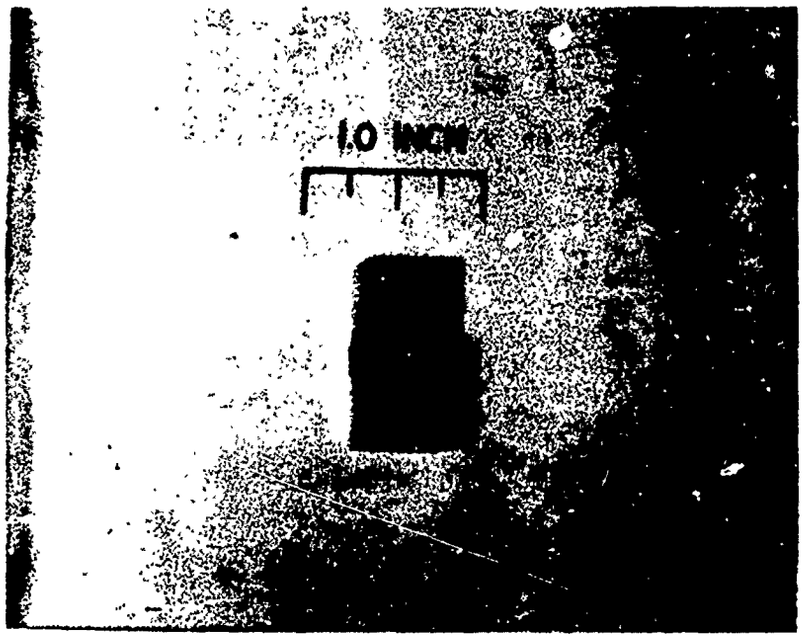

Figure 2 . End View of Fracture Surface Showing Initial Crack Length

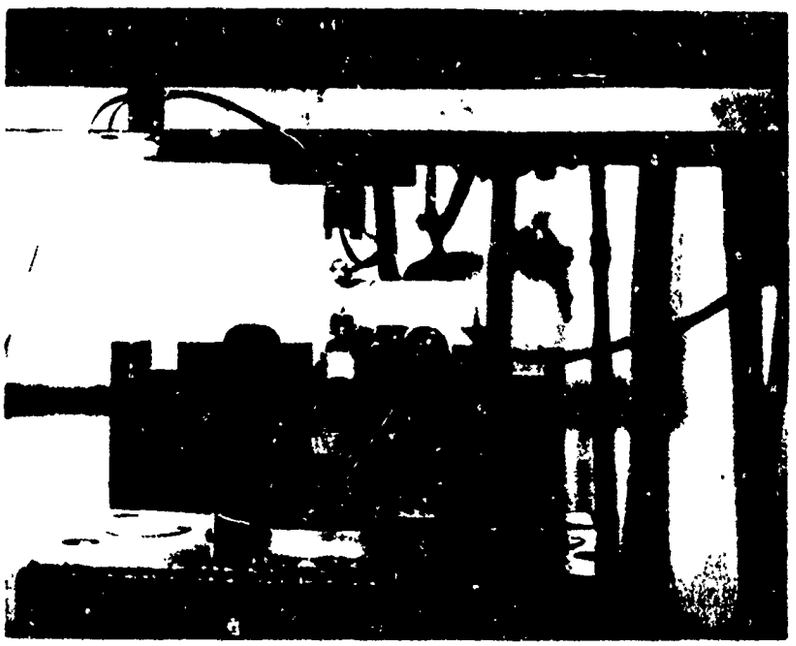

Figure 3. Fixture for Three Point Bend Test

load cell in place is shown in Figure 3. Also note in this figure the displacement gage attached at either side of the notch. It is made up of two cantilever beams and a spacing block. Strain gages are positioned on either side of each beam close to the spacing block. The transducer is attached to the specimen by means of knife edges which are tightly secured to both sides of the notch.

To conduct a satisfactory test, a record of the applied load versus the crack opening displacement is necessary. The amount of displacement per unit load should remain constant as long as the effective crack length remains constant. Therefore, the load-displacement record should be linear as long as there is no change in the effective crack length. The linearity of the load-displacement plot will help determine the validity of the test for determining the plane strain fracture toughness.

Two stresses will be mentioned in the results and their definitions must be made clear. The field stress is the stress that would exist at the crack location if the crack were not there, i.e. if the beam were solid. The nominal stress is the stress that exists at the tip of the crack excluding stress concentrations. Both stresses are found using simple beam theory.

Further details of the experimental procedure can be found in Reference 13.

Results

The most important results of these tests are displayed in Figures 4 to 12. The depth of all specimens was nominally 1.0 inches, and the displacement loading rate was 0.100 inches/minute, except when noted otherwise. Specimens were tested in groups, each group having similar material properties and similar specimen thicknesses. The crack length to specimen depth ratio, a/W, was varied from extremes of 0.167 to 0.765. Except in cases when the crack to depth ratio variation was of primary interest, a/W generally was around 0.5. When the stress intensity factor was plotted against a parameter other than a/W, the stress intensity factors were normalized to a constant a/W equal to 0.5. Figure 4 shows the critical value of the stress intensity factor, K_C versus the specimen thickness for all tests with a/W = 0.5. Each data point represents a group of four to nine specimens. The numbers represent the test series number and the corresponding material information is given in Table 1. Figure 4 looks similar when a/W = 0.3 or a/W = 0.7. The field stress was plotted as a function of the crack length ratio for varying thicknesses in Figures 5 to 8. A log-log plot was used and the line slope is noted in each case. Figure 9 shows the dependence of the nominal stress on the specimen thickness for all tests normalized to a/W = 0.5. The yield stress of the

material found by Koeneman (12) is marked by a dotted line. The effect of the void content is shown in Figure 10 for different thicknesses. Figure 11 demonstrates the dependence of K_C on the cross head speed. Figure 12 gives representative load-crack opening displacement curves for thicknesses of 0.1, 0.3, 0.5, and 1.0 inches.

TABLE I MATERIAL PROPERTIES AND SUMMARY OF RESULTS

Specimen Set	B(in)	Percent Content by Volume			Normalized
		Fiber %	Resin %	Void %	K_C(ksi - $\sqrt{in}$)
6219,6229	0.097	44.1	46.4	9.5	1.10
9100	0.102	43.2	55.7	1.0	1.52
9170	0.105	43.2	56.7	0.1	1.64
6239,6249	0.200	46.6	47.8	5.6	1.50
7149	0.292	45.3	48.0	6.7	1.85
9208	0.294	47.0	49.6	4.4	1.99
9110	0.294	41.9	51.7	6.4	1.96
9168	0.391	45.0	49.0	6.0	2.00
1210	0.411	43.1	54.3	2.6	2.06
1120	0.387	43.4	45.6	5.0	1.97
8169	0.485	43.0	47.9	9.1	1.95
8238	0.494	45.7	52.1	2.2	2.02
9120	0.493	41.4	50.9	7.7	2.09
3170	0.989	44.1	52.2	3.7	2.50
9130	0.988	41.6	52.4	6.0	2.25

Discussion

In the experimental study of the unidirectional specimens, several interesting phenomena emerged. Recall that in metals, a state of plane strain is necessary in the specimen to assure a valid fracture toughness test. A measure of this is the absence of appreciable plastic deformation at the crack tip. There are several ways of assuring this. The load-crack opening displacement curve must be linear. A square root singularity must exist. The nominal stress at the crack tip must be less than the yield stress of the material. The stress intensity factor must be a minimum and independent of specimen dimensions. Generally speaking, for metallic materials,

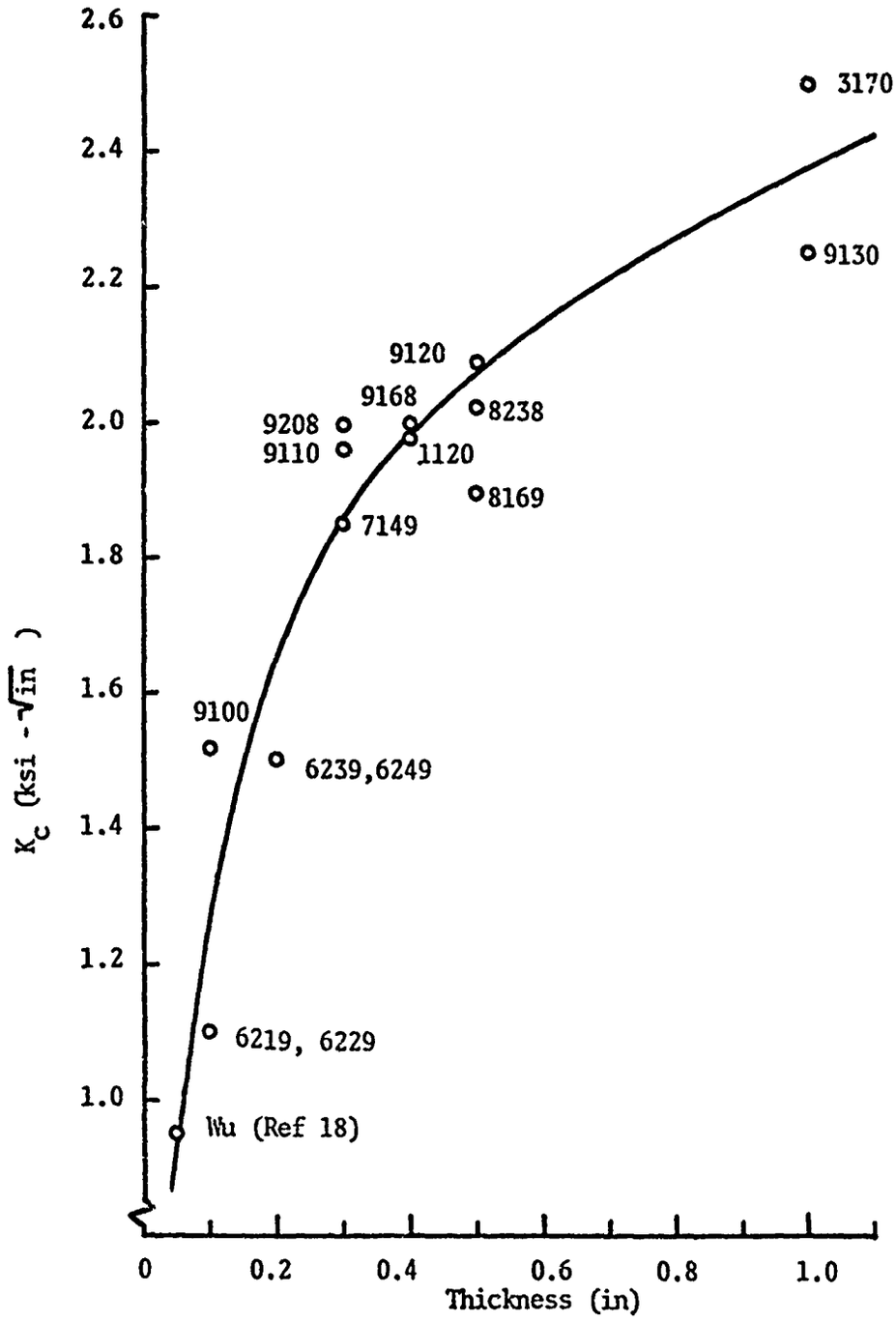

Figure 4. Influence of Specimen Thickness on Stress Intensity Factor, Crack Length Ratio = 0.5

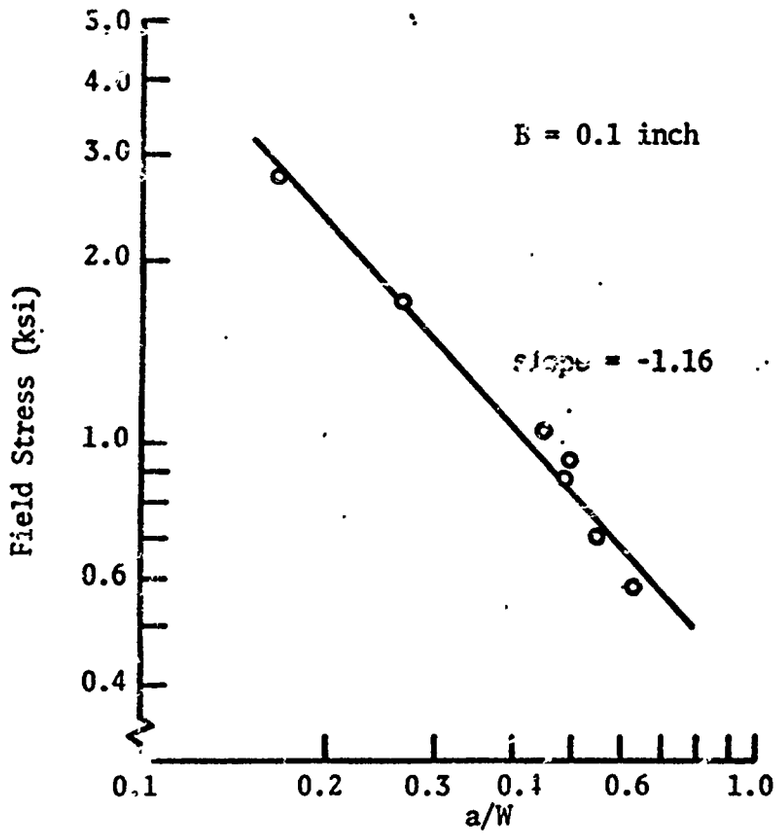

Figure 5. Influence of Crack Length Ratio on Field Stress, Specimens 9100, Thickness = 0.1 inch

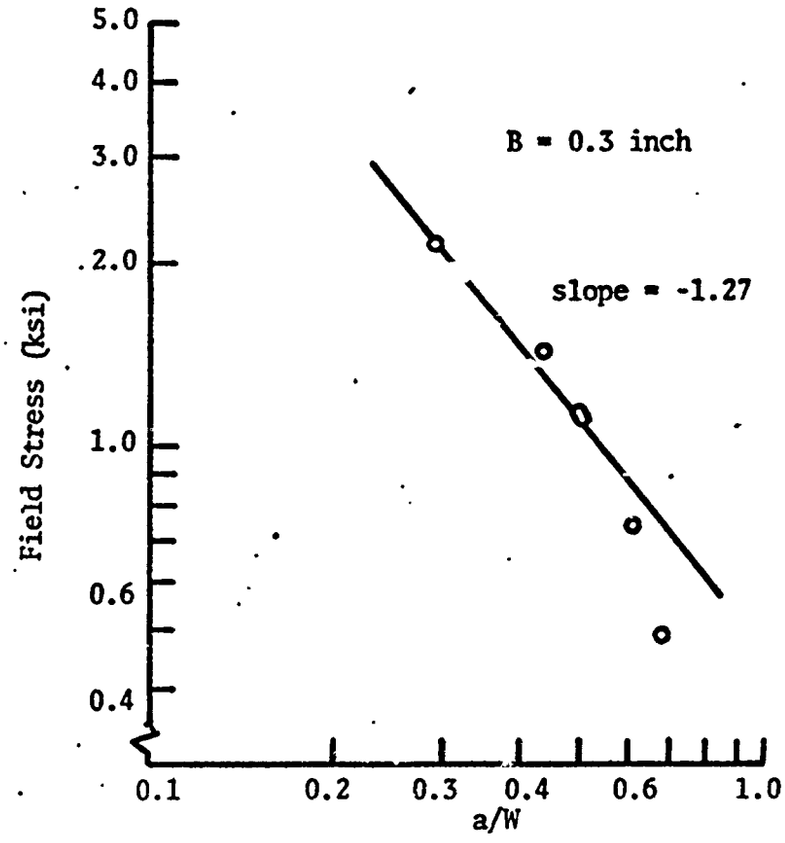

Figure 6. Influence of Crack Length Ratio On Field Stress, Specimens 9110, Thickness = 0.3 inch

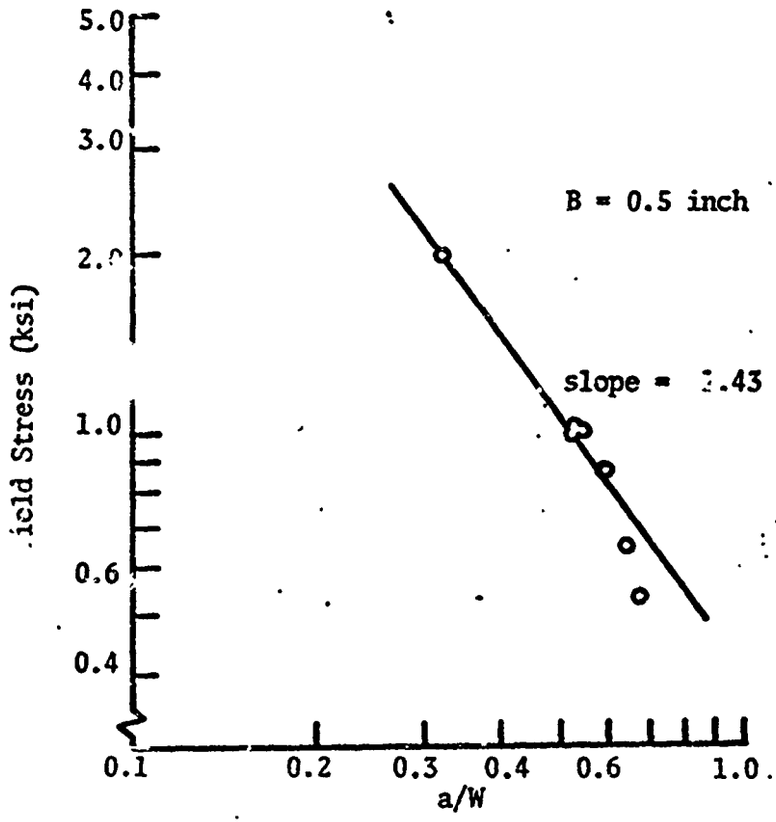

Figure 7. Influence of Crack Length Ratio on Field Stress, Specimens 9120, Thickness - 0.5 inch

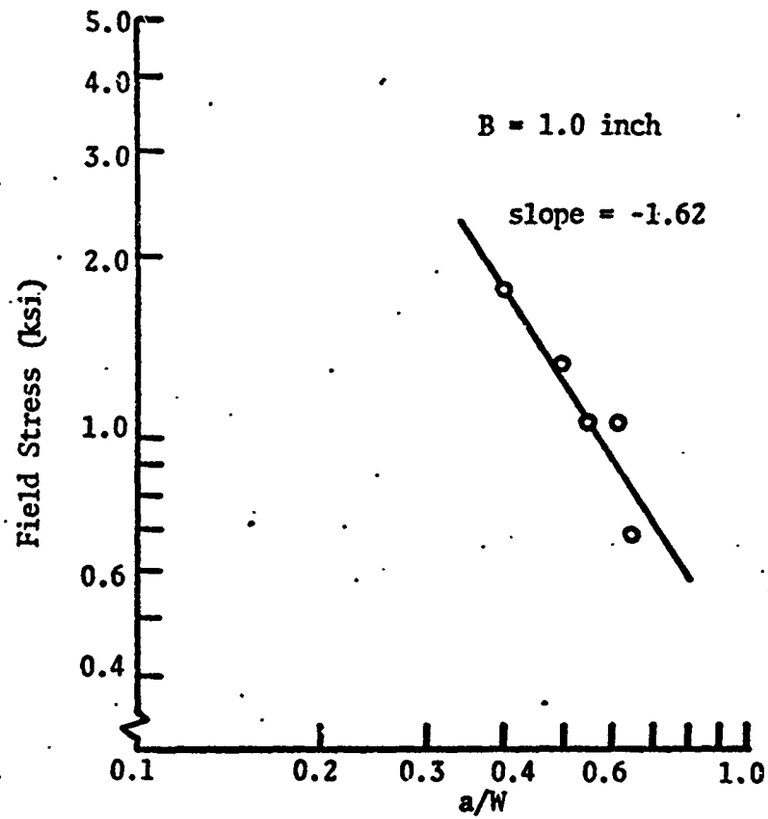

Figure 8. Influence of Crack Length Ratio on Field Stress, Specimens 9130, Thickness = 1.0 inch

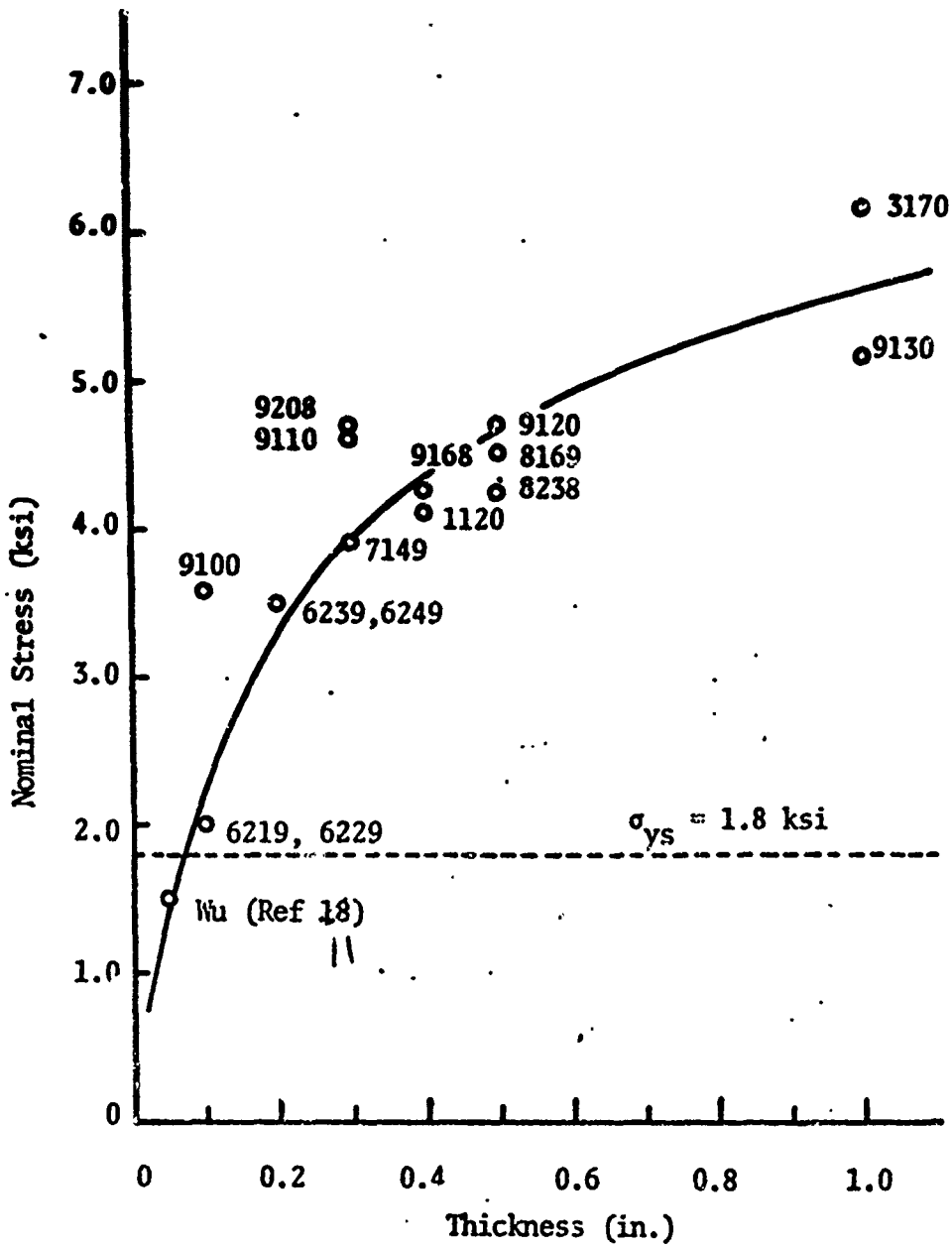

Figure 9. Influence of Specimen Thickness on Nominal Stress for all Specimens, Crack Length Ratio = 0.5

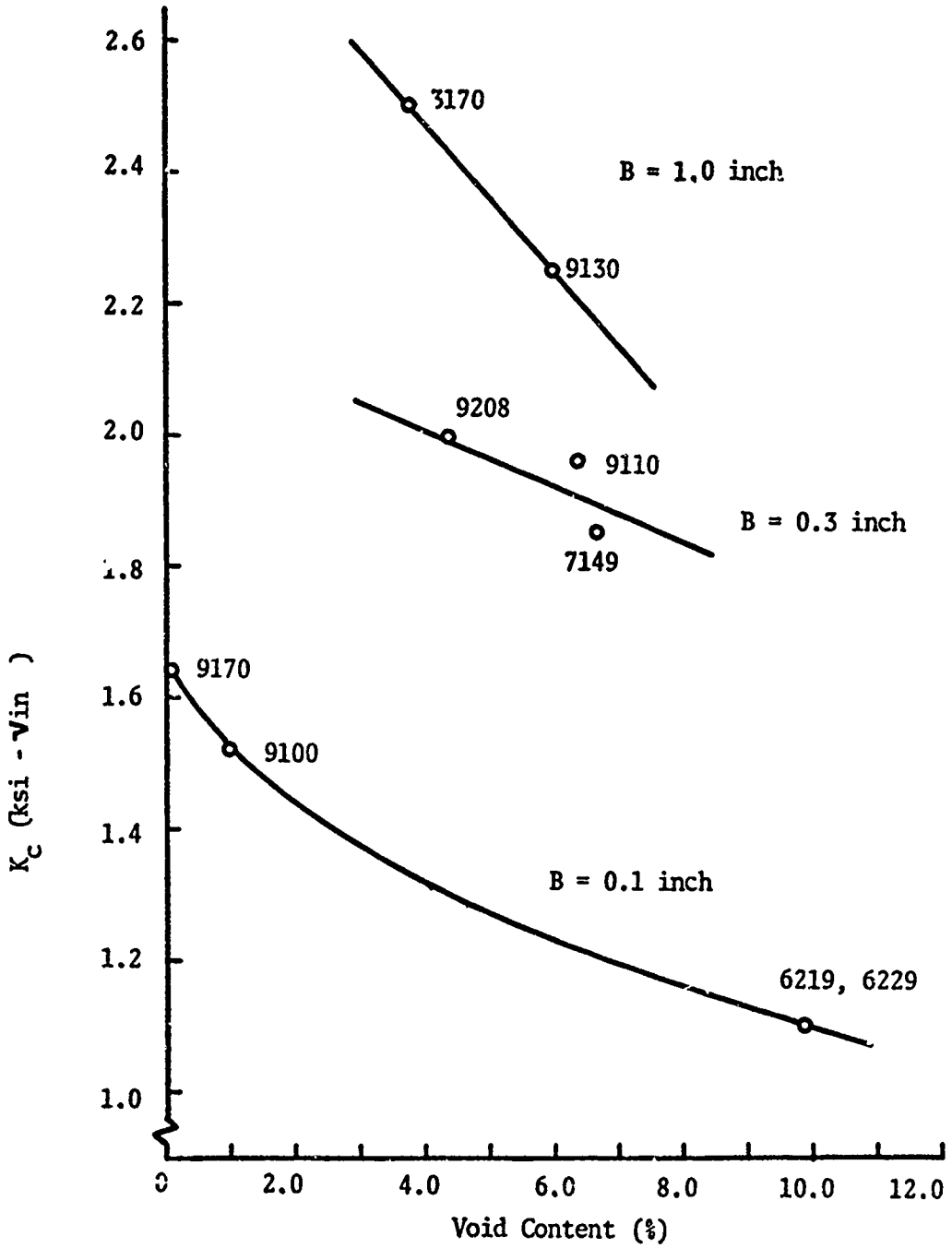

Figure 10. Influence of Void Content on Stress Intensity Factors for Various Thicknesses

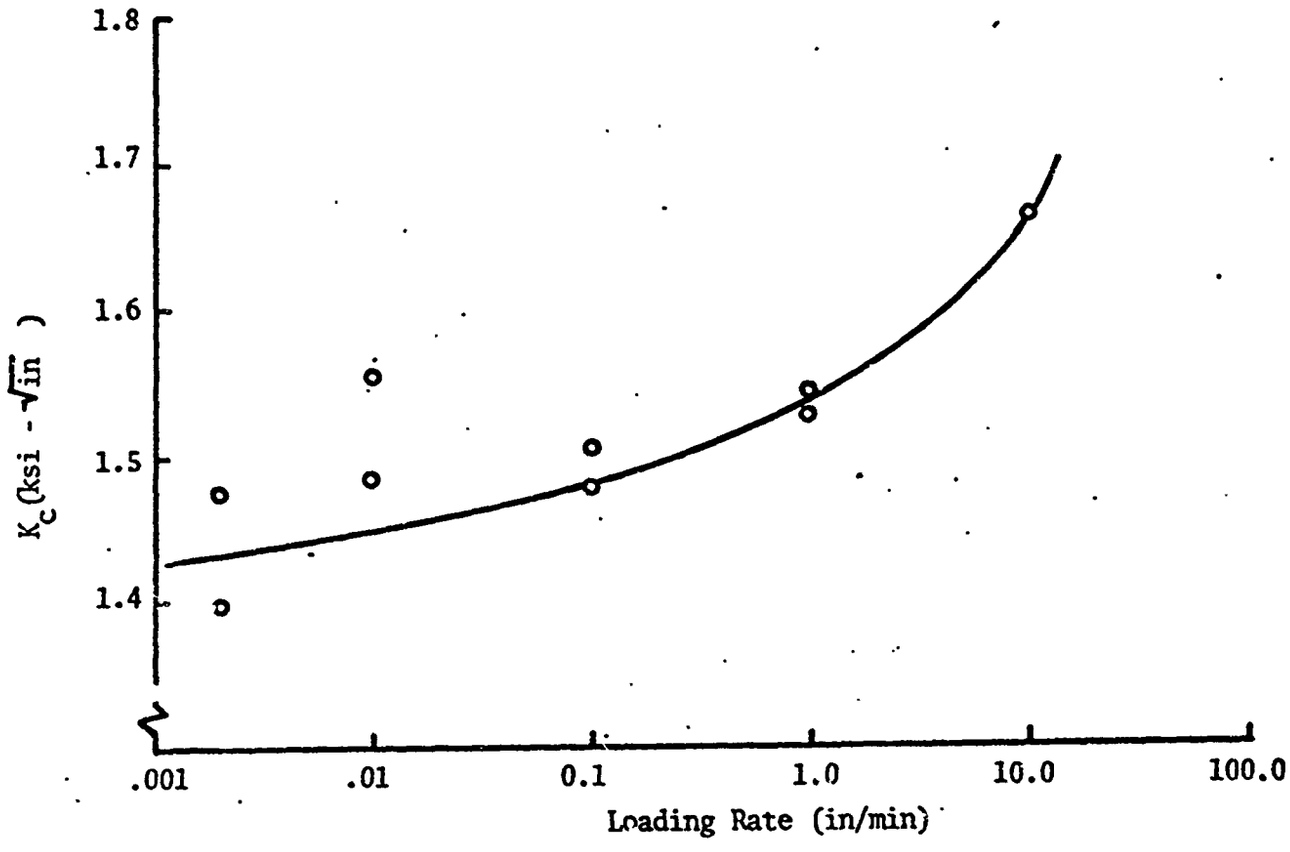

Figure 11. Influence of Loading Rate on Stress Intensity Factor, Specimens 8249

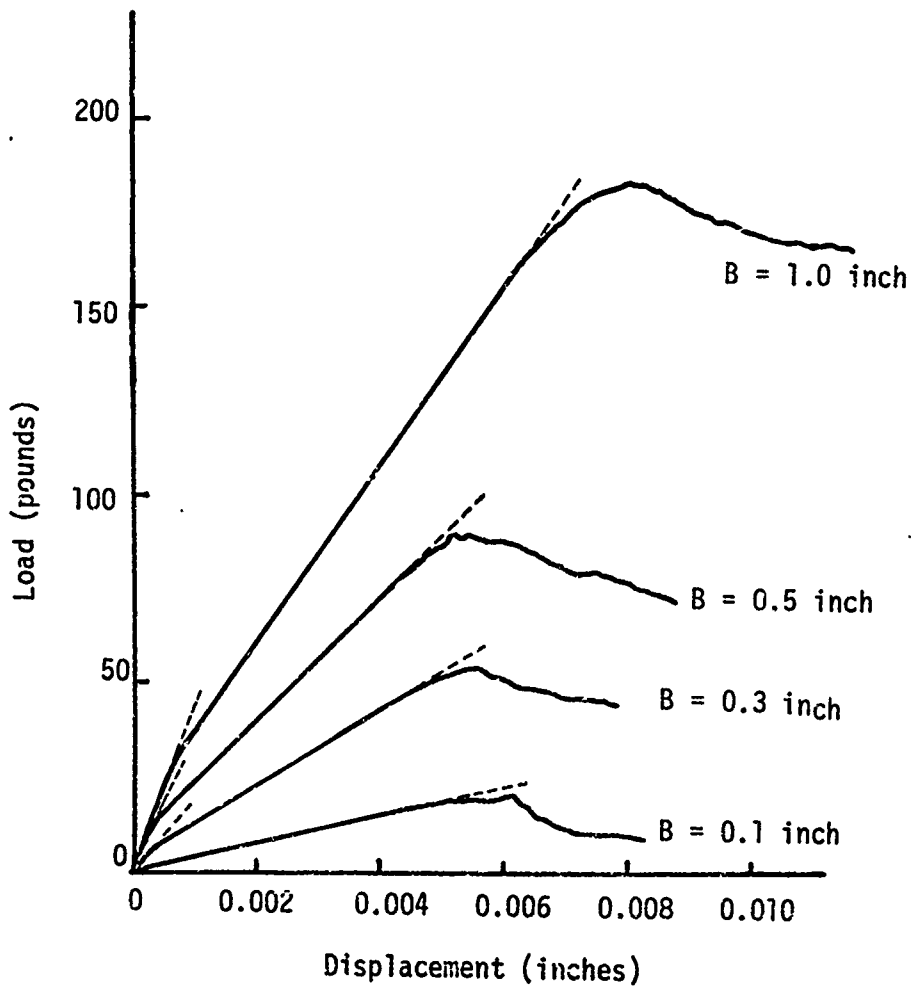

Figure 12. Load-Crack Opening Displacement Curves for Specimens with Varying Thicknesses

these phenomena are true as the thickness of the specimen increases. This does not appear to be true for composite materials.

The load-crack opening displacement records plotted during the test provide a method for evaluating the state of stress at the crack tip. Figure 12 gives representative records for specimen thicknesses of 0.1, 0.3, 0.5, and 1.0 inches. Note that for the 0.3, 0.5, and 1.0 inch specimen a rather large change of slope occurs at approximately 20% of the maximum load. Following this "knee" the record returns to a linear response. It is believed that this change of slope is not due to a change in the material but to a phenomena occuring in the fixture; possibly it could be attributed to the specimen seating itself on the rollers. A similar change of slope is often noted early in the load-displacement record for metallic specimens. It is generally very small, though.

This change of slope is accentuated for the composite specimens since the loads are very low. If the linear region past the "knee" of the curve is assumed to be the actual material linear elastic region, the change of slope between the original tangent line and the slope of the line passing through the maximum load can be calculated. For the specimen thickness of 0.1 inch, the slope decreases 18%; for the 0.3 inch specimen, the decrease is 9.5%; for the 0.5 inch, it is 8%; and for the 1.0 inch, it is 8.5%. The load level for the 0.1 inch specimen is low enough that the fixture nonlinearity could possibly correspond to the material nonlinearity so that for those specimens, the slope change of 18% cannot be solely attributed to material nonlinearities. The specimens with width of 0.3, 0.5, and 1.0 inches come close to satisfying the linear elasticity requirements; the results for the 0.1 inch specimen is inconclusive. Because of this question the maximum loads were always used for calculation of the stress intensity factors.

Another phenomena which indicates the presence of linear elastic deformation is the square root singularity. A plot of the log of the field stress versus the log of the crack depth should have a slope of -0.5 as determined from the relations in Chapter 2. Figures 5 to 8 shows these graphical relations for various widths. A plot of the slope of these lines as they depend on the specimen thickness is given in Figure 13. Note that as the specimen thickness decreases from 1.0 to 0.1 inches the slope decreases from -1.62 to -1.16. This is not yet close enough to -0.5 to allow linear elasticity, but the trend indicates that the 0.1 inch specimen is closer to satisfying the requirement of the square root singularity than the larger thickness specimens. In fact, Wu and Reuter (11) found that for 0.05 inch center crack tensile specimens, the square root singularity was satisfied. This might indicate that the thinner specimen comes closer to satisfying the requirements of linear elasticity.

There are two thickness requirements which must be satisfied for a valid fracture toughness test. One is that K_c be a minimum and

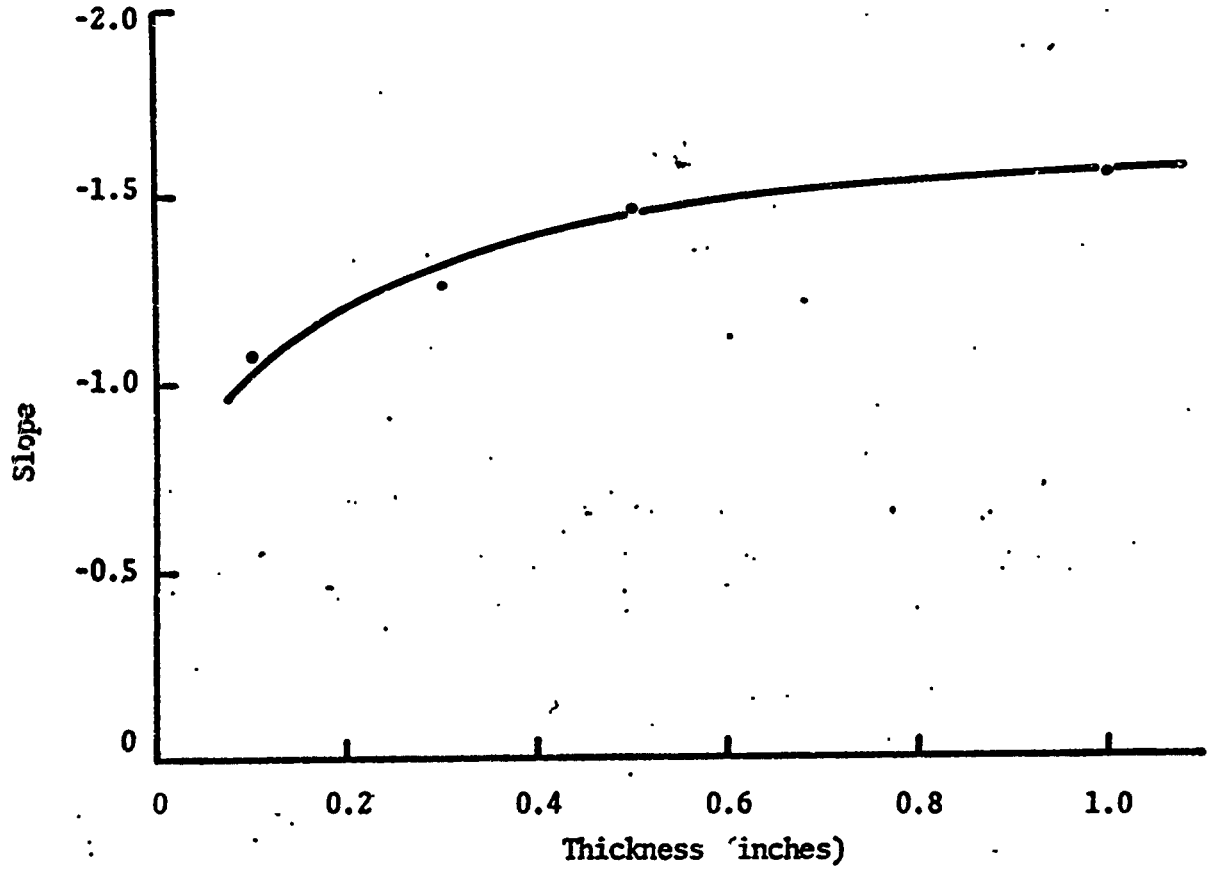

Figure 13. Influence of Specimen Thickness on the Slope of the Log Field Stress versus Log Crack Length Ratio Curve

unvarying under specimen thickness change, and the other is that the thickness be such that the nominal stress is less than the yield stress of the material. In metals, both of these requirements are satisfied for thick specimens. The reverse appears to be true for unidirectional composites.

Figure 4 is a plot of the stress intensity factor as a function of the specimen thickness. The point for 0.05 inch thickness was determined by Wu and Reuter (11) for a center cracked tensile plate in tension. The data was normalized to a crack to depth ratio of 0.5 but the void content varies. Note that as the thickness increases, the crack resistance increases, while in metals, the opposite is true. This indicates that the thin composite specimens give a value of stress intensity factor which, if used for design, will give conservative results. Thick metallic specimens in the plane strain state give similar conservative design results.

The nominal stress and its dependence on thickness is plotted in Figure 9. Note that the nominal stress decreases as the specimen thickness decreases. While for the thinnest specimen (0.1 inch) tested in this study, the nominal stress is still above the yield stress, it is approaching the yield value and the point attributed to Wu (18) is in fact below the yield point. Therefore, the conclusion can again be made that thin specimens better the criterion for linear elasticity.

Voids in the composite material decrease the energy necessary to propagate a crack, and therefore, decrease the value of the stress intensity factor. A plot of this relation is shown in Figure 10 for varying specimen thicknesses.

There are two possible reasons for the decrease in stress intensity factor for an increase in void content. It is unlikely that these are independent. One is that the voids act as stress concentrations. It is known that the voids are long and circular in shape. This gives a small radius at the ends which tend to raise the stress level several times. This would, in effect, increase the stress level at the tips of the crack and cause failure at a significantly reduced load.

The second possible reason that the stress intensity factor drops is, simply, that there is less material in the high void content specimen than there is in the low void content specimen. This would give the low void content material increased strength, and in this instance, increased resistance to crack propagation. As was mentioned, this probably does not work independently of the stress concentration argument, but a combination of both lead to the decrease in stress intensity factor.

The loading rate had an expected effect on the stress intensity factor. In most engineering materials, a higher strength accompanies

an increased loading rate. This was the case in this study where an increase from .001 inches/minute to 10 inches/minute gave an increase of 35%. The distribution is shown in Figure 11.

SECTION V

ANALYSIS AND DESIGN OF COMPOSITE STRUCTURES

Four studies were conducted to advance the analysis and design capabilities for composite material structures. A displacement method of analysis for laminated composite plates subjected to membrane compression, lateral pressure and temperature variation, was developed for subsequent use in a minimum weight design study. The analysis includes the effects of large displacements and represent an extension of work completed earlier in the program.

An approximate method for predicting the ultimate load carrying capacity of laminated plates loaded beyond the point of buckling is developed based on an extension of the Von Karman effective width concept. The method is verified by an extensive experimental program. In a related program, the effects of circular cut-outs with and without reinforcements are studied. Both analytical and experimental results are obtained.

The closed form exact solution was obtained for the buckling of laminated anisotropic cylindrical shells subjected to any combination of axial compression, lateral pressure and gross torsion.

A Finite Displacement Analysis of Laminated Composite Plate
(Professor T. P. Kicher and Mr. Patnaik)

The partial differential equations of the plate in the finite displacement domain are highly non-linear and the displacement variables u, v, w are coupled. The chances for an exact solution (except for special cases where the partial differential equations degenerate to ordinary differential equations) is beyond the scope of present day mathematics. This necessitates the examination of some numerical technique to solve the problem. The solution to determine the buckling load of an isotropic plate is known. From the non-linear column theory it was observed that once the out of plane displacement pattern is known from the linear buckling theory, the in-plane displacement u(z) is obtained in the close form, in terms of the out of plane displacement pattern. The constant associated with the out of plane displacement is obtained from the boundary conditions. Alternatively the out of plane displacement mode constant can be determined by minimizing the potential energy with respect to the unknown displacement constant. This is the technique adopted by Chan (.) to solve the problem under p_x alone.

From the boundary conditions and the load distribution, it is easy to observe that the displacement pattern for an isotropic plate

would be:

$$\bar{w} = A_n \cos n\pi\bar{x} \cos n\pi\bar{y} \quad .$$

The coordinate system is shown in Figure 1. The analysis procedure is as follows:

Step I

Assume the out of plane displacement $w = 0$, and solve for u and v from the membrane equilibrium equations. This is the homogeneous solution.

$$u_H = E_7 \bar{x} + E_8 \bar{y} + E_9 \tag{1}$$

$$V_H = C_7 \bar{x} + C_8 \bar{y} + C_9 \tag{2}$$

Step II

Assume $\bar{w} = A \cos\pi m\bar{x} \cos\pi n\bar{y}$

The $\bar{w}$ displacement satisfies the bending boundary conditions of a simply supported isotropic plate with the coordinate origin at the center of the plate. A , is the displacement at $x = y = 0$; m , n are positive integers.

Step III

Substitute $\bar{w}$ in the right hand side of membrane equilibrium equations. The right hand side of membrane equilibrium equations has the following form:

(i) RHS of U-Equilibrium equation

$$S_1 \sin 2m\pi\bar{x} + S_2 \sin 2n\pi\bar{y} + S_3 \sin m\pi\bar{x} \cos n\pi\bar{y}$$
$$+ S_4 \cos m\pi\bar{x} \sin n\pi\bar{y} + S_5 \sin 2m\pi\bar{x} \cos 2n\pi\bar{y}$$
$$+ S_6 \cos 2m\pi\bar{x} \sin 2n\pi\bar{y} \tag{3}$$

(ii) RHS of v-Equilibrium equation

$$t_1 \sin 2m\pi\bar{x} + t_2 \sin 2n\pi\bar{y} + t_3 \sin m\pi\bar{x} \cos n\pi\bar{y}$$
$$+ t_4 \cos m\pi\bar{x} \sin n\pi\bar{y} + t_5 \sin 2m\pi\bar{x} \cos 2n\pi\bar{y}$$
$$+ t_6 \cos 2m\pi\bar{x} \sin 2n\pi\bar{y} \tag{4}$$

S_i and t_i in Equations 3 and 4 are all known functions of elastic constants, geometric parameters and amplitude A.

Step IV

From Equations 3 and 4 the particular solution for u and v may be assumed as:

$$
\begin{aligned}
u_p = {} & E_1 \sin 2m\pi\bar{x} + E_2 \sin 2n\pi\bar{y} + E_3 \sin m\pi\bar{x} \cos n\pi\bar{y} \\
& + E_4 \cos m\pi\bar{x} \sin n\pi\bar{y} + E_5 \sin 2m\pi\bar{x} \cos 2n\pi\bar{y} \\
& + E_6 \cos 2m\pi\bar{x} \sin 2n\pi\bar{y} \qquad (5)
\end{aligned}
$$

$$
\begin{aligned}
v_p = {} & C_1 \sin 2m\pi\bar{x} + C_2 \sin 2n\pi\bar{y} + C_3 \sin m\pi\bar{x} \cos n\pi\bar{y} \\
& + C_4 \cos m\pi\bar{x} \sin n\pi\bar{y} + C_5 \sin 2m\pi\bar{x} \cos 2n\pi\bar{y} \\
& + C_6 \cos 2m\pi\bar{x} \sin 2n\pi\bar{y} \qquad (6)
\end{aligned}
$$

Step V

Substitute u_p and v_p in the left hand side of the membrane equilibrium equations and equate the coefficients of like terms. This yields the following algebraic equations:

$$
\begin{bmatrix}
M_1 & & & \\
& M_2 & & \\
& & M_3 & \\
& & & M_4
\end{bmatrix}
\begin{Bmatrix}
E_1 \\ C_1 \\ \hline E_2 \\ C_2 \\ \hline E_3 \\ E_4 \\ C_3 \\ C_4 \\ \hline E_5 \\ E_6 \\ C_5 \\ C_6
\end{Bmatrix}
= A^2
\begin{Bmatrix}
v_1 \\ \hline v_2 \\ \hline 0 \\ \hline V_4
\end{Bmatrix}
+ A
\begin{Bmatrix}
0 \\ \hline 0 \\ \hline V_3 \\ \hline 0
\end{Bmatrix}
+
\begin{Bmatrix}
0 \\ \hline 0 \\ \hline V_t \\ \hline 0
\end{Bmatrix}
\qquad (7)
$$

The known matrices M_1 - M_4 , and the vectors V_1 - V_4 and v_T are functions of material properties.

Step VI

The solution to Equation set 7 may be represented as:

$$E_1 = \bar{E}_1 A^2 \qquad C_1 = \bar{C}_1 A^2$$

$$E_2 = \bar{E}_2 A^2 \qquad C_2 = \bar{C}_2 A^2$$

$$E_3 = \bar{E}_3 A + tE_3 \qquad C_3 = \bar{C}_3 A + tC_3$$

$$E_4 = \bar{E}_4 A^2 + tE_4 \qquad C_4 = \bar{C}_4 A + tC_4$$

$$E_5 = \bar{E}_5 A^2 \qquad C_5 = \bar{C}_5 A^2$$

$$E_6 = \bar{E}_6 A^2 \quad \ldots(8) \qquad C_6 = \bar{C}_6 A^2 \quad \ldots(9)$$

In the above equations $\bar{E}_1 \ldots \bar{E}_6$ and $\bar{C}_1 \ldots \bar{C}_6$ are known constants obtained from Equation 7.

Step VII

Thus assuming an out of plane displacement mode, the two membrane equilibrium equations are solved, except for the unknown amplitude A.

Step VIII

The complete u and v displacement functions are

$$\begin{aligned} u = {} & E_1 \sin m\pi\bar{x} + E_2 \sin 2n\pi\bar{y} + E_3 \sin m\pi\bar{x} \cos n\pi\bar{y} \\ & + E_4 \cos m\pi\bar{x} \sin n\pi\bar{y} + E_5 \sin 2m\pi\bar{x} \cos 2n\pi\bar{y} \\ & + E_6 \cos 2m\pi\bar{x} \sin 2n\pi\bar{y} + E_7 \bar{x} + E_8 \bar{y} + E_9 \end{aligned} \qquad (10)$$

$$\begin{aligned} v = {} & C_1 \sin 2m\pi\bar{x} + C_2 \sin 2n\pi\bar{y} + C_3 \sin m\pi\bar{x} \cos n\pi\bar{y} \\ & + C_4 \cos m\pi\bar{x} \sin n\pi\bar{y} + C_5 \sin 2m\pi\bar{x} \cos 2n\pi\bar{y} \\ & + C_6 \cos 2m\pi\bar{x} \sin 2n\pi\bar{y} + C_7 \bar{x} + C_8 \bar{y} + C_9 \end{aligned} \qquad (11)$$

Step IX

The u and v displacements as defined in 10 and 11 contain the rigid body motions. These modes are eliminated by fixing the translation and rigid body rotation of one point in space, like

$$u = 0 \quad \text{at } \bar{x} = 0 , \quad \bar{y} = 0 \tag{12}$$

$$v = 0 \quad \text{at } \bar{x} = 0 , \quad \bar{y} = 0 \tag{13}$$

$$\frac{\partial u}{\partial y} - \frac{\partial v}{\partial x} = 0 \quad \text{at } \bar{x} = 0 , \quad \bar{y} = 0 \tag{14}$$

The above equations yield the following conditions:

$$E_9 = C_9 = 0 \tag{15}$$

$$C_7 = E_8 \tag{16}$$

Thus the complete in-plane displacement field is obtained except for the unknown amplitude A, and the constants E_7, E_8 and C_8 .

Step X

To determine the amplitude A, the Raleigh-Ritz procedure is adopted. The total potential energy is expressed in terms of the unknown constants A, E_7, E_8 and C_8 . The variation of the total potential with respect to the unknown constants yields a set of equations. The solution of these non-linear algebraic equations yields the unknowns, thus the complete u, v, w displacement field is obtained. Briefly the above procedure may be summarized as: Assuming a suitable out of plane displacement mode, the analysis is completed in closed form for in-plane displacements, and the out of plane displacement constant, and the constants associated with the homogeneous solution for the membrane displacements are obtained by Raleigh-Ritz procedure.

Determination of the Unknown Displacement Constants

The expression for the total potential energy is

$$\pi_p = U - W$$

π_p : Total potential function (17)

U : Strain energy stored in the deformed plate

W : Potential of work done due to external loads

Substituting u, v, w in the energy expression and integrating in the plane of the plate π_p reduces to:

$$\begin{aligned}\pi_p &= C_4A^4 + C_3A^3 + C_2A^2 + C_1A + C_0 \\ &+ Q(E_7, E_8, C_8) + L(E_7,E_8,C_8) \\ &+ A^2L'(E_7, E_8, C_8) + AL''(E_7, E_8, C_8) \\ &+ (F_1 E_7 + f_2 E_8 + f_3 C_8)\end{aligned} \tag{18}$$

C_4, C_3, C_2, C_1, C_0 are constants and dependent upon the material and geometric properties of the plate and upon the load distributions.

Q is a quadratic function of E_7, E_8 C_8. L, L', L" are linear functions of E_7, E_8, C_8 and f_1, f_2, f_3 are constants associated with the external traction and the plate properties.

$$\delta\pi_p = \frac{\partial\pi_p}{\partial E_7}\delta E_7 + \frac{\partial\pi_p}{\partial E_8}\delta E_8 + \frac{\partial\pi_p}{\partial C_8}\delta C_8 + \frac{\partial\pi_p}{\partial A}\delta A = 0 \tag{19}$$

yields the following independent equations:

$$\frac{\partial\pi_p}{\partial E_7} = \frac{\partial\pi_p}{\partial E_8} = \frac{\partial\pi_p}{\partial C_8} = 0 \tag{20}$$

$$\frac{\partial\pi_p}{\partial A} = 0 \tag{21}$$

The Equation set 20 reduces to:

$$\begin{bmatrix} & & \\ & K & \\ & & \end{bmatrix}\begin{Bmatrix} E_7 \\ E_8 \\ C_8 \end{Bmatrix} = \begin{Bmatrix} f_1+L_1 \\ f_2+L_2 \\ f_3+L_3 \end{Bmatrix} - A^2\begin{Bmatrix} L' \\ L_2' \\ L_3' \end{Bmatrix} - A\begin{Bmatrix} L'' \\ L_2'' \\ L_3'' \end{Bmatrix} \tag{22}$$

The matrices and vectors in Equation set 22 are all known. Solution to Equation 22 may be expressed as:

$$\begin{Bmatrix} E_7 \\ E_8 \\ C_8 \end{Bmatrix} = \begin{Bmatrix} \hat{E}_7 \\ \hat{E}_8 \\ \hat{C}_8 \end{Bmatrix} + A \begin{Bmatrix} \bar{E}_7 \\ \bar{E}_8 \\ \bar{C}_8 \end{Bmatrix} + A^2 \begin{Bmatrix} \bar{\bar{E}}_7 \\ \bar{\bar{E}}_8 \\ \bar{\bar{C}}_8 \end{Bmatrix} \tag{23}$$

$$\frac{\partial \pi_p}{\partial A} = 0 \quad ; \text{ yields}$$

$$4\,C_4A^3 + 3C_3A^2 + 2C_2A + C_1 + 2AL'(E_7,E_8,C_8)$$

$$+ \; L''(E_7,E_8,C_8) \tag{24}$$

Substituting for E_7, E_8 and C_8 from Equation 23 into Equation 24, and regrouping terms, Equation 24 reduces to:

$$(4C_4 + \beta_3)A^3 + (3C_3 + \beta_2 + \beta_6)A^2 + (2C_2 + \beta_1 + \beta_5)A + G = 0 \tag{25}$$

or,

$$\Phi_1A^3 + \Phi_2A^2 + \Phi_3A + \Phi_4 = 0 \tag{26}$$

$(\beta_1, \beta_2, \beta_3)$ and $(\beta_4, \beta_5, \beta_6)$ are terms associated with L' and L" and come from the non-linear coupling of membrane and bending displacements as expressed in 23.

Examination of the Deflection Curve

A critical examination of Equation 26 furnishes the following information.

Case 1.

$$\Phi_i \neq 0 \quad ; \quad 1 \leq i \leq 4$$

There is no bifurcation type of buckling. The load deflection curve is a continuous curve.

Case II. $\Phi_4 = 0$

Equation 26 reduces to:

$$(\Phi_1A^2 + \Phi_2A + \Phi_3)\,A = 0 \tag{27}$$

(i) One of the roots is always zero.

(ii) The other two roots could be imaginary. This represents the prebuckled state.

(iii) The two no zero roots are real. In this case the actual load deflection path is one corresponding to the least potential energy.

Case III

$$\Phi_4 = 0 \; ; \qquad \Phi_2 = 0 \tag{28}$$

This is the case for an isotropic pate for in-plane loads alone.

(i) Prebuckled State

$$\Phi_4 > 0 \tag{29}$$

$$\Phi_2 > 0 \tag{30}$$

One root at zero level and two roots are complex conjugate but pure imaginary with zero real part.

(ii) Buckling Condition.

$$\Phi_4 > 0 \tag{31}$$

$$\Phi_2 = 0 \tag{32}$$

This is the point on the load deflection curve at which bifurcation starts. One root at zero level, the other two roots start to become real numbers. This characterizes the appearance of out of plane displacement in an isotropic plate.

(iii) Post Buckling Condition.

$$\Phi_4 > 0 \tag{33}$$

$$\Phi_2 < 0 \tag{34}$$

One root at zero level, the other roots are real and equal in magnitude. This states that the plate can buckle out in a positive or negative z direction without any preference.

Imposition of Membrane Boundary Conditions

(1) The boundary is free to expand or contract in its own

plane. E_7, E_8 and C_8 are not restrained and are obtained by solving Equation set 22.

(2) The boundary in the $\bar{x}$ direction is $\bar{x} = \pm 1/2$ has a prescribed preassigned displacement x_{pres}. x_{pres} could be zero, positive or negative. The above boundary condition is readily realized by suitably manipulating the rows, columns and right hand side vectors of Equation 22, as shown below.

$$\begin{bmatrix} 1 & 0 & 0 \\ 0 & K_{22} & K_{23} \\ 0 & K_{32} & K_{33} \end{bmatrix} \begin{Bmatrix} E_7 \\ E_8 \\ C_8 \end{Bmatrix} = -A^2 \begin{Bmatrix} L_1' \\ L_2' \\ L_3' \end{Bmatrix} - A \begin{Bmatrix} L_1'' \\ L_2'' \\ L_3'' \end{Bmatrix} - \begin{Bmatrix} x_{pres} \\ f_2+L_2 \\ f_3+L_3 \end{Bmatrix} \tag{35}$$

(3) The boundary in the $\bar{y}$ direction is $\bar{y} = \pm 1/2$ has a prescribed preassigned displacement y_{pres}. y_{pres} could be zero, positive or negative. The boundary condition in the $\bar{y}$ direction is readily realized by suitable manipulation of Equation 20 as shown below.

$$\begin{bmatrix} K_{11} & K_{12} & 0 \\ K_{21} & K_{22} & 0 \\ 0 & 0 & 1 \end{bmatrix} \begin{Bmatrix} E_7 \\ E_8 \\ C_8 \end{Bmatrix} = \begin{Bmatrix} f_1+L_1 \\ f_2+L_2 \\ y_{pres} \end{Bmatrix} - A^2 \begin{Bmatrix} L_1' \\ L_2' \\ L_3' \end{Bmatrix} - A \begin{Bmatrix} L_1'' \\ L_2'' \\ L_3'' \end{Bmatrix} \tag{36}$$

(4) The boundary in both $\bar{x}$ and $\bar{y}$ directions at $\bar{x} = +1/2$; $\bar{y} = \pm 1/2$, have prescribed preassigned displacements x_{pres}, y_{pres}. This boundary condition is realized by the superposition of boundary conditions 2 and 3. Equation 20 reduces to:

$$\begin{bmatrix} 1 & 0 & 0 \\ 0 & K_{22} & 0 \\ 0 & 0 & 1 \end{bmatrix} \begin{Bmatrix} E_7 \\ E_8 \\ C_8 \end{Bmatrix} = \begin{Bmatrix} x_{pres} \\ f_2+L_2 \\ y_{pres} \end{Bmatrix} - A^2 \begin{Bmatrix} L_1' \\ L_2' \\ L_3' \end{Bmatrix} - A \begin{Bmatrix} L_1'' \\ L_2'' \\ L_3'' \end{Bmatrix} \tag{37}$$

The out of plane displacement pattern of the laminated composite was taken to be the exact buckling mode of an isotropic plate. It may be logical to assume that for an isotropic plate the initial buckling mode is preserved in the post buckled domain in the proximity of the buckling load. Thus, the post-buckled behavior by this method should be a good approximation to the exact solution of an isotropic plate. The out of plane displacement mode of an isotropic plate, when used for the analysis of a laminated composite anisotropic plate will only yield an approximate solution. Because of the approximate nature of the out of plane displacement mode, additional constraints are imposed on the plate and the resistance of the plate to deformation is increased as a result. In this section a refined analysis is done by expanding the out of plane displacement pattern in a fourier series, retaining only 9 terms. The membrane displacement pattern of Equations 5 and 6 is used in this section, with the E's and C's as independent variables.

The out of plane displacement mode is assumed as:

$$\begin{aligned}\bar{w} = {} & X_1 \cos\pi\bar{x} \cos\pi\bar{y} + X_2 \cos\pi\bar{x} \cos 3\pi\bar{y} \\ & + X_3 \cos\pi\bar{x} \cos 5\pi\bar{y} + X_4 \cos 3\pi\bar{x} \cos\pi\bar{y} \\ & + X_5 \cos 3\pi\bar{x} \cos 3\pi\bar{y} + X_6 \cos\pi 3\,\bar{x} \cos 5\pi\bar{y} \\ & + X_7 \cos 5\pi\bar{x} \cos\pi\bar{y} + X_8 \cos 5\pi\bar{x} \cos 3\pi\bar{y}\end{aligned} \tag{38}$$

$$\begin{aligned}\bar{u} = {} & E_1 \sin 2\pi\bar{x} + E_2 \sin 2\pi\bar{y} + E_3 \sin\pi\bar{x} \cos\pi\bar{y} \\ & + E_4 \cos\pi\bar{x} \sin\pi\bar{y} + E_5 \sin 2\pi\bar{x} \cos 2\pi\bar{y} \\ & + E_6 \cos 2\pi\bar{x} \sin 2\pi\bar{y} + E_7\,\bar{x} + E_8\,\bar{y}\end{aligned} \tag{39}$$

$$\begin{aligned}\bar{v} = {} & C_1 \sin\pi\bar{x} + C_2 \sin 2\pi\bar{y} + C_3 \sin\pi\bar{x} \cos\pi\bar{y} \\ & + C_4 \cos\pi\bar{x} \sin\pi\bar{y} + C_5 \sin 2\pi\bar{x} \cos 2\pi\bar{y} \\ & + C_6 \cos 2\pi\bar{x} \sin 2\pi\bar{y} + C_7\,\bar{x} + C_8\,\bar{y}\end{aligned} \tag{40}$$

The unknowns are $\{\langle X_1 \ldots X_9\rangle, \langle E_1 \ldots E_8\rangle, \langle C_1 \ldots C_8\rangle\}$.
The 25 unknowns will be obtained by the minimization of the potential energy. Davidon-Fletcher-Powell method, a gradient method will be used as the minimization algorithm. In the following section the potential function and the gradient to the potential function will be formulated.

The Discretized Potential Function

The discretized potential function, when displacement modes as given in Equations 38, 39 and 40 are substituted as fp; pws

$$\pi_p = \{E\}^7 [K^{uu}] \{E\} + \{E\}^T [K^{uv}] \{C\} + \{C\}^T [K^{vv}] \{C\}$$
$$+ \{E\}^T [K^{uw}] \{x\} + \{C\}^T [K^{vw}] \{x\}$$
$$+ \{E\}^T [K^{uww}] \{y\} + \{C\}^T [K^{vww}] \{y\}$$
$$+ \{x\}^T [K^{w2}] \{x\} + \{x\}^T [K^{w3}] \{y\}$$
$$+ \{y\}^T [K^{w4}] \{y\} - \{E\}^T \{P_1\} - \{C\}^T \{P_2\} - \{x\}^T \{P_3\} - \{y\}^T \{P_4\} \tag{41}$$

where

$$\{E\}^T = \langle E_1, E_2 \ldots E_8 \rangle \tag{42}$$

$$\{C\}^T = \langle C_1, C_2 \ldots C_8 \rangle \tag{43}$$

$$\{x\}^T = \langle x_1, x_2 \ldots x_8 \rangle \tag{44}$$

$$\{y\}^T = \langle x_1x_1, x_1x_2 \ldots x_9x_9 \rangle \tag{45}$$

$[K^{uu}]$, $[K^{uv}]$, $[K^{vv}]$ are 8 x 8 square matrices and represent the membrane energy of the structure.

$[K^{uw}]$, $[K^{vw}]$, $[K^{uww}]$, $[K^{vww}]$ are matrices as dimensioned in Equation 41 and represent the coupling energy.

$[K^{w2}]$, $[K^{w3}]$, $[K^{w9}]$ are matrices as dimensioned in Equation 41 and represent the energy associated with the out of plane displacements.

$\{P_1\}$, $\{P_2\}$, $\{P_3\}$, $\{P_4\}$ are vectors as dimensioned in Equation 41 and represent the work equivalent loads for both mechanical and thermal loads. All the matrices are automatically generated in the computer and the potential function π_p is obtained by proper matrix vector multiplications. In generating the matrices for linear structural analysis problems, the stiffness matrices are often made symmetric. Such a procedure is essential only when displacements are southt by direct solutions of matrix equations. In obtaining

the solution by minimization scheme, the matrices need not be made symmetric, although, that the matrices are not symmetric, should be remembered while calculating the gradient vector to the potential function

Gradient of the Potential Function

It may be observed that {Y} as defined in quation 46 is not an independent vector, but depends upon the x-variables. Thus the total number of variables is ~~25~~ ; ~~8~~ ~~ES~~ ± 8CS ± 9XS .

Gradient of Y vector with respect to the independent variables.

$$\frac{\partial\{Y\}}{\partial\{E\}} = \frac{\partial\{Y\}}{\partial\{C\}} = 0 \tag{46}$$

To determine the gradient of {Y} with respect to {X} , the following procedure is adopted.

$$Y(I) = X\{IA(I)\} \cdot X\{IBCI\} \; ; \quad \forall \quad 1 \leq I \leq 45 \tag{47}$$

$$\frac{\partial Y(I)}{\partial x_k} = X\{IA(I)\} \cdot \frac{X}{x_k} \{IB(I)\}$$

$$+ \frac{\partial}{\partial x_k} \{IA(I)\} \cdot X\{IB(I)\} \; ; \; \forall \; 1 \leq I \leq 45 \tag{48}$$

$$\frac{\partial X(IA(I))}{\partial x_k} = \begin{cases} 0 & \text{if } IA(J) \neq k \\ 1 & \text{if } IA(I) = k \end{cases} \; ; \quad \forall \quad 1 \leq I \leq 45 \tag{49}$$

$$\frac{\partial X(IB(I))}{\partial x_k} = \begin{cases} 0 & \text{if } IB(I) \neq k \\ 1 & \text{if } IB(I) = k \end{cases} \; ; \quad \forall \quad 1 \leq I \leq 45 \tag{50}$$

$$\text{Let} \quad \{\beta(I)\}^T = \{ \frac{\partial Y(I)}{\partial x_1} \; \ldots\ldots \; \frac{\partial Y(I)}{\partial x_9} \} \tag{51}$$

and

$$[S] = \begin{matrix} \beta(1) \\ \beta(2) \\ \beta(45) \end{matrix} \tag{52}$$

With the above definition the gradient of the Y vector becomes

$$\frac{\partial\{Y\}}{\partial\{X\}} = [S]\,\{X\} \tag{53}$$

$$\text{Let } \underset{1\times 25}{\langle \tilde{X} \rangle} = \langle \underset{1\times 8}{E^T} \; \underset{1\times 8}{C^T} \; \underset{1\times 9}{X^T} \rangle \tag{54}$$

With the above definition of [S] and {X} the gradient of the potential energy function with respect to X may be obtained as follows while calculating the gradient. The square matrices are not assumed to be symmetric.

$$\{\nabla\pi_p\} = \begin{Bmatrix} \dfrac{\partial\pi_p}{\partial E} \\ \\ \dfrac{\partial\pi_p}{\partial C} \\ \\ \dfrac{\partial\pi_p}{\partial X} \end{Bmatrix} \tag{55}$$

or,

$$\{\nabla\pi_p\} = \begin{Bmatrix} [[K^{uu}]+[K^{uu}]^T]\{E\}+[K^{uv}]\{C\}+[K^{uw}]\{X\}+[K^{ww}]\{Y\} \\ \text{- -} \\ [K^{uv}]^T\{E\}+ [[K^{vv}]+[K^{vv}]^T]\{C\}+[K^{vw}]\{X\}+[K^{vww}]\{Y\} \\ \text{- -} \\ [K^{uw}]^T\{E\}+[K^{vw}]^T\{C\}+[S][K^{uww}]^T\{E\} + \\ [S][K^{vww}]^T\{C\}+[[K^{w2}]+[K^{w2}]^T]\{X\} + \\ [S[[K^{w3}]^T\{X\}+[K^{w3}]\{Y\}+[[S][[K^{w4}]+[K^{w4}]^T]]\{Y\} \end{Bmatrix} \tag{56}$$

PROBLEM 1.

Isotropic Plate:

Material Constant Table

$$\begin{Bmatrix} \sigma_x \\ \sigma_y \\ \tau_{xy} \end{Bmatrix} = \begin{bmatrix} 33000.0 & 9900.0 & 0.0 \\ 99000.0 & 33000.0 & 0.0 \\ 0.0 & 0.0 & 11500.0 \end{bmatrix} \begin{Bmatrix} \varepsilon_x \\ \varepsilon_y \\ \gamma_{xy} \end{Bmatrix}$$

$\alpha_x = \alpha_y = 6\text{x}10^{-6}$ in/in°F ; a = b = 100"; t = 1.0" ; N_x alone

Problem 1.1 Sides Y = $\pm \frac{b}{2}$ free.

Problem 1.2 Sides Y = $\pm \frac{b}{2}$ restrained.

Problem 1.3 Sides Y = $\pm \frac{b}{2}$ Pre-strained in Tension $\bar{v}$ = + 1.0.

Problem 1.4 Sides Y = $\pm \frac{b}{2}$ Prestrained in Compression $\bar{v}$ = - 1.0.

The results are shown in Figure 2.

PROBLEM 2. Orthotropic Plate

2. Material Constant Table

$$\begin{Bmatrix} \sigma_x \\ \sigma_y \\ \tau_{xy} \end{Bmatrix} = \begin{bmatrix} 25375.0 & 374.0 & 0.0 \\ 374.0 & 1207.0 & 0.0 \\ 0.0 & 0.0 & 650.0 \end{bmatrix} \begin{Bmatrix} \varepsilon_x \\ \varepsilon_y \\ \gamma_{xy} \end{Bmatrix}$$

10 ply plate Thornel

Laminate axis along coordinate axis

a = b = 50.0"

t = 1.0"

Case 2.1 N_x and N_y both increasing: $N_x = N_y$

The results are shown in Figure 3.

PROBLEM 3

3. Orthotropic Plate

Material - same as Problem 2

$a = b = 20"$; $t = 1.0"$

3.1 Q_0 alone

3.2 Q_0 increasing Pretension $N_x = N_y = -55.0$

3.3 Q_0 increasing Precompression $N_x = N_y = 55.$

The results are shown in Figure 4.

B. Post Buckling Strength of Anisotropic Plates (Professor Kicher and Dr. Islam)

1. Introduction

The present report is a condensation of Ref. (1) which was prepared on the basis of the investigation performed in this section. The investigation encompasses three areas of work each of which is of importance by itself.

1. Theoretical prediction of post-buckled strength of orthotropic and anisotropic composite material plates.

2. Unbuckled compression testing of plate materials for stress-strain and strength determination.

3. Buckling and post-buckling testing of rectangular plates under uniaxial edge compressive loading.

The work grew out of a desire to obtain post-buckled strength prediction capability for composite materials. The study of anisotropic plate stability and post-buckling behavior has recently come into focus in response to the development of fiber reinforced composite materials. It has been known for a long time that a flat plate supported along its edges and subjected to loading in its plane can support loads much higher than their bifurcation load. In many applications, especially in aircraft construction, higher than critical loads are actually allowed. Investigations on composite material plates have shown similar existance of load capacities

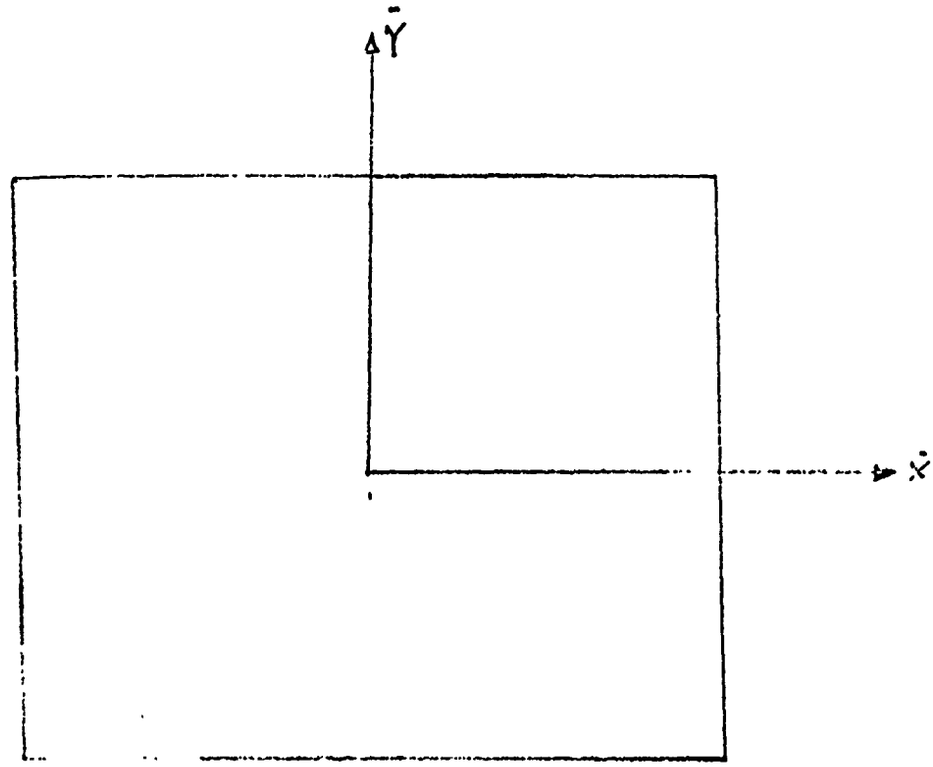

Figure 1. Planform view of Laminated Plate

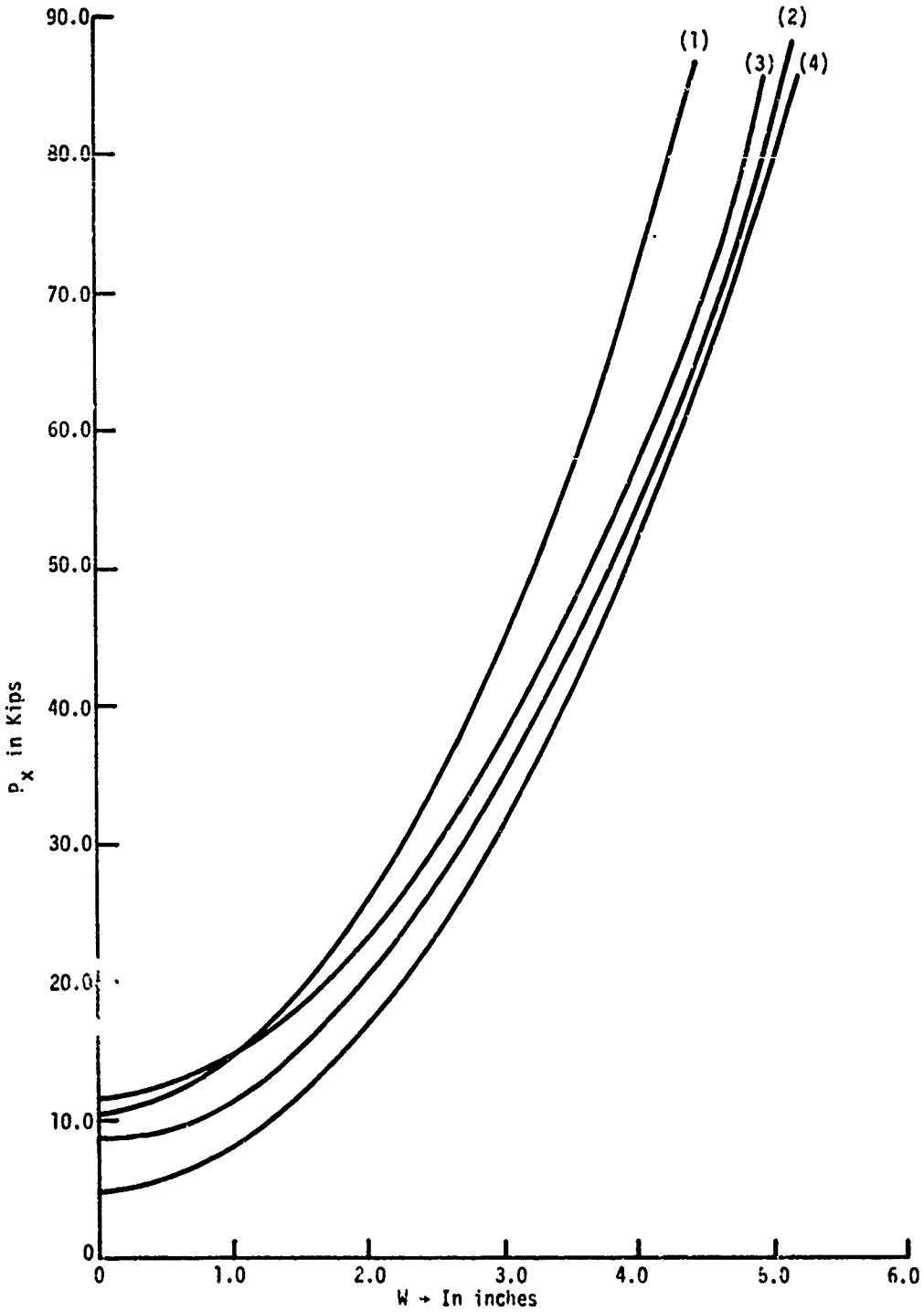

Figure 2. Solutions to Problem Set #1

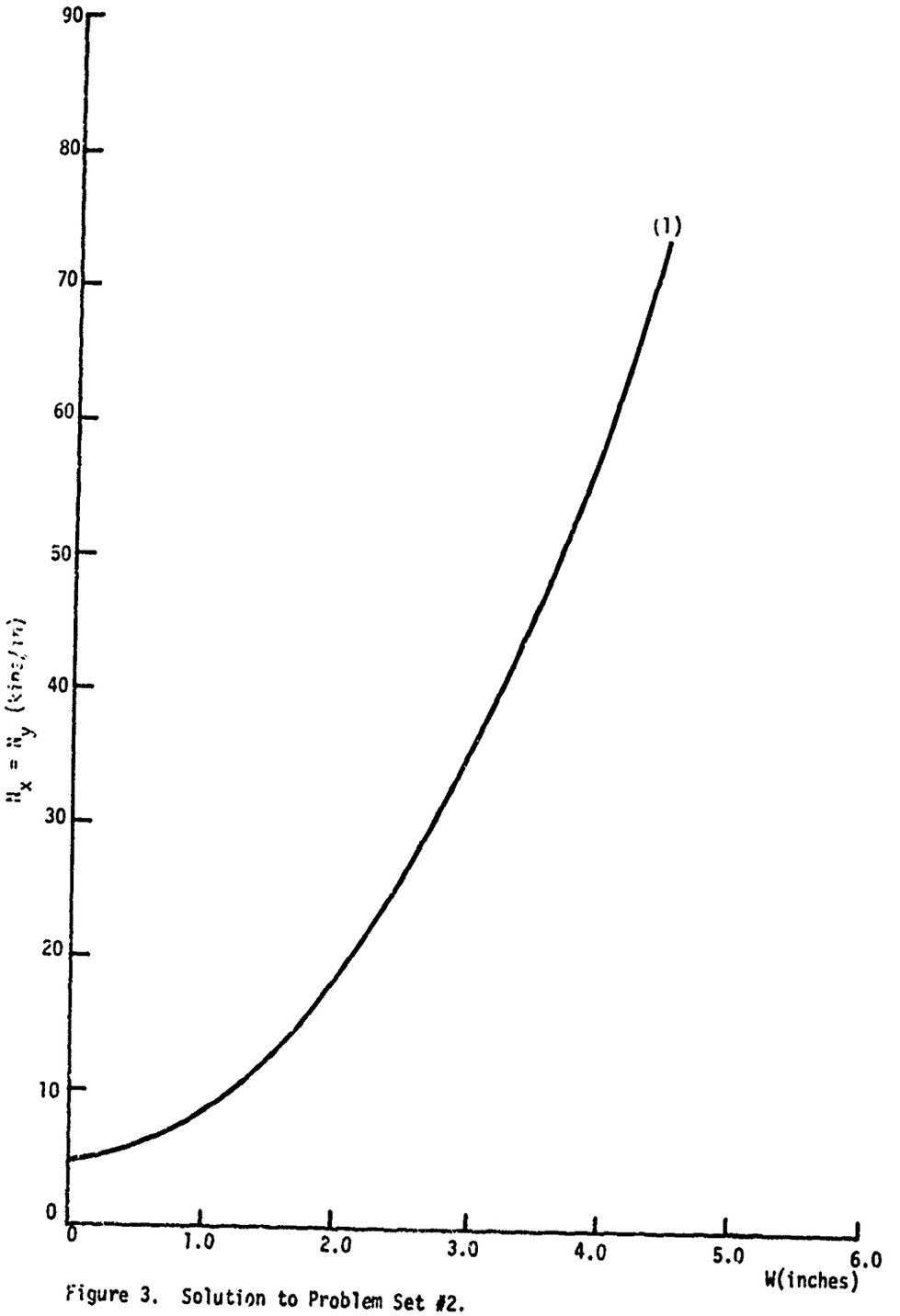

Figure 3. Solution to Problem Set #2.

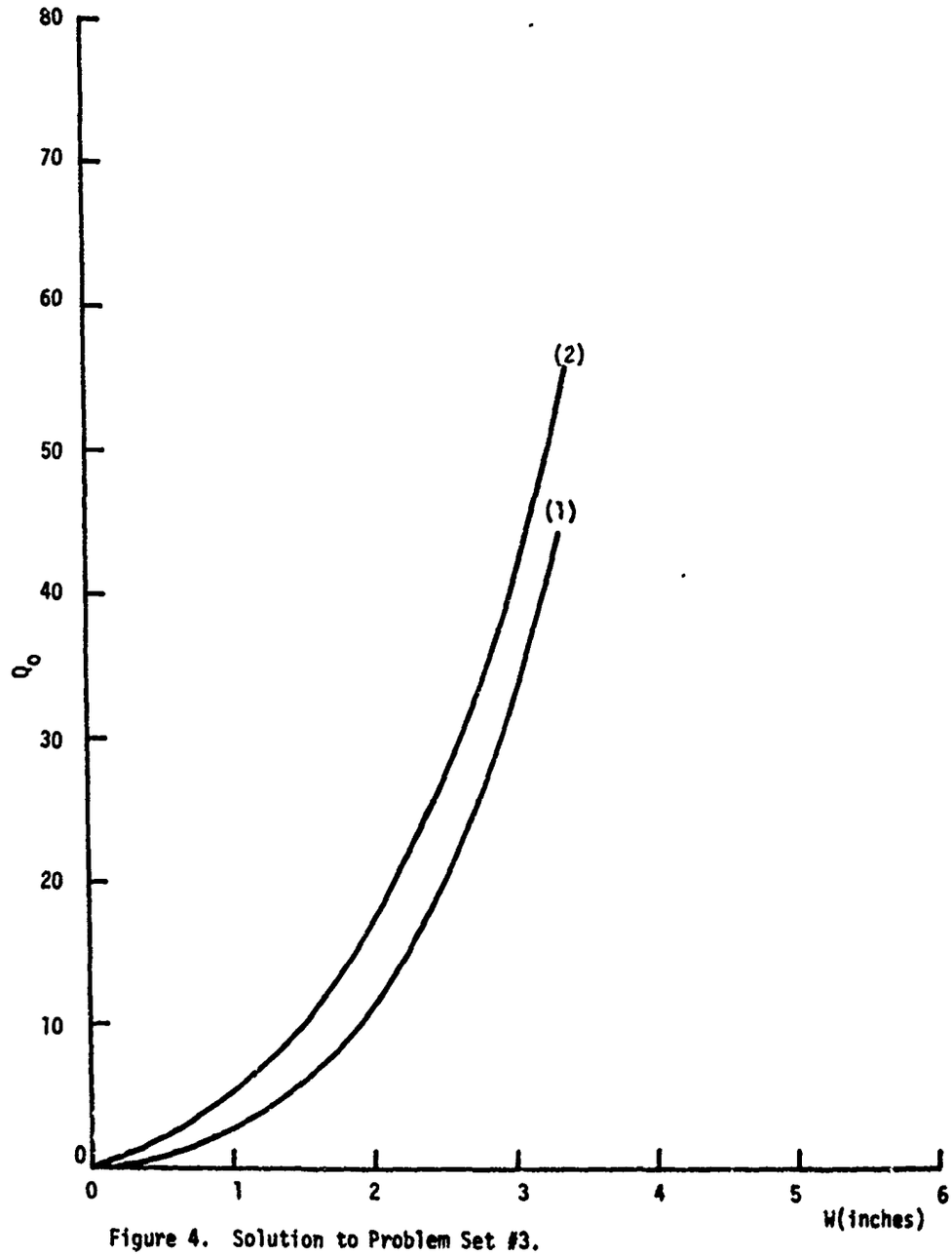

Figure 4. Solution to Problem Set #3.

beyond the point of buckling. (2) The high stiffness of composites leads to thin laminates for lightly loaded structures, consequently the high strength potential is not utilized. If methods of predicting the post-buckling strength were available then designers could utilize the full potential of the post-buckling region.

Historical Note:

Although the post-buckled behavior of isotropic material plates has been the subject of investigation by many people, little work has been done on the post-buckled behavior of orthotropic and anisotropic material plates. Analytical work on post-buckled anisotropic plates has been done by Monforton (3) and Chan (4). Monforton used a finite element formulation to obtain the post-buckling response for composite materials plates. Chan's theoretical predictions were obtained by assuming modes for the out-of-plane deformation and solving for the u and v displacements from the membrane displacement equation. Neither has attempted to predict the post-buckled ultimate load capacity.

2. Formulation

The loads acting on a structure can usually be represented in terms of a unit load system and load parameter η. A state of equilibrium is obtained from the unstrained state by monotonically increasing η from zero. For sufficiently small values of η a stable equilibrium exists which is called the fundamental state.

In many applications the fundamental state becomes unstable upon exceeding a certain value η_1. The load corresponding to η_1 is called the buckling or critical load for which the equilibrium is at the stability limit. At this buckling load, neighboring infinitesimally deviating equilibrium states are present in addition to the fundamental state. Similarly, at loads slightly different from the buckling load neighboring states of equilibrium also exist. The response of the structures at these loads depend on the nature of stability of equilibrium at the buckling load, (5), i.e., on whether the limiting case of equilibrium at the critical load is among the stable or already among the unstable states of equilibrium. When the equilibrium at the critical load is stable, as is the case with flat plates with supported edges, neighboring states of equilibrium exist for loads above the buckling load only and these states are stable, therefore loads larger than buckling can be sustained.

2.1 General Edge Loading

The strain displacement relations for plates under large deflection can be given by

$$\varepsilon_x = \overset{\circ}{\varepsilon}_x + z\kappa_x$$

$$\varepsilon_y \quad \overset{\circ}{\varepsilon}_y \quad z\kappa_y \tag{1}$$

$$\gamma_{xy} = \overset{\circ}{\gamma}_{xy} + z\kappa_{xy}$$

where Kirchoff-Love Conditions are assumed and z is measured from the reference surface. The reference surface strains are given by

$$\overset{\circ}{\varepsilon}_x = u_x + \frac{1}{2} w_x^2$$

$$\overset{\circ}{\varepsilon}_y = v_y + \frac{1}{2} w_y^2 \tag{2}$$

$$\overset{\circ}{\gamma}_{xy} = u_y + v_x + w_x w_y$$

and the curvature terms are

$$\kappa_x = -w_{xx}$$

$$\kappa_y = -w_{yy} \tag{3}$$

$$\kappa_{xy} = -2w_{xy}$$

The subscripts of u, v and w terms indicate partial derivatives. The force deformati n relationship for the general anisotropic plate is then

$$\begin{Bmatrix} N \\ M \end{Bmatrix} = \begin{bmatrix} A & B \\ B & D \end{bmatrix} \cdot \begin{Bmatrix} \overset{\circ}{\varepsilon} \\ \kappa \end{Bmatrix} \tag{4}$$

where

$$\{N\} = \begin{Bmatrix} N_x \\ N_y \\ N_{xy} = N_{yx} \end{Bmatrix} \qquad \{M\} = \begin{Bmatrix} M_x \\ M_y \\ M_{xy} = M_{yx} \end{Bmatrix}$$

$$\{\overset{\circ}{\varepsilon}\} = \begin{Bmatrix} \overset{\circ}{\varepsilon}_x \\ \overset{\circ}{\varepsilon}_y \\ \overset{\circ}{\varepsilon}_{xy} \end{Bmatrix} \qquad \{\kappa\} = \begin{Bmatrix} \kappa_x \\ \kappa_y \\ \kappa_{xy} \end{Bmatrix}$$

$$A = [a_{ij}]$$

$$B = [b_{ij}] \qquad \{i,j = 1,2,6\}$$

$$D = [d_{ij}]$$

Now define

$$\begin{aligned}
U_1 = \frac{1}{2} \int_s \{ & [a_{11} u_y^2 + a_{22} v_y^2 + a_{66} (u_y + v_x)^2 + 2a_{12} u_x u_y \\
& + 2a_{16} (u_y + v_x) u_x + 2a_{26} (u_y + v_x) v_y] \\
& -2 [b_{11} u_x w_{xx} + b_{22} v_y w_{yy} + 2b_{66} (u_y + v_x) w_{xy} \\
& + b_{12} (v_y w_{xx} + u_x w_{yy}) + b_{16} (u_y + v_x) w_{xx} \\
& + 2b_{16} u_x w_{xy} + b_{26} (u_y + v_x) w_{yy} + 2b_{26} v_y w_{xy}] \\
& + [d_{11} w_{xx}^2 + d_{22} w_{yy}^2 + 4d_{66} w_{xy}^2 + 2d_{12} w_{xx} w_{yy} \\
& + 4d_{16} w_{xx} w_{xy} + 4d_{26} w_{yy} w_{xy}] \} \, ds
\end{aligned} \tag{5}$$

$$\begin{aligned}
U_2 = \frac{1}{2} \int_s \{ & [a_{11} u_x w_x^2 + a_{22} v_y w_y^2 + 2a_{66} (u_y + v_x) w_x w_y \\
& + a_{12} (u_x w_y^2 + v_y w_x^2) + a_{16} (u_y + v_x) w_x^2 + a_{16} u_x w_x w_y \\
& + a_{26} (u_x + v_x) w_y^2 + a_{26} v_y w_x w_y] - [b_{11} w_{xx} w_x^2
\end{aligned}$$

$$+ \; b_{22}\, w_{yy}\, w_y^2 + 4b_{66}\, w_x\, w_y\, w_{xy} + b_{12}\,(w_{xx}\, w_y^2 + w_{yy}\, w_x^2)$$

$$+ \; b_{16}\,(2w_{xy}\, w_x^2 + w_x\, w_y\, w_{xx}) + b_{26}(2w_{xy}\, w_y^2 + w_x\, w_y\, w_{yy})]\}\, ds \quad (6)$$

$$U_3 = \frac{1}{2} \int_s \{ \frac{1}{4} [a_{11}\, w_x^4 + a_{22}\, w_y^4] + [a_{66} + \frac{1}{2} a_{12}]\, w_x^2\, w_y^2$$

$$+ \; 2[a_{16}\, w_x^3\, w_y + a_{26}\, w_x\, w_y^3]\}\, ds \quad (7)$$

where s indicates the surface of the plate. Then the strain energy of the plate is

$$U = U_1 + U_2 + U_3 \quad (8)$$

The potential of the applied load is

$$W = \oint_y [\bar{N}_x\, u + \bar{N}_{xy}\, v + \bar{Q}_{xz}\, w - \bar{M}_x\, w_x - \bar{M}_{xy}\, w_y]\, dy$$

$$- \oint_x [\bar{N}_{yx}\, u + \bar{N}_y\, v + \bar{Q}_{yz}\, w - \bar{M}_{yx}\, w_x - \bar{M}_y\, w_y]\, dx \quad (9)$$

where $\bar{N}_x$, $\bar{N}_y$, $\bar{N}_{xy}$, $\bar{N}_{yx}$, $\bar{Q}_{xz}$, $\bar{Q}_{yz}$ are forces and $\bar{M}_x$, $\bar{M}_y$, $\bar{M}_{xy}$, $\bar{M}_{yx}$ are moments applied on the edges of the plate.

The total potential energy π_p of the plate is: $\pi_p = U - W$ (10)

For the prescribed kinematical boundary conditions, states of equilibrium of the plate will correspond to stationary values of the elastic energy. Under hinged or built in edge conditions the elastic energy consists of the energy of the plate only. For elastically restrained plate edge conditions the elastic energy of the stringers must be added to obtain the total elastic energy. In any case the stationary value of the elastic energy may be calculated as a function of the applied deformation $\bar{\varepsilon}$. The approximate solution may be obtained by Rayleigh's or Rayleigh-Ritz's principle. Let the

solution obtained by $u(\bar{\varepsilon})$, $v(\bar{\varepsilon})$, $w(\bar{\varepsilon})$ for applied deformation $\bar{\varepsilon}$. Call the elastic energy which is a function of $\bar{\varepsilon}$, $U(\bar{\varepsilon})$.

Then

$$\frac{\partial \pi_p}{\partial \varepsilon} = 0 = \frac{\partial}{\partial \varepsilon} (U - W) \tag{11}$$

or

$$\frac{dU}{d\bar{\varepsilon}} = \bar{F} \tag{12}$$

where $\bar{F}$ is the edge load (vector). The ultimate load capacity is

$$\bar{F}_u = \max_{\bar{\varepsilon}} \left\{ \frac{dU}{d\bar{\varepsilon}} \right\} \tag{13}$$

Equation (13) assumes unlimited validity of the Hooke's Law. For real plates it may be necessary to include plasticity and failure of the material. A failure criteria must be used for this purpose.

Thus

$$\bar{F}_u = \max_{\bar{\varepsilon}} \frac{dU}{d\bar{\varepsilon}} \{ \phi \mid \phi(x,y) \leq \phi_f \} \tag{14}$$

where $\phi = \phi_f$ indicates failure of the material. The failure criterion may be chosen in terms of stress or strain.

In actual computation it will be necessary to check ϕ at a few discrete number of points. Test results obtained indicate these points should be chosen at the corners of the plate.

2.2 End Compressive Loading

Consider an orthotropic or anisotropic plate of length a and width b under a compressive load P . The load is applied through a rigid bar at the end, and the plate is supported on all sides.

During the fundamental or unbuckled state, the plate suffers uniform compressive strain ε across the width, and the load is distributed uniformly along the edge. After buckling, the center of the plate bows out while the sides are prevented from doing so. Because of the membrane stretching caused by the deflection at the middle, the compressive stress there is reduced. To support the same load, the sides of the plate then carry proportionately greater

parts of the total load P. In the far post-buckled state the load distribution is as shown in Figure 1 where the entire load is carried by two strips of width d , one on each side. The loading is considered to be uniformly distributed across these two strips each carrying half the total load P. Let the membrane compressive load on these strips be N_x . Then

$$P = 2dN_x \quad . \tag{15}$$

The plate is assumed to be simply supported on all sides. The lateral deflection w along the edges is thus zero. For the purpose of analysis, the middle strip without edge loading is ignored. (Figure 2).

Orthotropic Case

Classical orthotropic buckling theory can now be applied to the orthotropic plate with material axes aligned with structural axes of the plate, and with the plies oriented symmetrically about the mid-plane of the plate. This theory gives the lateral deflection w due to compressive load along the x axis by

$$D_{11}\, w_{,xxxx} + 2D_3 w_{,xxyy} + D_{22} w_{,yyyy} + N_x\, w_{,xx} = 0 \tag{16}$$

where D_{ij} are flexural stiffnesses and $D_3 = D_{12} + 2D_{66}$.

$$w = \bar{w} \sin \frac{\pi x}{\lambda} \sin \frac{\pi y}{2d} \tag{17}$$

where λ is the length of a half wave along the x direction Equation (17) satisfies the boundary conditions of the plate, i.e., $w = 0$ and $w_{,xx} = 0$ at $x = 0$ or a and $w = 0$ and $w_{,yy} = 0$ at $y = 0$ or 2d. Substitutiong (17) in (18) and dividing through by

$w \sin \frac{\pi x}{\lambda} \sin \frac{\pi y}{2d}$ we get

$$N_x = \pi^2 \left[\frac{D_{11}}{\lambda^2} + \frac{2D_3}{4d^2} + \frac{\lambda^2 D_{22}}{16d^4} \right] \tag{18}$$

We assume the two strips carrying the load are at the stability limit corresponding to the most dangerous wave length λ . (6) Differentiating the terms inside the square brackets with respect to λ and equating it to zero

$$\frac{2D_{11}}{\lambda^3} - 2\lambda \frac{D_{22}}{16d^4} = 0$$

$$\lambda = \sqrt[4]{\frac{D_{11}}{D_{22}}}\ 2d .$$

Substituting in (18)

$$N_x = \frac{\pi^2}{2d^2} [\sqrt{D_{11} D_{22}} + D_3] \tag{19}$$

$$d = \frac{\pi}{\sqrt{2N_x}} [\sqrt{D_{11} D_{22}} + D_3]^{1/2} \tag{20}$$

and

$$P = 2dN_x = \sqrt{2}\ \pi\ [\sqrt{D_{11} D_{22}} + D_3) N_x]^{1/2} \tag{21}$$

Replacing N_x by $\sigma_x t$

$$d = \frac{\pi}{\sqrt{2\sigma_x t}} [\sqrt{D_{11} D_{22}} + D_3]^{1/2} \tag{22}$$

$$P = \sqrt{2}\ \pi\ [(\sqrt{D_{11} D_{22}} + D_3)\ \sigma_x t]^{1/2} \tag{23}$$

Equations (22 and 23) give the relation between the effective width and the load. These equations hold up to the elastic limit or yield point for the material. However, they may be used beyond the elastic limit if D_{11}, D_{22} and D_3 are computed on the basis of the tangent moduli for the material of the plate. For composites where the material is elastic up to the stress corresponding to

failure tne ultimate load capacity is

$$P_{ult} = \sqrt{2}\ \pi\ [(\sqrt{D_{11}\ D_{22}} + D_3)\ \sigma_{xc} t]^{1/2} \tag{24}$$

where σ_{xc} is the failure stress in longitudinal compression for the composite.

Anisotropic Case

In the general anisotropic case, classical orthotropic buckling theory is not applicable. The governing equation for deflection for such a plate is

$$M_{x,xx} + 2M_{xy,xy} + M_{y,yy} + N_x\ w_{,xx} = 0 \tag{25}$$

along with the force deformation relationship

$$\begin{Bmatrix} \{N\} \\ \{M\} \end{Bmatrix} = \begin{bmatrix} [A] & [B] \\ [B] & [D] \end{bmatrix} \begin{Bmatrix} \{\varepsilon\} \\ \{\kappa\} \end{Bmatrix} \tag{26}$$

The solution for {M} from Equation (26) is

$$\{M\} = [D - BA^{-1}B]\ \{\kappa\} - [BA^{-1}]\ \{N\} \tag{27}$$

For simplicity neglecting the term $[BA^{-1}]\ \{N\}$ in Equation (25) leads to the governing equation

$$D^*_{11}\ w_{,xxxx} + 2D^*_3\ w_{,xxyy} + D^*_{22}\ w_{,yyyy} + N_x\ w_{,xx} = 0 \tag{28}$$

where the D* terms are elements of the matrix $[D-BA^{-1}\ B]$.

Equation (28) is of the same form as (16), and analogous treatment as in the orthotropic case gives

$$d = \frac{\pi}{\sqrt{2\sigma_x t}}\ [\sqrt{D^*_{11}\ D^*_{22}} + D^*_3\ ]^{1/2} \tag{29}$$

$$P = \sqrt{2}\ \pi\ [(\sqrt{D^*_{11}\ D^*_{22}} + D^*_3)\ \sigma_x t\ ]^{1/2} \tag{30}$$

Equations (29 and 30) give the relation between the effective width and the load. As in the orthotropic case these equations hold up to the elastic limit but may be used beyond the elastic limit if the D^*_{11} , D^*_{22} and D^*_3 are computed on the basis of tangent moduli. For composite materials which remain elastic up to failure, we obtain the ultimate load capacity

$$P_{ult} = \sqrt{2}\ \pi\ [(\sqrt{D^*_{11}\ D^*_{22}} + D^*_3)\ \sigma_{xc} t]^{1/2} \tag{31}$$

where σ_{xc} is the failure stress for the anisotropic composite in longitudinal compression.

Equations (24 and 31) have been used to compute the ultimate load capacities of various composite plates with different ply lay-ups and thicknesses. Results indicated considerable reserve strength beyond the buckling load. Experiments were conducted to obtain post-buckling strength data and verify the theoretical results. These works are presented in the subsequent sections.

Separation of Stiffness and Strength Influences

Examination of Equations (24 & 31) reveals that the post-buckled load capacity depends on the composite stiffness properties as well as on the compressive strength. The effect of the elastic constants of the plate may be considered separately from the influence of strength. Thus

$$P_{ult} = \lambda I \tag{32}$$

where $I = \sqrt{2}\ \pi\ [(\sqrt{D_{11}\ D_{22}} + D_3)t]^{1/2}$ or $\sqrt{2}\ \pi\ [(\sqrt{D^*_{11}\ D^*_{22}} + D^*_3)t]^{1/2}$

which may be called the Index for post-buckled strength. The parameter λ is a factor depending upon the stress strain curve. For materials which are elastic up to failure $\lambda = \sqrt{\sigma_{xc}}$. For material which yields at the ultimate load $\lambda = \sqrt{\sigma_y}$ may be used.

3. Un-Buckled Compression Testing of Composite Sheets and Plates

In order to compute the ultimate load capacities of plates using formulas (24 and 31) it is necessary to know the compression stress-strain and strength properties of the plate material. Although compression testing of composite materials has been the subject of investigation by many people (7,8,9,10) a satisfactory method has not yet been developed. Methods ASTM and Federal LP 406 are currently in use for compression testing. However, in these methods there is friction and failure usually occurs at the ends. In order to overcome these problems a method was developed for the accurate determination of the unbuckled compression stress-strain and strength of plate materials in which failure is obtained in the gage section. Description of the test fixture and details of the tests are given in Reference (10). Table (I) gives the list of specimens tested and the test results are summarized in Table II.

4. Buckling and Post Buckling Strength Tests

In order to verify the theoretical predictions and obtain test data for the post-buckling strength, the work of this chapter was undertaken. In this program, a method has been developed for the accurate buckling and post-buckling testing of rectangular plates. In particular a fixture has been designed for testing 10 x 10 inch plates.

The post-buckling strength tests for simply supported edge condition have been the subject of investigation by many people. A bibliography of such works is given in Reference (14). Such investigations have concentrated on isotropic metallic plates.

The crippling strengths are conventionally performed using square tubes and V-groove fixtures. However, in both these methods at large deflections, the plate edges do not remain simply supported. The V-groove method of loading will also have friction and a line loading resulting in local yielding of the material. The method of testing developed as part of this study eliminates the above problems. Description of the fixture and details of the tests are given in Reference (10). Table III gives the list of plates tested and a summary of results is given in Table IV.

Comparision of Predicted Strength with Observed Failure Loads

Table V lists the predicted strengths together with the experimentally observed failure load data. The agreement between the test results and the theoretical predictions is seen to be very good. Deviation of observed strength values from the theoretically predicted strengths is from -3.5 to 6.5%.

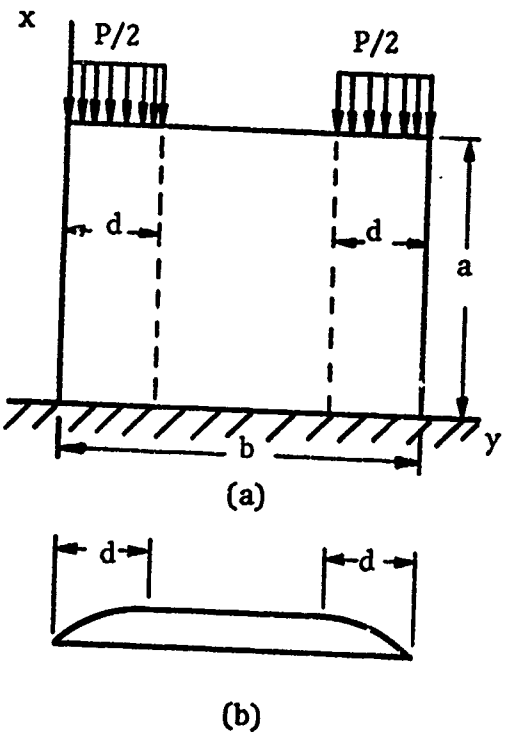

Fig. 1

Post Buckling Load Distribution

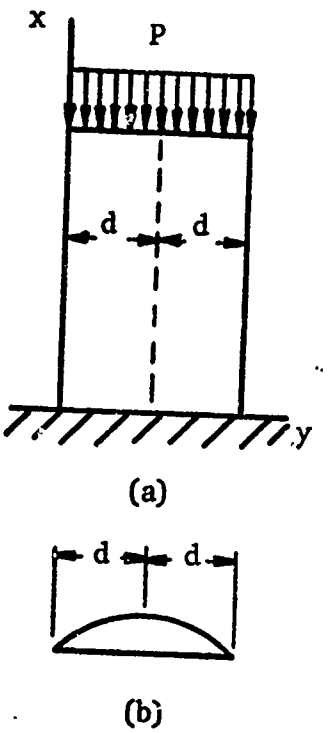

Fig. 2

Post Buckling Analysis Model

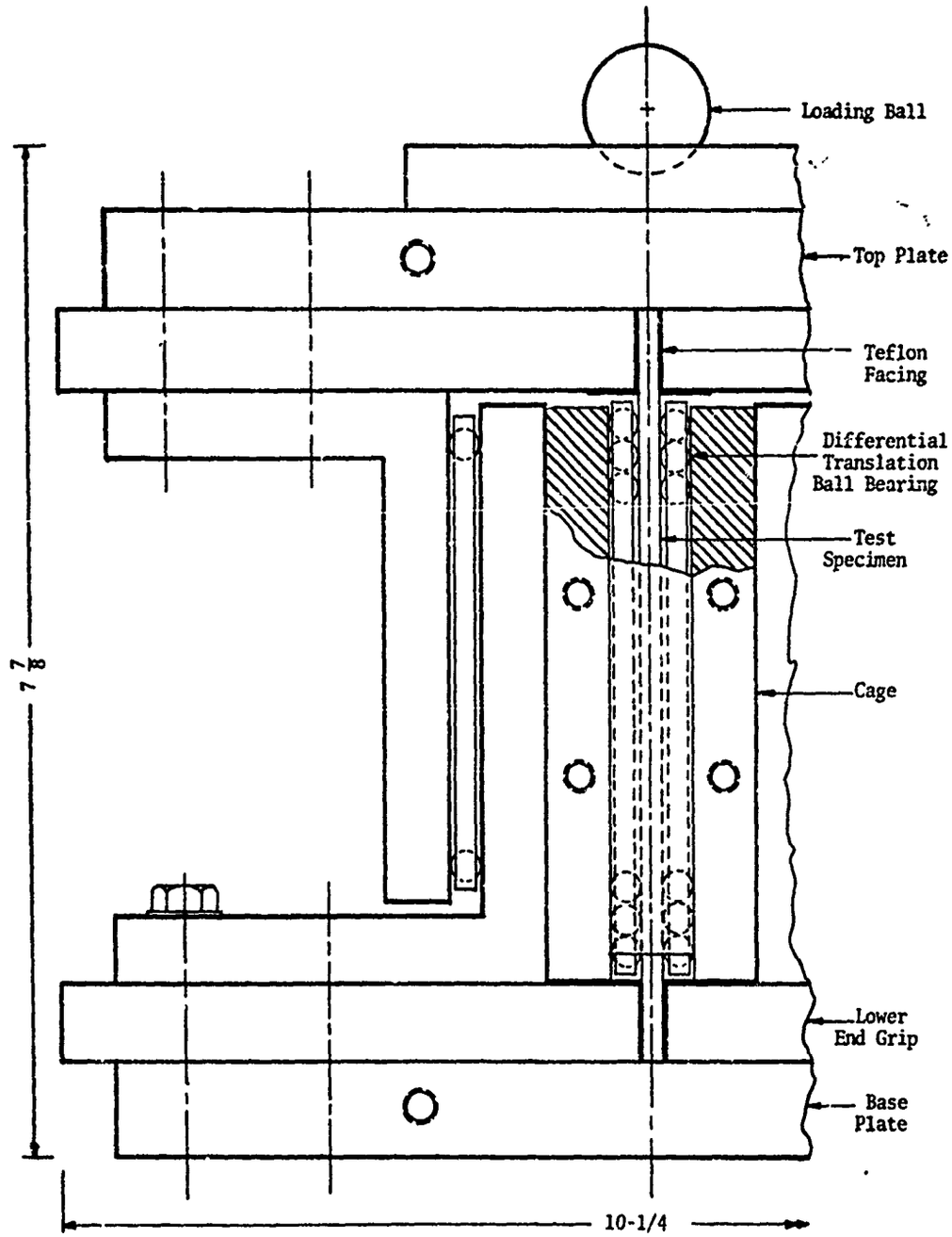

Figure 3 Schematic Diagram for Unbuckled Compression Testing Fixture without Deformation Measurement Attachment

TABLE I. LIST OF SPECIMENS TESTED

Specimen No.	Material	Thickness Inches	Ply Orientation
1	Aluminum 6061-T4	.03125	
2	Fiberglass Epoxy	.050	5(0,90,0,90,0)
3	"	.050	5(0,90,0,90,0)
4	"	.050	5(0,90,0,90,0)
5	"	.050	5(0,90,0,90,0)
6	"	.050	5(90,0,90,0,90)
7	"	.050	5(90,0,90,0,90)
8	"	.030	3(0,90,0)
9	"	.030	3(0,90,0)
10	"	.030	3(0,90,0)
11	"	.030	3(90,0,90)
12	"	.030	3(90,0,90)
13	"	.130	13(0,90,0,90,0,...,0)
14	"	.130	13(0,90,0,90,0,...,0)
15	"	.100	10(5(45°),5(-45°))
16	"	.062	7(0,45,-45,90,-45,45,0)

TABLE II SUMMARY OF RESULTS: UNBUCKLED COMPRESSION TESTS

Specimen No.	Modulus of Elasticity Measured psi x 10^6	Computed Modulus of Elasticity psi x 10^6	Failure Stress psi x 10^3	Failure Location	Yield Stress .2% off set psi x10^3
1	9.98				20.3
2	3.7	3.67	70.1	Gage Sect.	
3	3.65(Fig.3-21) 3.91(Fig.3-22)	3.67	53	End	
4	3.86	3.67	58.3	End	
5	3.53	3.67	65.8	End	
6	2.95	3.0	44.4	Gage Sec.	
7	3.1	3.0		Not failed	
8	3.82	3.89	26.3	Gage	
9	Not Measured	3.89	26	Gage	
10	Not Measured	3.89	25.5	Gage	
11	2.73	2.78	15.4	Gage	
12	2.76	2.78	14.7	Gage	
13	3.56	3.46	83	Not failed	
14	3.47	3.46	63.5	End	
15	2.0	1.995	20		10.9
16	2.86	2.9	50.2	Gage	

TABLE III LIST OF PLATES TESTED

Plate	Material	Thickness Inches	Ply Orientation	Size In x In.
1	Aluminum 6061-T4	.03125		10 x 10
2	Aluminum 2024-T3	.0625		"
3	Aluminum 2024-T3	.0625		"
4	Fiberglass Epoxy	.050	5(0,09,0,90,0)	"
5	"	.050	5(90,0,90,0,90)	"
6	"	.030	3(0,90,0)	"
7	"	.030	3(90,0,90)	"
8	"	.100	10(5(45) 5(-45))	"
9	"	.060	7(0,45,-45,90, -45,45,0)	"
10	"	.060	6(45,-45,45,-45, 45,-45)	"

TABLE IV CRITICAL LOAD, PREDICTED AND OBSERVED POST BUCKLED ULTIMATE STRENGTHS

Plate No.	Critical[a] Load lbs.	Predicted Post Buckled Load Capacity lbs.	Observed Post Buckled Load Capacity lbs.
1	130	845	860
2	1100	5180	5300
3	1100	5180	5200
4	108.2	1840	1775
5	112.7	1465	1475
6	23.07	394	409
7	24.63	302	325
8	991	3120	3270
9	214	2250	2285
10	258	1235	1315

(a) Computed values by classical or reduced flexural stiffness method.

C. Buckling of Laminated Composite Plates with Cutouts
(Professor T. P. Kicher and Mr. J. Martin)

This outline will summarize the work completed on the problem of The Buckling of Laminated Composite Plates with Cutouts. The buckling response and the postbuckling response are investigated for laminated composite square plates with centeral circular holes. The plates are simply-supported on all four edges and uniformly compressed in one direction. The completed work can be separated into two parts: the experimental work (including a literature search of material on the subject), which was done between September 1969 and May 1970, and the theoretical work, which was done between September 1970 and May 1971.

Although there is a large volume of literature on the stability of isotropic and anisotropic plates under various loading conditions (most of the research on the stability of anisotropic plates; an extensive amount of work on the stability of orthotropic plates was done in the U.S. by the Forest Products Laboratory, Madison, Wisconsin, during World War II), the corresponding literature on the stability of plates with cutouts has been meager. There is a small amount of published literature on the buckling of isotropic plates with cutouts, however this author has found no published material concerning the buckling of laminated composite plates with cutouts.

A preliminary experimental investigation was made on an 8-ply laminated square plate, 10 in. by 10 in., by .080 in., with 2-in. and 4-in. diameter circular cutouts in the center. The plate was made from "Scotchply" Reinforced Plastic Type 1002, a moldable epoxy-glass laminate, and the ply orientations were 0, 45, -45, 90, 90, -45, 45, 0. The buckling loads were found experimentally and the plate was loaded axially and simply-supported on all four edges.

A fabrication process to produce laminated composite plates was developed using a Patterson-Kelly autoclave. Laminated square plates, 12 in. by 12 in. by .100 in. were fabricated by a vacuum bag technique. Woven glass and teflon were used between the uncured laminate and a piece of rubber was placed on top of the final layer of woven glass. Gage pressure inside the autoclave was maintained at 18-20 psi, and temperature was maintained at 330-340°F during the 35 minute cure cycle. After the cure cycle had been completed the plate was allowed to cool very slowly inside the autoclave while the gage pressure and vacuum were still maintained. This procedure produced a plate which was very flat; fiber wash was found to be negligible, and void content was low.

Now, in regard to the theoretical work completed, analytic expressions were chosen for the displacements u, v, and w of a simply-supported square plate uniformly compressed in one direction, with a

central circular hole. These expressions contain the effect of the hole in both the prebuckling and post-buckling deflections and satisfy the condition of zero deflection at the edges of the plate. "Additional relations" between the coefficients of the assumed displacements were determined by satisfying the following boundary conditions "in the large":

(a) zero total force on the unloaded edges of the plate,
(b) the total force on the loaded edges of the plate is equal to the applied external load, and
(c) zero total normal force on the boundary of the hole.

Two additional parameters in the assumed displacements were determined by satisfying approximately on the boundary of the hole the conditions of zero total moment and zero total resultant shear force (for the isotropic perforated plate this is also equivalent to satisfying approximately at each point on the boundary of the hole the conditions of zero moment and resultant shear force).

The resultant forces and moments are related to the reference-surface strains and curvatures by the familiar equations containing the matrices [A], [B], and [D]. At this point three different cases were investigated:

Case I: the perforated plate is isotropic.

Case II: the perforated plate is midplane symmetric and specially orthotropic, i.e., [B] = 0 and $A_{16} = A_{26} = 0$. Also for this case a circular reinforcement was added around the hole; therefore, we can determine the effect of the reinforcement on the post-buckling response and the buckling load of the perforated plate.

Case III: the general case for which [B] $\neq$ 0 and the [A], [B], and [D] matrices are fully populated. Also, the circular reinforcement was added around the hole.

Next, the total potential energy was determined for each case. While the total potential energy was varied the additional relations were enforced between the coefficients of the assumed displacements.

For Case I and Case II the solution of the resulting simultaneous linear equations led to the classical solution for the postbuckling

response (parabolic response) and the buckling load. Solving the resulting simultaneous linear equations for Case III leads to the response curve, but now, due to the coupling matrix [B], we no longer have a classical buckling problem but a deflection problem; i.e., the perforated plate deflects under any value of the applied external load, no matter how small. An interesting feature of the derivation of the response curve for Case III is that the total solution can be represented as the sum of two portions: an uncoupled portion and a coupled portion. If the coupling matrix is set equal to zero then the total solution reduces to the uncoupled portion only.

Inherent in the solution for all three cases is the numerical integration of single and double integrals of certain functions which reflect the assumed displacements. For Case I a computer program was written to carry out these integrations; also, all remaining calculations were programmed. A set of numerical solutions were obtained for the postbuckling response and the buckling load for the values of γ between .1 and .5, where γ is the ratio of the diameter of the hole to the length of the edge of the plate. After plotting the buckling load vs. γ and comparing the results with existing experimental data (Tom Esselman, Elastic Stability of the Square Plate with Central Circular Hole under Edge Compression, 1969) the agreement was found to be good. For no hole the solution for the buckling load, based on the assumed displacements, reduces to the classical buckling solution for a simply-supported square plate uniformly compressed in one direction, namely $(\bar{N}_y)_{cr} = 4\pi^2 D$. The postbuckling curves clearly show that the postbuckling deflection of the perforated plate is greater than that for the corresponding plate with no hole, for any given value of the applied external load.

The detailed numerical calculations resulting in the postbuckling response and the buckling load have only been completed for Case I, i.e., for the isotropic perforated plate without the reinforcement. At the present time work is in progress to extend the numerical calculations to Case III; therefore, Case II will be included as a special subclass of problems. Once this is done the effect of the reinforcement on the postbuckling response and the buckling load, for Case I and Case II, can be determined. Since, in general, the reinforcement will increase the buckling load, we can then determine the size of the reinforcement; which is necessary in order to increase the buckling load a specified amount; these results can afterwards be illustrated in terms of design curves.

For the general coupled plate, Case III, the effect of the coupling matrix leads to a deflection problem right from the beginning; however, there is the possibility of reducing the coupling effect in the plate. Since the uncoupled problem leads to the classical bifurcation solution, corresponding to the uncoupled

portion of the total solution for Case III, there is the possibility of defining a measure of coupling as the distance $\tilde{w}_0$ in the load-deflection curve, $\bar{N}_y$ vs. w_0, corresponding to a given difference δ between the total solution and the corresponding uncoupled portion of the total solution. Let us call $\tilde{w}_0$ the coupling parameter. Then, as the coupling matrix tends to zero, the coupling parameter also tends to zero; i.e., the total solution approaches the uncoupled portion of the total solution (bifurcation solution). The coupling parameter then serves as a measure of the amount of coupling present in the plate. Now, by adding the reinforcement in the proper manner, i.e., either on one side of the plate or the other, etc., it might be possible to decrease the coupling parameter, and thereby decrease the coupling effect. If the application of the reinforcement (in the proper manner) causes a decrease in the coupling parameter then we can say that the reinforcement cuases a decrease in the coupling effect. This investigation is presently being pursued. A preliminary investigation of coupled plates with no holes tends to substantiate the possibility of reducing the coupling effect in coupled perforated plates.

The individual programs which have been written to numerically calculate the different portions of the solution have been extended to include the general case (i.e., Case III) and have been combined into one program. Work is commencing to fabricate a number of laminated composite plates, coupled and uncoupled, with reinforcements and without reinforcements, test them, and then compare the experimental data with the corresponding values from the theoretical analysis.

D. Buckling of Anisotropic Circular Cylindrical Shells (Professor T. P. Kicher and Dr. Chi-Hwa Wu)

A theoretical analysis of the buckling of a general anisotropic cylindrical shell under the combined radial pressure, axial compression, and torsion is presented. A modification of Cheng and Ho's method is used; a set of displacement modes, which satisfies the equilibrium equations, is assumed; four boundary conditions at each end of a shell are satisfied by imposing the vanishing of the boundary determinant. Eight sets of boundary conditions of different combinations are considered.

Twenty numerical examples are presented to demonstrate the effectiveness of the method. The numerical results show that the difference between Donnell's and Flugge's buckling loads is as high as 30% for the cases with the circumferential wave number $n = 2$, and the deviation is less than 2.5% for the cases with $n = 6$ or higher. The effects of classical boundary condition SS4 and free

boundary condition SS1 are investigated. It is shown that the difference in buckling loads between SS1 and SS4 is significant for short cylinders, and that there is little difference for long cylinders. It is also shown that, in general anisotropic shells are less sensitive to different boundary conditions than isotropic shells.

Introduction

Because of their light weight and high strength, composite materials, such as carbon fibers, glass fibers, are increasingly used in aerospace structures. Many researchers, including Cheng and Kuenzi,(1) Hess,(2), Thielemann, Schnell and Fischer, (3) Schnell and Bruhl, (4) and Tsai (5) have worked on the buckling of orthotropic cylindrical shells under axial compression or radial pressure. Tsai, for example, used Donnell-type equations (in terms of a stress function and a radial displacement) to study the buckling of a three layer orthotropic cylindrical shell under axial compression. A set of displacement and stress function modes are assumed to satisfy the Donnell-type equations and the simply supported boundary conditions. The results show that the heterogeneity generally has a deleterious effect on the stability of unpressurized, composite cylinders.

A general, linear buckling solution for arbitrary boundary conditions and combined loads has been presented by Cheng and Ho.(6,7) The method of solution is capable of tr ating the buckling problem of shells under radial pressure, axial compression, and torsion. Eight sets of boundary conditions are considered. However, the numerical results do not include the axial compression case, which is one of the most important parts of the buckling problem.

The same method has been applied by Tasi, Feldman and Stang (8) to the analysis of orthotropic cylinders with clamped support (C2) when axial compression is applied on the shell. The analytical results have been compared with the experimental results obtained from a series of tests on the three layer orthotropic cylinders. The comparison reveals that the experimental buckling loads are 65% - 85% of the analytical buckling loads. Recently, Lei and Cheng (9) have also applied the same method to orthotropic cylinders. The method, however, is restricted to orthotropic cylinders and to a cylinder loaded with radial pressure and axial compression while torsion is excluded. The characteristic equation is a fourth degree polynomial, and the boundary determinatnt is only 4 x 4. The buckling loads for 8 sets of boundary conditions have been compared. The results show that the boundary conditions have strong influence on the buckling loads.

The present work deals with the buckling of general anisotropic cylindrical shells of finite length subjected to radial pressure, axial comprssion, and torsional force. Cheng and Ho's method is used to formulate the boundary determinant. Eight sets of boundary

conditions are considered, i.e., four simple supports, SS1---SS4 and four clamped supports, C1---C4. The four sets of boundary conditions for simple supports and clamped supports are distinguished by the four different combinations of the vanishing of membrane displacements and membrane forces. The numerical examples include:

(a) Isotropic, orthotropic, and general anisotropic cases.

(b) Single loadings: radial pressure, axial compression, and torsional force.

(c) Combined loadings: (1) radial pressure and axial force, (a) axial force and torsional force, and (3) torsional force and radial pressure.

The mathematical formulation of buckling problem is presented in the Ph.D. Thesis by C. H. Wu. Both Flugge's and Donnell's theories are used in this work.

Mathematical Formulation of the problem of Shell Buckling

Basic Assumptions

For buckling analysis, two different theories are used in this study: Flugge's theory and Donnell's theory. Except for minor modification, Love's first approximation to the theory of thin elastic shell is used as the basis for buckling analyses. Love's postulates are:

(a) The shell is thin ($h/r \ll 1$).

(b) The deflections of the shell are small.

(c) The transverse normal stress is negligible.

(d) Normals to the reference surface of the shell remain normal to it and undergo no change in the length during deformation.

Donnell's theory is based on all four assumptions, while Flugge's theory utilizes all but the first assumption. In Flugge's theory the first assumption is modified as follows:

$(h/r)^3$ is negligible as compared with unity.

The force-displacement relations can be obtained from Hooke's Law for anisotropic material, the kinematics of deformation neglecting transverse shear deformations, and the resultant force definitions in terms of stresses. Thus, the force-displacement relation, in matrix form, becomes:

$$
\begin{Bmatrix} N_x \\ N_\theta \\ N_{x\theta} \\ N_{\theta x} \\ M_x \\ M_\theta \\ M_{x\theta} \\ M_{\theta x} \end{Bmatrix}
=
\left[\begin{array}{c|c|c|c|c|c}
A_{11}+\frac{B_{11}}{r} & A_{12}+\frac{B_{12}}{r} & A_{16}+\frac{B_{16}}{r}+\frac{D_{16}}{2r^2} & B_{11}+\frac{D_{11}}{r} & B_{12} & B_{16}+\frac{D_{16}}{2r} \\
A_{12} & A_{22} & A_{26}+\frac{D_{26}}{2r^2} & B_{12} & B_{22}-\frac{D_{22}}{r} & B_{26}-\frac{D_{26}}{2r} \\
A_{16}+\frac{B_{16}}{r} & A_{26}+\frac{B_{26}}{r} & A_{66}+\frac{B_{66}}{r}+\frac{D_{66}}{2r^2} & B_{16}+\frac{D_{16}}{r} & B_{26} & B_{66}+\frac{D_{66}}{2r} \\
A_{16} & A_{26} & A_{66}+\frac{D_{66}}{2r^2} & B_{16} & B_{26}-\frac{D_{26}}{r} & B_{66}-\frac{D_{66}}{2r} \\
B_{11}+\frac{D_{11}}{r} & B_{12}+\frac{D_{12}}{r} & B_{16}+\frac{D_{16}}{r} & D_{11} & D_{12} & D_{16} \\
B_{12} & B_{22} & B_{26} & D_{12} & D_{22} & D_{26} \\
B_{16}+\frac{D_{16}}{r} & B_{26}+\frac{D_{26}}{r} & B_{66}+\frac{D_{66}}{r} & D_{16} & D_{26} & D_{66} \\
B_{16} & B_{26} & B_{66} & D_{16} & D_{26} & D_{66}
\end{array}\right]
\begin{Bmatrix} \varepsilon_x^o \\ \varepsilon_\theta^o \\ \gamma_{x\theta}^o \\ \kappa_x \\ \kappa_\theta \\ \kappa_{x\theta} \end{Bmatrix}
$$

where
$$
\begin{Bmatrix} A_{ij} \\ B_{ij} \\ D_{ij} \end{Bmatrix} = \int_{-\frac{h}{2}}^{\frac{h}{2}} C_{ij} \begin{Bmatrix} 1 \\ z \\ z^2 \end{Bmatrix} dz, \quad i,j=1,2,6.
$$

Flugge's linear buckling equations in terms of forces can be written as follows (Reference 10 p. 422):

$$\frac{\partial N_x}{\partial x} + \frac{1}{r}\frac{\partial N_{\theta x}}{\partial \theta} - p\left(\frac{1}{r}\frac{\partial^2 u}{\partial \theta^2} - \frac{\partial w}{\partial x}\right) - P\frac{\partial^2 u}{\partial x^2} - 2T\frac{1}{r}\frac{\partial^2 u}{\partial x \partial \theta} = 0$$

$$\frac{1}{r}\frac{\partial N_\theta}{\partial \theta} + \frac{\partial N_{x\theta}}{\partial x} + \frac{1}{r^2}\frac{\partial M_\theta}{\partial \theta} + \frac{1}{r}\frac{\partial M_{x\theta}}{\partial x} - \frac{p}{r}\left(\frac{\partial^2 v}{\partial \theta^2} + \frac{\partial w}{\partial \theta}\right)$$

$$- P\frac{\partial^2 v}{\partial x^2} - \frac{2T}{r}\left(\frac{\partial^2 v}{\partial x \partial \theta} + \frac{\partial w}{\partial x}\right) = 0$$

$$\frac{1}{r^2}\frac{\partial^2 M_\theta}{\partial \theta^2} + \frac{1}{r}\left(\frac{\partial^2 M_{x\theta}}{\partial x \partial \theta} + \frac{\partial^2 M_{\theta x}}{\partial x \partial \theta}\right) + \frac{\partial^2 M_x}{\partial x^2} - \frac{N_\theta}{r}$$

$$- p\left(\frac{\partial u}{\partial x} - \frac{1}{r}\frac{\partial v}{\partial \theta} + \frac{1}{r}\frac{\partial^2 w}{\partial \theta^2}\right)$$

$$- P\frac{\partial^2 w}{\partial x^2} + \frac{2T}{r}\left(\frac{\partial v}{\partial x} - \frac{\partial^2 w}{\partial x \partial \theta}\right) = 0$$

where the positive values of p , P , and T are, respectively, the external radial pressure, the axial compression per unit length, and the torsional force per unit length. The positive sense of these quantities are shown in Figure 1a.

Substituting for the resultant forces and moments the following equilibrium equations in terms of displacements (or the Navier equations) have been developed:

$$(A_{11} + \frac{B_{11}}{r} - P) \frac{\partial^2 u}{\partial x^2} + \frac{2}{r} (A_{16} - T) \frac{\partial^2 u}{\partial x \partial \theta} + (\frac{A_{66}}{r^2} - \frac{B_{66}}{r^3} + \frac{D_{66}}{r^4} - \frac{p}{r}) \frac{\partial^2 u}{\partial \theta^2}$$

$$+(A_{16} + \frac{2B_{16}}{r} + \frac{D_{16}}{r^2}) \frac{\partial^2 v}{\partial x^2} + (\frac{A_{12}}{r} + \frac{A_{66}}{r} + \frac{B_{12}}{r^2} + \frac{B_{66}}{r^2}) \frac{\partial^2 v}{\partial x \partial \theta} + \frac{A_{26}}{r^2} \frac{\partial^2 v}{\partial \theta^2}$$

$$-(B_{11} + \frac{D_{11}}{r}) \frac{\partial^3 w}{\partial x^3} - (\frac{3B_{16}}{r} + \frac{D_{16}}{r^2}) \frac{\partial^3 w}{\partial x^2 \partial \theta} - (\frac{B_{12}}{r^2} + \frac{2B_{66}}{r^2} - \frac{D_{66}}{r^3}) \frac{\partial^3 w}{\partial x \partial \theta^2}$$

$$-(\frac{B_{26}}{r^3} - \frac{D_{26}}{r^4}) \frac{\partial^3 w}{\partial \theta^3} + (\frac{A_{12}}{r} + p) \frac{\partial w}{\partial x} + (\frac{A_{26}}{r^2} - \frac{B_{26}}{r^3} + \frac{D_{26}}{r^4}) \frac{\partial w}{\partial \theta} = 0$$

$$(A_{16} + \frac{2B_{16}}{r} + \frac{D_{16}}{r^2}) \frac{\partial^2 u}{\partial x^2} + (\frac{A_{12}}{r} + \frac{A_{66}}{r} + \frac{B_{12}}{r^2} + \frac{B_{66}}{r^2}) \frac{\partial^2 u}{\partial x \partial \theta} + \frac{A_{26}}{r^2} \frac{\partial^2 u}{\partial \theta^2}$$

$$+ (A_{66} + \frac{3B_{66}}{r} + \frac{3D_{66}}{r^2} - P) \frac{\partial^2 v}{\partial x^2} + (\frac{2A_{26}}{r} + \frac{4B_{26}}{r^2} + \frac{2D_{26}}{r^3} - \frac{2T}{r}) \frac{\partial^2 v}{\partial x \partial \theta}$$

$$+ (\frac{A_{22}}{r^2} + \frac{B_{22}}{r^3} - \frac{p}{r}) \frac{\partial^2 v}{\partial \theta^2} - (B_{16} + \frac{2D_{16}}{r}) \frac{\partial^3 w}{\partial x^3}$$

$$- (\frac{B_{12}}{r} + \frac{2B_{66}}{r} + \frac{D_{12}}{r^2} + \frac{3D_{66}}{r^2}) \frac{\partial^3 w}{\partial x^2 \partial \theta} - (\frac{3B_{26}}{r^2} + \frac{2D_{26}}{r^3}) \frac{\partial^3 w}{\partial x \partial \theta^2} - \frac{B_{22}}{r^3} \frac{\partial^3 w}{\partial \theta^3}$$

$$+ (\frac{A_{26}}{r} + \frac{B_{26}}{r^2} - \frac{2T}{r}) \frac{\partial w}{\partial x} + (\frac{A_{22}}{r^2} - \frac{p}{r}) \frac{\partial w}{\partial \theta} = 0$$

$$(B_{11} + \frac{D_{11}}{r}) \frac{\partial^3 u}{\partial x^3} + (\frac{3B_{16}}{r} + \frac{D_{16}}{r^2}) \frac{\partial^3 u}{\partial x^2 \partial \theta} + (\frac{B_{12}}{r^2} + \frac{2B_{66}}{r^2} - \frac{D_{66}}{r^3}) \frac{\partial^3 u}{\partial x \partial \theta^2}$$

$$+ (\frac{B_{26}}{r^3} - \frac{D_{26}}{r^4}) \frac{\partial^3 u}{\partial \theta^3} - (\frac{A_{12}}{r} + p) \frac{\partial u}{\partial x} + (- \frac{A_{26}}{r^2} + \frac{B_{26}}{r^3} - \frac{D_{26}}{r^4}) \frac{\partial u}{\partial \theta}$$

$$+ (B_{16} + \frac{2D_{16}}{r}) \frac{\partial^3 v}{\partial x^3} + (\frac{B_{12}}{r} + \frac{2B_{66}}{r} + \frac{D_{12}}{r^2} + \frac{3D_{66}}{r^2}) \frac{\partial^3 v}{\partial x^2 \partial \theta}$$

$$+ \left(\frac{3B_{26}}{r^2} + \frac{2D_{26}}{r^3} \right) \frac{\partial^3 v}{\partial x \partial \theta^2} + \frac{B_{22}}{r^3} \frac{\partial^3 v}{\partial \theta^3} + \left(- \frac{A_{26}}{r} - \frac{B_{26}}{r^2} + \frac{2T}{r} \right) \frac{\partial v}{\partial x}$$

$$+ \left(- \frac{A_{22}}{r^2} + \frac{p}{r} \right) \frac{\partial v}{\partial \theta} - D_{11} \frac{\partial^4 w}{\partial x^4} - \frac{4D_{16}}{r} \frac{\partial^4 w}{\partial x^3 \partial \theta} - \left(\frac{2D_{12}}{r^2} + \frac{4D_{66}}{r^2} \right) \frac{\partial^4 w}{\partial x^2 \partial \theta^2}$$

$$- \frac{4D_{26}}{r^3} \frac{\partial^4 w}{\partial x \partial \theta^3} - \frac{D_{22}}{r^4} \frac{\partial^4 w}{\partial \theta^4} + \left(\frac{2B_{12}}{r} - P \right) \frac{\partial^2 w}{\partial x^2}$$

$$+ \left(\frac{4B_{26}}{r^2} - \frac{2D_{26}}{r^3} - \frac{2T}{r} \right) \frac{\partial^2 w}{\partial x \partial \theta} + \left(\frac{2B_{22}}{r^3} - \frac{2D_{22}}{r^4} - \frac{p}{r} \right) \frac{\partial^2 w}{\partial \theta^2}$$

$$+ \left(- \frac{A_{22}}{r^2} + \frac{B_{22}}{r^3} - \frac{D_{22}}{r^4} \right) w = 0$$

where $(\bar{A}_{ij}, \bar{B}_{ij}, \bar{D}_{ij}) = (A_{ij}, \frac{B_{ij}}{r}, \frac{D_{ij}}{r^2}) / (\frac{D_{22}}{r^2})$

and $(q_1, q_2, q_3) = (pr, P, T) / (\frac{D_{22}}{r^2})$

are nondimensionalized quantities. The bars do not imply complex conjugates. These equations are valid for cylindrical shells made of anisotropic materials loaded with any combination of radial pressure, axial compression, and torsion.

Boundary Conditions

In addition to the above mentioned equations, the boundary conditions are required to complete the formulation of the buckling problem. Four boundary conditions are needed to satisfy at each end of the shell. A total of eight possible combinations of boundary conditions are considered in the analysis. They are classified and designated as follows:

For simply supported boundary conditions:

SS1 : $w = 0$, $M_x = 0$, $N_x + \frac{T}{r}\frac{\partial u}{\partial \theta} = 0$, $T_x + P\frac{\partial v}{\partial x} = 0$

SS2: $w = 0$, $M_x = 0$, $u = 0$, $v = 0$

SS3: $w = 0$, $M_x = 0$, $u = 0$ $T_x + P\frac{\partial v}{\partial x} = 0$

SS4: $w = 0$, $M_x = 0$, $N_x + \frac{T}{r}\frac{\partial u}{\partial \theta} = 0$, $v = 0$

For clamped boundary conditions:

C1: $w = 0$, $\frac{\partial w}{\partial x} = 0$, $N_x + \frac{T}{r}\frac{\partial u}{\partial \theta} = 0$, $T_x + P\frac{\partial v}{\partial x} = 0$

C2: $w = 0$, $\frac{\partial w}{\partial x} = 0$, $u = 0$, $v = 0$

C3: $w = 0$, $\frac{\partial w}{\partial x} = 0$, $u = 0$, $T_x + P\frac{\partial v}{\partial x} = 0$

C4: $w = 0$, $\frac{\partial w}{\partial x} = 0$, $N_x + \frac{T}{r}\frac{\partial u}{\partial \theta} = 0$, $v = 0$

where $T_x = N_{x\theta} + \frac{M_{x\theta}}{r}$ is the Kirchhoff boundary force. SS4 is usually known as the classical boundary condition, and SS1 is called the free boundary condition.

Method of Solution and Numerical Computations

The problem of shell buckling can be viewed as an eigenvalue proglrm. It is to find a set of displacement modes for u, v, and w which satisfy the equilibrium equations and a given set of boundary conditions. By inspection, it is not likely to find a solution which will satisfy both the equilibrium equations and the boundary conditions simultaneously. However, it is possible to find a set of displacement modes satisfying the equilibrium equations only. The homogeneous boundary conditions are then forced to be satisfied by setting the determinant of the boundary equations to zero.

Displacement Modes and Characteristic Determinant

The following displacement modes are used in the analysis of

shell buckling:

$$u = U \sin\left(\frac{\lambda x}{r} + n\theta\right)$$

$$v = V \sin\left(\frac{\lambda x}{r} + n\theta\right)$$

$$w = W \cos\left(\frac{\lambda x}{r} + n\theta\right)$$

where n is the number of waves in the circumferential direction, and U, V, and W are the undetermined coefficients. The displacement modes satisfy the equilibrium equations but do not satisfy the boundary conditions in general.

Substituting the assumed modes into the equilibrium equations, one obtains:

$$\begin{bmatrix} F_{11}-q_2\lambda^2-2q_3n\lambda-q_1n^2 & F_{12} & F_{13}+q_1\lambda \\ F_{12} & F_{22}-q_2\lambda^2-2q_3n\lambda-q_1n^2 & F_{23}-2q_3\lambda-q_1n \\ F_{13}+q_1\lambda & F_{23}-2q_3\lambda-q_1n & F_{23}-q_2\lambda^2-2q_3n\lambda-q_1n^2 \end{bmatrix} \begin{Bmatrix} U \\ V \\ W \end{Bmatrix} = 0$$

where $F_{11} = (\bar{A}_{11}+\bar{B}_{11})\lambda^2 + 2\,\bar{A}_{16}n\lambda + (\bar{A}_{66}-\bar{B}_{66} + D_{66})n^2$

$$F_{12} = (\bar{A}_{16}+2\bar{B}_{16}+\bar{D}_{16})\lambda^2 + n(\bar{A}_{12}+\bar{A}_{66}+\bar{B}_{12}+\bar{B}_{66})\lambda + \bar{A}_{26}\,n^2$$

$$F_{13} = (B_{11}+D_{11})\lambda^3 + n(3\bar{B}_{16}+\bar{D}_{16})\lambda^2 + n^2(\bar{B}_{12}+2\bar{B}_{66}-\bar{D}_{66}) + \bar{A}_{12}\lambda$$

$$+ n^3(\bar{B}_{26}-\bar{D}_{26}) + n(\bar{A}_{26}-\bar{B}_{26}+\bar{D}_{26})$$

$$F_{22} = (\bar{A}_{66}+3\bar{B}_{66}+3\bar{D}_{66})\lambda^2 + n(2\bar{A}_{26}+4\bar{B}_{26}+2\bar{D}_{26})\lambda + (\bar{A}_{22}+\bar{B}_{22})n^2$$

$$F_{23} = (\bar{B}_{16}+2\bar{D}_{16})\lambda^3 + n(\bar{B}_{12}+2\bar{B}_{66}+\bar{D}_{12}+3\bar{D}_{66})\lambda^2 + n^2(3\bar{B}_{26}+2\bar{D}_{26})\lambda$$

$$+ (\bar{A}_{26}+\bar{B}_{26})\lambda + \bar{B}_{22}\,n^3 + \bar{A}_{22}\,n$$

$$F_{33} = \bar{D}_{11}{}^{4} + 4\bar{D}_{16}\, n\lambda^3 + (2\bar{D}_{12}+4\bar{D}_{66})n^2\lambda^2 + 2\bar{B}_{12\lambda}{}^{2} + 4\bar{D}_{26}\, n^3\lambda$$

$$+ (4\bar{B}_{26}-2\bar{D}_{26})n\lambda + (2\bar{B}_{22}-2\bar{D}_{22})n^2 + (\bar{A}_{22}-\bar{B}_{22}+\bar{D}_{22}) + \bar{D}_{22}\, n^4$$

For the existence of the nontrivial solution to U, V, and W, the determinant of the coefficient matrix must be zero, i.e.:

$$\begin{vmatrix} F_{11}-q_2\lambda^2-2q_3n\lambda-q_1n^2 & F_{12} & F_{13}+q_1\lambda \\ F_{12} & F_{22}-q_2\lambda^2-2q_3n\lambda-q_1n^2 & F_{23}-2q_3\lambda-q_1n \\ F_{13}+q_1\lambda & F_{23}-2q_3\lambda-q_1n & F_{33}-q_2\lambda^2-2q_3n\lambda-q_1n^2 \end{vmatrix} = 0$$

The determinant is called the characteristic determinant.

By expanding the determinant it can be written as an eighth degree polynomial in terms of the characteristic λ :

$$a_8\lambda^8+a_7\lambda^7+a_6\lambda^6+a_5\lambda^5+a_4\lambda^4 + a_3\lambda^3 + a_2\lambda^2 + a_1\lambda + a_0 = 0$$

where a's are the coefficients in terms of $\bar{A}_{ij}$, $\bar{B}_{ij}$, $\bar{D}_{ij}$, n , and q_i. The characteristic roots are, in general, complex numbers. Since the coefficients a_i of the characteristic equations are real constants, the complex roots must form conjugate pairs. All eight roots, of course, satisfy the equilibrium equations. By the principle of superposition:

$$u = \sum_{k=1}^{8} U_k \sin\left(\frac{\lambda_k x}{r} + n\theta\right)$$

$$v = \sum_{k=1}^{8} V_k \sin\left(\frac{\lambda_k x}{r} + n\theta\right)$$

$$w = \sum_{k=1}^{8} W_k \cos\left(\frac{\lambda_k x}{r} + n\theta\right)$$

Special Cases for n = 0 and 1

For the cases of n = 0 and 1 a special treatment is required. Some of the previous investigators on shell stability either were not aware of or simply ignored this problem. The reason for the special treatment for n = 0 and 1 will be clear when the characteristic equation is further investigated.

By setting n = 0, the characteristic determinant is drastically simplified, and the characteristic equation is reduced. This equation has four repeated zero roots; therefore, the displacement modes should be modified as follows:

$$u = U_1 + U_2x + U_3x^2 + U_4x^3 + \sum_{k=5}^{8} U_k \sin \frac{\lambda_k x}{r}$$

$$v = V_1 + V_2x + V_3x^2 + V_4x^3 + \sum_{k=5}^{8} V_k \sin \frac{\lambda_k x}{r}$$

$$w = W_1 + W_2x + W_3x^2 + W_4x^3 + \sum_{k=5}^{8} W_k \cos \frac{\lambda_k x}{r}$$

Because n vanishes the variable θ is dropped out of the equations. This implies that the displacements, and consequently the stresses of the shell, are independent of the circumferential variable θ. Following similar procedure presented in the preceding section, a boundary determinant for n = 0 can be obtained.

For the case of n = 1 the characteristic equation reduces and produces two repeated zero roots, the displacement modes would become:

$$u = (U_1 + U_2x) \sin \theta + \sum_{k=3}^{8} U_k \sin \left(\frac{\lambda_k x}{r} + \theta \right)$$

$$v = (V_1 + V_2x) \sin \theta + \sum_{k=3}^{8} V_k \sin \left(\frac{\lambda_k x}{r} + \theta \right)$$

$$w = (W_1 + W_2x) \cos \theta + \sum_{k=3}^{8} W_k \cos \left(\frac{\lambda_k x}{r} + \theta \right)$$

However, the second terms, $U_2x \sin \theta$, etc., do not satisfy the

equilibrium equations. Thus, these equations are not suitable for $n = 1$ case. Further efforts to search for a set of appropriate displacement modes ended with no results. To the author's belief, it is unlikely to be able to find a set of displacement modes which will satisfy the equilibrium equations and the condition of the multiple zero roots. As a result, the effort to analyze the buckling of general anisotropic shells with $n = 1$ had to be discontinued. However, the analysis for $n = 1$ can be done with the restrictions that the shell is orthotropic, and that no torsional force is applied. The displacement modes are modified slightly to:

$$u = (U_1 + U_2 x + \sum_{k=3}^{8} U_k e^{\lambda_k x}) \sin \theta$$

$$v = (V_1 + V_2 x + \sum_{k=3}^{8} V_k e^{\lambda_k x}) \cos \theta$$

$$w = (W_1 + W_2 x + \sum_{k=3}^{8} W_k e^{\lambda_k x}) \sin \theta$$

The boundary determinant for this restricted case can be obtained by using the same procedure as mentioned before.

Numerical Computations

In the preceding section the buckling problem has been formulated as the problem of solving the Navier equations (the equilibrium equations in terms of displacements) subject to the boundary conditions. With the displacement modes the problem has been reduced to the determination of the buckling load which satisfies both the characteristic determinant and the boundary determinant. By observation it is found that these determinants are functions of the circumferential wave number n, the length to radius ratio L/r, the buckling load parameter $\bar{P}$, and the characteristic roots λ. They are all unknown quantities. Considering the complexity of the equilibrium equations and the variety of the boundary conditions, it is very unlikely that a closed form solution is obtainable for the buckling problem.

An iteration scheme has been developed to find the critical buckling load. The procedure is described as follows:

(a) Calculate the stiffness coefficients $\bar{A}$, $\bar{B}$, and $\bar{D}$ for the given material properties, layer configuration, and the length to radius ratio.

(b) Start with the circumferential wave number $n = 2$.

(c) Select the initial load $\bar{P}$ and the load increment $\Delta\bar{P}$.

(d) Calculate the eight characteristic roots λ from the characteristic equation. This is done by using the Bairstow method (11) to solve the eighth degree polynomial. The Bairstow method is particularly powerful to find the complex roots, because it is based on the successive extraction of quadratic factors from the polynomial.

(e) Evaluate the boundary determinant.

(f) Increase the load by $\Delta\bar{P}$ and repeat the steps (d) and (e) until the determinant sign is changed. Interpolate for the load corresponding to the zero determinant. This load is the critical load for the given L/r and $n = 2$.

(g) Increase n and repeat the steps (c), (d), (e), and (f), the critical load for this n is determined.

(h) The minimum value of the critical loads for all n's is the buckling load for the given L/r. The n corresponding to the minimum critical load is the critical circumferential wave number.

Remarks on Numerical Computations

The buckling load for any specified shell length and material properties is the one which satisfies both the characteristic determinant and the boundary determinant. The characteristic determinant is automatically satisfied, because the λ's are obtained by solving the characteristic equation. The only condition to be satisfied in the numerical computations is the vanishing of the boundary determinant. The exact zero determinant cannot be easily obtained from the numerical computation. Therefore, in the numerical iteration, it is assumed that there exists at least one zero determinant between two determinants of different signs. The load corresponding to the zero determinant is the buckling load. However, the problem of the false sign change of the determinant occurs frequently in the actual numerical computation. The false sign change results in obtaining an incorrect buckling load. It is well known that if matrix B is obtained from matrix A by interchaning any two of its rows (or columns), then $|B| = -|A|$. In the numerical computation of the characteristic roots, λ's, should be arranged in a certain order. Sometimes, they come out in a different order. The order of the columns of the boundary determinant is arranged in the same order as λ's. Therefore, it λ's accidentally change their order of

arrangement in the process of numerical computation, then the columns of the boundary determinant also change their order accordingly. As a result, the determinant changes its sign accidentally. This is the principal cause of the problem of the false sign change.

To eliminate the problem of the false sign change it is important to make sure that the arrangement of λ's are in the same order for all iterations.

Numerical Results

Some numerical examples are presented in this section to demonstrate the capability for analyzing the buckling problem of anisotropic cylindrical shells using the method described in the preceding chapters. The isotropic case is compared with Flugge's well-known results (10) in order to show the effectiveness and accuracy of the method. Some examples of orthotropic and anisotropic cases are then presented. The elastic constants of the materials are given as follows:

For orthotropic 3(0, 90,0):

$E_L = 40 \times 10^6$ psi

$E_T = 1.8 \times 10^6$ psi

$G_{LT} = 2.24 \times 10^6$ psi

$\mu_{LT} = 0.434$

For "Thornel 50" 4(0, $\mp$ 22.5, 90),

$E_L = 30.2 \times 10^6$ psi

$E_T = 1.26 \times 10^6$ psi

$G_{LT} = 0.778 \times 10^6$ psi

$\mu_{LT} = 0.302$

For isotropic case:

$E = 23.33 \times 10^6$ psi

$G = 10 \times 10^6$ psi

Table III Classification of Numerical Examples

Case No.	Layer Configuration	Loading Condition**	Boundary Condition	Analysis Method	Material	$\frac{r}{h}$	$k=h^2/12r^2$	$\frac{L}{r}$	Figure No.
1	Isotropic	q_2	SS4	Flügge	Isotropic	64.5	2×10^{-5}	0.015-100	3
2	3(0,90,0)	q_1	C1	Flügge	Orthotropic	64.5	2×10^{-5}	0.2-100	6
3	3(0,90,0)	q_2	C1	Flügge	Orthotropic	64.5	2×10^{-5}	0.07-200	7
4	3(0,90,0)	q_3	C1	Flügge	Orthotropic	64.5	2×10^{-5}	0.2-500	8
5	4(0,±22.5,90)	q_1	SS4	Flügge	Thornel 50*	150	3.7×10^{-6}	0.15-100	9
6	4(0,±22.5,90)	q_2	SS4	Flügge	Thornel 50	150	3.7×10^{-6}	0.015-150	11
7	4(0,±22.5,90)	q_2	SS1	Flügge	Thornel 50	150	3.7×10^{-6}	0.015-150	12
8	4(0,±22.5,90)	q_3	SS4	Flügge	Thornel 50	150	3.7×10^{-6}	0.07-400	13
9	4(0,±22.5,90)	q_1	SS4	Donnell	Thornel 50	150	3.7×10^{-6}	0.15-100	14
10	4(0,±22.5,90)	q_2	SS4	Donnell	Thornel 50	150	3.7×10^{-6}	0.015-150	15
11	4(0,±22.5,90)	q_3	SS4	Donnell	Thornel 50	150	3.7×10^{-6}	0.07-400	16
12	4(0,±22.5,90)	$q_1 + q_3$	SS4	Donnell	Thornel 50	161.6	3.19×10^{-6}	2	17
13	4(0,±22.5,90)	$q_1 + q_3$	SS4	Flügge	Thornel 50	161.6	3.19×10^{-6}	2	19
14	4(0,±22.5,90)	$q_2 + q_3$	SS4	Flügge	Thornel 50	161.6	3.19×10^{-6}	2	20
15	4(0,±22.5,90)	$q_1 + q_2$	SS4	Flügge	Thornel 50	161.6	3.19×10^{-6}	2	21
16	4(0,±22.5,90)	$q_1 + \frac{1}{2}q_2$****	SS4	Flügge	Thornel 50	64.5	2×10^{-5}	0.07-40	22
17	4(0,±22.5,90)	$q_1 + \frac{1}{2}q_2$	SS4	Donnell	Thornel 50	64.5	2×10^{-5}	0.07-40	23

* "Thornel 50" is a graphite fiber

** Loading condition: q_1 = radial pressure
q_2 = axial compression
q_3 = torsion

**** Hydrostatic pressure.

$\mu = 1/6$

The layer designation 4(0, ∓ 22.5, 90), for example, means that the shell is made of 4 layers of fiber composite with the fiber orientations 0°, -22.5°, +22.5°, and 90°. The 0° layer is the inner layer, and the 90° layer is the outer layer (see Figure 1b). The orientation angle is the angle between the fiber and the generatrix of the cylinder. The positive angle is the angle generated by the rotation around the outward adial direction z (or w) according to the left hand screw rule (see Figure 1a). It is noted that the elastic constants E and G for the isotropic case are fictitious and are made up to match the poisson's ratio $\mu = 1/6$ which has been used by Flugge.

A total of twenty cases are investigated. The layer configuration, the applied loads, the boundary conditions, the analysis theory, the shell material, the radius to thickness ratio, the k-parameter, and the length to radius ratio are tabulated for each case in Table 1. The orthotropic 3(0, 90, 0) layer configuration is chosen as the representative of the orthotropic case. The "Thornel 50" with the 4(0, ∓22.5, 90) layer configuration represents the general anisotropic case.

The boundary conditions used in the example cases are SS1, SS4 and C1. In most cases, the classical boundary condition SS4 is used. This is the one most commonly used sets of boundary conditions by previous investigators. The formulation and solution method presented in the preceding chapters are still valid for other boundary conditions.

The analysis for the circumferential wave numbers n = 0 and 1 is not included in the numerical examples. It is recognized that the cases of n = 0 and 1 require special treatment. The procedure was described in the previous section.

In the following sections the buckling characteristics for isotropic, orthotropic and anisotropic cases will be studied. The effect of Flugge's and Donnell's theories, the boundary conditions, the loading conditions, and the layer configurations on the buckling behavior of shells will be investigated.

Isotropic Case

As a test case, the isotropic cylindrical shell is chosen. The shell is under axial compression with the classical boundary condition SS4, i.e.,: $w = M_x = v = N_x + \frac{T}{r}\frac{\partial u}{\partial \theta} = 0$. For this special

case, the term involved with the torsional force T is dropped out. In order to be comparable with Flugge's results (see Reference 6, page 428) k ($= \frac{h^2}{12r^2}$) is chosen to be 2×10^{-5} or $\frac{r}{h}$ is 64.5. The range of L/r ratio is from 0.015 to 100. The result is plotted with $P(1-\mu^2)/Eh$ versus L/r and is shown in Figure 3. Only the complete curves for n = 2, 10, 14 and portions of the curves n = 3, 4, 5, 6, 7 are shown in the figure. The curves go rapidly upward for very short shells. On the other hand they remain horizontal for very long shells. As mentioned above, the curves for n = 0, 1 are not included in the figure. This curve coincides completely with the curve of $k = 2 \times 10^{-5}$ given by Flugge in Reference 10.

Orthotropic Case

As the example for orthotropic case, a 3(0,90,0) layer configuration is used. The r/h and k are chosen the same as the isotropic case. The elastic properties of the plywood are given in the first part of this section. The buckling loads for the shell under the loading of radial pressure, axial compression, or torsional force are shown in Figures 4, 5, 6 respectively. The boundary condition is C1, i.e.,

$$w = \frac{\partial w}{\partial x} = N_x + \frac{T}{r}\frac{\partial u}{\partial \theta} = T_x + P\frac{\partial v}{\partial x} = 0 \quad .$$

For the radial pressure and torsion cases, the buckling curves in Figures 4 and 6 rise monotonically as L/r ratios decrease. The shape of the buckling curves for orthotropic is similar to that of the isotropic case (Reference 10, p. 433). This implies that the buckling characteristic of an orthotropic shell under radial pressure or torsional force shall be the same as the isotropic case. The circumferential wave number n is 2 for long cylinder and gradually increases to over 25 as the cylinder becomes shorter. For the very long cylinder n is always 2 and the buckling load remains constant. It should be noted that the buckling curves have an unusual behavior for the very short cylinder. As shown in Figure 4, the curves drop back drastically for $L/r < 1$. For the torsion case the buckling load reaches the value of 0.239 at $L/r \approx 0.08$, and it remains constant thereafter. (The points are beyond the upper limit of Figure 6, therefore they are not shown in the figure). The cause of this strange behavior is not yet known.

For the axial compression case, the buckling curves are different from those for radial pressure and torsional force cases. The buckling loads remain fairly constant for $1 < L/r < 15$. They drop

about 80% of the previous value for $L/r = 20$ and remain constant for $L/r > 100$. For the very short cylinder ($L/r < 1$) the buckling loads increase rapidly. The critical circumferential wave number is 2 for very long and very short cylinders. However, it becomes 6 or 7 for the medium cylinder length.

General Anisotropic Case

Single Loading

The layer configuration of $4(0, \mp 22.5, 90)$ is chosen as examples for the anisotropic case, because the membrane-bending coupling stiffness matrix B has six non-zero elements, i.e.,

$$B = \begin{bmatrix} x & 0 & x \\ 0 & x & x \\ x & x & 0 \end{bmatrix}$$

Cases 5 through 11 are considered in this section. The shell material is "Thornel 50" fibers in an epoxy matrix (ERL 2256 with MPDA). The radius to thickness ratio r/h is 150. This is equivalent to $k = 3.7 \times 10^{-6}$. Three different loadings are considered: the external radial pressure, the axial compression, and the torsion force. Both Flugge's and Donnell's theories are used in the buckling analysis. The boundary condition imposed at the ends of the shell is the classical boundary condition SS4. For the purpose of comparison the free boundary condition SS1 is also used for the axial compression with Flugge's theory (Case 7).

The shapes of the buckling curves, Figures 7 are, in general, the same as those of the isotropic and orthotropic case. For the radial pressure and torsional force cases, the buckling load is the lowest for long cylinders, and it increases as the cylinder becomes shorter. The increasing rate of the buckling load for the radial pressure is higher than that for the torsional force case. The critical circumferential wave number is also lower ($n = 2$) for long cylinders and higher for short cylinders.

The differences between Flugge's theory and Donnell's theory are insignificant for most cases. However, the differences are quite significant whenever the critical circumferential wave numbers are small ($n = 2,3$). The reason for this deviation is obvious from the well known fact found by Hoff (12) that the characteristic roots obtained by Donnell's theory are inaccurate for $n < 4$. In the numerical examples the buckling loads are significantly different: (a) in $L/r > 10$ for radial pressure case (Figures 7 and 11); (b) in $L/r > 30$ for torsional force case (Figures 10 and 13); and (c) in

L/r > 10 for axial compression case (Figures 8 and 12). Particularly in the axial compression case, the discrepancies are not only in the buckling loads but also in the critical circumferential wave numbers mostly n = 2,3 for Flugge's theory in contrast to n = 12, 13 14 for Donnell's theory.

Combined Loading

The same layer configuration of 4(0, ∓22.5,90) and shell material "Thornel 50" in epoxy are used for combined loading cases, Cases 12 through 17. The classical boundary condition SS4 is imposed on the ends of the shells. The following combinations of loading conditions are applied to the cylinders: (a) radial pressure and torsion, (b) axial and torsional forces, (c) radial pressure and axial force, (d) hydrostatic pressure. The last case occurs if a cylinder with both ends closed is submerged into deep water. The cylindrical tank is subjected to hydrostatic pressure on all surfaces; this is equivalent to a cylindrical shell (without end surfaces) loaded with one unit of external radial pressure on the cylinder surface and 1/2 unit of axial compression at both ends of the cylinder.

For cases 12 through 15 the load ratio is varied while the L/r ratio is fixed at 2. For the hydrostatic cases (Cases 16 and 17) the load ratio is fixed at 1: 1/2 while the L/r ratio is varied.

Figures 14 through 20 show the numerical results of the combined loading cases. Figure 15 shows the detail of Case 12 in the external pressure region. It is seen clearly how the critical circumferential wave number n changes from 8 for purely external pressure to 10 for pure torsion.

The shape of the buckling curves for the hydrostatic case (Figures 19 and 20) is similar to that of radial pressure case. Although the ratio of radial pressure to axial compression is 1 to 1/2, the buckling behavior for this case is strongly dominated by the radial pressure.

The effects of the layer configuration can be seen from Figures 14,16 and 17. The buckling loads are slightly higher in the negative torsion region than in the positive torsion region. This is due to the unbalanced lamination of the shell with 4(0,∓22.5,90).

Special Topics

In the preceding sections the buckling analysis is discussed separately for the isotropic, the orthotropic, and anisotropic cases. The following is a discussion on the specific topics concerning all cases.

Effects of Flugge's and Donnell's theories

To illustrate the effects of different shell theories on the buckling loads the following numerical results are given in tabulated form:

Table 2. Buckling Loads and Circumferential Wave Numbers

Case	L/r	Flugge (n)	Donnell (n)	$(1-\frac{\text{Flugge}}{\text{Donnell}})(\%)$
5 and 9 (q_1)	2	$0.35887\times10^{-4}(8)$	$0.36057\times10^{-4}(8)$	0.4
	100	$0.14250\times10^{-5}(2)$	$0.18560\times10^{-5}(2)$	23.2
6 and 10 (q_2)	2	$0.70538\times10^{-3}(13)$	$0.72380\times10^{-3}(13)$	2.5
	100	$0.5050\times10^{-3}(2)$	$0.82085\times10^{-3}(2)$	38.5
8 and 11 (q_3)	2	$0.15729\times10^{-3}(10)$	$0.15735\times10^{-3}(10)$	0.0
	100	$0.23810\times10^{-4}(2)$	$0.26215\times10^{-4}(2)$	9.2
12 and 13 (q_1+q_3)*	2	$0.30884\times10^{-4}(8)$	$0.30987\times10^{-4}(8)$	0.3
16 and 17 ($q_1+\frac{1}{2}q_2$)**	2	$0.12719\times10^{-3}(6)$	$0.13000\times10^{-3}(6)$	2.2
	30	$0.8\times10^{-5}(2)$	$0.1\times10^{-4}(2)$	20.0

* $q_1 : q_3 = 1 : 1$

** Hydrostatic pressure

These are only a small number of samples taken out of the figures of the numerical examples presented in the previous sections. The number in the parenthesis listed after the buckling load is the corresponding circumferential wave number. The table shows that the differences range from 9.2% to 38.5% for the cases with $n = 2$, and that the differences are less than 2.5% for the cases with $n > 2$. As mentioned in previous discussion, the cause for this deviation is obviously due to the inaccuracy of Donnell's theory with $n = 2,3$. It has been shown by Hoff that the characteristic roots of Donnell's equations with $n < 4$ are inaccurate in isotropic cases. (12)

Effects of Boundary Conditions

The effects of boundary conditions on the buckling loads have been studied by many investigators. Hoff (13) has found that the buckling load of isotropic cylinders under axial compression with boundary condition SS1 is 1/2 of the classical buckling load (SS4). Later, Lei and Cheng (9) have investigated the orthotropic cylinders and have found that the minimum critical axial compression of a shell with SS1 boundary condition is as low as 79% of the minimum critical axial compression of a shell with SS4 boundary condition.

Three different cases are investigated in this study, i.e.: isotropic, orthotropic, and anisotropic. The buckling loads are calculated for cylinders under axial compression with boundary conditions SS1 and SS4. Flugge's equations are used. Some of the results are tabulated as follows:

Table 3. Buckling Loads of Axial Compression (K_p)

	L/r	For SS1 (n)	For SS4 (n)	$\frac{SS1}{SS4}$ (%)
Isotropic	0.3	0.4091×10^{-2}(2)	0.8820×10^{-2}(7)	46.4
($\frac{R}{h}$ = 64.5)	0.5	0.4493×10^{-2}(2)	0.8825×10^{-2}(7)	50.9
($k=2 \times 10^{-5}$)	1	0.4582×10^{-2}(2)	0.8370×10^{-2}(6)	54.8
	100	0.5584×10^{-2}(2)	0.5250×10^{-2}(2)	105.4
Orthotropic 3(0,90,0)	2	0.1502×10^{-2}(7)	0.1586×10^{-2}(7)	94.7
($\frac{R}{h}$ = 64.5)	100	0.1428×10^{-2}(2)	0.1446×10^{-2}(2)	98.7
Anisotropic 4(0,∓22.5,90)	0.5	0.5425×10^{-3}(9)	0.7249×10^{-3}(12)	75.0
($\frac{R}{h}$ = 150)	2	0.5634×10^{-3}(6)	0.7054×10^{-3}(13)	79.8
	20	0.5828×10^{-3}(2)	0.7140×10^{-3}(2)	81.7
	100	0.5044×10^{-3}(2)	0.5050×10^{-3}(2)	99.8

For the isotropic case, the buckling loads with the SS1 boundary condition are only 46.4% to 54.8% of those with the SS4 boundary condition for short cylinders ($L/r < 1$). However, for long cylinders ($L/r > 100$), the buckling load of SS1 is 5% higher than that of SS4.

For the orthotropic case the effects of the boundary conditions are insignificant - - less than 5% difference. The boundary effect for the anisotropic case is moderate. It ranges from 75% for the very short cylinder ($L/r = 0.5$) to 99.8% for the very long cylinder ($L/r > 100$).

In general, the boundary condition has significant influence on the buckling loads for short cylinders, but has little effect for long cylinders.

In addition to the above mentioned effects the boundary condition also influences the shapes of the buckling curves. For the SS1 case the critical buckling load for the medium length cylinders increases steadily as the length increases (see Figure 9). This is in contrast to the SS4 case for which the buckling load decreases slightly as the length increases (see Figure 8). The critical circumferential wave numbers range from 3 to 9 for SS1 as compared with $n = 12, 13, 14$ for SS4.

Combined Loading and Buckling Surface

The study on the buckling of anisotropic cylindrical shell under combined loading is done for a specific shell with $4(0,\mp 22.5,90)$ layer configuration, SS4 boundary condition, $r/h = 161.6$ and $L/r = 2$. The results have been given in Figures 16 through 18.

Figure 16 shows that the interaction curve of the radial pressure and torsional force is slightly deviated from symmetry about the axis of the radial pressure, and that the buckling load due to the negative torsional force is a little higher than that of the positive torsional force. It is observed that the internal radial pressure tends to strengthen the cylinder while the external radial pressure tends to weaken the cylinder. The interaction curve resembles the shape of a parabola, and its open end is on the side of the internal pressure. Therefore, the cylinder will never buckle under internal radial pressure alone.

The interaction curve of the axial and torsional force given in Figure 17 is similar to that of the radial pressure and torsional force. The cylinder is slightly stronger against the combined axial and negative torsional forces than against the combined axial and positive torsional forces. The reason is clearly due to the

unbalanced layer configuration of the cylinder. The unbalanced layer configuration also contributed to the fact that the highest strength against the axial compression is not under the pure axial compression but under the axial compression combined with a small negative torsional force. Also in a similar manner, the axial compression tends weaken the cylinder while the axial tension tends to strengthen the cylinder. The cylinder will never buckle under axial tension alone.

The combined radial pressure and axial force as shown in Figure 18 is completely different from the other two cases mentioned above. If the figure is divided into four quadrants as shown, the cylinder will buckle in quadrant I, i.e., the combination of the external radial pressure and the axial compression; the cylinder will be stronger with increasing internal radial pressure in quadrant II and also with increasing axial tension in quadrant IV; it will never buckle in quadrant III, i.e., under internal radial pressure or axial tension or any combination of both.

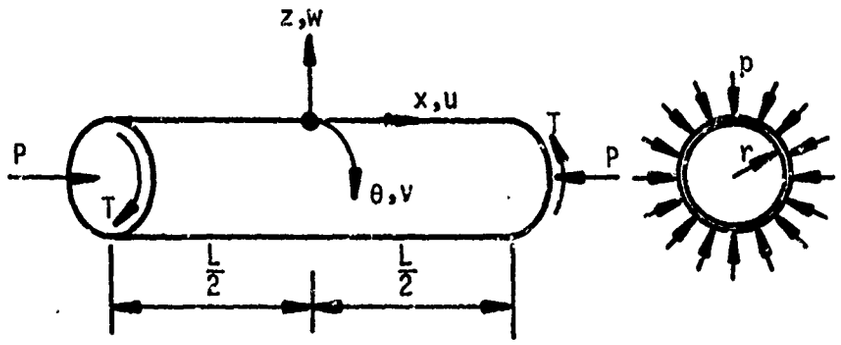

(a) Shell Coordinate System and Applied Loads

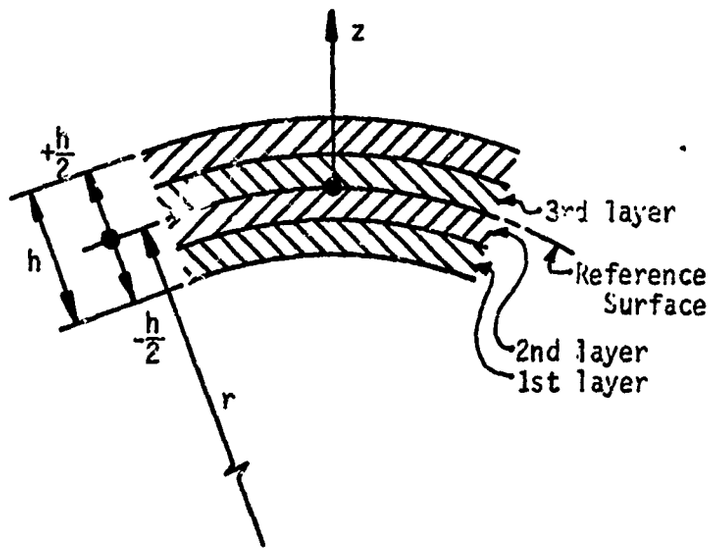

(b) Layer Configuration

Figure 1. Shell Geometry and Layer Configuration

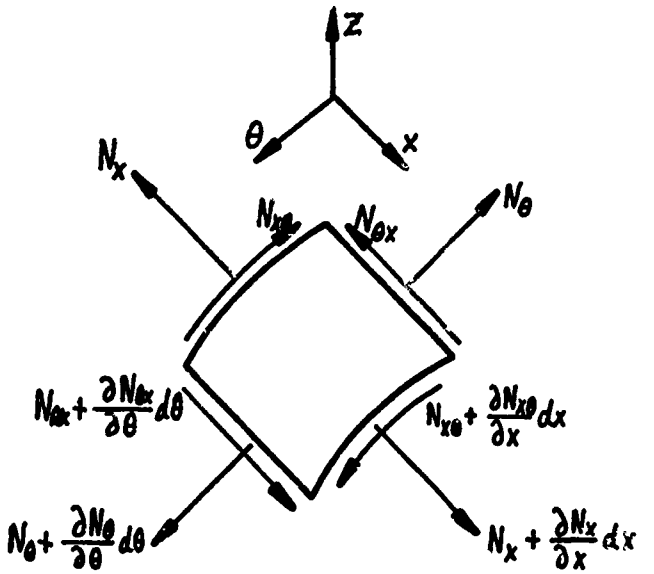

(Transverse Shearing Stress
Resultants not Shown)

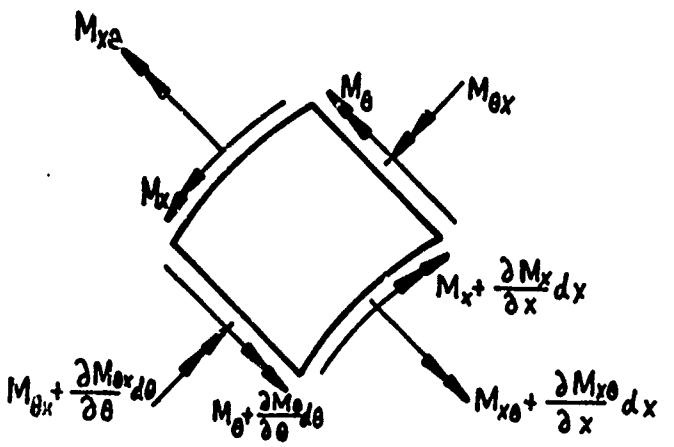

Figure 2. Stress Resultants and Stress Couples in Shell Element

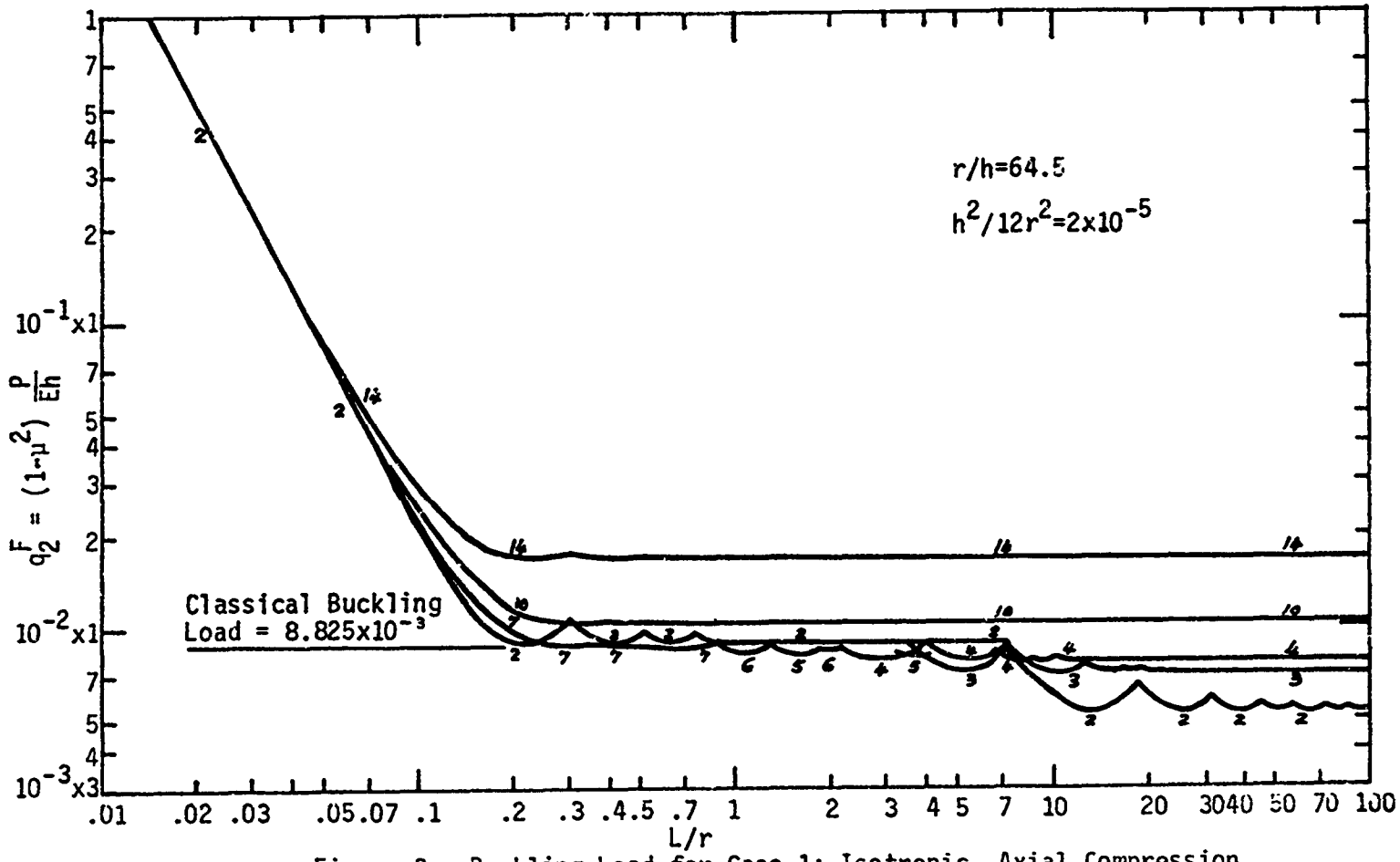

Figure 3. Buckling Load for Case 1: Isotropic, Axial Compression, SS4, Flügge's Theory

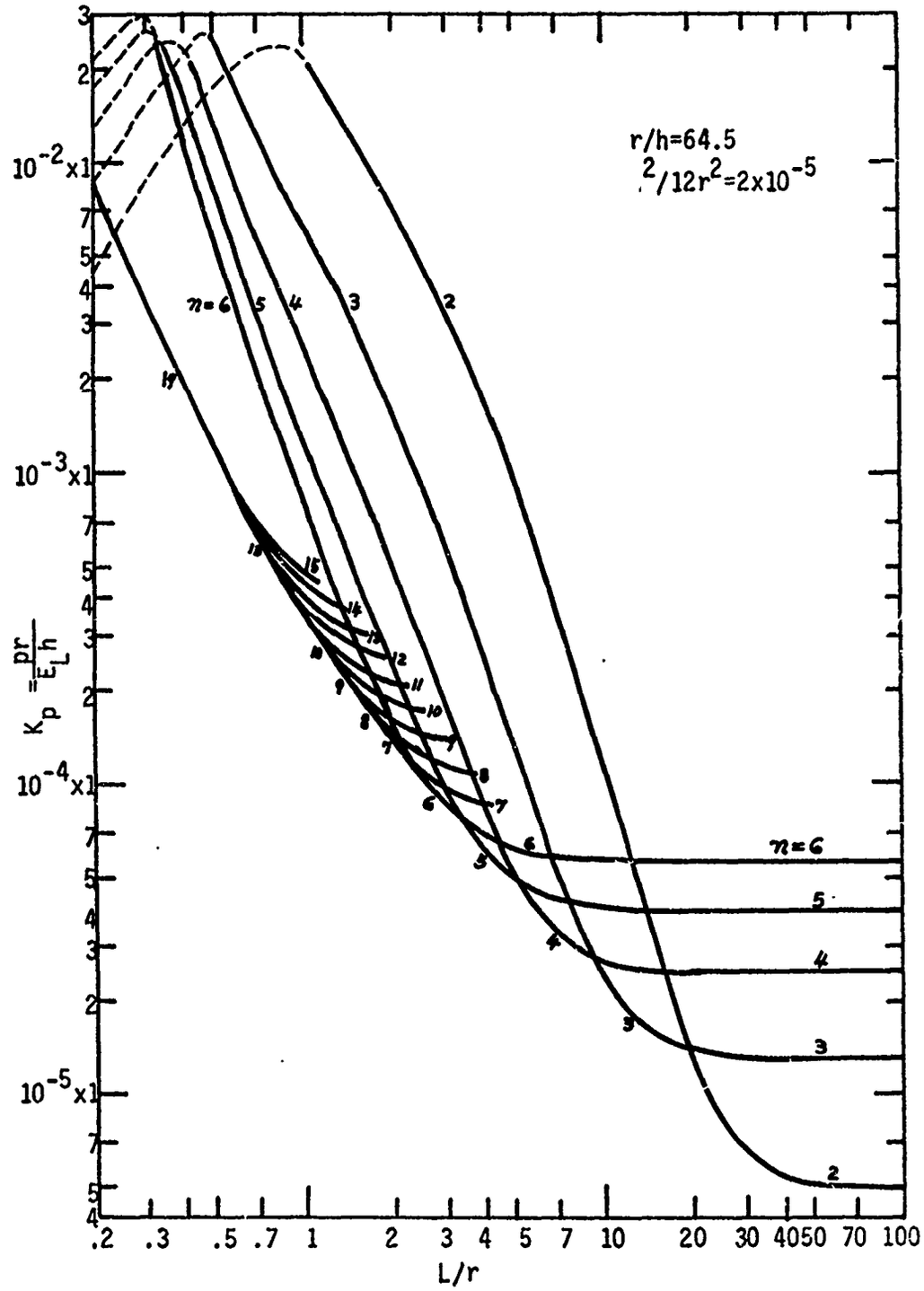

Figure 4. Buckling Load for Case 2: 3(0, 90, 0), Radial Pressure, C1, Flügge's Theory

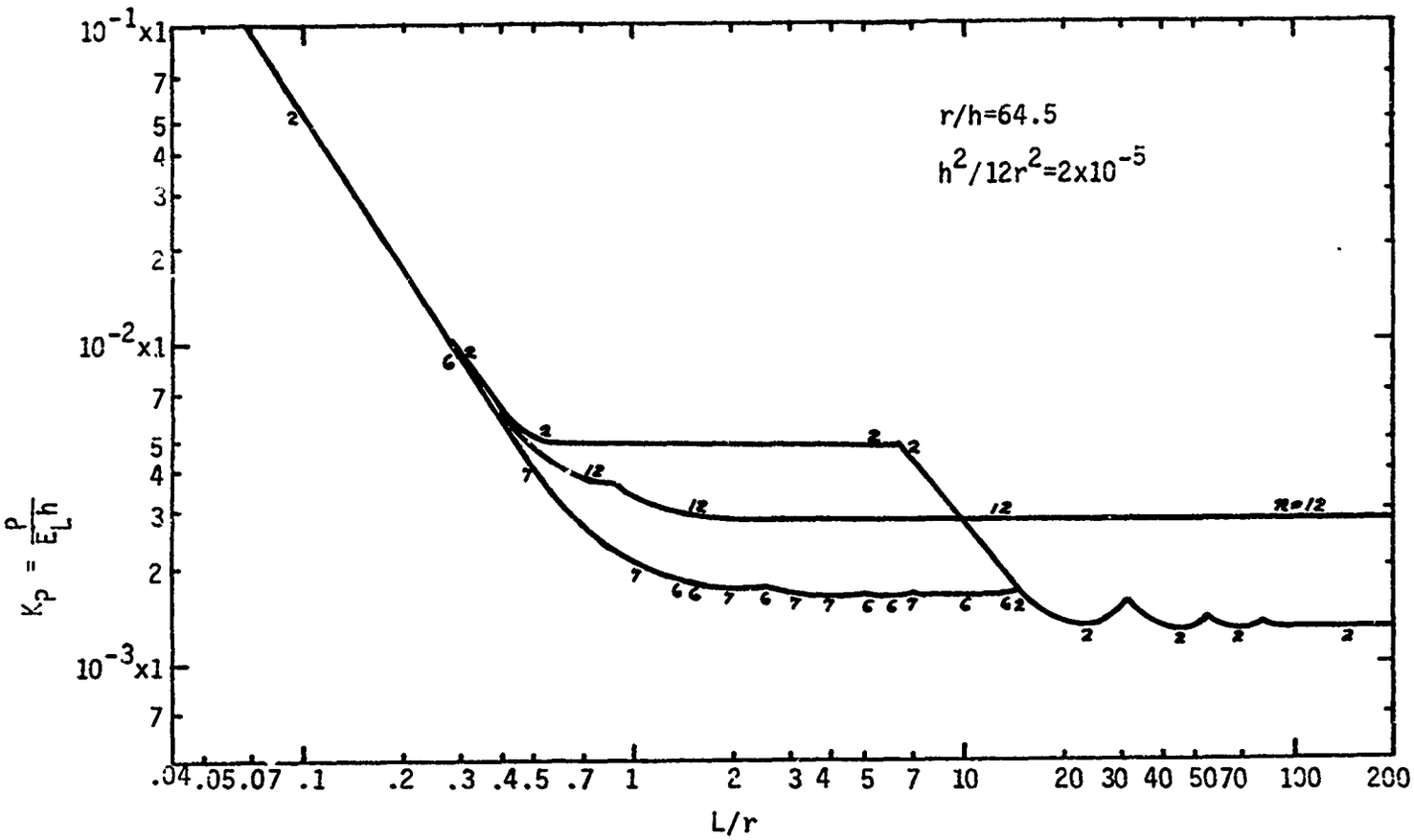

Figure 5. Buckling Load for Case 3: 3(0, 90, 0), Axial Compression, C1, Flugge's Theory

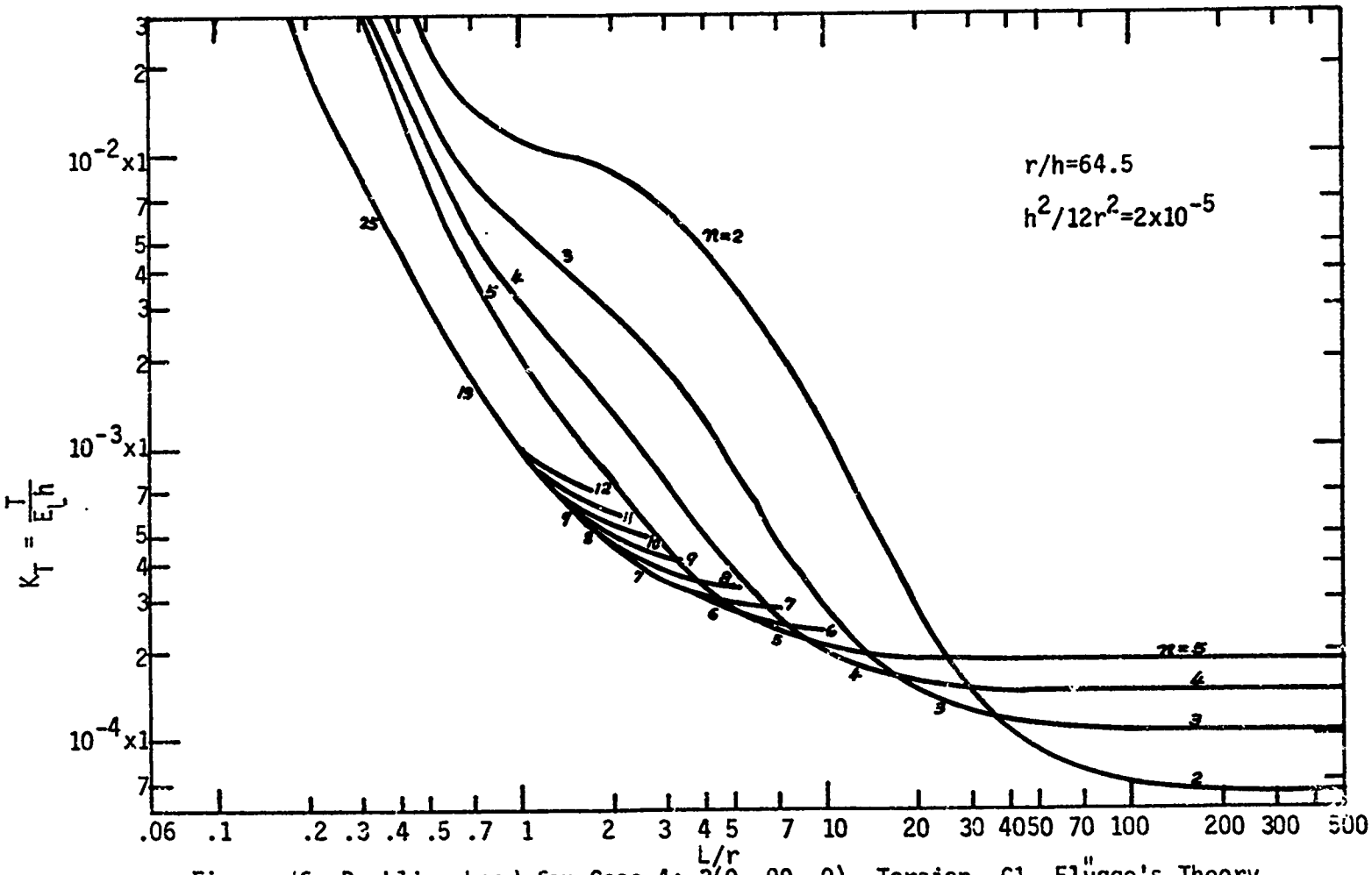

Figure 16. Buckling Load for Case 4: 3(0, 90, 0), Torsion, C1, Flügge's Theory

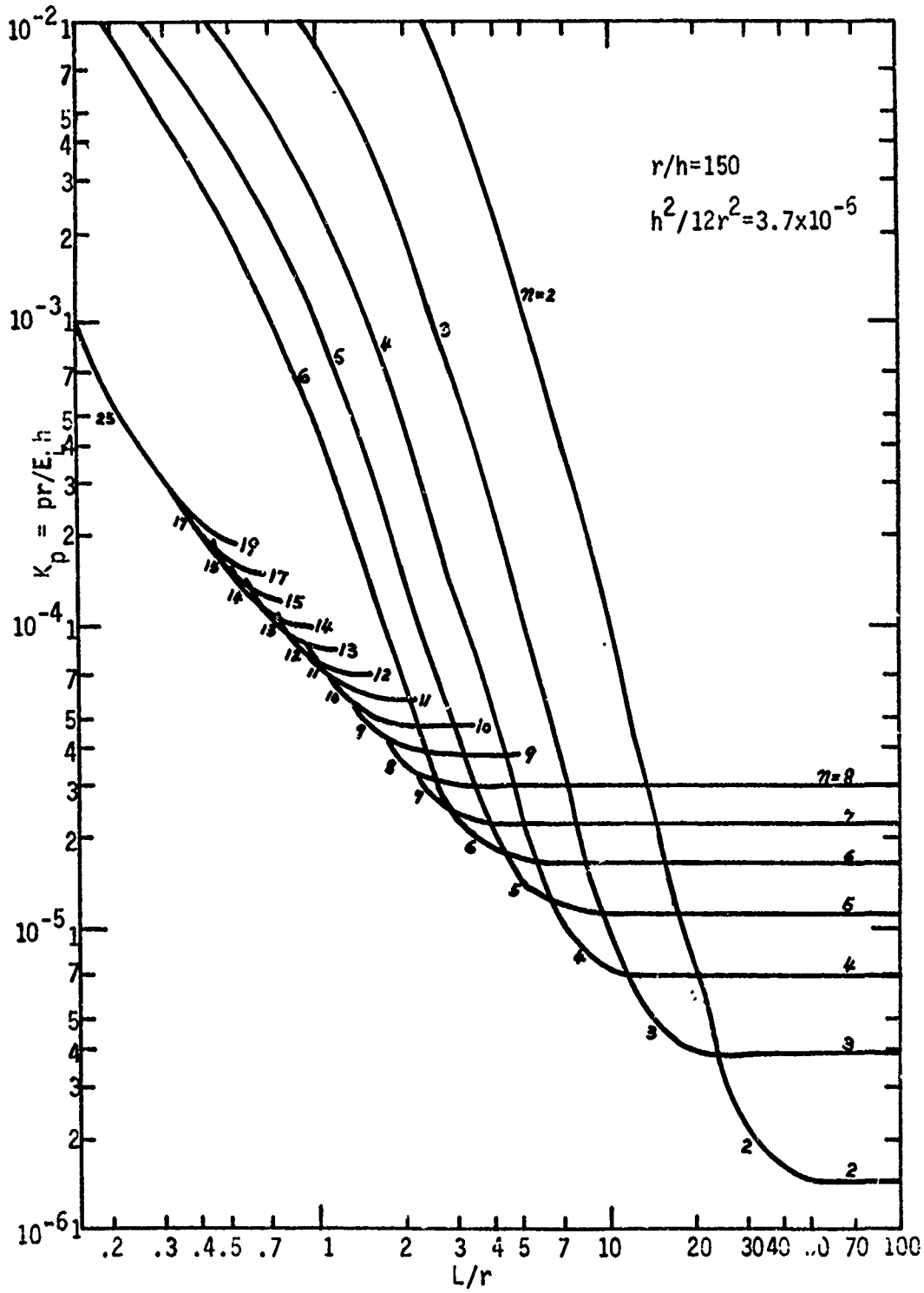

Figure 7. Buckling Load for Case 5: 4(0,±22.5, 90), Radial Pressure, SS4, Flugge's Theory

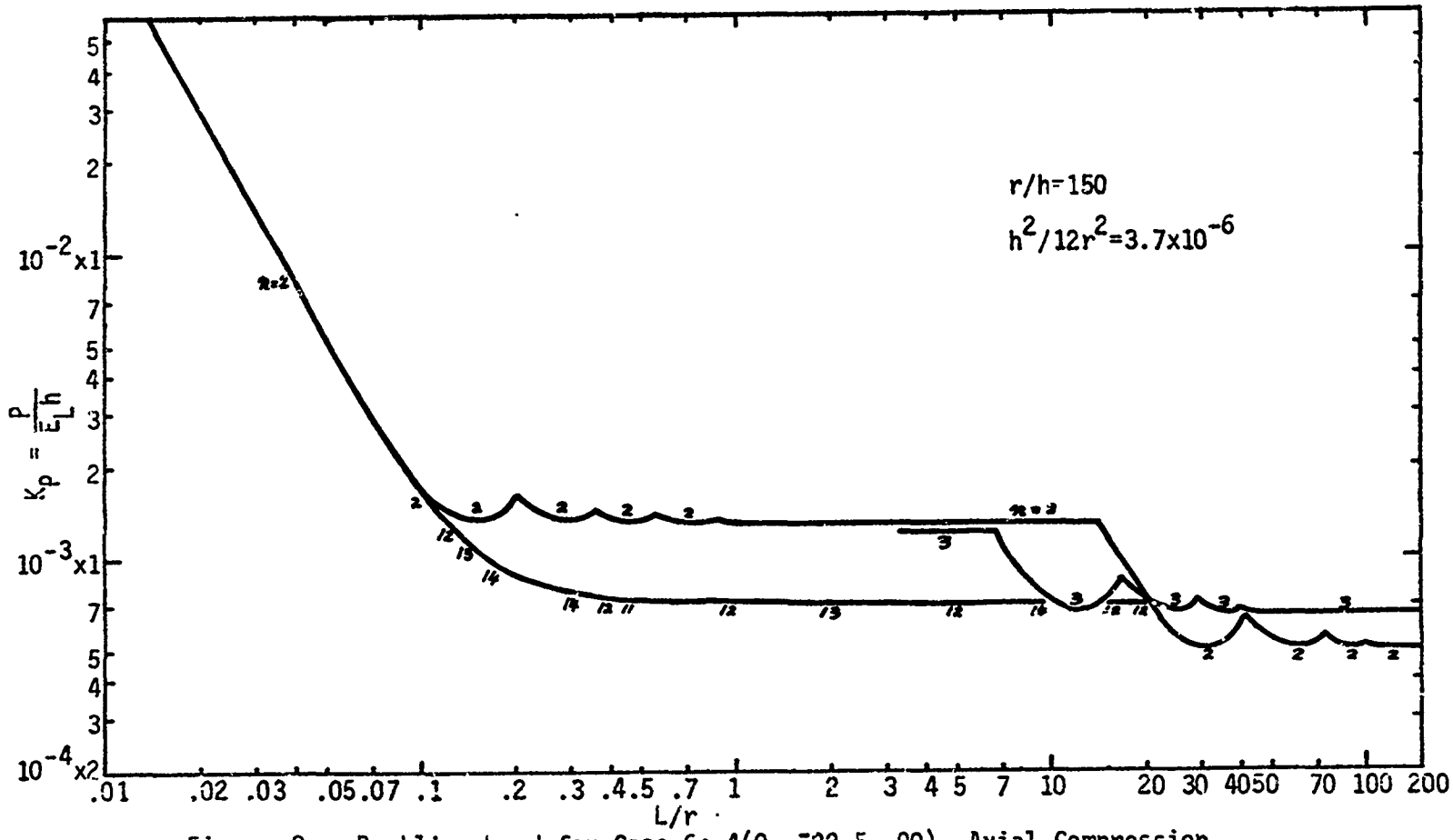

Figure 8. Buckling Load for Case 6: 4(0, ∓22.5, 90), Axial Compression, SS4, Flugge's Theory

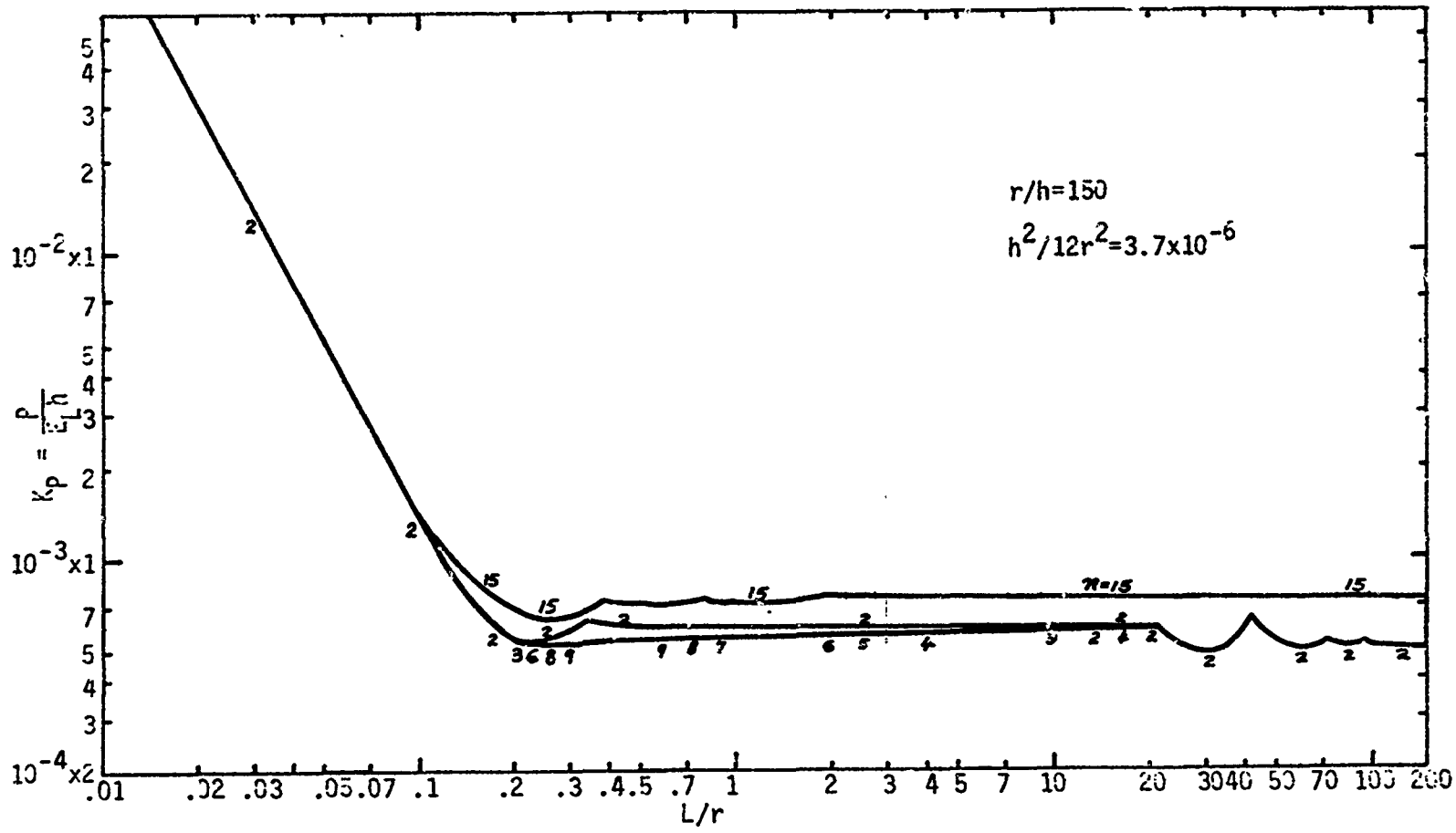

Figure 9. Buckling Load for Case 7: 4(0, ∓22.5, 90), Axial Compression, SS1, Flügge's Theory

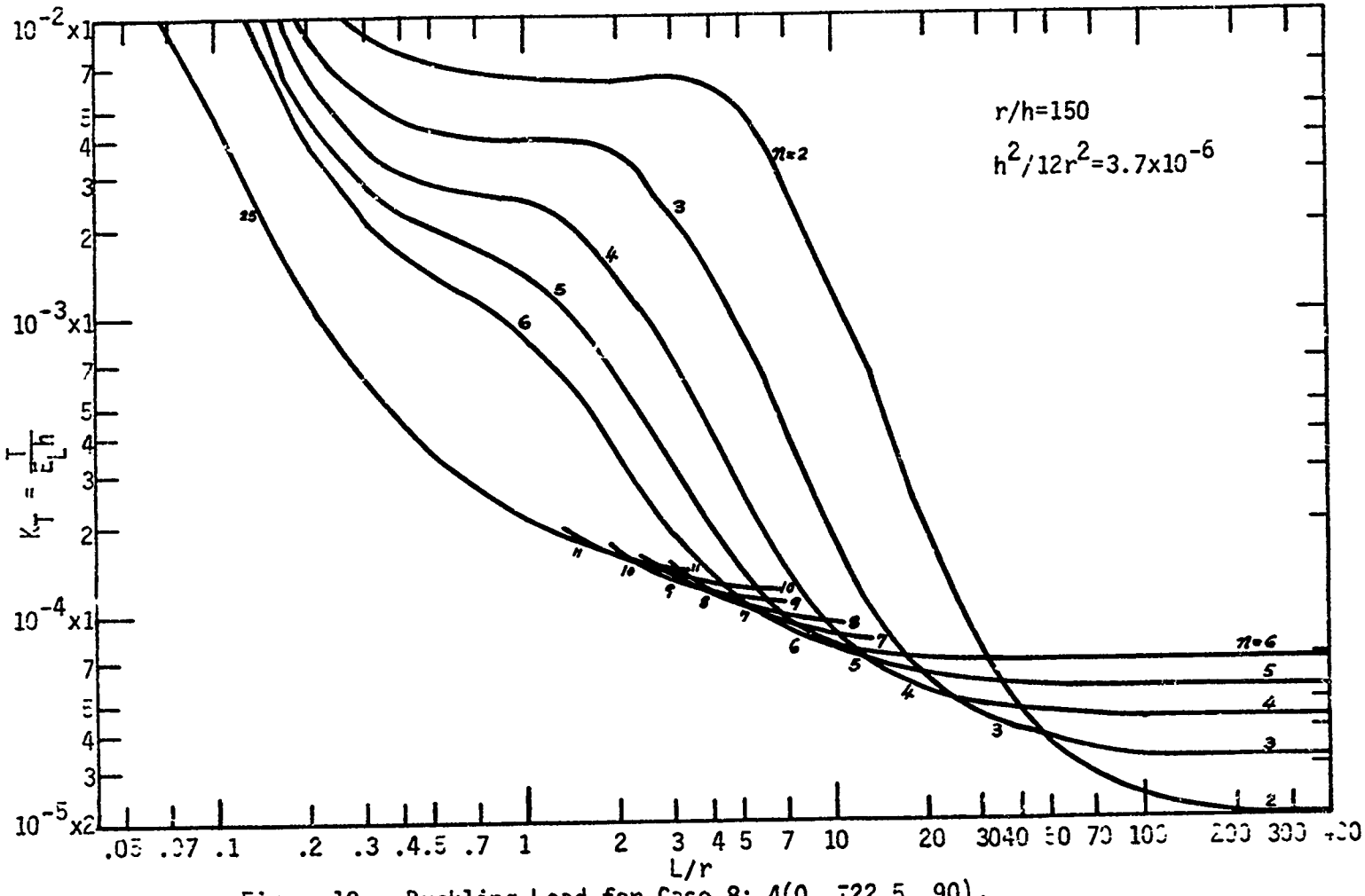

Figure 10. Buckling Load for Case 8: 4(0, ∓22.5, 90), Torsion, SS4, Flügge's Theory

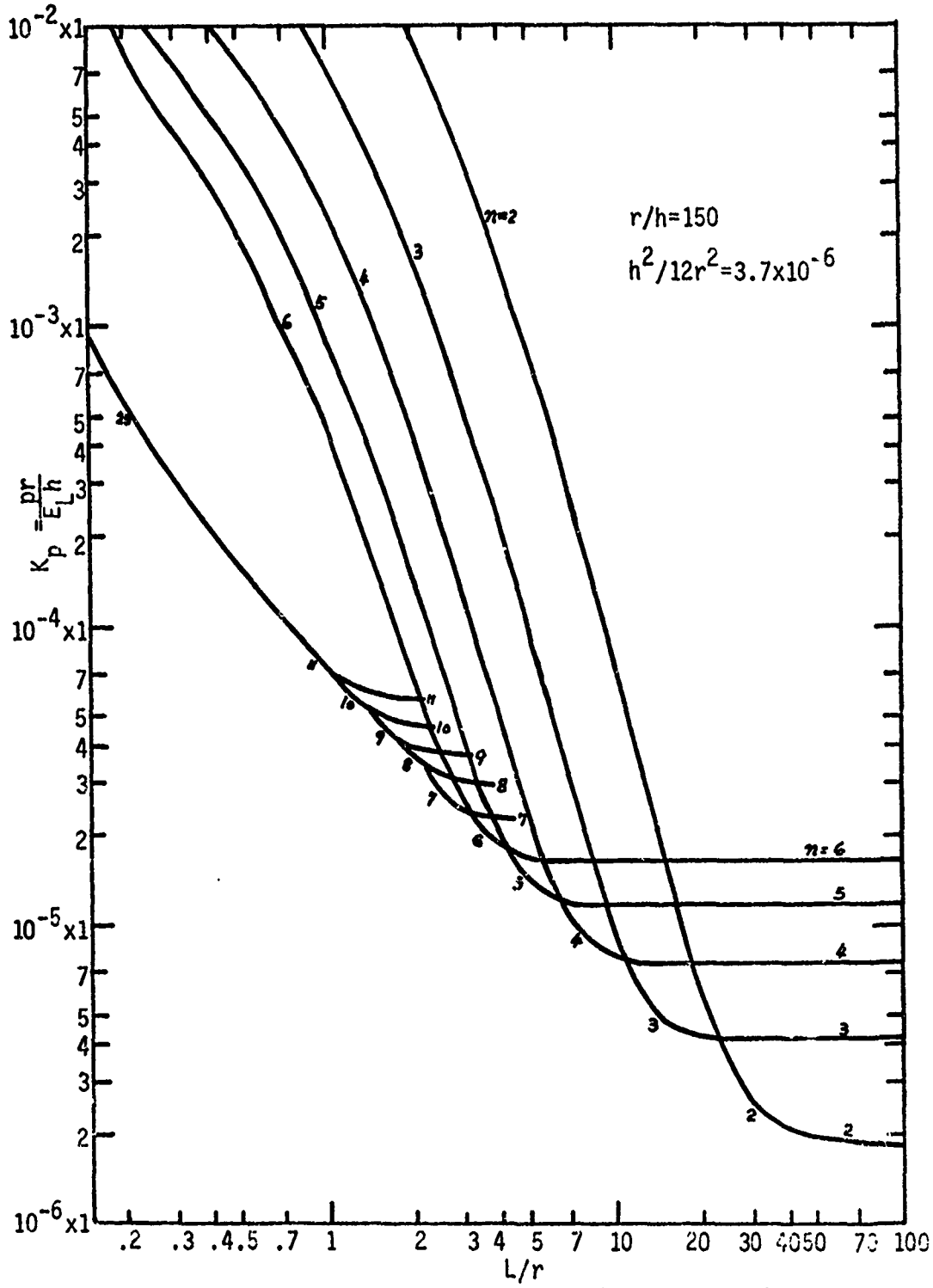

Figure 11. Buckling Load for Case 9: 4(0, ∓22.5, 90), Radial Pressure, SS4, Donnell's Theory

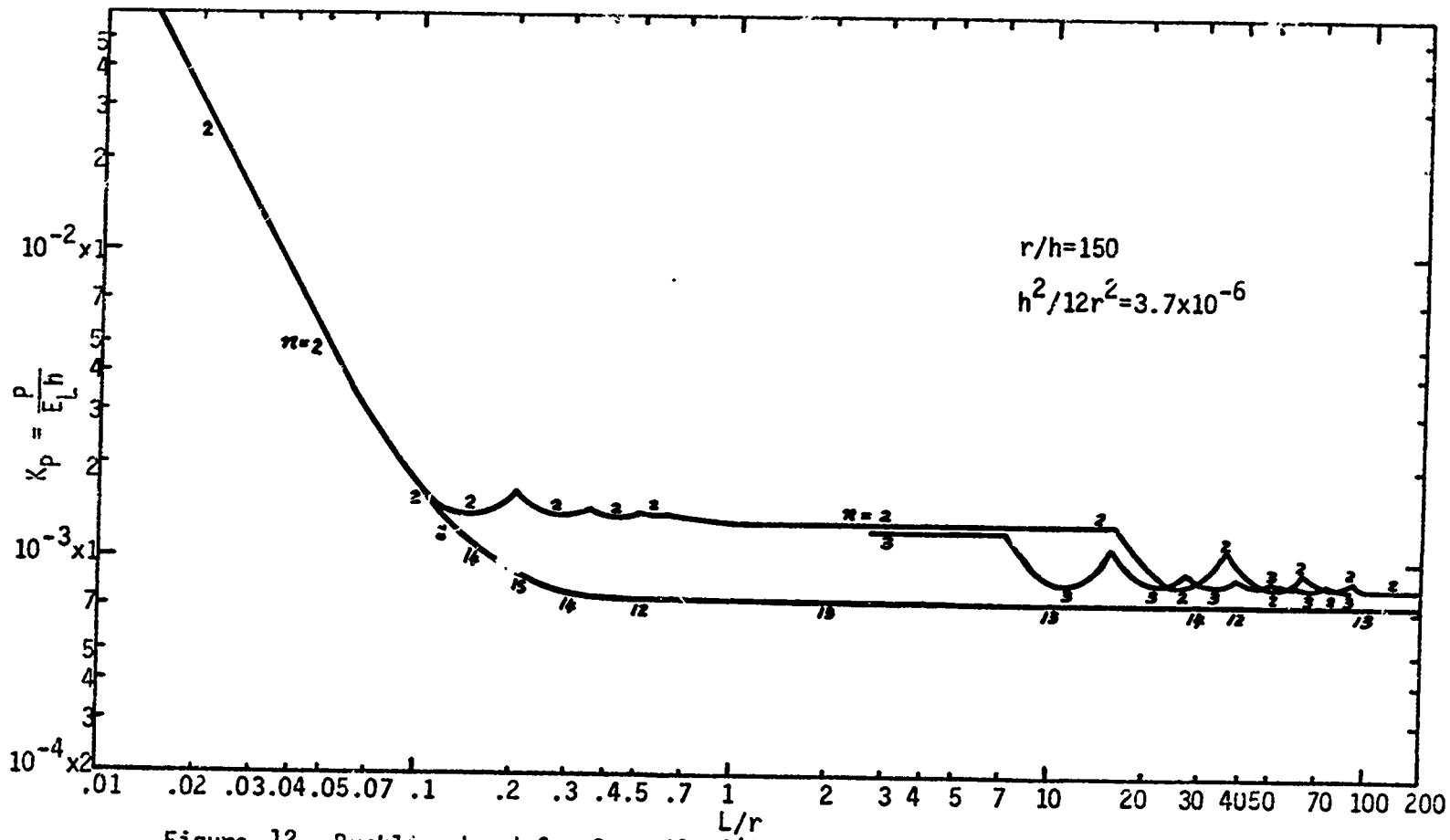

Figure 12. Buckling Load for Case 10: 4(0, ∓22.5, 90), Axial Compression, SS4, Donnell's Theory

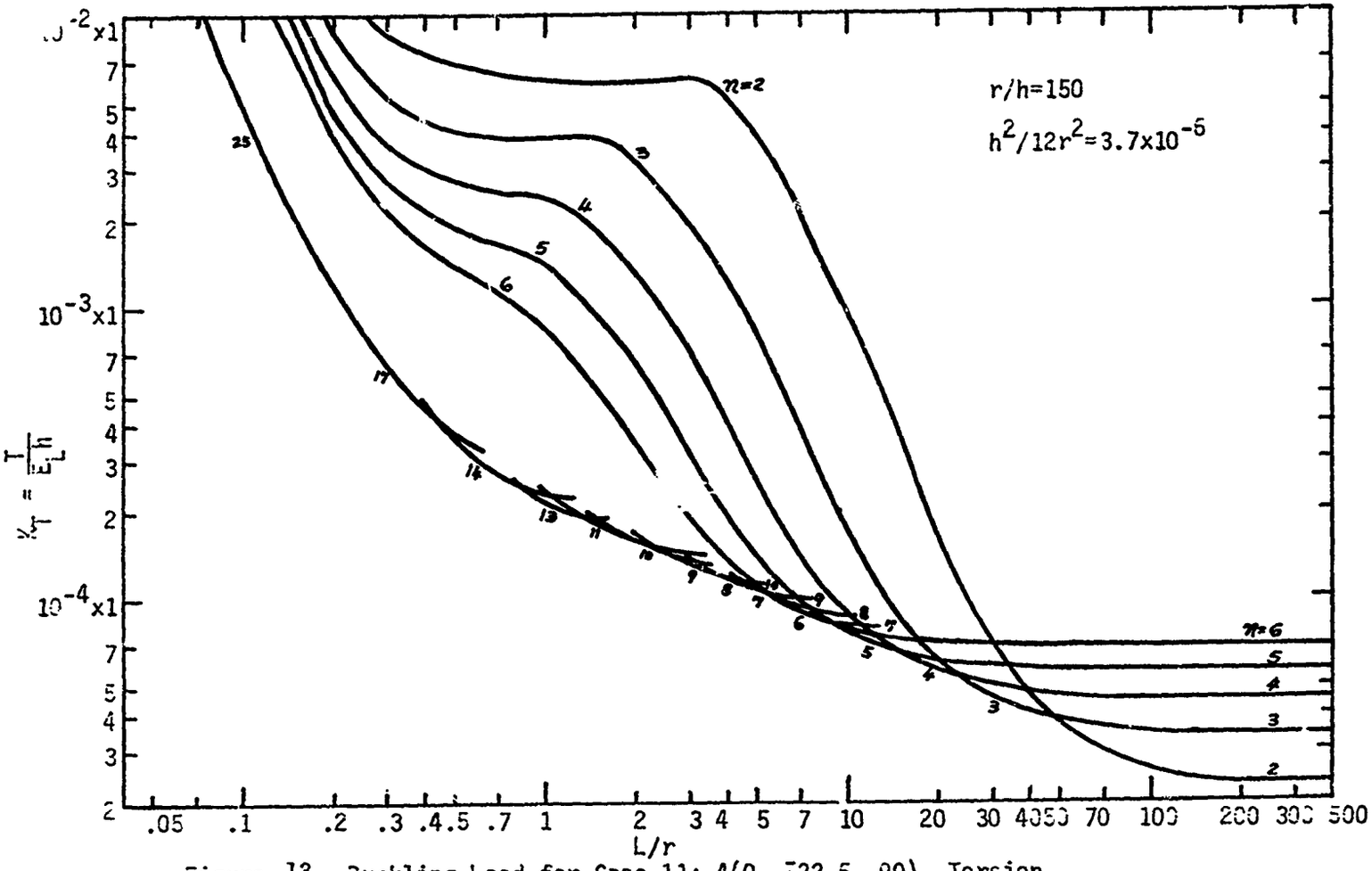

Figure 13. Buckling Load for Case 11: 4(0, ∓22.5, 90), Torsion, SS4, Donnell's Theory

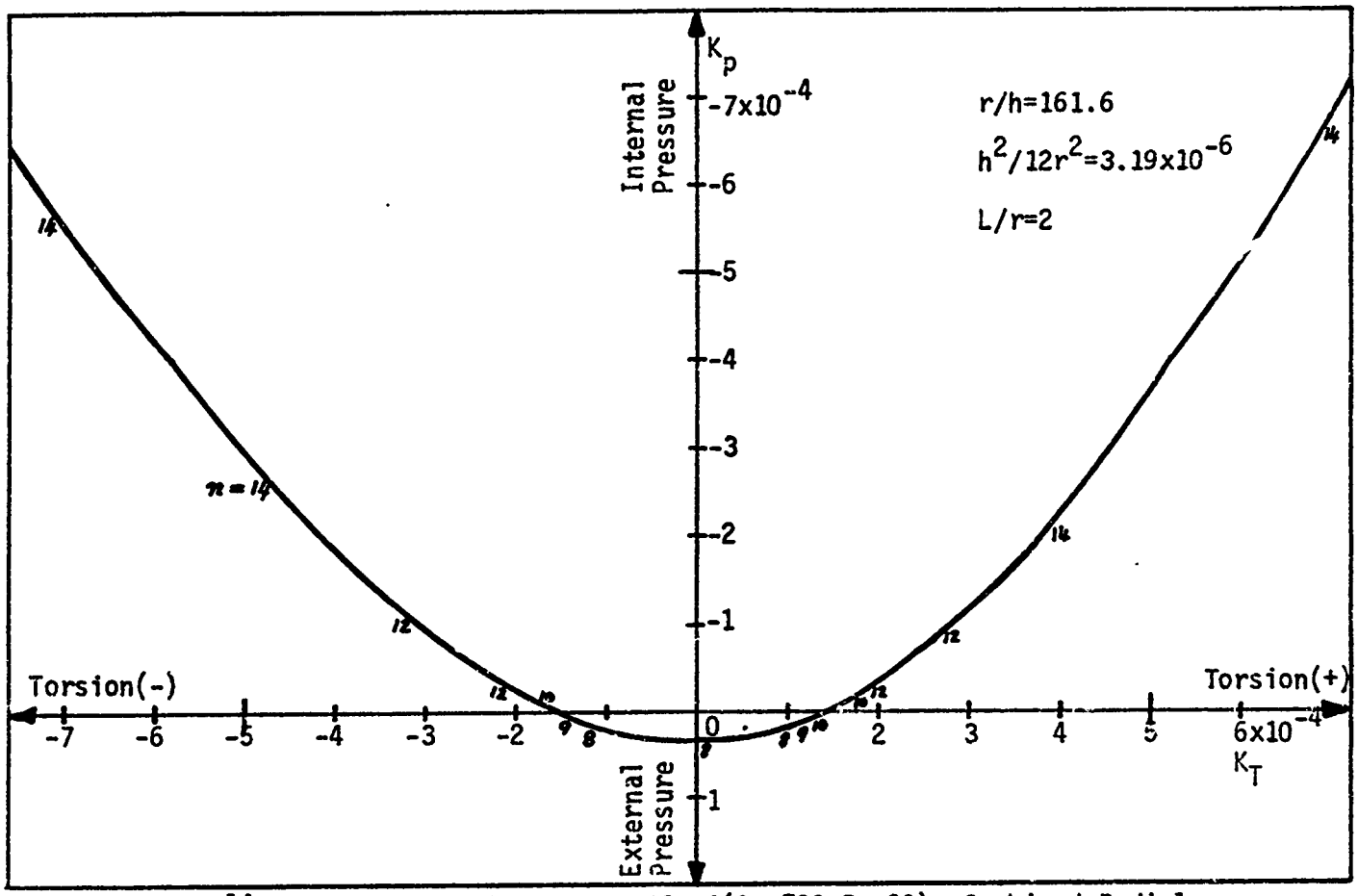

Figure 14. Buckling Load for Case 12: 4(0, ∓22.5, 90), Combined Radial Pressure and Torsion, SS4, Donnell's Theory

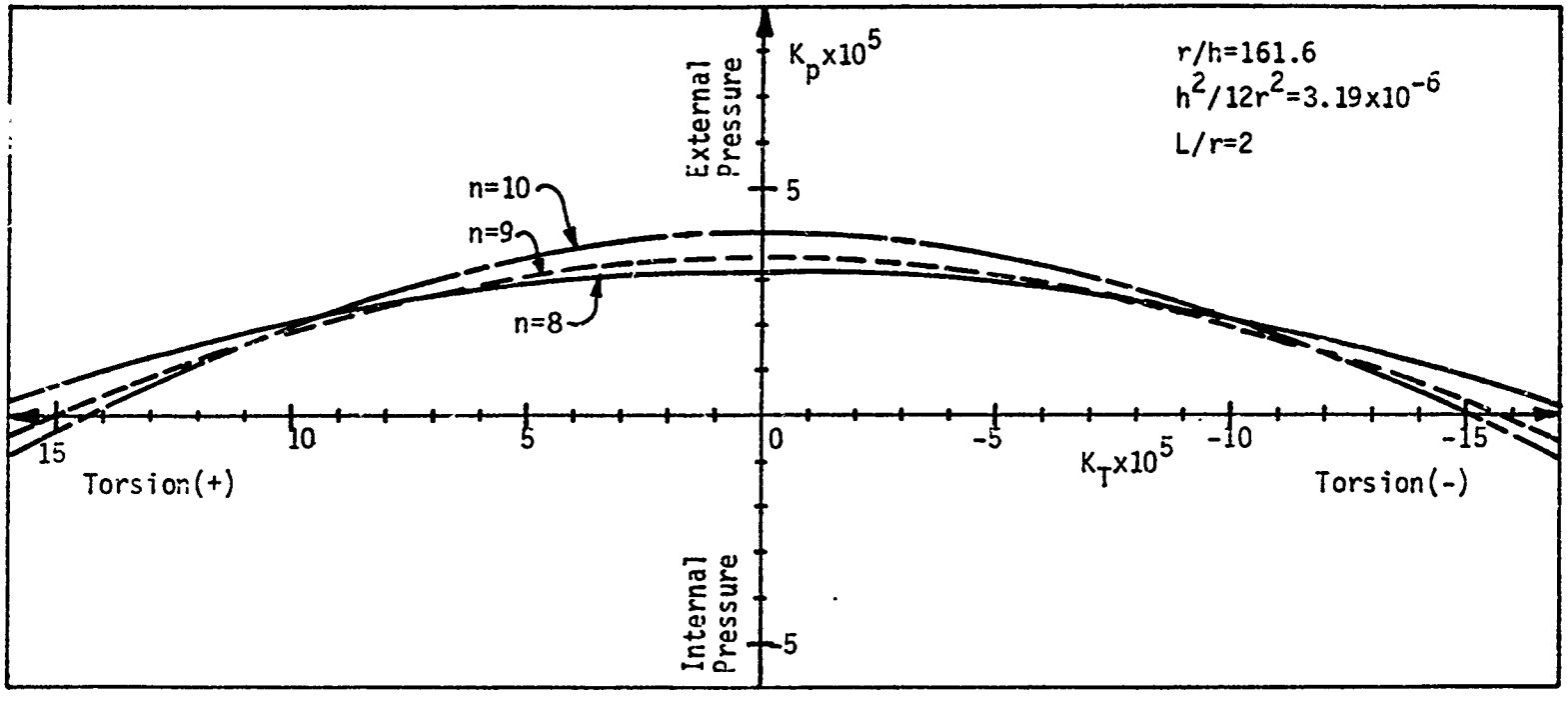

Figure 15. Buckling Load for Case 12: External Pressure Portion Enlarged

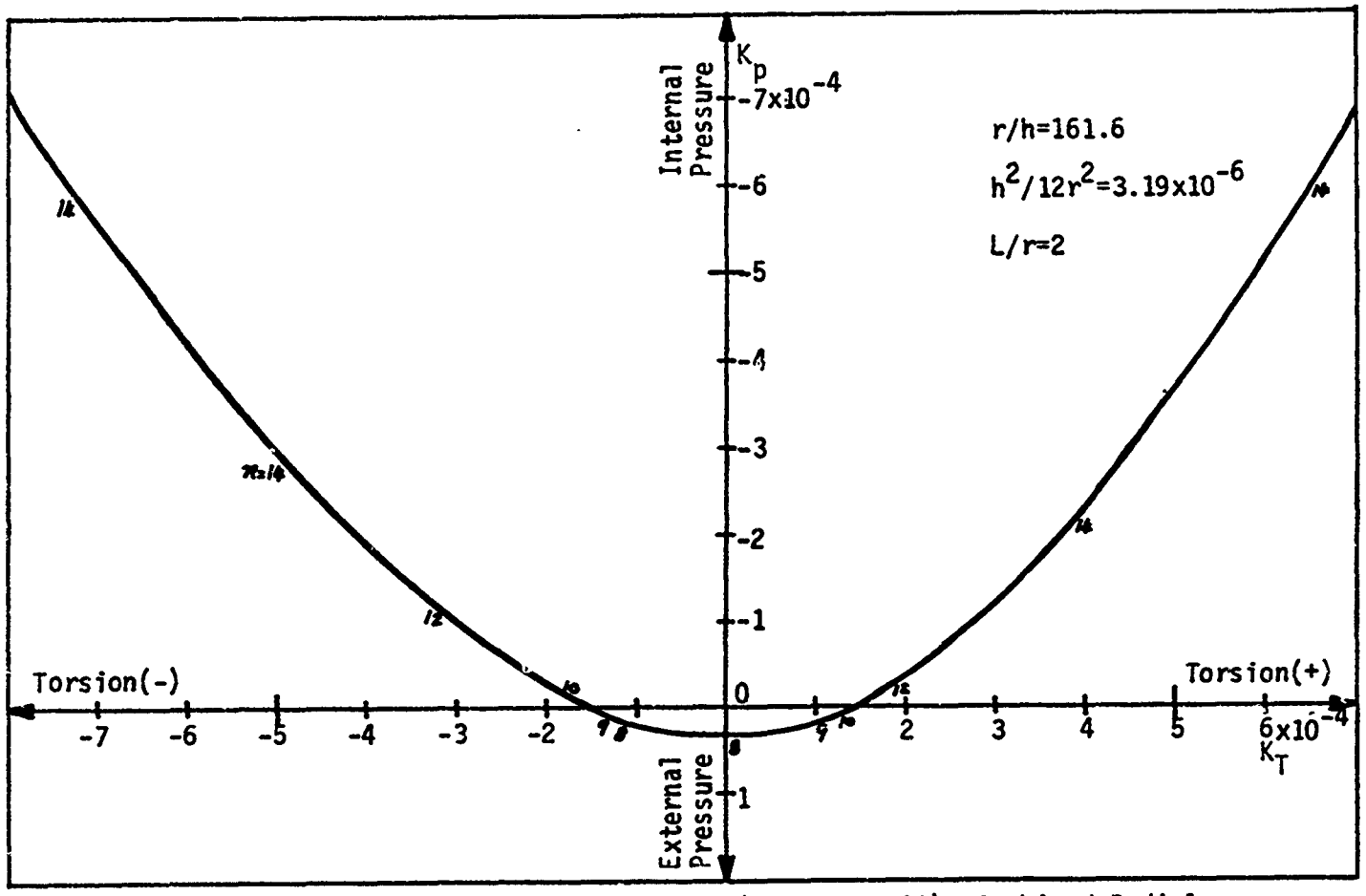

Figure 16.. Buckling Load for Case 13: 4(0, ∓22.5, 90), Combined Radial Pressure and Torsion, SS4, Flügge's Theory

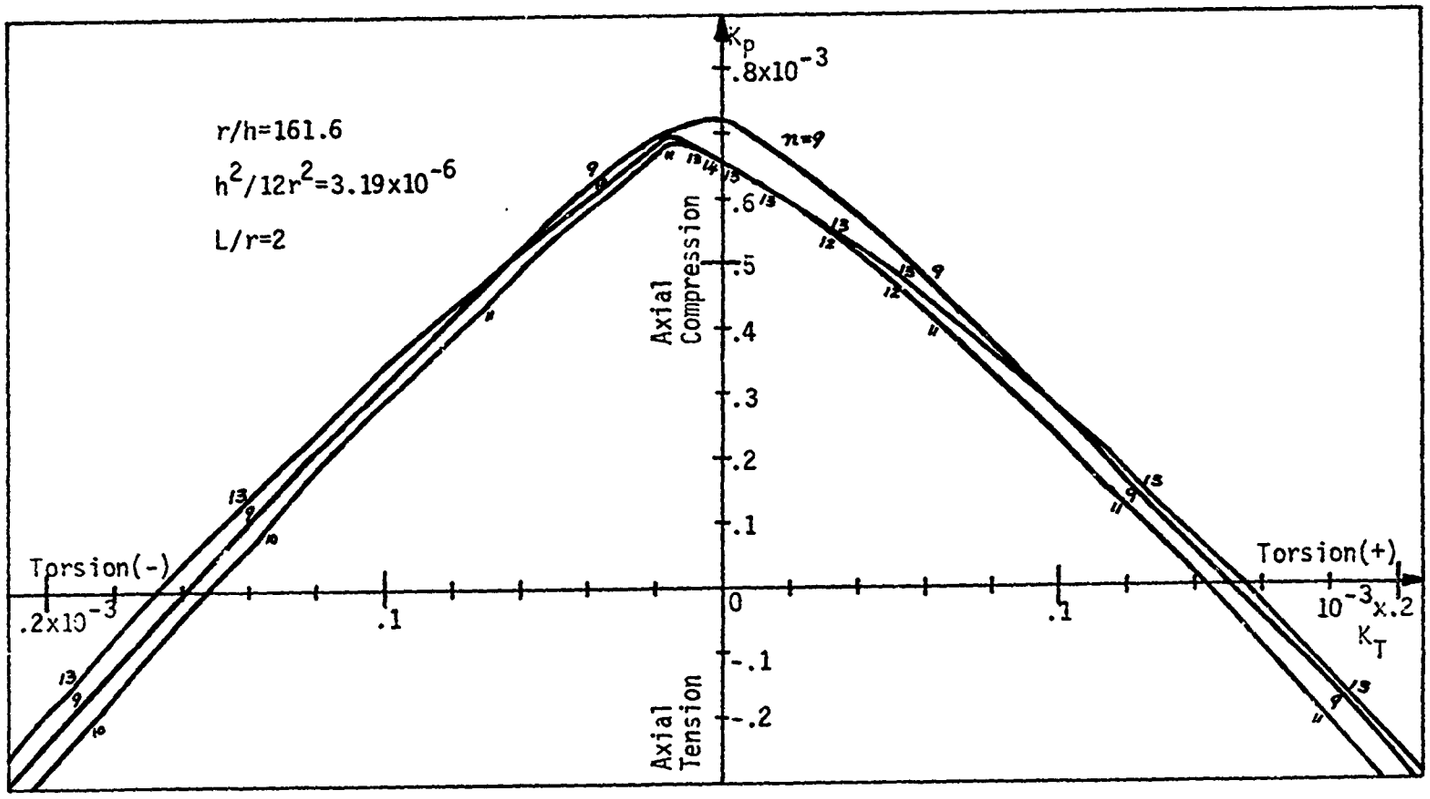

Figure 17. Buckling Load for Case 14: 4(0, ∓22.5, 90), Combined Axial Pressure and Torsion, SS4, Flugge's Theory

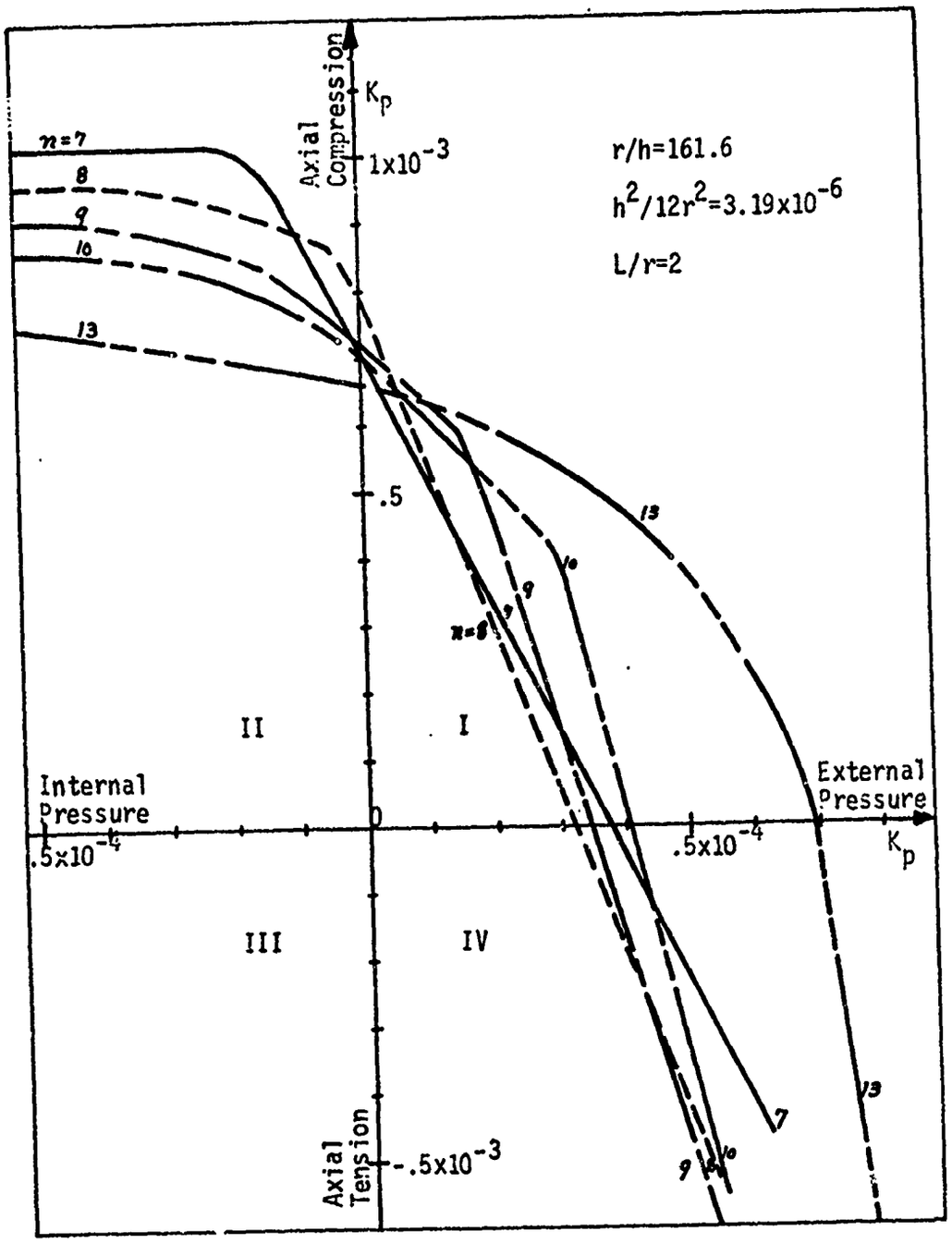

Figure 18. Buckling Load for Case 15: 4(0, ∓22.5, 90), Combined Axial Pressure and Radial Pressure, SS4, Flügge's Theory

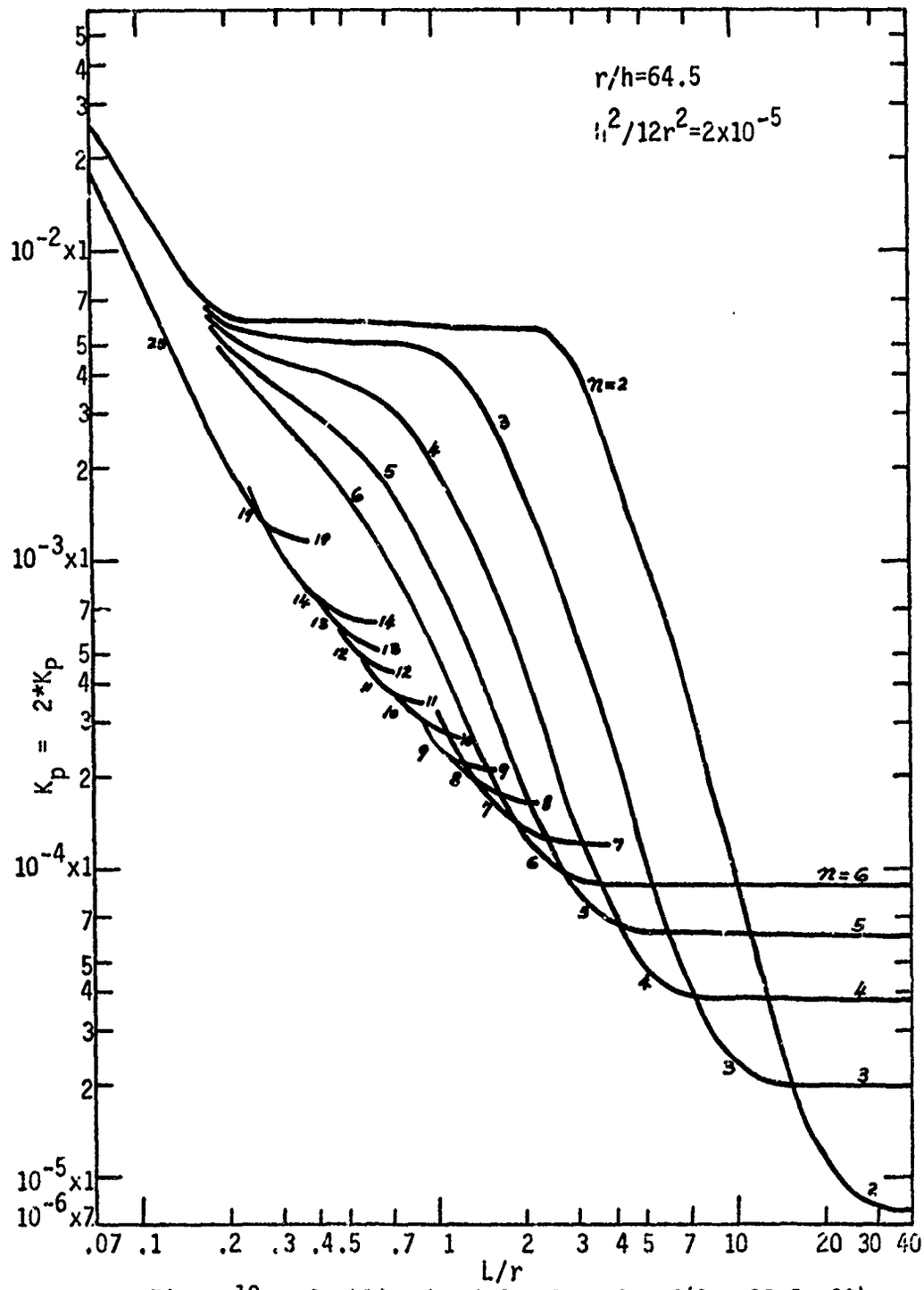

Figure 19. Buckling Load for Case 16: (0, ∓22.5, 90), Hydrostatic Pressure, SS4, Flügge's Theory

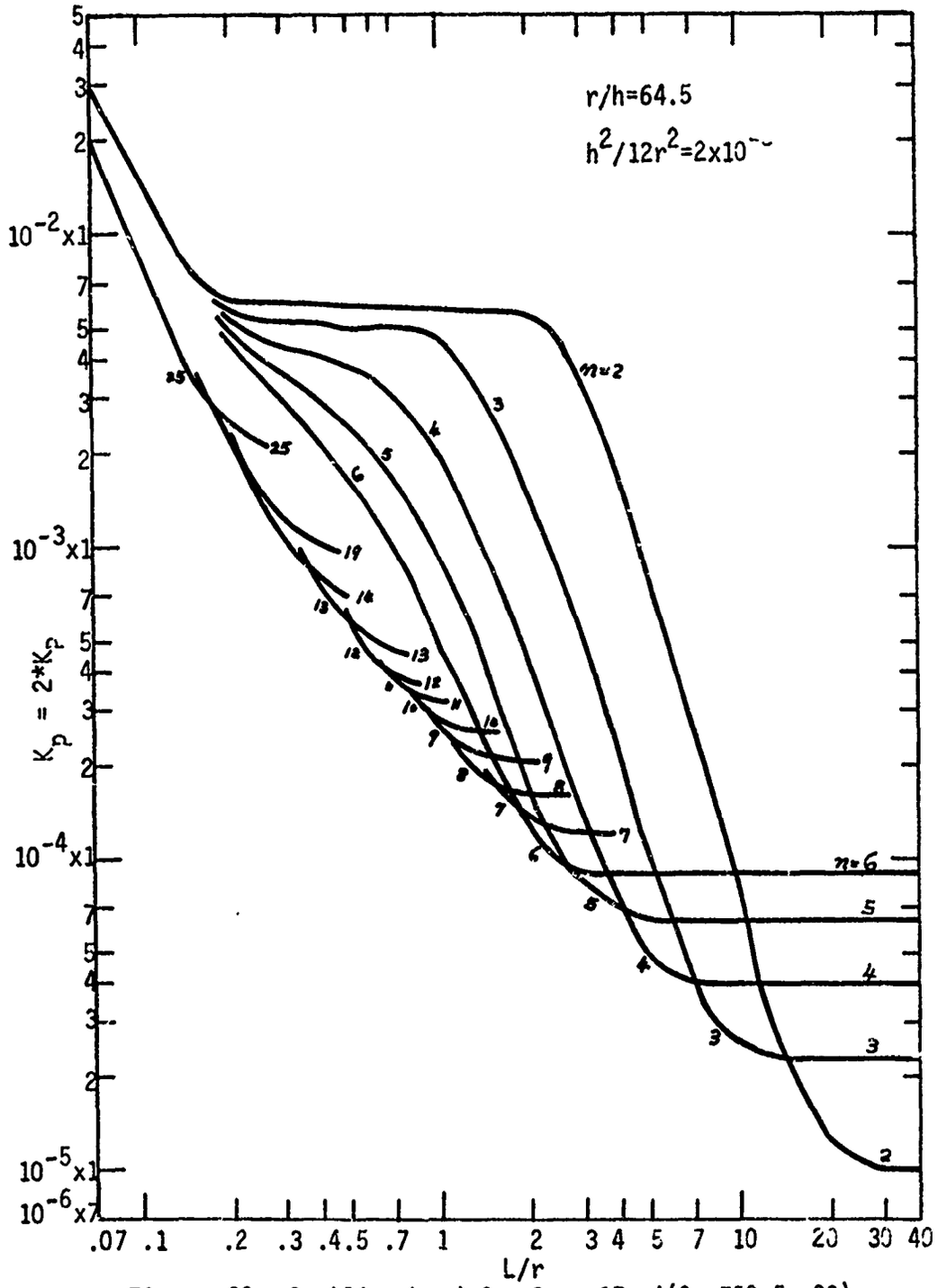

Figure 20. Buckling Load for Case 17: 4(0, ∓22.5, 90), Hydrostatic Pressure, SS4, Donnell's Theory

REFERENCES BY SECTION

REFERENCES FOR SECTION (III-A)

1. G. C. Cranch, "Unique Properties of Flexible Carbon Fibers," Proc. Fifth Conf. Carbon, Symposium Publication Div., Pergamon Press. New York, N. Y., 589 (1962).

2. R. Bacon and W. A. Schalamon, "Physical Properties of High Modulus Graphite Fibers Made from a Rayon Precursor," J. Appl. Polymer Science, Appl. Polymer Symposium. 9, 285 (1969).

3. R. Bacon, A. A. Pallozzi and S. E. Slosarik, "Carbon Filament Reinforced Composites," Proc. 21st Annual Technical Conf., S.P.I. Reinforced Plastics Division, Feb. 8-10, 1966.

4. J. W. Herrick, "Graphite Fiber Reinforced Ebony Composites," Advances in Structural Composites, Soc. Aerospace Material and Process Engineers, Vol. 12, Sec. AC-8 (1967).

5. D. W. Marshall, "The Effect of Certain Resin and Surface Variables on the Interlaminar Lap Shear Strength of Carbon Clothes," Advances in Structural Composites, Soc . Aerospace Material and Process Engineers, Vol. 12, Sec. P-7 (1967).

6. R. Sprague, "Serial Replication of Selected Areas of Carbon Fibers," J. Appl. Phys. 37, 3923 (1966).

7. S. C. Liang, "On the Calculation of Thermal Transpiration," J. Phys. Chem. 57, 910 (1953).

8. P. J. Moller and T. Fort, Jr. to be published.

9. J. O. Hirschfelder, C. F. Curtiss, and R. B. Bird, "Molecular Theory of Gases and Liquids," John Wiley Publishers. New York, N. Y. (1954).

10. J. Frenkel, "Kinetic Theory of Liquids," Clarendon Press, Oxford, V. K. (1946).

11. G. D. Halsey, "Physical Adsorption on Non-Uniform Surface," J. Chem. Phys. 16, 931 (1948).

12. T. L. Hill, "Statistical Mechanics of Multimolecular Adsorption. I and II," J. Chem. Phys. 14, 264, 441 (1946).

13. T. L. Hill, "Statistical Mechanics of Multimolecular Adsorption. III. Introductory Treatment of Horizontal Interactions, Capillary Condensation and Hysteresis," J. Chem. Phys. 15, 747 (1947).

14. T. L. Hill, "Statistical Mechanics of Adsorption. V. Thermodynamics and Heat of Adsorption," 17, 520, 668 (1949).

15. S. Brunauer, P. H. Emmett, and E. Teller, "Adsorption of Gases in Multimolecular Layers," J. Am. Chem. Soc. 60, 309 (1938).

16. P. H. Emmett and S. Brunauer, "The Use of Low Temperature van der Waals Adsorption Isotherms in Determing the Surface Areas of Various Adsorbents," J. Am. Chem. Soc. 59, 1553, 2682 (1937).

17. M. G. Kagamer, "A New Method for the Determination of Specific Adsorption Surface of Adsorbents and Other Finely Dispersed Substances," Zh. Fiz. Khim. 33, 2202 (1959).

18. C. Pierce, "The Universal Nitrogen Isotherm," J. Phys. Chem. 72, 3673 (1968).

19. B. C. Lippens, B.G. Linsen and J. H. de Boer, "Studies of Pore Systems in Catalysis. I. The Adsorption of Nitrogen; Apparatus and Calculations," J. Catalysis 3, 32 (1964).

20. R. Didchenko, "Carbon and Graphite Surface Properties Relevant to Fiber Reinforced Composites," AFML-TR-68-45 (1968).

21. T. L. Hill, "Thermodynamics of Adsorption," Trans. Faraday Soc. 47, 376 (1951).

22. T. L. Hill, "Theory of Physical Adsorption," Adv. Catalysis 4, 212 (1952).

23. D. H. Everett, "Thermodynamics of Adsorption. I. General Consideration," Trans. Faraday Soc. 46, 453 (1950).

24. R. A. Beebe et al., "Heats of Adsorption of Argon on a Series of Carbon Blacks Graphitized at Successively Higher Temperatures," J. Phys. Chem. 58, 93 (1954).

25. R. N. Smith, C. Pierce et al., "Area of Uniform Graphite Surfaces," J. Phys. Chem. 68, 2562 (1964).

26. G. D. Halsey et al., "Interaction of Single Argon Atoms with Graphitized Carbon Black P-33 (2700)", J. Chem. Phys. 27, 1433 (1957).

27. S. Ross and J. P. Olivier, "On Physical Adsorption," Interscience Publishers, New York, N. Y. (1964).

28. A. V. Kiselev et al., "Adsorption Isotherms of Nitrogen, Benzene and n-Hexane and the Heats of Adsorption of Benzene and n-Hexane on Graphitized Carbon Blacks. III. The Thermodynamic Characteristics of Adsorption Equilibria," J. Phys. Chem. 66, 210 (1962).

29. J. Rappeneau, A. F. Filliatre and M. Yvare, "Effects des Traitements Thermiques Sur La Structure de Ouelques Noirs de Carbone," Rev. Gen. Caoutchouc, 41, 394 (1964).

30. A. Fordeaux et al., "La Structure des Fibers de Carbone," C. R. Acad. Sci., Ser. C. 296, 1597, (1969).

31. R. Bacon and A. F. Silvaggi, "Microstructure of 'Ordinary' and High Modulus Carbon Fibers," Carbon 6, 230 (1968).

32. W. Ruland, "The Relationship between Preferred Orientation and Young's Modulus of Carbon Fibers," J. Appl. Polymer Sci., Appl. Polymer Symposium 9, 293 (1969).

33. E. Baer, M. Litt, J. Lando and J. Koenig, "New Concepts on Fiber-Matrix Interfacial Behavior for Composite Materials," 26th Ann. Tech. Conf., Reinforced Plastics/Composite Div., S.P.I., 1971.

34. R. Perret and W. Ruland, "Single and Multiple X-ray Small Angle Scattering of Carbon Fibers," J. Appl. Crystallography 2, 209 (1969).

35. M. H. Polley, W. D. Schaeffer and W. R. Smith, "Development of Adsorption Isotherms on Carbon Black Surfaces," J. Phys. Chem. 57, 496 (1953).

36. D. Graham, "Geometric Heterogeneity in the Adsorption of Nitrogen on Graphitized Carbon Surfaces," J. Phys. Chem. 61, 1310 (1957).

37. R. C. Fanning and J. N. Fleck, "Transverse Thermal Expansion Characteristics of Graphite Fibers," Tenth Biennial Conf. Carbon, June 22-July 2, 1971, Bethlehem, Pa.

38. L. G. Overholser and J. F. Blakely, "The Degassing Behavior of Commercial Graphites," Proc. Fifth Conf. Carbon, Symposium Publications Div., Pergamon Press, New York, N. Y., P. 194 (1962).

39. Y. A. Zarifyants, V. Z. F. Kiselev and O. Nikitima, "Synthesis and Functional Group Analysis of Oxygen Complexes on the Surface of Graphite," Doklady Akad. Nauk SSSR, 143, 1358 (1962).

40. D. W. McKee and V. J. Mimeault, "Surface Properties of Carbon-Graphite Fibers," Tenth Biennial Conf. Carbon, June 22-July 2, 1971, Bethlehem, Pa.

41. Th. Van dei Plas in B. G. Linsen Ed., "Physical and Chemical Aspects of Adsorbents and Catalysis, " Academic Press, New York, N. Y. (1970).

REFERENCES FOR SECTION (III-B)

1. R. Bacon, A. A. Pallozzi, and S. E. Slosarik, "Carbon Filament-Reinforced Composites," Proceedings of the 21st Annual Technical Conference, S.P.I. Reinforced Plastics Division (Feb. 8-10, 1966).

2. J. W. Herrick, P. E. Gruber and F. T. Mansur, "Surface Treatments for Fibrous Carbon Reinforcements," AFML-TR-66-178, Part I. AD 489187 (July 1966).

3. J. W. Herrick, "Surface Treatments for Fibrous Carbon Reinforcements," AFML-TR-66-178 (June 1967).

4. J. W. Herrick, "Graphite Fiber Reinforced Ebony Composites," Advances in Structural Composites, Society of Aerospace Material and Process Engineers, Vol. 12, Sec. AC-8 (1967).

5. R. A. Beebe, P. L. Evans, T. C. W. Kleinsteuber, and L. W. Richards, "Adsorption Isotherms and Heats of Adsorption by Frontal Analysis Chromatography," J. Phys. Chem., 70(4), 1009 (1966).

6. P. E. Eberly, Jr., "Measurement of Adsorption Isotherms and Surface Areas by Continuous Flow Method," J. Phys. Chem., 65, 1261 (1961).

7. J. J. Kipling and E. H. M. Wright, "Adsorption from Binary System of Limited Concentration Range: Application of Some Fundamental Concepts," J. Chem. Soc. (London), 855 (1962).

8. J. J. Kipling, "Adsorption from Solutions of Non-Electrolytes," Academic Press (1965). Chapter 7, Figure 7.24.

9. C. S. Brooks and D. A. Scola, "An Examination of the Surface Reactivity of Graphite Fibers by Gas-Solid Chromatography," J. Colloid and Interface Science, 32(4), 561 (1970).

10. R. Didchenko, "Carbon and Graphite Surface Properties Relevant to Fiber-Reinforced Composites," AFML-TR-68-45, Feb. (1968).

11. P. J. Moller and T. Fort, Jr. "Structure Analysis of Graphite Fiber Surfaces through Low Temperature Inert Gas Adsorption and Mass Spectrometry," Paper presented at the 45th National Colloid Symposium held at Atlanta, Georgia (June 21-23, 1971).

REFERENCES FOR SECTION IV-A

1. D. F. Adams and S. W. Tsai, "The Influence of Random Filament Packing on the Elastic Properties of Composite Materials," The Rand Corporation, RM-5608-PR (1968).

2. D. F. Adams and S. W. Tsai, "The Influence of Random Filament Packing on the Transverse Stiffness of Unidirectional Composites" Journal of Composite Ma erials, Vol. 3, 368-381, (1969).

3. D. F. Adams and D. R. Doner, "Longitudinal Shear Loading of a Unidirectional Composite," Journal of Composite Materials, Vol. 1, 4-17 (1967).

4. C. H. Chen, "Fiber-Reinforced Composites Under Longitudinal Shear Loading," Journal of Applied Mechanics, Vol. 37, Trans. A.S.M.E., Series E, Vol. 92, 198-208 (1970).

5. G. A. Van Fo Fy, "Stressed and Deformed State of Synthetic Materials in Shear" (in Russian), Prikladnaia Mekhanika, Vol. 1, No. 5, 111-119 (1965).

6. C. H. Chen and S. Cheng, "Mechaical Properties of Fiber Reinforced Composites," Journal of Composite Materials, Vol. 1, 30-41, (1967).

7. G. Pickett, "Elastic Moduli of Fiber Reinforced Plastic Composites" in (Schwartz & Schwartz, eds.) Fundemental Aspects of Fiber Reinforced Plastic Composites, Interscience Publishers, New York (1968), pp. 13-27.

8. R.L. Foye,"Advanced Design Concepts for Advanced Composite Airframes", AFML-TR-68-91, Vol. 1, (July 1968).

9. R. Hill, "Theory of Mechanical Properties of Fiber-Strengthened Materials: I. Elastic Behavior", J. Mech. Phys. Solids, Vol. 12, 213-218 (1964).

10. Z. Hashin and B. W. Rosen, "The Elastic Moduli of Fiber-Reinforced Materials", Journal of Applied Mechanics, Vol. 31, 223-232 (1964).

11. L. M. Milne-Thomson, Antiplane Elastic Systems, Springer-Verlag, Berlin, 1962.

12. G. P. Sendeckyj, "Multiple Circular Inclusion Problems in Longitudinal Shear Deformation," Submitted for publication.

13. R. Hill, "Elastic Properties of Reinforced Solids: Some Theoretical Principles," J. Mech. Phys. Solids, Vol. 11, 357-372 (1963).

14. E. T. Whittaker and G. N. Watson, A Course of Modern Analysis, 4th Edition, Cambridge University Press (1965).

15. C. B. Ling, "Evaluation at Half Periods of Weierstrass' Elliptic Function with Rectngular Primitive Period-Parallelogram", Mathematics of Computation, Vol. 14, No. 69, 67070 (Jan. 1960).

16. A. A. Kilchinskii, "Approximate Method for Determining the Relation Between the Stresses and Strains for Reinforced Materials of Fiber glass Type" (in Russian), Thermal Stresses in Elements of Construction, Vol. 6 (Naukova Dumka, Kiev: 1966), p. 123.

17. Z. Hashin, "Viscoelastic Fiber Reinforced Materials," AIAA Journal, Vol. 4, 14-1-1417 (1966).

18. N. E. Quackenbush and R. L. Thomas, "Investigation of Carbon Filament Reinforced Plastics," Philco-Ford, AD 820492 (1967).

19. G. T. Symm, "The Longitudinal Shear Modulus of a Unidirectional Fibrous Composite," Journal of Composite Materials, Vol. 4, 426-428 (1970).

20. R. L. Hewitt and M. C. Malhombe, "An Approximation for the Longitudinal Shear Modulus of Continusous Fibre Composites," Journal of Composite Materials, Vol. 4, 280-282 (1970).

21. G. A. Van Fo Fy and V. V. Klyavlin, "Investigation of Dependence of Mechanical Properties and Internal Stress Field on Shear on Type of Microstructure of Reinforced Media," (in Russian) Mekhanika Polimerov, Vol. 3, (1967), P. 667.

22. M. Abramowitz and I. A. Stegun, Handbook of Mathematical Functions, (Dover, New York: 1965).

REFERENCES FOR SECTION IV-B

1. G. P. Sendeckyj, "Elastic Inclusion Problems in Plate Elastostatics," Int. J. Solids Structures, Vol. 6, (1970), pp. 1535-43.

2. Ing-Wu Yu, "Multiple Circular Inclusion Problems in Plate Elastostatics," Ph.D. Dissertation, Case Western Reserve University (June 1971).

3. Ing-Wu Yu and G. P. Senueckyj, "Multiple Circular Inclusion Problems in Plate Elastostatics," submitted for publication.

4. G. P. Sendeckyj and Ing-Wu Yu, "Some Exact Results in Transverse Deformation of Fiber Reinforced Composites," submitted for publication.

5. I. S. Sokolnikoff, Mathematic Theory of Elasticity, 2nd Edition, (McGray-Hill:1956).

6. J. Dundurs, "Some Properties of Elastic Stresses in a Composite," in (A. C. Eringen, ed.) Recent Advances in Engineering Science, Vol. 5, Part 1, (1970), pp. 203-216.

7. A. E. Green and W. Zerna, Theroetical Elasticity, (Oxford, 1954).

8. G. P. Sendeckyj, "Longitudinal Shear Deformation of Composites - Effective Shear Modulus," Journal of Composite Materials, Vol. 5 (1971), pp. 82.

9. M. Abramowitz and I. A. Stegun, Handbook of Mathematical Functions, (Dover, New York: 1965).

10. I. M. Frantsevich and D. M. Karpanos, Composite Materials with Fibrous Structure (inRussian), (Nankova Dumka, Kiev: 1970).

11. R. L. Roye, "Advanced Design Concepts for Advanced Composite Airframes," AFML-TR-68-91, Vol. 1 (July 1968).

12. A. R. Forsyth, Theory of Functions of a Complex Variable, 3rd Edition, Vol. (Dover, New York), p. 150.

13. L. E. Hulbert and E. F. Rybicki, "Boundary Point Least Squares Analysis of the Free Edge Effects in Some Unidirectional Fiber Composites," Journal of Composite Materials, Vol. 5, (1971). p. 164.

REFERENCES FOR SECTION (IV-D)

1. G. R. Irwin, "Analysis of Stresses and Strain Near the End of a Crack Traversing a Plate," Journal of Applied Mechanics, Vol. 24, Trans ASME, Vol. 79, 1957, pp. 361-364.

2. G. C. Sih, P. C. Paris, G. R. Irwin, "On Cracks in Rectilinearly Anisotropic Bodies," International Journal of Fracture Mechanics, Vol. 1, No. 3, 1965.

3. E. M. Wu, "Application of Fracture Mechanics to Orthotropic Plates," T & AM Report No. 248, Univ. of Illinois, June, 1963.

4. D. D. Ang and M. L. Williams, "Combined Stresses in an Orthotropic Plate having a Finite Crack," Journal of Applied Mechanics, Sept. 1961, pp. 372-378.

5. A. N. Stroh, "Dislocations and Cracks in Anisotropic Elasticity," Philosophical Magazine, No. 3, 1958, pp. 625-646.

6. T. J. Willmore, "The Distribution of Stress in the Neighborhood of a Crack," Quarterly Journal of Mechanics and Applied Math, Vol. II, Part 1, 1949, pp. 53-63.

7. G. R. Irwin, "Analytical Aspects of Crack Stress Field Problems," University of Illinoise, T & AM Report No. 213, 1962.

8. C. Atkinson, "The Propagation of a Brittle Crack in Anisotropic Material," International Journal of Engineering Science, Vol. 3, pp. 77-91, Parmagon Press, 1965.

9. E. M. Wu, "Application of Fracture Mechanics to Anisotropic Plates," Journal of Applied Mechanics, 1967, pp. 1-8 .

10. B. Gross and J. E. Strawley, "Stress-Intensity Factors for Three-Point Bend Specimens by Boundary Collocation," Technical Note D-3092, NASA, December 1965.

11. E. M. Wu and R. C. Reuter, Jr., "Crack Extension in Fiberglass Reinforced Plastics, University of Illinois, T & AM No. 275, 1965.

12. J. B. Koeneman, "Interfiber Failure of Composite Materials," Ph.D. Thesis, Case Western Reserve University, December 1969.

13. T. C. Esselman, "An Experimental Study of the Fracture Properties of Composite Materials," M. S. Thesis, Case Western Reserve University, January 1971.

14. "Tentative Method of Test for Plain Strain Fracture Toughness of Metallic Materials," ASTM Designation E399-70T, 1970, Book of ASTM Standards.

REFERENCE FOR SECTION (V-A)

1. David P. Chan, "An Analytical Study of the Post Buckling of Laminated Anisotropic Plates. Ph.D. Thesis, Case Western Reserve University, September 1970.

REFERENCES FOR SECTION (V-B)

1. Islam, M. R., "Buckling and Post Buckling Strength of Anisotropic Plates," Ph.D. Thesis, Case Western Reserve University, Division of SMSMD, 1971.

2. Mandell, John F., "An Experimental Study of the Buckling of Anisotropic Plates," Report 23, Case Western Reserve University, Division of SMSMD, 1968.

3. Monforton, Gerard R., "Discrete Element Finite Displacement Analysis of Anisotropic Sandwich Shells," Ph.D. Thesis, Case Western Reserve University, 1970.

4. Chan, David P. "An Analytical Study of the Post Buckling of Laminated Anisotropic Plates," Ph.D. Thesis, Case Western Reserve University, 1970.

5. Koiter, W. T. "On the Stability of Elastic Equilibrium," NASA TTF-10, 883, 1967.

6. Von Karman, T., Sechler, E. E., and Donnell, L. H., "The Strength of Thin Plates in Compression," ASME Trans., APM-54-5, Vol. 54, No. 2, Jan. 30, 1932, pp. 53-57.

7. "Put the Strength and Stiffness Where You Need It," Reinforced Plastics Div., 3M Co.

8. Hoggatt, J. T., "Test Methods for High Modulus Carbon Yarn and Composites," Composite Materials Testing and Design, ASTM STP 460. America Society for Testing Materials, 1969, pp. 48-61.

9. Elkin, R. A., G. Fust and D. P. Hanley, "Characterization of Graphite Fiber/Resin Matrix Composites," ASTM STP 460, 1969, pp. 321-335.

10. Adsit, N. R. and J. D. Forest, "Compression Testing of Aluminum-Boron Composites," ASTM STP 460, 1969, pp. 108-121.

11. Data Sheets on Scotchply 1002, 3M Co., May 1, 1969.

12. Wu, E. M. and R. C. Reuter, Jr., "Crack Propagation in Fiberglass Reinforced Plastics," T & AM Report No. 275, Department of Theoretical and Applied Mechanics, Univ. of Illinois, 1965.

13. Tsai, S. W., "Experimental Determination of the Elastic Behavior of Orthotropic Plates," Journal of Engineering for Industry, August 1965, pp. 315-318.

14. Gerard, G., "Handbook of Structural Stability Part IV, Failure of Plates and Composite Elements," NACA TN 3784, 1957.

15. Anderson, R. A. and Anderson, M. S., "Correlation of Crippling Strength of Plate Structures with Material Properties," NACA TN 3600.

REFERENCES FOR SECTION (V-D)

1. Cheng, S., and Kuenzi, E. W., "Buckling of Orthotropic or Plywood Cylindrical Shells under External Radial Pressure," Proceedings of the 5th International Symposium on Space Technology and Science, Tokyo, 1963, pp. 527-542.

2. Hess, T. E., "Stability of Orthotropic Cylindrical Shells Under Combined Loading," ARS Journal, Vol. 31, No. 2, February 1961, pp. 237-246.

3. Thielemann, W. F., Schnell, W., and Fischer, G., "Buckling and Post Buckling Behavior of Orthotropic Circular Cylindrical Shells Subject to Combined Axial and Internal Pressure," Zeitschrift Für Flugwissenschaften, Vol. 8, No. 10/11, 1960, pp. 284-293.

4. Schnell, W., and Brühl, C., "Die längsgedrückte orthotrope Kreiszylinderschale bie Innendruck," Zeitschrift für Flugwissenschaften, Vol. 7, (1969), No. 7. pp. 201-207.

5. Tsai, J., "Effect of Heterogeneity on the Stability of Composite Cylindrical Shells Under Axial Compression," AIAA Journal, Vol. 4, No. 6, (June 1966), pp. 1058-1062.

6. Cheng, S. and Ho, B. P. C., "Stability of Heterogeneous Aeolotropic Cylindrical Shells Under Combined Loading," AIAA Journal, Vol. 1, No. 4, pp. 892-898 (1963).

7. Ho, B. P. C. and Cheng, S., "Some Problems in Stability of Heterogeneous Aeolotropic Cylindrical Shells Under Combined Loading," AIAA Journal, Vol., No. 7, pp. 1603-1607 (1963).

8. Tsai, J., Feldman, A., and Stang, D. A. "The Buckling Strength of Filament-Wound Cylinders Under Axial Compression," CR-266, NASA, July 1965.

9. Lei, M. M., and Cheng, S., "Buckling of Composite and Homogeneous Isotropic Cylindrical Shells Under Axial and Radial Loading," Journal of Applied Mechanics, Transactions of ASME, Vol. 36, No. 12, pp. 791-798, (December 1969).

10. Flügge, W., Stresses in Shells, Springer-Verlag, Berlin, 1962.

11. McCalla, T. R., Introduction to Numerical Methods and FORTRAN Programming, John Wiley & Sons, New York, 1967.

12. Hoff, N. J., "The Accuracy of Donnell's Equations," Journal of Applied Mechanics, Vol. 22, No. 3, Transctions ASME, Vol. 77, (September 1955), pp. 329-344.

13. Hoff, M. J., "Low Buckling Stresses of Axially Compressed Circular Cylindrical Shells of Finite Length," Journal of Applied Mechanics, Transactions of ASME, Vol. 32, No. 9, (September 1965), pp. 533-541.